UNIVERSIDAD DE ALCALÁ

ESCUELA POLITÉCNICA SUPERIOR

Programa de Doctorado en Electrónica

Sistemas Electrónicos Avanzados. Sistemas Inteligentes

Doctoral Thesis

Infrared Ranging in Multipath Environments for Indoor Localization of Mobile Targets

David Salido Monzú

2015

UNIVERSIDAD DE ALCALÁ

ESCUELA POLITÉCNICA SUPERIOR

Programa de Doctorado en Electrónica

Sistemas Electrónicos Avanzados. Sistemas Inteligentes

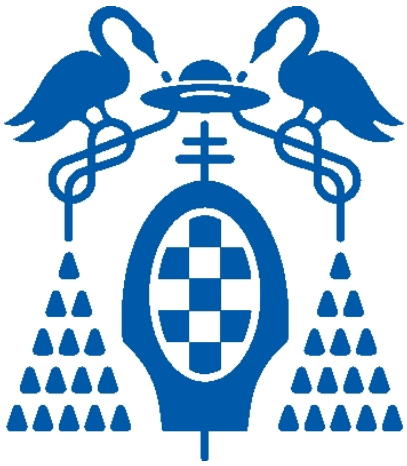

Infrared Ranging in Multipath Environments for Indoor Localization of Mobile Targets

Author

David Salido Monzú

Supervisors

Dr. José Luis Lázaro Galilea

Dr. Ernesto Martín Gorostiza

2015

Doctoral Thesis

A mi madre y a mi padre,
por lo que han sido, son y serán para mí.

"Andaluces de Jaén,
aceituneros altivos,
decidme en el alma: ¿quién,
quién levantó los olivos?"

Miguel Hernández

Agradecimientos

A mis padres, por haberme dado lo necesario con mayúsculas, por haber sabido siempre distinguirlo, porque lo que tengo de valor en mi interior es un regalo suyo; mis raíces y mis alas.

A Elena, por haber crecido conmigo, por haberme ayudado a crecer, por estar tan viva, porque me ha enseñado más de lo que podré explicarle nunca, por todo lo que nos queda.

A mi familia, por hacerme sentir cosas tan injustas como que la justicia es que todo el mundo tenga una familia como la mía; por estar siempre, siempre, siempre.

A Ernesto Martín, porque un día confió en mí y no me ha dejado en paz desde entonces, por acompañarme en este viaje y enseñarme tanto.

A José Luis Lázaro por no haber dejado de apoyarme desde que entré por la puerta del laboratorio hace decenas de años, por aconsejarme y enseñarme a avanzar cuando parece que no hay camino.

A los profesores, profesoras y personal del departamento que me han ayudado y mostrado su apoyo durante estos años, por hacer de la escuela un sitio al que venir. A los compañeros de este camino, los perennes habitantes del fondo 21 y 33 y demás espacios inteligentes del edificio; todos los que, a base de compartir penas y dudas y cenas y risas han dejado de ser compañeros: a mis amigos de la escuela.

A todos los que han colaborado para aportar rigor técnico a la tesis, en especial a Javier Meca, Francisco Escribano y Eduardo Martos por las interesantísimas conversaciones técnicas y personales, por ayudar tanto y siempre tan fácilmente.

A los estudiantes que han colaborado conmigo durante estos años y me han ayudado mucho más allá de su interés, en especial a Álvaro de la Llana por hacer las cosas tan fáciles y esforzarse en ayudarme disimulando el esfuerzo.

To Andreas Wieser for his confidence, support and advice, and the people at ETH for making me feel at home from the very first day. To the people at Max Planck for their inspiring ideas, support and warm welcome. A Alejandro Durán por guiarme a través del entrenamiento de guerrilla y convertirse en mi amigo, por ayudarme tanto.

A Raquel, por ser la calma, la sonrisa y el hombro de cada día.

A mis amigos, porque después de todo y de tanto, lo son cada vez más; porque el mundo apenas tendría sentido sin mi puñadito de personas importantes.

Y a Dane, por aparecer donde menos la esperaba, por aparecer; por saber atravesar el océano cada minuto para apoyarme e ilusionarme incondicionalmente; por lo que nos viene.

Resumen

Esta tesis aborda el problema de la medida de diferencias de distancia mediante señales ópticas afectadas por multicamino, aplicada a la localización de agentes móviles en espacios interiores.

Los avances en robótica, entornos inteligentes y vehículos autónomos han creado un campo de aplicación específico para la localización en interiores, cuyos requerimientos de precisión (en el rango de los cm) son muy superiores a los demandados por las aplicaciones de localización orientadas a personas, en cuyo contexto se han desarrollado la mayor parte de las alternativas tecnológicas. La investigación con métodos de geometría proyectiva basados en cámaras y de multilateración basados en medida de distancia con señales de radiofrecuencia de banda ancha, de ultrasonido y ópticas han demostrado un rendimiento potencial adecuado para cubrir estos requerimientos. Sin embargo, todas estas alternativas, aún en fase de investigación, presentan dificultades que limitan su aplicación práctica. En el caso de los sistemas ópticos, escasamente estudiados en este contexto, los trabajos previos se han basado en medidas de diferencia de fase de llegada de señales infrarrojas moduladas sinusoidalmente en intensidad. Una infraestructura centralizada computa medidas diferenciales, entre receptores fijos, de la señal emitida desde el móvil a posicionar, y calcula la posición del móvil mediante trilateración hiperbólica a partir de éstas. Estas investigaciones demostraron que se pueden alcanzar precisiones de pocos centímetros; sin embargo, las interferencias por multicamino debidas a la reflexión de la señal óptica en superficies del entorno pueden degradar esta precisión hasta las decenas de centímetros dependiendo de las características del espacio. Así pues, el efecto del multicamino es actualmente la principal fuente de error en esta tecnología, y por tanto, la principal barrera a superar para su implementación en situaciones reales.

En esta tesis se propone y analiza un sistema de medida con señales ópticas que permite obtener estimaciones de diferencias de distancia precisas reduciendo el efecto crítico del multicamino. El sistema propuesto introduce una modulación con secuencias de ruido pseudoaleatorio sobre la modulación sinusoidal típicamente usada para medida de fase por onda continua, y aprovecha las propiedades de ensanchamiento en frecuencia de estas secuencias para reducir el efecto del multicamino. El sistema, que realiza una doble estimación de tiempo y fase de llegada, está compuesto por una etapa de sincronización que posibilita la demodulación parcialmente coherente de la señal recibida, seguida de un medidor diferencial de fase sobre las componentes desensanchadas tras la demodulación. Las condiciones de multicamino óptico típicas en espacios interiores, con una componente de camino directo claramente dominante, permiten que el proceso de demodulación recupere más potencia del camino directo que del resto de contribuciones, reduciendo el efecto del multicamino en la estimación final.

Todas las etapas del sistema han sido diseñadas y evaluadas individualmente teniendo en cuenta el efecto de las contribuciones dominantes de error: ruido, multicamino y efectos dinámicos introducidos tanto por el desplazamiento del móvil a posicionar como por la asincronía entre emisor y receptores. Las pruebas se han realizado con una implementación digital del sistema propuesto y señales de entrada generadas con una plataforma de emulación de enlace óptico. Los resultados demuestran que con los dispositivos disponibles actualmente y utilizando una configuración con receptores separados 3.5 m, se puede obtener un error total debido a ruido y efectos dinámicos inferior a 10 cm en un 90% de las medidas, para un rango amplio de alturas prácticas y permitiendo velocidades del móvil de hasta 1 m/s. La evaluación de la propuesta en condiciones de multicamino demuestra que la capacidad de mitigación del sistema está fuertemente condicionada por el ancho de banda del enlace óptico y la altura del entorno de localización. Así, con el rendimiento de un enlace actualmente viable, se obtienen ratios de mitigación inferiores al 20% respecto a un sistema de medida de fase estándar operando en las mismas condiciones, cuando la altura del entorno es inferior a 3 m. Sin embargo, en entornos cuya altura es superior a 4 m, el ratio de mitigación se encuentra entre el 70% y el 95%, reduciendo el error de multicamino por debajo de 1 cm en la gran mayoría de las situaciones.

Los resultados obtenidos demuestran que la aplicación del método propuesto permitiría realizar posicionamiento a partir de señales ópticas con el rendimiento adecuando para aplicaciones de robótica y guiado de vehículos en espacios interiores; además, el progresivo aumento de la potencia y el ancho de banda de los dispositivos optoelectrónicos disponibles permite esperar un incremento considerable de las prestaciones de la propuesta en los próximos años.

Contacto: David Salido Monzú <david.salido@depeca.uah.es>.

Abstract

This dissertation focusses on the problem of the measurement of distance differences with optical signals affected by multipath, applied to indoor localization of mobile targets.

Last advances in robotics, intelligent environments and autonomous vehicles have created a specific application field for indoor localization. Accuracy requirements in this context (in the cm level) are much stronger than the ones needed in human-oriented systems, which draw most of the technological development interest. Research on projective geometry methods (based on cameras) and multilateration (used with ultrawideband radiofrequency signals, ultrasounds and optical signals), have demonstrated potential performance to meet these requirements. However, all the alternatives, still under research, find some limitations when applied to real scenarios. Regarding optical systems, less studied in this context, previous works have been based on the measurement of differential phase of arrival using sinusoidally-modulated infrared signals. A centralized infrastructure computes the phase differences between fixed receivers from a signal emitted by the mobile target. The position is then obtained by hyperbolic trilateration. This research showed that precisions of few cm are achievable but, depending on the environment features, multipath interferences due to signal reflection in the surfaces may reduce accuracy up to tens of cm. Therefore, multipath effects are currently the main error source in this approach and, in consequence, the main handicap towards its practical implementation.

In this thesis, a system to obtain accurate distance difference estimations reducing the critical effect of multipath is proposed. The approach is based on performing a pseudo random noise modulation on the sinusoidally-modulated signal typically used for continuous wave phase measurement, making use of the frequency spreading properties of these sequences to reduce multipath. The system, which sequentially performs a time and phase of arrival estimation, is composed of a synchronization stage, which enables partially coherent demodulation of the received signal, followed by a differential phase meter operating with the components dispread in the demodulation. Typical optical indoor multipath situations, with a clearly dominant line-of-sight component, allow the demodulation stage to recover higher amount of power from this contribution than from any other, consequently reducing multipath effects in the final estimation.

All stages of the system have been designed and tested taking into account the relevant error sources: noise, multipath and dynamic effects due to target movement and emitter-receiver asynchronous operation. Tests have been carried out on a digital implementation of the proposed system and input signals have been generated with an emulation platform of the optical link. The results show that, considering the properties of up-to-date devices and with receivers separated 3.5 m, a global error below 10 cm is obtained in 90% of the cases, including noise

and dynamic effects, for a wide room-height range and target velocities up to 1 m/s. Multipath tests demonstrate that the mitigation capabilities of the system are strongly conditioned by the optical link bandwidth and the environment height. Therefore, with the features of a currently available link, mitigation ratios bellow 20%, with respect to a standard phase measuring system operating in the same conditions, are obtained if the height is lower than 3 m. However, for environments with height greater than 4 m the mitigation ratio is between 70% and 95%, reducing multipath errors below 1 cm in most cases.

The results obtained show that the application of the proposed method would contribute to enabling indoor localization using optical signals with an adequate performance for robotic and vehicle guidance applications. Furthermore, a significant improvement in the performance of the proposal is expectable in next years due to the progressive increase in the power and bandwidth of optoelectronic devices.

Contact: David Salido Monzú <david.salido@depeca.uah.es>.

Contents

List of Figures

List of Tables

List of Acronyms

3D	Three Dimensions.
AAF	Anti-Aliasing Filter.
AAL	Ambient Assisted Living.
ADC	Analog-to-Digital Converter.
AFG	Arbitrary Function Generator.
AGNSS	Assisted Global Navigation Satellite System.
AoA	Angle of Arrival.
APD	Avalanche Photodiode.
ASIC	Application-Specific Integrated Circuit.
AWGN	Additive White Gaussian Noise.
BOC	Binary Offset Carrier.
BPSK	Binary Phase-Shift Keying.
CADLL	Coupled Amplitude Delay-Locked Loop.
CCD	Charge-Coupled Device.
CDMA	Code Division Multiple Access.
Cell-ID	Cell Identification.
CFDR	Coherent Frequency Domain Reflectometry.
CoO	Cell of Origin.
CRLB	Cramér-Rao Lower Bound.
CSS	Complementary Sets of Sequences.
CV	Computer Vision.
CW	Continuous Wave.
D/A	Digital-to-Analog.
DA	Deconvolution Approach.
DBPSK	Differential Binary Phase-Shift Keying.
DC	Direct Current.

DLL	Delay-Locked Loop.
DSSS	Direct-Sequence Spread Spectrum.
DToA	Differential Time of Arrival.
EDM	Electronic Distance Measurement.
EKF	Extended Kalman Filter.
ELDLL	Early-Late Delay-Locked Loop.
FCC	Federal Communications Commission.
FDMA	Frequency Division Multiple Access.
FFT	Fast Fourier Transform.
FHSS	Frequency Hopping Spread Spectrum.
FM	Frequency Modulation.
FMCW	Frequency Modulated Continuous Wave.
FoV	Field of View.
FPGA	Field Programmable Gate Array.
FSF	Frequency-Shifted Feedback.
GNSS	Global Navigation Satellite System.
GPS	Global Positioning System.
GSM	Global System for Mobile Communications.
HSGNSS	High Sensitive Global Navigation Satellite System.
HW	Hardware.
I/Q	In-Phase and Quadrature.
IMDD	Intensity Modulation Direct Detection.
IMU	Inertial Measurement Unit.
IR	Infrared.
IR-UWB	Impulse-Radio Ultrawideband.
JBSF	Jump Back and Search Forward.
KF	Kalman Filter.
LBS	Location Based Service.
LED	Light-Emitting Diode.
LFSR	Linear Feedback Shift Register.
LIDAR	Light Detection and Ranging.

LIGO	Laser Interferometer Gravitational-Wave Observatory.
LISA	Laser Interferometer Space Antenna.
LOS	Line-of-Sight.
LPS	Local Positioning System.
LS	Least Squares.
LTI	Linear Time-Invariant.
MEDLL	Multipath Estimating Delay-Locked Loop.
ML	Maximum Likelihood.
MLS	Maximum Length Sequence.
MUSIC	Multiple Signal Classification.
NLOS	Non-Line-of-Sight.
OFDR	Optical Frequency Domain Reflectometry.
PC	Personal Computer.
PLL	Phase-Locked Loop.
PoA	Phase of Arrival.
POCS	Projection onto Convex Sets.
PRN	Pseudo Random Noise.
PSD	Power Spectral Density.
RADAR	Radio Detection and Ranging.
RAIM	Receiver Autonomous Integrity Monitoring.
RF	Radio Frequency.
RFID	Radio Frequency Identification.
RSS	Received Signal Strength.
RSSI	Received Signal Strength Indicator.
SBS	Serial Backward Search.
SINAD	Signal-to-Noise and Distortion Ratio.
SLAM	Simultaneous Localization and Mapping.
SW	Software.
TCXO	Temperature-Controlled Crystal Oscillator.
TDC	Time-to-Digital Converter.
TDMA	Time Division Multiple Access.
ToA	Time of Arrival.

ToF	Time of Flight.
TWR	Two-Way Ranging.
US	Ultrasound.
UWB	Ultrawideband.
VLC	Visible Light Communication.
WLAN	Wireless Local Area Network.

Chapter 1

Preface

1.1 Introduction

The last two decades have seen a growing interest on the development of indoor localization technologies. The number of potential applications that require information about the location of a person or mobile target in indoor scenarios is rapidly increasing nowadays, partly as a natural extension of GNSS[1]-based outdoor localization but also as an area with an specific scope. These applications cover diverse fields such as pedestrian navigation, LBSs[2], emergency response, AAL[3] or machine, robot and autonomous vehicle guidance [Mautz, 2012]. This has motivated a sustained research effort to develop alternatives that provide practical indoor localization. There is currently a wide variety of solutions based on different technologies such as inertial sensors [Harle, 2013, Skog et al., 2010], RF[4] signals both from established communication networks like WLAN[5] [Liu et al., 2007] and GSM[6] [Varshavsky et al., 2007], or specifically deployed infrastructures like RFID[7] [Saad and Nakad, 2011], pseudolites [Barnes et al., 2002, Wan and Zhan, 2011] or some UWB[8] systems [Kuhn et al., 2010, Zhou et al., 2011]. There are also extensive works on systems based on cameras [Mautz and Tilch, 2011] and US[9] [Ward et al., 1997, Priyantha, 2005], and, to a lesser extent, using optical signals [Want et al., 1992, Nasipuri and El Najjar, 2006]. Unlike outdoor localization, where GNSS-based solutions cover most application requirements, there is not a dominant technology in its indoor counterpart, and the suitability of the different alternatives is strongly dependent on the specific application demands.

It is worth highlighting the high number of human-centered applications under development based on WLANs in offices or public spaces such as leisure centers, museums or airports, which provide very convenient localization solutions for smartphones with adequate results for a wide range of services. These systems present very interesting advantages such as the very cheap

[1] Global Navigation Satellite System
[2] Location Based Services
[3] Ambient Assisted Living
[4] Radio Frequency
[5] Wireless Local Area Network
[6] Global System for Mobile Communications
[7] Radio Frequency Identification
[8] Ultrawideband
[9] Ultrasound

adaptability to the infrastructure and the easy accessibility for the user; they, however, lack the required precision for more demanding applications where the integration of mobile units in complex environments is required.

The increasing interest in indoor localization is also related with the expanding research area of intelligent spaces. This concept, addressed also by other terms such as smart environments or context-aware spaces, has evolved from the annals of ubiquitous computing established in the late eighties. Intelligent spaces are human-centered environments able to acquire information, process it and take decisions that lead to some action to provide a service to the users in the space. The design of these spaces is guided by the concept of affordance in the sense of intuitive and organic interaction with the user. Localization systems have been naturally incorporated to this kind of spaces as fundamental sensorial systems, gaining even more relevance with the growing inclusion of mobile robotics as basic actuator units [Hashimoto, 2005].

In addition to the application of localization for robotics derived from the intelligent space concept, the tendency towards highly automated manufacturing environments and warehouses in modern industries, and the increasing research on intelligent transport systems, promotes this specific and very attractive application field for indoor localization. Applications in those contexts are mainly related to navigation of mobile robots or autonomous vehicles, what creates some very specific requirements. Unlike most human-centered applications, which can operate properly with accuracies in the meter level and update rates of some seconds, automated navigation requires more accurate, fast and reliable localization solutions, with accuracies in the cm level and sub-second update rates. The research approaches that have focused on this context and demonstrated potential to reach those requirements are either based on projective geometry using cameras [Fernández et al., 2007, Pizarro et al., 2009], or on multilateration approaches using range information delivered by UWB [González et al., 2009, Segura et al., 2010], pseudolites [Rizos et al., 2010] and US systems [Ureña et al., 2007, Kim and Kim, 2013].

On the other hand, optical ranging in its various alternatives is the technology of reference in industrial metrology and surveying. Geodetic instruments such as laser trackers, laser scanners, theodolites or total stations can provide accuracies in the order of tens of μm operating in typical indoor environments. This range information, applied in a multilateration approach, would translate into sub-mm positioning accuracies. Despite this excellent performance, geodetic instruments are rarely considered as a practical indoor localization solution given their high price and complexity, what makes them only suitable for critical indoor construction and industrial manufacturing problems.

The lack of specific studies on the application of optical ranging to indoor localization, focused on finding an efficient balance between performance and reduced costs, motivated the research in [Martín-Gorostiza et al., 2010, Martín-Gorostiza, 2011, Martín-Gorostiza et al., 2011], which form the direct background of this thesis. These works studied the possibility of performing accurate and fast indoor localization in the cm level using IR[10] ranging with a DToA[11] approach, where differential phase shifts were measured on the signals propagating from the target to pairs of fixed receivers in the ceiling of the environment. This configuration using differential computations

[10] Infrared
[11] Differential Time of Arrival

is very convenient for robotics applications, enabling to keep the hardware boarded on the robot simple and independent from the infrastructure. All the signal processing and position computation is performed in the environment, and synchronism is achieved between receivers independently from the emitter. On the other hand, the use of PoA[12] ranging instead of direct ToF[13] measurements allows to maximize the use of the optical link, providing better accuracy than a time-based approach considering indoor ranges and available bandwidth in free-space IR links that fulfill the application requirements.

The results achieved in these works showed a promising potential in this technological approach to implement indoor localization for demanding applications, yielding positioning errors below 2.5 cm with tens of ms update-rates, with a cost wise competitive solution compared to alternatives with similar performance. However, multipath effects were identified as a critical source of error, affecting the position error at the cm to dm level depending on the environment geometry and reflective properties. The mitigation of this error is, therefore, a key step to enable practical implementations of the proposed technology.

This thesis is centered on addressing this problem by defining a measuring method that reduces the critical impact of multipath interferences on the measurement accuracy in IR ranging applied to indoor localization, while still providing precise multiuser estimations with a practical implementation in terms of reproducibility and calibration requirements.

Multipath effects are a relevant source of error in several localization and ranging technologies. It has been extensively studied in GNSSs, where typical mitigation approaches in the measurement system level are either focused on the design of tracking stages that provide inherent multipath rejection using special signal and correlator designs [Van Dierendonck et al., 1992, Braasch, 2001] or on multiparameter estimation techniques that can resolve the simultaneous measurement of LOS[14] and NLOS[15] components [van Nee, 1992, Fenton and Jones, 2005]. The latter has become more popular in the last years due its higher efficiency when applied to high performance receivers, although these methods require some a priori information on the approximate multipath situation in terms of the number of relevant multipath components. The multipath problem has been also addressed in the context of UWB technology applied to ranging and localization, exploiting the high signal bandwidth to apply estimation algorithms for time-resolved multipath cancellation [Dardari et al., 2009] or ranging in NLOS situations [Wu et al., 2007]. In the optical domain, multipath has been studied in high sensitivity interferometric displacement metrology. Scattered light, leakages and doubly-reflected beams cause multipath effects, usually referred to as cyclic errors, that limit the ranging accuracy. BPSK[16] modulation of the optical carrier with PRN[17] has been proposed in this context to reduce multipath or perform multiple delay estimations in a single receiver by exploiting the properties of the coherent/non-coherent demodulation of the interference signals [Lay et al., 2007, Isleif et al., 2014]. These methods provide good multipath rejection on bandlimited receivers, although an

[12] Phase of Arrival
[13] Time of Flight
[14] Line-of-Sight
[15] Non-Line-of-Sight
[16] Binary Phase-Shift Keying
[17] Pseudo Random Noise

approximate knowledge of the expected LOS delay is required.

Bandwidth limitation is a determining factor in the analysis of the non-coherent and non-directional ranging problem in the context of this work. The starting point of the multipath mitigation study in this work was to attempt to maintain a PoA approach to the extent possible, given its better performance under strict frequency limitations than a direct time-based method. The solution proposed in this thesis relies on applying a PRN modulation on the sinusoidal intensity modulated ranging signal and exploiting the power despreading that occurs in a coherent demodulation process to enhance the power of the LOS component prior a standard sinusoidal PoA estimation. Unlike the interferometric problem, the delay required for the partially coherent demodulation of the received signal is not known and has to be estimated. The correlation properties of the PRN-modulated emitted signal are used for this delay estimation, using a tracking stage based on an ELDLL[18] synchronization architecture typical from RF communications and GNSS. In addition, the narrow correlator concept [Van Dierendonck et al., 1992] used in these kind of RF receivers to mitigate multipath is also applied in the proposed design for further rejection.

The core of this dissertation is the detailed description, analysis and optimization of this proposal, and its experimental validation to evaluate its potential and conditionings as a solution to enable IR-DToA indoor localization.

1.2 Motivation and objectives

In summary, the motivation of this thesis is to advance towards bridging the gap for the application of direct detection IR ranging for localization in real indoor scenarios, what implies addressing the problem of multipath while otherwise maintaining the performance provided by previous solutions.

This defines the goal of this thesis, being the definition of an optical ranging system that can operate efficiently in multipath environments, aiming to use it as the fundamental measuring unit to form an indoor localization system whose performance is adequate for guidance and navigation of mobile targets.

This goal can be divided into the following specific objectives:

- Propose a method for indoor non-directional ranging between mobile targets and fixed reference points using optical signals. This method must be able to provide:
  - Mitigation of the effect of multipath interferences on accuracy in typical indoor multipath scenarios.
  - Precise and robust noise-related performance, considering expected signal quality levels in indoor scenarios.
  - Continuous tracking of moving targets at typical speed ranges in indoor robotics and autonomous vehicles.

[18] Early-Late Delay-Locked Loop

  - Robustness against the effects derived from asynchronous emitter-receiver operation considering realistic frequency errors in the system timing.
  - Adequate calibration and reproducibility requirements as to allow simple and cheap scalability.
  - High coverage per measuring unit so that the required sensor deployment to cover certain area is as small as possible.
  - Simultaneous tracking of several targets without reduction of performance by an efficient multiplexing of the receivers infrastructure and signal processing.

- Define an architecture that implements the proposed method, including the specific signal structure and the signal processing stages.
- Derive and validate a theoretical model for the behavior of the proposed system affected by the relevant error contributions: noise, dynamic and asynchronism errors, and multipath.
- Carry out practical tests to evaluate the validity, conditionings and trade-offs of the proposal.

1.3 Thesis background

This thesis describes original work developed in the GEINTRA Research Group[19] of the Electronics Department[20] at the University of Alcalá[21].

GEINTRA is an official group of the University of Alcalá formed by 24 professors and assistant professors, and many PhD, Master and Bachelor thesis students. The main goal of the group is to develop fundamental and applied research activities in the fields of intelligent spaces and intelligent transport and infrastructure systems. This goal includes research lines related to: mobile robotics, localization systems, human-machine interfaces, embedded digital systems, sensors, sensor networks, sensorial fusion, intelligent transport, distributed control and automation, e-health and independent living.

Within this framework, this thesis is contextualized in the two application fields of the group: intelligent spaces and intelligent transport and infrastructures, being specifically related to the research lines of localization and sensors.

This work has been mainly supported by the following research projects:

- ESPIRA (ref. DPI2009-10143) [Spanish Ministry of Science and Innovation]: Contribution to intelligent spaces by developing and integrating positioning sensors (in Spanish). PI: Dr. José Luis Lázaro Galilea.

  The goal of this project was to develop sensor systems based on discrete IR sensors and distributed/centralized processing architectures based on FPGAs[22], to increase the sensorial and processing capacities of intelligent spaces. The general objective was to provide

[19] http://www.geintra-uah.org/en
[20] http://www.depeca.uah.es/
[21] https://portal.uah.es/portal/page/portal/portal_internacional
[22] Field Programmable Gate Arrays

localization of mobiles such as robots, wheelchairs or industrial vehicles for future smart spaces built in environments like hospitals, offices or warehouses.

This thesis dealt with the tasks related to the development of the localization system, namely, the implementation of fully-digital signal processing units for IR differential distance measurements and the study of acquisition techniques that allowed reducing the digitization requirements of the system.

- ALCOR (ref. DPI2013-47347-C2-1-R) [Spanish Ministry of Economy and Competitiveness]: Optimization of wireless sensor network and network control system for the cooperation of mobile units in intelligent spaces (in Spanish). PI: Dr. Felipe Espinosa Zapata, Dr. José Luis Lázaro Galilea.

  This project is devoted to contributing toward the flexible and cooperative tasking between robot units in extensive indoor industrial scenarios. This goal is addressed with three complementary research lines: remote event-based control techniques for the mobile units to minimize the communication requirements and the complexity of the on-board systems, optical localization sensors and means for their interconnection to provide accurate localization with versatile detection areas, and optimization of the communication network to provide service to the former considering the mobility of some of the nodes (mobile units) and the reconfigurable network topology of others (localization sensors).

  Within this project, the present thesis addressed part of the tasks of the research line related to localization sensors, specifically the optimization of the sensor modules to reduce the effect of multipath interferences and the increase in accuracy and coverage of the sensorial system by improving the features of the optical link.

This thesis has also been supported by the University of Alcalá through the FPI/UAH predoctoral fellowships program (ref. FPI/UAH2010) and the FPI/UAH mobility program. The latter made possible research stays for collaboration in the Max Planck Institute for Gravitational Physics (Albert Einstein Institute) in Hannover (Germany), the Institute of Geodesy and Photogrammetry of the ETH Zürich (Switzerland) and the Institute of Materials Science and Technology of the University of La Habana (Cuba).

1.4 Outline of the document

This dissertation is organized as follows:

- Chapter 2: "*State of the art*". In this chapter the available technological solutions and current state of the research in the specific topics that are of interest to this work are reviewed. Indoor positioning is introduced with an overview of the fundamental measuring principles and localization strategies, followed by a review of the main research and industrial proposals for the principal indoor positioning technologies. The previous research in IR-PoA indoor localization, that serves as direct background to this work, is specifically revised next. The main techniques applied in optical ranging are then introduced and

the latest approaches and solutions in this line are presented. Finally, some guidelines on multipath effects in different fields and a review of the research on multipath mitigation methods applied to several localization and ranging technologies are provided.

- Chapter 3: "*Problem statement and proposed solution*". This chapter provides a detailed definition of the specific problems and requirements of the system addressed in this thesis, including current technological limits and working conditions. Next, the specific multipath problem that affects indoor IR ranging is analyzed and two indoor multipath propagation models, used further in the document to evaluate the proposal, are presented. Finally the proposed techniques and architecture are explained, to be studied in depth in chapters 4 and 5, and some fundamental definitions and derivations related to the proposed signals structure are provided.

- Chapter 4: "*Signal synchronization*". The signal synchronization of the proposed ranging architecture, formed by a delay acquisition stage and a delay tracking stage based on an ELDLL, is explained and analyzed in this chapter. The effect of the main error sources that affect these stages is derived and validated with numerical simulations and measured data using synthesized signals.

- Chapter 5: "*Range estimation*". The differential range estimation of the proposed architecture, basically formed by a DSSS[23] demodulation stage and a differential phasemeter based on I/Q[24] demodulation, is explained and analyzed in this chapter. The demodulation process is modeled depending on the delay estimation error from the previous synchronization stage and the properties of the received signal. Next, considering the properties of the demodulated signal, the effect of the main error contributions on the phasemeter is studied and again validated with numerical simulations and measured data using synthesized signals.

- Chapter 6: "*Results*". These chapter provides the results measured on a digital implementation of the complete proposed architecture based on Simulink, using input signals obtained from a wired emulation of the IR link required for this system, which is currently under development. An error model of the complete system is provided first, encompassing and summarizing the theoretical expressions derived in chapters 4 and 5. A practical example of the low-level operation of measuring architecture is provided next, followed by the definition of the test set-up and scenario used for the results. The global performance of the proposal in the defined scenario is evaluated next by comparison with the theoretical error model, and the multipath behavior is specifically evaluated by comparison with the theoretically expected results from a standard single-frequency PoA approach under the same conditions.

- Chapter 7: "*Conclusions and future works*". In this chapter, the most relevant conclusions, contributions and results derived from this thesis are presented. The publications in international journals, and international and national conferences derived from this work

[23] Direct-Sequence Spread Spectrum
[24] In-Phase and Quadrature

are listed next. Finally, the future perspectives in this research line are commented, and relevant future works are proposed together with suggestions on how to address them.

Chapter 2

State of the art

This chapter provides an overview of the current state of the research and the available technological solutions in the knowledge areas which are more closely related to this work.

This thesis, despite having a clear direct background in previous research in the Electronics Department of the University of Alcalá in IR-PoA indoor positioning, has a diverse theoretical and research base. This is reflected in the diversity of the contents in this state of the art chapter.

In one hand, an adequate knowledge of the application context of the research, i.e., indoor localization, is fundamental to understand the general requirements and limitations of any technology developed within this framework. In addition, understanding the difficulties and solutions found in current research in the different technological alternatives that are applied to implement indoor localization is of deep interest to address the specific problems of an specific technology in a practical and direct way, discarding or making use of solutions already developed for common problems in different approaches. Thus, a general overview on indoor localization, including a brief introduction on the different measuring principles and positioning strategies usually employed and, mainly, the alternative technological approaches that have been studied and developed so far, is given in section 2.1.

Section 2.2 focuses on previous research on IR phase-based DToA indoor localization. The general functioning and contributions of previous proposals are detailed, and the problems detected in those works are analyzed, playing a very important roll in the definition of the main goals of this thesis.

As commented above and in the introduction chapter, this work is focused on providing a localization solution based on optical ranging. It is clear that an adequate understanding of optical ranging technologies, including the different ways of measuring distance using optical signals and the technological limitations associated with free-space optical links, is fundamental in the definition and tests of a proposal to solve the given problem. An overview of the principal measuring principles in which optical ranging systems are typically based, followed by the latest research lines that are of interest to the present work are given in section 2.3.

Finally, the main problem addressed in this work is the unacceptable error introduced by multipath interferences in many indoor scenarios. It is, therefore, fundamental to review previous

research efforts that address the effect of multipath on different technologies, mainly those related to ranging and localization, and to analyzed the solutions already developed in those systems to find out whether those approaches could be adapted to the given context or inspire an specific solution to the problem under study. Section 2.4 specifically focuses on multipath effects and their mitigation.

2.1 Indoor positioning

Indoor positioning is an area of knowledge whose interest for both the research community and the industry has grown fast since the middle nineties. In one hand, GNSSs have already been widely integrated in modern societies for many years. The possibility of providing the final user with a private and accurate localization solution in most outdoor scenarios, together with the availability of cheap receivers thanks to their large scale production and integration in consuming electronics, enables the regular presence of a large number of applications based on outdoor localization in personal and professional situations in everyday life. The extension or adaptation of many of these applications to indoor scenarios feels like a natural and useful transition for the user. GNSSs, however, cannot provide a solution for these applications due to lack of coverage or unacceptable inaccuracies caused by multipath errors and the strong attenuation that the GNSS microwave signals experience when going through typical construction materials. On the other hand, a wide range of potential indoor-specific applications has been also created in the last years, given the strong integration of interconnected portable devices in current societies and the increase of context-aware services provided, in many cases, by buildings and infrastructures in modern cities. Some of these current or short-future applications are pedestrian navigation, LBSs, emergency response, AAL or machine, robot and vehicle guidance and monitoring. These framework of potential applications have been progressively drawing the interests of the research community for more than 20 years towards the development of technological approaches that can provide practical indoor localization solutions.

From the technological point of view, the terms indoor positioning or indoor localization encompass the technologies and methods involved in the process of estimating the position of a target in certain, usually fixed, reference system in an indoor environment. These technologies and methods can be generally classified into two main topics: measuring principles and positioning strategies.

Measuring principle

It is the basic observation or method applied to obtain information about the target to be located that is somehow dependent on its position in the environment. The measuring principles basically depend on the property or magnitude that is observed to extract some information relative to the target position. The basis of the most typical measuring principles are briefly explained next.

- ToA[1] / DToA

  This measuring principle is based on obtaining information of the distance or distance differences from a signal that propagates thought a free-space channel following a LOS path by a direct or indirect measurement of its propagation time.

  - ToF: the distance is estimated by a direct measurement of the delay suffered by a signal propagating between two transceivers or the round trip delay of a signal retuning to the same transceiver after active or passive reflection. Implementations of this technique with dedicated RF, US and optical signals can provide high ranging accuracy in the indoor localization context.
  - PoA: the delay is estimated indirectly by measuring the phase added to the signal during its propagation. Similarly to ToA methods, ad-hoc implementations can reach high accuracy.
  - TWR[2]: an estimation of the propagation delay is extracted form the timing between acknowledge messages in a communication system. This method is mainly applied to RF technology for low accuracy estimations and requires a good a priori knowledge of the processing delays in the involved devices.

- AoA[3]

  The AoA principle is based on the measurement of the reception angle to estimate the direction of certain incoming signal. Similarly to some ToA methods, certain implementations of AoA, primarily those using coherent optical signals, can provide very accurate measurements, although their application towards positioning usually require employing complex mechanical or optical sweeping systems.

- RSS[4]

  The RSS measuring principle includes all those methods that use information relative to the strength of certain received signal. This information is usually applied to a distance estimation based on some signal propagation model or to a direct location estimation based on a map of previously registered values in the same scenario. These methods can be very useful for implementing low-cost localization by re-utilizing already installed communications networks. The accuracies obtained in these approaches, however, is usually low. Higher precisions can be achieved in map-based alternatives at the cost of significantly high efforts in the initial set-up and periodical maintenance tasks.

  This measuring principle includes several alternatives depending on the type of signal which is used: such as flux density measurements for magnetic-based systems, or RSSI[5] for systems based on some kinds of RF communication networks.

[1] Time of Arrival
[2] Two-Way Ranging
[3] Angle of Arrival
[4] Received Signal Strength
[5] Received Signal Strength Indicator

- Cell-ID[6] / CoO[7]

  This principle can be considered as a coarse approximation of distance or location estimation based on signal strength in certain RF communications networks such as GSM. When a mobile communication device is known to be connected to a specific antenna, this data, together with a priori knowledge on the antenna position and covered area, informs of an area of possible positions for the device in the antenna surroundings.

- Capacitance

  The observed magnitude in this case is the variation of certain capacitance or capacitances matrix caused by the presence of a target. The precision of methods based on this principle is strongly related with the deployed infrastructure, which defines the resolution of the sensorial network, hence accurate estimations require large and expensive installations.

- Pressure

  This measuring principle is similar to the previous one, using pressure variations caused by the target on a deployed infrastructure typically covering the environment floor. Equally to the capacitance method, accuracy is directly related to the density of the deployed infrastructure, hence its installation costs.

- CV[8] / Photogrammetry / Projective geometry

  The basic concept behind methods based on CV is the use of video data obtained with standard or depth-cameras to locate certain target in the video frames and relate its position in the image with the environment using the information about the camera position and its optical calibration parameters. The combined use of several cameras provide stereoscopic vision for 3D[9] localization. Depth or ToF-cameras, providing range information images, can be used for 3D localization with single-camera set-ups.

- Interferometry

  Interferometric ranging extracts information about the propagation delays of coherent optical signals by exploiting optical interference effects between a signal propagating through the path to be measured and a replica of this signal which propagates though a known reference path. Interferometry is, by far, the most accurate relative distance estimation method but requires, however, very stable and precise set-ups for proper functioning, what impedes its use in most application environments.

- Mechanical

  This measuring principle is based on direct contact of the measuring instrument with some point in the environment to define the position of the point within the instrument coordinate system. This is usually performed by measuring the angle or displacement of several movable parts of the instrument using very accurate electronic encoders. This

[6] Cell Identification
[7] Cell of Origin
[8] Computer Vision
[9] Three Dimensions

systems can also provide very high localization accuracy. The required physical contact with the point of interest, however, limits their use to specific industrial applications and usually involves a human operator.

Positioning strategy

It is the method used to relate the information obtained by means of certain measuring principle with the reference system in the environment, so that the position of the target can be estimated within that reference system.

- Lateration

  Also referred to as trilateration or multilateration, it is the estimation of a target position from distance or differential measurements between the target and a series of known reference points in the environment. This method can be applied to any system that uses some kind of distance estimation such as ToA, DToA or RSS with propagation models. When absolute distances are available, spherical lateration is used and minimum number of 3 reference points is required for 3D positioning. On the other hand, if the measuring system provides differential distance estimations, hyperbolic trilateration is applied to obtain the target positions, and 4 references are required for 3D positioning. Redundancy is usually applied together with optimum estimation methods such as ML[10] or LS[11] to increase accuracy. Figure 2.1 shows an example of spherical and hyperbolic lateration applied in the same scenario depending on the available measurements being ToA or DToA.

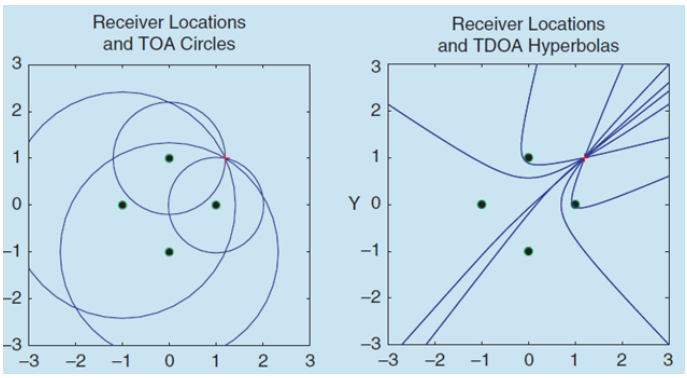

Figure 2.1: Example of spheric and hyperbolic lateration with four receivers. Graphic by [Gustafsson et al., 2005]

- Angulation

  It is the process of estimating the position of a target from angle measurements between the target and several reference points of known location. It is the typical method used in geodetic measurements based on theodolites for high accuracy determination of the position of critical points in natural or man-made structures, usually applied outdoors. Its use in indoor localization, apart from the specific and complex geodetic use, can be found

[10] Maximum Likelihood
[11] Least Squares

in low accuracy RF approaches using directional antennas for AoA determination and in some optical high accuracy applications, also in the context of geodesy and mainly applied to construction, where angular sweeps of laser planes are used.

Figure 2.2 shows a simple diagram of angulation-based positioning, in which the target is localized at point x by the AoA measurements θ_A and θ_B from the reference points A and B.

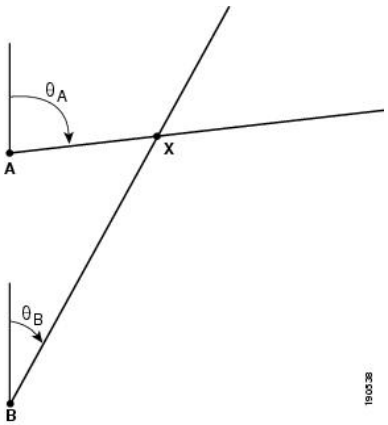

Figure 2.2: Example of position estimation using angulation. Graphic by Cisco Systems, Inc [http://www.cisco.com/c/en/us/td/docs/solutions/Enterprise/Mobility/WiFiLBS-DG/wifich2.html]

- Fingerprinting

  Fingerprinting is a database method generally formed by two phases. Initially, an off-line calibration phase is performed, in which measurements are taken in the application environment aiming to map measured values of the observed magnitude with positions of the environment. During the second phase, being the actual system operation, the current measured values are compared to the database to decide the position in the map that yields best agreement between both. This method is usually applied to RSSI or other RSS measurements, although it can be applied to different information for matching, such as acoustic signals, light intensity or visual patterns.

  Figure 2.3 shows an example of a WLAN RSS map developed by [Chan et al., 2009] for fingerprinting based localization.

- Dead reckoning

  Dead reckoning is the estimation of the current position of a target based on some previously known position and the information of speed (including its direction) and elapsed time. This information is usually obtained by direct measurement, usually applied in mobile robotics using encoders or estimated indirectly from acceleration measurements, such as accelerometers in portable devices or IMUs[12], more commonly applied to pedestrian navigation. The direction information can be estimated from previous information and probabilistic approaches using map-matching, or directly measured using a gyroscope or a compass.

[12]Inertial Measurement Units

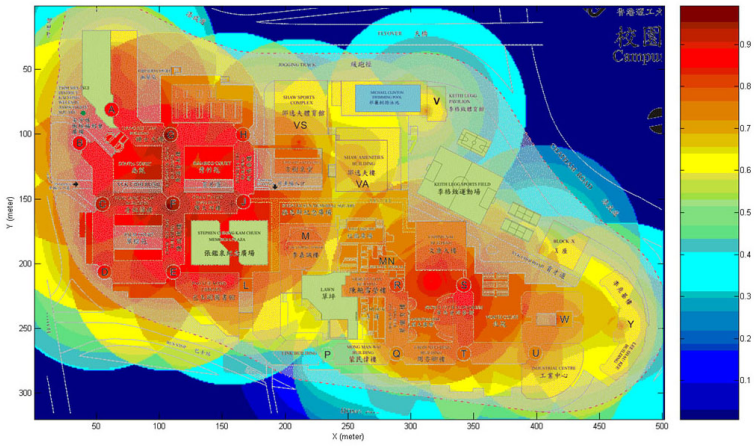

Figure 2.3: Example of WLAN RSS map for location fingerprinting. Graphic by [Chan et al., 2009] [http://www.comp.polyu.edu.hk/lab/wins/research_area.htm]

- Cell-ID / CoO

  As previously explained, Cell-ID or CoO can be considered either a measuring principle or a positioning strategy, based on associating the position of the user with communication cell the user is currently connected to. Figure 2.4 shows a clear example of this method.

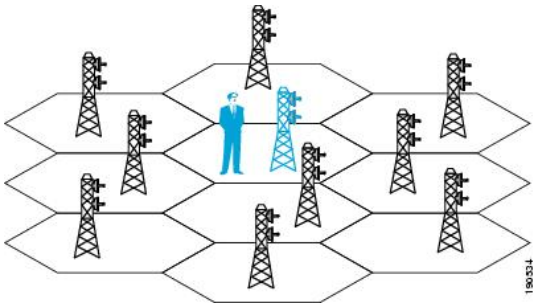

Figure 2.4: Example of CoO localization. Graphic by Cisco Systems, Inc [http://www.cisco.com/c/en/us/td/docs/solutions/Enterprise/Mobility/WiFiLBS-DG/wifich2.html]

2.1.1 Positioning techniques

The technological approach, encompassing a measuring principle and a positioning strategy, is usually referred to as positioning technique or positioning technology. Those are classified and briefly explained in this section, addressing the latest works and approaches for each case.

Figure 2.5 shows a representation, according to [Mautz, 2012], that classifies most current approaches to indoor localization as a function of their typical accuracies and covered areas.

IMUs

[Dead reckoning]

IMUs are electronic devices that measure speed, orientation and gravitational forces using a combination of gyroscopes and accelerometers. Some IMUs also include magnetometers, usually

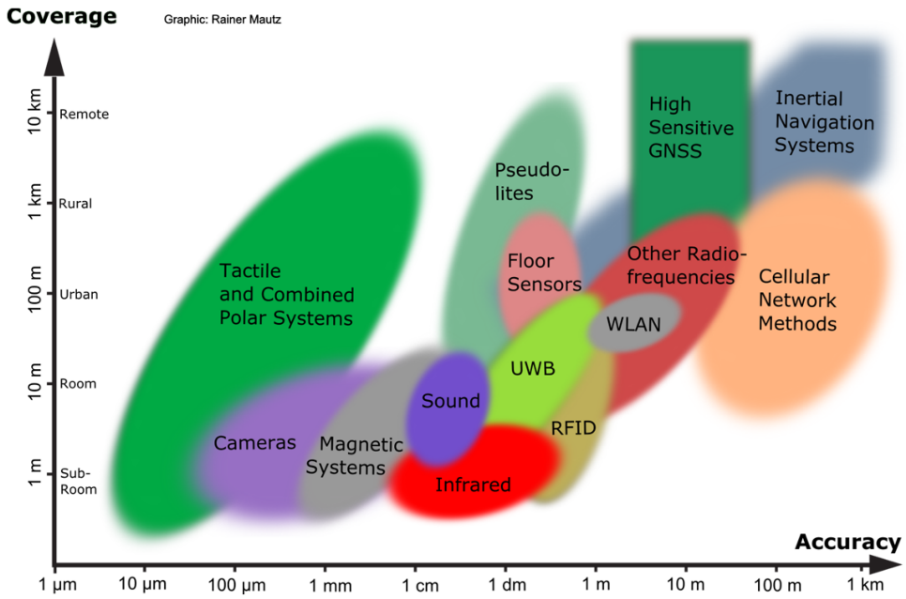

Figure 2.5: Overview of indoor positioning techniques depending on coverage and accuracy according to [Mautz, 2012]. Graphic by [Mautz, 2012]

applied in localization for floor determination. IMU-based indoor localization relies on dead reckoning and its mainly applied to pedestrian navigation in the indoor localization context, where step and heading detection are usually implemented. [Harle, 2013] provides an overview of the several alternatives regarding step estimations, data fusion, map building and dead reckoning techniques, and reviews the main challenges found nowadays in this expanding research area.

The main advantage of these systems is the lack of required infrastructure. However, the high drifts caused by the inherent error accumulation of dead reckoning impedes their long-term independent operation. To solve this drawback, these systems are usually implemented together with some other non-relative positioning technology that provides periodical updates of the target position.

There are several works fusing IMU-information with other localization technologies. Passive RFID tags are used as markers in [House et al., 2011] to correct the user position in relevant locations, while ranging information derived from active tags RSS measurements is coupled with the IMU-data in [Jiménez-Ruiz et al., 2012] using a KF[13] and applying the zero velocity and angular rate update algorithms to reduce drifts derived from the IMU estimations. Downward oriented cameras are used in [Hide et al., 2010] and [Zhang et al., 2014] to reduce the inertial information drift in low-cost implementations adapted to smartphones, and [Mostofi et al., 2014] demonstrate SLAM[14] fusing a camera and a magnetometer-equipped IMU. Some multi-sensor approaches involving IMUs have been proposed, such as [Cheng et al., 2014], where it is fused using an EKF[15] with GPS[16] and WLAN fingerprinting to achieve seamless outdoor/indoor pedestrian navigation. In some cases, the inertial navigation is conceived as a secondary system used to increase the robustness of a more accurate localization technology. This approach, rather

[13]Kalman Filter
[14]Simultaneous Localization and Mapping
[15]Extended Kalman Filter
[16]Global Positioning System

extended in robotics where odometry is used instead of IMUs, is applied in [Hol et al., 2009] to provide continuity in the coverage-denied or severely multipath-affected areas of an UWB-based positioning system.

The main advantage of this technique is the cost and simplicity, since most approaches only make use of the sensors usually available in modern smartphones or low-cost foot-mounted IMUs for increased accuracy. The foot-mounted alternative helps improving the step-related estimations by using zero velocity or angular rate updates [Skog et al., 2010]. The main disadvantage of IMU-based localization is error accumulation, what, despite its fusing with other systems for periodic updates, limits its use to pedestrian navigation where meter accuracy is acceptable.

Enhanced GNSS

[DToA, lateration]

These category refers to improved GNSS-based receivers, in which some method is applied to overcome the low-signal and multipath problems that impedes the indoor application of standard GNSS receivers. Two alternatives, not initially developed for indoor use, but for increasing GNSS performance in other circumstances, have been applied in this context:

- AGNSS[17] is a standardized GNSS positioning method used outdoors in devices with internet access. The device data link is used to obtain satellite, timing and differential corrections information that would be normally obtained at a much slower rate directly from the satellites. Apart from speeding-up initial acquisition, the availability of more information on the satellites and timing allows the use of weaker signals, hence improving sensitivity and enabling indoor use in some cases.
- HSGNSS[18] refers to the implementation of parallel correlation and long integration time to achieve higher post-correlation SNR in the receivers.

The joint use of both techniques, although enabling the use of GNSS in some particular indoor scenarios such as wooden houses, still shows poor performance for practical applications in general indoor scenarios. Studies made in [Zhang et al., 2010] with static AGNSS-HSGNSS and in [Kjæ rgaard et al., 2010] with HSGNSS showed accuracies between 10 and 60 m in various indoor environments, only reaching smaller errors in non-deep indoor scenarios built with low-absorption materials.

Pseudolites

[DToA, lateration]

Pseudolite is the contraction of pseudo-satellites. They are ground-based stations that function as a GNSS satellite by emitting a GNSS-like ranging signal. Initially conceived for aircraft landing assistance and to increase kinematic GPS accuracy with differential measurements [Cobb, 1997], they are nowadays also used for test purposes and to provide positioning for applications in GNSS-denied environments such as deep canyons, pit mines or indoor scenarios.

[17] Assisted Global Navigation Satellite System
[18] High Sensitive Global Navigation Satellite System

The use of pseudolites in indoor positioning presents, apart form the need to deploy the pseudolites network, several inherent problems [Wan and Zhan, 2011], mainly: multipath interferences, near-far problem caused by the high difference in received signal power and synchronization issues because of not having access to the GNSS constellation atomic clocks. Despite those, good results have been demonstrated for indoor applications with some commercial pseudolites developments such as Locata [Barnes et al., 2002, Rizos et al., 2010], reaching cm level accuracy in indoor environments using specific antenna designs for multipath reduction.

UWB

[DToA, AoA, RSS, lateration, angulation, fingerprinting]

UWB refers to RF technologies using very high bandwidth, namely more than 500 MHz or 25% of the central frequency according to the FCC[19]. Initially conceived for RADAR[20] imaging, it is nowadays mainly used for high-bandwidth short-range communications with low-power devices. UWB-based localization can rely on several techniques applied to other RF technologies, such as RSS fingerprinting or AoA, however, most effective solutions make use of the high time resolution provided by its bandwidth to achieve accurate ToA/DToA ranging where a significant part of the multipath components can be time-resolved, while the penetration properties of the signals allow NLOS ranging in some circumstances.

Three main methods are used to perform ranging for localization using UWB signals: (i) CW[21] systems use frequency sweeping for measuring delays in the frequency domain similarly to FMCW[22] RADARs, as in [Alsindi et al., 2009], where performance in NLOS scenarios is also evaluated, this method, however, usually require large antennas for efficient transmissions; (ii) direct ToF measurements are performed using very short pulses, similarly to optical laser telemetry systems, in the so-called IR-UWB[23]. [Pietrzyk and von der Grun, 2010] demonstrated ranging accuracies below 2 cm at 5 m LOS distances using an analog energy detector, and [De Angelis et al., 2013] developed a high-rate reflective sensor achieving dm precision in 10 m ranges; and (iii) spread spectrum ranging, using PRN modulations on the UWB signals has also been investigated, mainly for through-wall imaging applications [Kocur et al., 2009, Wang et al., 2009], and localization [Segura et al., 2010, García-Núñez, 2013].

The implementation of these ranging techniques to develop practical indoor localization solutions has an important drawback in the requirement of specific emitter-receiver infrastructure with demanding electronic designs. On the other hand, very high performance systems have been presented in the last years and this technology will probably be present in many future applications that requite high accuracy such as mobile robotics. Examples of these are [Kuhn et al., 2010], where combined coherent and non-coherent detection is used to provide sub-cm accuracy of both static and dynamics targets; [Zhou et al., 2011], achieving cm precision with non-coherent detection and simplifying synchronism using a known emitter-receivers set-up where the target acts as a repeater for the pulses sent by the fixed emitter; [Segura et al., 2010],

[19] Federal Communications Commission
[20] Radio Detection and Ranging
[21] Continuous Wave
[22] Frequency Modulated Continuous Wave
[23] Impulse-Radio Ultrawideband

where the location of a robot in relation to fix transmitters in the environment is computed by DToA measurements of DBPSK[24]-modulated signals on a receiver boarded in the robot, achieving an accuracy in both LOS and NLOS conditions better than 20 cm; or [García-Núñez, 2013], where a system with a similar configuration to the former one is implemented to be used as a testbed for some specific spreading sequences derived from CSS[25]. Also related to robotics, [González et al., 2009] makes an experimental characterization of a commercial pulsed UWB-TWR sensor, and use the data to derive a probabilistic model that is used by a particle filter together with odometric information provided by the robot. This approach helps improving the location accuracy despite using multipath affected range estimations.

There are also several interesting works in UWB-localization specifically focused on multipath performance and mitigation. Those will be commented in the multipath section of this chapter (2.4).

WLAN

[RSS, DToA, AoA, fingerprinting, CoO, lateration, angulation]

WLAN-based localization is clearly the area of indoor positioning where more works have been developed. The high availability of WLAN infrastructures in most indoor environments nowadays, together with the user access to WLAN receivers integrated in a very high number of modern portable devices such as smartphones and laptops, make this technology extremely attractive, although the reachable accuracy is rather limited due to the properties of the signals and the use of a non-dedicated infrastructure, hence not optimized for localization. On the other hand, research in this area does not usually require any HW[26] development, what makes test and implementation of new proposals faster than in other technological approaches.

Four different methods are used for WLAN-based positioning [Liu et al., 2007]: CoO, lateration [Liu et al., 2013, He et al., 2013], propagation modeling [Mazuelas et al., 2009], also known as analytical fingerprinting, and empirical fingerprinting. The latter is, with difference, the most widely used. CoO methods provide very poor accuracy (in the tens of meters range taking into account typical antennas coverage), lateration methods based on ToA, DToA or AoA require specific or modified infrastructures and receivers, and propagation modeling reach poor results due to the high environmental dependences of the RSSI in WLAN.

Fingerprinting performance in WLAN is highly related with the number of access points and the effort made in the calibration stage to define a high density RSS map. The accuracy reach by these systems, even if extensive location fingerprinting is perform, is still above 1 meter due to the variability of RSSI with changes in the environment furniture and the presence of people. Research efforts are mainly focused on improving precision in the measurements, such as [Chang et al., 2010], where differential measurements are performed to reduce common errors or [Yang and Shao, 2015], where the transmitted messages are enhanced to reduce the number of required access points and their bandwidth; and improving the RSSI-maps reliability [Leppäkoski et al., 2010, Atia et al., 2013].

[24] Differential Binary Phase-Shift Keying
[25] Complementary Sets of Sequences
[26] Hardware

RFID

[RSS, CoO, fingerprinting]

RFID systems are based on a RF reader and several RF tags which send their ID to the reader when interrogated. When applied to localization, the reader is mounted on the target to be located and the tags are distributed in fixed and known positions of the environment. RFID systems are formed by either passive or active tags.

Passive tags are powered with the signal received form the reader by inductive coupling, which gives them enough power to send their tag back to the reader. These tags are small, simple and inexpensive, however, their range is usually below 2 meters, what demands a high density deployment. Localization using passive tags is basically based in the CoO principle, associating the target position to the known position of the tag that is currently interrogated by the reader. These approach is usually applied for navigation aiding in approximately predefined paths. Examples of this are [Saad and Nakad, 2011], where tags are deployed in a predefined robot path every 1.2 meters, allowing to maintain its position errors below 10 cm, or the commercial solution NaviFloor [27] from FuturShape, which offers preintalled floor coverings in 1 m times 50 m rolls to install a 50 cm grid of tags plus a control SW[28] for robot or people navigation.

Active tags are self-powered with internal batteries, increasing the cost and complexity of the tags but enabling ranges up to 30 m and much more reliable received signals that allow performing RSS measurements in the reader, where location is usually obtained by fingerprinting. Works in active RFID indoor localization are usually related to its fusion with other technologies such as IMUs in [Jiménez-Ruiz et al., 2012], IMUs and GNSS in [Peng et al., 2011] or US in [Holm, 2009].

The main general limitation of RFID-based localization is the tight relationship between performance and deployed infrastructure. Sub-meter precision that surpasses WLAN alternatives can only be reached if high-density active-tags deployments are made.

US

[DToA, RSS, lateration, fingerprinting]

These systems use US acoustic waves to perform, in most cases, DToA ranging, and localize an emitter in a fixed set of synchronized receivers or vice versa by applying multilateration. The main advantages and drawbacks of US systems compared to other optical or RF ToA approaches are related to the differences in the free-space propagation of the acoustic signals and the properties of the available transducers. In one hand, the relatively slow propagation of acoustic waves makes the effect of the target speed or air temperature variations non-negligible compared to its electromagnetic counterparts, often requiring Doppler-effect corrections and temperature compensation mechanisms; on the other hand, the slow propagation speed allows time-resolved LOS estimations in many multipath situations, and the small signal bandwidth compared to the RF and optical domains significantly reduces the acquisition and processing requirements of the receivers. The fast decay of acoustic waves, however, limits typical US

[27] http://www.future-shape.com/en/technologies/32
[28] Software

transducers LOS ranges to around 10 m, what makes the infrastructure deployment rather costly and can create near-far problems depending on the set-up geometry.

US ranging can be performed by direct pulse detection, FM[29] or chirp signals, or correlation-based time estimations, the later being the most extended technique in localization. Spread spectrum PRN modulations are used to provide multiplexing by CDMA[30] and immunity against background acoustic noise. A performance comparison of US rangers using DSSS and FHSS[31] was made by [Segers et al., 2014], concluding that the more standard DSSS technique provides better accuracy but slightly worse reliability in multi-user operation.

Implementations in which the signals are broadcast both from and to the target can be found. In the first case, the US signal is emitted from the target and DToA is calculated from the arrival times to the receivers in the environment, which are synchronized by some wired, optical or RF link to compute the differential estimations. The main disadvantage of this configuration, apart from requiring higher power in the mobile target, is the requirement of some form of multiplexing mechanism for scaling it to several targets, while also increasing the acoustic channel occupation. Active Bat [Ward et al., 1997], one of the earliest approaches to US localization, demonstrated a 3D accuracy below 5 cm in large multiuser set-ups. A more modern example of this configuration can be found in the systems commercialized by Hexamite, claiming sub-cm accuracy up to 15 m ranges per sensor with an US-RFID fusion.

The alternative and more widely applied configuration is to broadcast the ranging signals from synchronized transceivers placed in the environment, measuring the DToA in the emitter. In this case, some multiplexing mechanism, usually TDMA[32] or CDMA, must be applied so that the target can make the difference between the emitters, but this multiplexing does not increases its complexity when more targets are added to the system. The Cricket system, presented in [Priyantha, 2005] reaching a 3D accuracies of 2 cm up to 10 m ranges, is probably the best known ultrasonic LPS[33] since, thanks to its open HW design, it has been used as a test platform for many other implementations. Other representative works using this configuration can be found in [Medina et al., 2013], where a TDMA low-power approach is shown, using quadrature detection and envelope interpolation to increase reception performance without coding, reaching accuracies below 1 cm for up to 6 m ranges; or [Prieto et al., 2009], where bidirectional broadband transducers are used to reach sub-cm accuracies and high immunity against environmental effects. This work provides an extensive evaluation of the proposal that also includes tests on a centralized configuration broadcasting from the target and a bidirectional mode for increased accuracy.

Some proposals specifically conceived for mobile robotics can also be found. A system for efficient self-localization of multiple robots is presented in [Ureña et al., 2007], where Kasami codes are used in a CDMA scheme for periodic simultaneous emissions with the aforementioned configuration, using wired synchronization between the fixed emitting beacons. [Kim and Kim, 2013] propose an hybrid system where robot localization is achieved by fusing distance information

[29] Frequency Modulation
[30] Code Division Multiple Access
[31] Frequency Hopping Spread Spectrum
[32] Time Division Multiple Access
[33] Local Positioning System

from an US multi-emitter/multi-receiver configuration with the robot odometric information and previously estimated pose.

Research regarding RSS with US transducer arrays has also been developed in [Holm and Nilsen, 2010], using transmitter arrays to send steered coded signals for sub-room positioning applications such as patient presence determination in shared hospital rooms.

US indoor localization, although requiring a specific deployed infrastructure, can provide very high accuracy compared to other approaches, and is often considered one of the most useful alternatives for mobile robotics applications.

Optical

[DToA, AoA, RSS, lateration, angulation, CoO]

This category comprises approaches that use coherent or non-coherent optical signals without image-forming. Camera-based alternatives that use images and projective geometry are addressed specifically in the next subsection.

This is the category in which the IR localization approach that served as a starting point for this work would fit in. This system, detailed in the next section 2.2, would be classified as a multilateration DToA-based solution.

There is not a common approach regarding optical systems and, unlike some other technologies, there is not a wide variety of works in this area. [Nasipuri and El Najjar, 2006] proposed a system based on rotating optical beacons and differential AoA measurements in the target built with low-cost devices, claiming dm-level performance. A similar approach, targeting much higher precision for industrial manufacturing and construction applications is used in the commercial system iGPS/iSpace[34], developed by Nikon Metrology. iGPS is formed by at least two fixed transmitters, each sending two rotating laser planes with different tilt plus a broadcast reference IR pulse. The position of the receiver is calculated by DToA with the planes and reference pulse detection times, achieving very high 3D precision in the sub-mm level at 40 Hz rates, what enables accurate dynamic tracking. Nikon states that areas up to 1200 m^2 are properly covered with 8 transmitters.

The iGPS, considering its application field and cost, is closer to the geodetic metrology field. There are other optical systems widely used in geodesy and surveying that could also be considered for indoor localization, if the application requires very high accuracy and allows the very high associated costs. These would include high-end systems such as laser scanners, laser trackers, theodolites or total stations, the latter formed by a theodolite and a laser distance meter.

An early approach to localization that made use of body-mounted IR-emitters was Active Badge [Want et al., 1992], where coded identifiers where transmitted to provide room-level localization based on CoO. Some alternatives using illumination-oriented infrastructure can also be found. [Jung et al., 2011] propose a DToA system using ceiling LED[35] lamps, claiming an accuracy smaller than 1 cm in standard room dimensions, this performance, however, is

[34] http://www.nikonmetrology.com/en_EU/Products/Large-Volume-Applications/iGPS/iGPS
[35] Light-Emitting Diode

not demonstrated by any practical validation, and noise and multipath is not considered in the simulations, being the main accuracy-limiting factors in such an approach. [Zhang and Kavehrad, 2012] proposed a system using RSS-distance estimations based on radiation models of LED lamps for VLC[36], where the receiver is a camera and privacy is obtained by encoding every emitter position in its emission, multiplexing them by TDMA. Sub-cm precision is demonstrated by simulation, however, no practical implementation and tests are addressed.

Cameras

[CV, photogrammetry, projective geometry]

Camera-based systems include any alternative that uses image sensors, typically CCD[37], to obtain the information for localization. There is a wide variety of works in this area, often applied to robotics due to the achieved performance, reaching dm to sub-dm accuracies in many implementations after a very accurate calibration of the camera position and optical parameters.

A comprehensive survey of camera-based alternatives, classified according on how the images are referenced to the environment, is provided by [Mautz and Tilch, 2011]. Some representative examples are given next. System referenced to building models, images data-bases, deployed or projected markers and natural features of the target and the environment can be found.

[Kohoutek et al., 2010] proposes a system based on a ToF-camera which obtains its location by referencing to a 3D model of a building interior. [Ido et al., 2009] proposed a method for humanoid robot navigation based on image matching with data obtained with the same system in a previous training stage, focusing on proper operation under unstable camera conditions. Deployed reference targets has been extensively used to increase robustness and accuracy. These markers can be placed both in fixed reference points in the environment to help locating the camera, or in the target to be located by a fixed set-up of cameras. The optical version of Sky-Trax [38], developed by TotalTrax Inc., offers vehicle tracking localization with sub-dm accuracy for warehouses, by mounting upwards-oriented cameras on them and deploying a grid of passive coded marks in the ceiling of the environment. In [Fernández et al., 2007] 4 IR-LEDs are mounted on a robot to provide robust localization in changing or bad illumination conditions, and localization is performed from a set of fixed and synchronized cameras. [Pizarro et al., 2009] proposal is also based on a set of calibrated cameras, where a robot position and orientation is obtained by recovering and tracking 3D points that belong to the structure of the robot assuming that it behaves as a rigid object, without using any artificial mark nor a priori information. The measured position error in real tests are below 10 cm in most cases using 2 cameras and generally smaller than 5 cm with 3 and 4 cameras. The robustness of the algorithm against quick occlusions and illumination changes is also demonstrated. A similar configuration that can operate in both single and multi-camera set-ups is used in [Losada et al., 2010], achieving simultaneous 3D localization of two robots with an accuracy better than 30 cm.

Taking into account the current achieved performances of the many approaches for camera-

[36] Visible Light Communication
[37] Charge-Coupled Device
[38] http://www.totaltraxinc.com/index.php/smart-forklift-solutions/forklift-tracking/sky-trax

based localization, the high available computer power and the availability of low-cost image sensors with increasing quality, camera-based solutions are expected to become a relevant alternative for market products in the near future.

Other

The main categories in which most research and industrial solutions for indoor localization fit in, have been described above. However, a number of works using other methods can also be found in the literature.

Although UWB, WLAN and RFID are the main RF-based approaches to indoor localization, other alternatives can be found. There are works using communication standards similarly to WLAN systems, such as the low-power ZigBee protocol used in [Larranaga et al., 2010] with a propagation model approach or the Bluetooth response-time fingerprinting approach of [Bargh and de Groote, 2008]. [Lymberopoulos and Priyantha, 2013] propose an ad-hoc deployment of transmitters for RSS fingerprinting, where FM signals are used to avoid the strong influence of the human body in the GHz band typical from WLAN and other communication protocols, and [Varshavsky et al., 2007] uses a multiple-CoO fingerprinting method for GSM signals. These alternative RF-based method offer accuracies in the m level, adequate for human navigation and some applications for object tracking, similarly to most WLAN systems.

Some works can be found based on floor sensors, where capacitance [Valtonen et al., 2009] or pressure [Branzel et al., 2013] variation caused by the local presence of the target are used. The accuracy of this approaches is directly related to the density of the deployed sensors, as well as their cost.

[Haverinen and Kemppainen, 2009] demonstrated that magnetic fields from both natural sources and man-made building metallic structures are stable enough as to provide reliable fingerprints, which is proposed for visual impaired people navigation in [Riehle et al., 2011]. The use of artificially created DC[39] magnetic fields is proposed in the lateration approach of [Blankenbach and Norrdine, 2010], where the magnetic flux in the target coming from coils in fixed reference positions is measured for ranging, based on an attenuation model.

2.1.2 Conclusions on indoor positioning

The following general conclusions can be drawn from the review of the state of the art in indoor positioning:

- Unlike outdoor positioning, there is not a dominant method or technology that can properly meet the relevant requirements of most indoor localization problems. Different measuring principles and localization strategies have been used in a wide variety of proposals to implement localization systems. Each technology has shown particular strengths and drawbacks, and its benchmarking is strongly dependent on the specific application needs.
- Technologies with a similar application scope to the current proposal, i.e., accurate localization of moving targets such as mobile robots, are UWB, US, and some camera-based

[39] Direct Current

and optical approaches. Except for the camera-based systems, all the other alternatives rely on some kind of ToA or DToA range estimation and a multilateration localization strategy.

- UWB systems can reach very high accuracy based on the high time resolution of the signals, what also allows temporal discrimination of many multipath components. In addition, these systems can perform NLOS ranging in certain situations due to the penetration properties of the signals in solid materials, although multipath effects become much more critical in these NLOS conditions. On the other hand, UWB systems have to deal with near-far problems and require high performance digitization stages and carefully designed high-frequency electronics to achieve good accuracy. US systems can reach high accuracy by using high performance transducers and acquisition stages, easier to achieve thanks to the small signal bandwidth compared to other alternatives, what simplifies the design of the conditioning electronics and reduces digitization requirements, simplifying also the synchronization between beacons. Moreover, these alternatives can be generally adapted to provide multiplexed service to a high number of targets with little or no degradation in the performance. The propagation speed of acoustic waves make these systems more dependent on the environmental conditions and Doppler effect than RF or optical alternatives, although this feature also allows time-resolving multipath arrivals in many situations. Camera-based solutions do not have to deal with the complexity of the sensor hardware design which, on the other hand, is translated to the algorithms. They are low-cost systems thanks to the mass-production of cameras and image sensors, although careful calibration processes are required to achieve good accuracy, and highly multiplexed operation without reducing performance is harder to achieve.

- Optical ranging, a widely used method in its different alternatives in industrial metrology and surveying, has hardly been studied in the indoor positioning context. A proposal with a similar DToA approach to the one used in the background investigations of this work (detailed in the next section) can be found in [Jung et al., 2011]. An RSS model-based ranging approach is proposed in [Zhang and Kavehrad, 2012]. However, only simulation results are presented in both, lacking a practical implementation and validation that proves feasibility in real conditions. The benefits from this technology rely on the possibility of achieving high accuracy thanks to the low distortion and contamination of the optical channels, the efficiency and continuously increasing performance of optoelectronic devices and the direct downconversion of the carrier frequencies in the receivers. Considering the results achieved in previous works, optical ranging can provide a valid alternative for accurate indoor localization whose further research is of interest.

2.2 IR-PoA indoor positioning

The direct background of this thesis is the previous research in the GEINTRA Research Group in IR-based indoor positioning [Martín-Gorostiza, 2011].

This work meant the first approach to performing accurate indoor localization for mobile

targets using IR DToA measurements. The basic idea of the proposal was to locate a robot by measuring differential distances from it to pairs of receivers placed in fixed reference points of the environment. An example of a possible location cell for this system is depicted in figure 2.6.

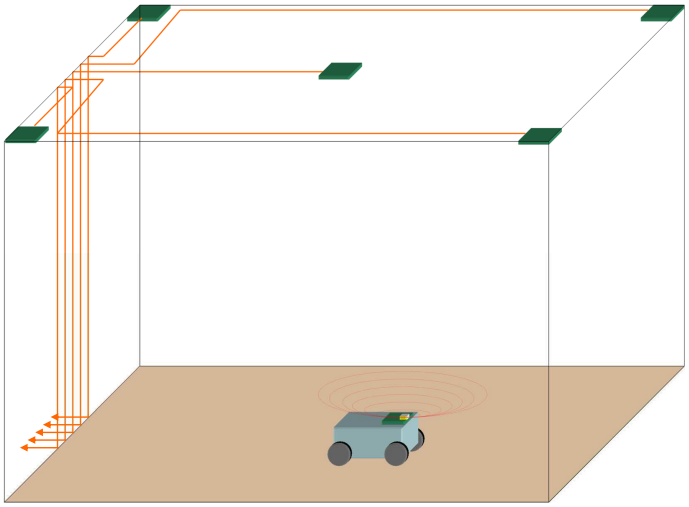

Figure 2.6: Example of a locating cell of the IR-PoA positioning system

The differential distances are extracted from differential PoA estimations between receivers of a 4 MHz sinusoidally intensity modulated signal emitted from the robot. The position of the robot is calculated from the differential distance measurements by hyperbolic trilateration, and the trilateration equation system is solved by a non-linear-LS estimation plus a further numerical solution using the Gauss-Newton iterative method.

The emitter boarded on the robot is a simple circuit with a Lambertian (n=1) 940 nm LED plus the driving electronics. The receivers are based on a Silicon PiN photodiode, a transimpedance amplifier and another low level stage for filtering and further amplification. The selection of the optoelectronic devices was made focusing on maximizing the trade-off between power transmitted in the IR link and available bandwidth, since the achieved precision is directly proportional to both parameters. Special care were also put in the design of the receiver electronics to provide low noise amplification and maximize phase stability at the modulation frequency against environmental conditions.

The differential phase measurement is performed using analog I/Q demodulation, where the I/Q references are generated by PLL[40]-recovering the received signal with the highest power, which is dynamically selected. The selected receiver is also taken as reference beacon for the differential measurements to minimize noise propagation in the estimations. The output of the demodulator is low pass filtered to remove the double-frequency beat note and the remaining low frequency I/Q signals are digitized. An arctangent estimation is then applied on the digital sequences to calculate the phase-shifts between every receiver and the reference one, to be delivered to the lateration solver. A diagram of the sensorial and measuring systems is show in figure 2.7 for a location cell with 5 receivers.

One of the main difficulties in the development of this system was to achieve good SNR in the reception. Most ranging systems, as will be seen in the next section, use collimated emission, at

[40]Phase-Locked Loop

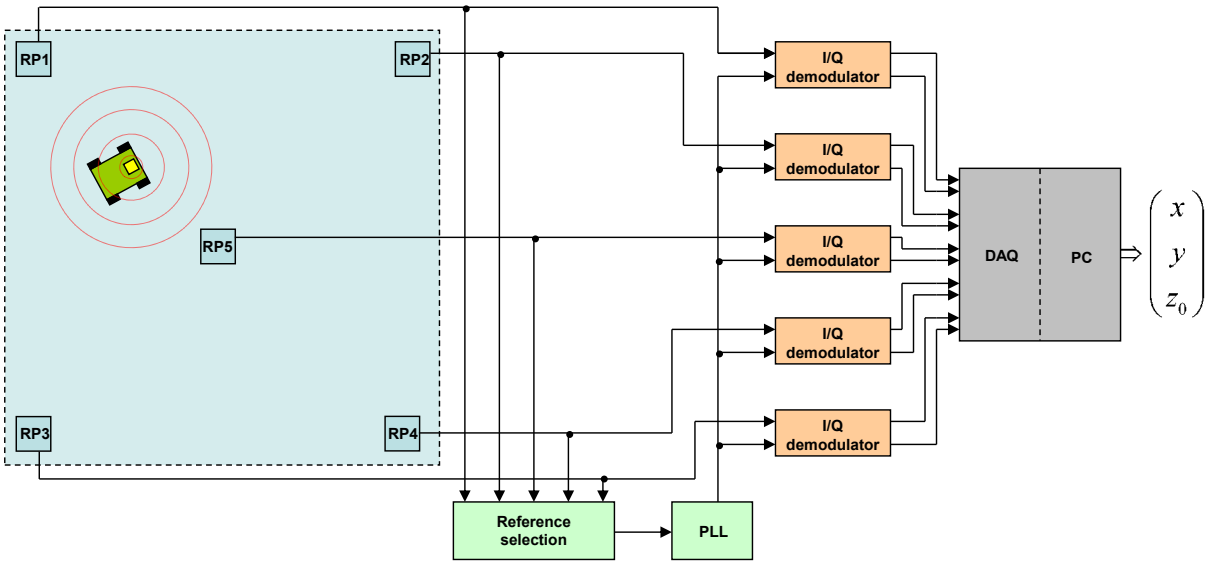

Figure 2.7: Diagram of the sensorial and phase measuring stages of the IR-PoA positioning system

least in part of the propagation path, e.g., half of the path before diffuse reflection in reflectorless ranging. In addition, the reception angle is usually known, so that optics can be applied in the photodetectors to focus on an specific direction and increase their effective sensitive area, hence received power. This is not the case of this system where: (a) the emitter has to distribute its energy in a wide solid angle so that the signal reaches simultaneously enough receivers as to solve the lateration problem and (b) the receivers cannot use optics because a wide FoV[41] is required to maximize coverage and minimize the number of deployed sensors.

The complete definition, modeling and validation of the proposal is described in detail in [Martín-Gorostiza, 2011], while the ranging and localization methods are summarized in [Salido-Monzú et al., 2011]. [Martín-Gorostiza et al., 2010] presents the error model of the system and a coverage-mapping method for robot localization, based on this model. The ad-hoc IR sensors developed for the proposed localization system are analyzed in detail in [Martín-Gorostiza et al., 2011]. [Salido-Monzú, 2011] focuses on the system optimization by increasing the performance of the IR link doubling the available bandwidth without power reduction. This work also makes a preliminary approach to the reduction of calibration issues by implementing most of the signal processing in the digital domain, eliminating the need of frequency-locking and studying possible alternatives to reduce the digitization requirements with sub-Nyquist sampling techniques.

The measurements with the prototype of the system served to validate the error model and yielded a precision below 2.5 cm in 2 standard deviations. The tests revealed, however, that the accuracy results where strongly affected by multipath effects, adding errors in the cm-to-dm level depending on the geometrical configuration of the environment and the reflective properties of the surrounding surfaces. These tests also revealed that a important part of this multipath interferences were due to the double reflection in ceiling and floor. Wall reflections can generally be avoided by limiting the FoV of nearby receivers so that only potential target positions are covered. This limits most wall-reflected multipaths in a simple approach. This

[41] Field of View

method, however, cannot be applied to the aforementioned double reflection because arrival angles in this case could also belong to potential target positions so they cannot be limited. The ceiling-floor multipath situation was, therefore, detected as the primary error source of the proposed system, hence the fundamental gap to bridge towards its practical implementation.

This works demonstrated the potential of using a phase-based IR-DToA approach for indoor localization with an adequate performance for robot navigation and autonomous vehicle guidance. The applicability of this system as a competitive alternative to other technologies with the same scope depends on the mitigation of the aforementioned multipath effects while maintaining the precision achieved in these background research.

2.3 Optical ranging

Optical ranging is a technology of reference in geodetic surveying, industrial metrology and construction. It is fundamentally based on extracting the information contained in an optical signal due to its propagation along certain path. A vast majority of the applications that require displacement or absolute distance measurements are solved using some of the available optical ranging methods. In contrast with other ranging technologies also based in electromagnetic signals, the use of optical frequencies offers several benefits for non-contact metrology, such as: directionality/power concentration using collimated sources, very narrowband devices (wavelength selectivity), low interference (low contamination in the optical band) or direct downconversion of the carrier frequencies in the devices.

Note that only direct ranging techniques are considered in this review, not including methods that derive range information from other quantities such as angle measurements.

The optical ranging methods can be divided in two broad categories: coherent detection and direct detection methods.

Coherent detection

Coherent detection implies that the information of a coherent optical carrier is somehow preserved in the detected signal although the bandwidth of the photosensitive device is much smaller than the optical carrier frequency. This is achieved by non-linear mixing with a reference beam, typically applying either homodyne or heterodyne interferometry.

When the reference beam comes from the same source as the probe signal and shares its frequency, the process is referred to as homodyne interferometry. The intensity of the resulting interference that reaches a photodetector depends on the phase difference between both beams, i,e, the distance traveled by the probe signal. In static conditions, when the length of the probe path is not varying, the output of the photodetector is a constant value that contains information about the length of the probe signal path. To achieve measurements more independent from the received power and avoid extracting the information of interest from a close-to-DC band, where error contributions form the photodetectors and electronics are greater, heterodyne interferometry is more typically used for ranging.

In heterodyne interferometry, the reference signal has a different frequency than the measurement one. This is usually achieved by slightly shifting the wavelength of the same laser source or by using two frequency-locked lasers with a controlled difference between them. In this case, the intensity in the photodetector is a varying component, and its output due to the non linear mixing contains, apart from a DC component, a downconverted signal at the frequency difference between both beams whose phase depends on distance traveled by the probe beam. This is, the heterodyne interferometer allows measuring phase-shifts that occur in the THz optical carriers, hence achieving very high sensitivity, over much lower and easy to process frequencies. Apart from recovering the information of interest from a narrowband far from DC where other error contributions have a smaller effect, the heterodyne process adds a gain in the mixing with the local reference, what eases the detection of weak signals, increasing the measured ranges and precision. Heterodyne interferometry can reach extremely high precision down to the sub-nm level if stabilized laser sources and noise cancellation techniques are applied.

One of the limitations of both interferometric techniques is the measurement range. In one hand, the region free of cyclic uncertainty is limited to half a wavelength (hundreds of nm). To avoid this limitation, a non-interferometric coherent method called CFDR[42] was applied to optical ranging in [Wang et al., 2001]. In this method, the laser frequency is linearly varied with time in a chirp-like modulation, and the length is measured by estimating the optical frequency difference between the incoming and the reference beam. This is measured using photo-emf sensors, whose output is proportional to the wavelength difference between two received beams. Using this methods, an extended spatial resolution in the tens of μm range is achieved while still providing sub-wavelength precision. Other works propose a multi-wavelength approach to allow absolute distance measurements, either using more than one wavelength for simultaneous measurements [Gelmini et al., 1994] or time-multiplexed measurements with different wavelengths [Williams and Wickramasinghe, 1986, Xiaoli and Katuo, 1998]. These approaches can measure absolute distances up to some mm with μm resolution.

On the other hand, the maximum measurement range is limited to the coherent range of the laser source, which depends on its frequency stability. Noise-frequency-modulations has been applied in [Baetz et al., 2005] to extend this range by measuring the mean beat frequency in the detector, which is proportional to the delay difference between the reference and probe beams. This technique can provide measurements well over the coherence length of the employed laser source in exchange for poorer precision.

One of the most demanding applications for long-range displacement measurements, in which heterodyne interferometry has been used with impressive results, are gravitational wave detectors. These systems require measuring relative displacements over distances of 4 km in the LIGO[43] earth-based detector [Abramovici et al., 1992, Evans et al., 2002] and 1 million km in the latest version of the LISA[44] project [Gerberding et al., 2013, Esteban Delgado et al., 2009, Esteban et al., 2009], both of them requiring sensitivities in the pm/$\sqrt{\text{Hz}}$ level in different bands.

[42] Coherent Frequency Domain Reflectometry
[43] Laser Interferometer Gravitational-Wave Observatory
[44] Laser Interferometer Space Antenna

In general, these methods are based on mapping optical frequencies to electronic frequencies, which allows high sensitivity measurements. Coherent detection techniques yield the highest precision among optical ranging methods, however, they require complex and very stable set-ups for the adequate mixing of the beams and detection of the interference signal. This requirement strongly limits the use of these techniques in the dynamic and unstable conditions of mobile targets localization.

Direct detection

In direct detection, the receiver is only sensitive to the intensity of the received radiation, hence an intensity modulation has to be applied in the emitted signal to be measured after detection for ranging. The method, with its various alternatives, is usually know as IMDD[45]. The most typical modulation schemes are short pulses and CW signals (typically sinusoidal patterns for phase measurements), although FM and PRN modulation have also been applied.

The most extended approach for long distance measurements with non-cooperative targets (without specific reflectors that guarantee strong received signals) is the pulsed method. This is generally applied in commercial reflectorless range-finders, geodetic instruments or LIDAR[46]. The distance is estimated by a direct measurement of the ToA of the pulse. This arrival time can be referenced to the emitted signal in reflective ranging or to the ToA of another signal in differential ranging (DToA). The main advantage of using pulsed signals is that a high amount of energy can be concentrated in short duration pulses without going over safety emitted power limits, so that enough power can be collected after diffuse reflection in far targets. The main disadvantages of pulsed ranging are related to the achievable accuracy. The integrated information is small, since it basically corresponds to the detection instant of the arrival edge. This can be improved by averaging a number of measurements, but most of the signal duration still remains unused. On the other hand, accuracy in the estimation is strongly related with the time resolution of the measuring electronics and the bandwidth of the optoelectronic devices. Achieving cm accuracy in single measurements require time resolutions of some tens of ps, what itself requires very fast electronics for accurate timing. In addition, high bandwidth optoelectronic devices are needed for achieving good quality pulses, what usually implies less available power. Nevertheless, interesting research efforts have been made to overcome both limitations.

[Kilpela et al., 2001] focuses on both frequency limitations. They use a semiconductor laser in Q-switching mode to generate pulses of 35 ps and 200 W, and integrate a high bandwidth (1 GHz) APD[47] and an ASIC[48] with the conditioning electronics and a TDC[49], using an hybrid circuit board to reduce parasitic effects that limit the circuitry response time. 2 mm in both accuracy and precision in one standard deviation are achieved over 34.5 m ranges. The improvements in the manufacturing of single photon counting devices such as photomultiplier tubes and Geiger-mode APDs has allowed the implementation of very fast detectors for flash-LIDAR or single ranging schemes. The latter are used in [Massa et al., 1998, Massa et al., 2002], together

[45] Intensity Modulation Direct Detection
[46] Light Detection and Ranging
[47] Avalanche Photodiode
[48] Application-Specific Integrated Circuit
[49] Time-to-Digital Converter

with coherent integration of the received pulses using time-correlated single-photon-counting to achieve accuracies below 400 μm up to 13 m. Equivalently, [Pesatori et al., 2012] makes use of the advances in fast and stable pulsed laser sources and uses a femtosecond comb with a repetition rate of 250 MHz that contains harmonics up to 1 GHz. The phase delay of downconverted beat notes from high harmonics is measured, what increases the sensitive in a ratio that depends on the original and downconverted frequencies, similarly to an heterodyne process. The downsize of the method is the proportional increase in acquisition time. An accuracy of 100 μm was achieved with this technique in laboratory conditions over a 3 cm path. The authors claim its applicability in industrial ranging by solving temperature stabilization issues and, presumably, increasing the power of the femtosecond comb sources.

The usually called CW method is also very extended in short range construction telemeters or long range geodetic instruments that operate with cooperatives targets such as corner cube reflectors. In this case, the delay information is derived from PoA measurements, usually from a sinusoidal intensity modulation in the MHz band. This technique reaches smaller ranges than the pulsed method, since the short duration of the latter allows higher intensity than the continuously transmitted sinusoidal modulations without infringing eye safety regulations. On the other hand, all the collected samples from the received signal contain useful information, making integration much more efficient. For a given source power and integration time, the phase method would reach higher precision than the direct time estimation of pulses, even if repetitive measurements over a pulse train are used and averaged. Apart from the energy limitation, the PoA method presents a trade-off between precision and unambiguous range due to cycle uncertainty. Higher modulation frequencies yield higher distance resolution but reduce the measurable absolute distance. Schemes using two or three modulation frequencies are usually applied to solve this limitation. Another drawback is their inability to resolve multipath interferences or multitarget reflections. This, however, only applies to long delays between components given that the ability of pulsed methods to resolve multiple arrivals is strongly dependent on the optical bandwidth and current fastest photodetectors still cannot time-resolve paths differences in the cm level. [Weilenmann, 2010] has recently patented a complex mathematical apparatus for multitarget estimation in PoA using specifically tailored periodic signal instead of sines. The patent, however, only provides the mathematical demonstration in noise-free conditions and no real experiment or results applying this technique can be found. [Hinderling, 2006], from Leica Geosystems, also patented a multitarget method using a different concept, in which the estimation is neither time nor phase based. Modulated components at several frequencies, not specified in the document, are used in the receiver to estimate the delay by analyzing the signal form of the system response. The information on the document does not provide more specific details on the implementation, however, the same method is further described in [Bayoud, 2006]. The system, designed to be applied in Leica's total stations, has the capacity to dynamically choose the number and fundamental frequencies of several simultaneous pulse trains, in the MHz to GHz range. When low signal conditions are detected, the number of frequencies is increased to improve precision at the cost of also increasing measurement time. The complete received signal is analyzed in the time and frequency domain to extract the distance information using a ML algorithm, aiming to maximize the use of the received information. Leica's phase-based

instruments reach 2 mm accuracy up to 300 m with reflectorless targets, the document claims that this method can improve such accuracy 4 to 6 times while extending the measurement range above 1000 m.

Although pulsed and CW methods are clearly the most extended, some other approaches derived from other technologies have also been used in the optical domain.

FMCW is often applied in RADAR altimeters. A (usually linear) frequency modulation is applied to the emitted signal and the distance is estimated from the frequency difference with the received one. A simple mixing of both signals produces a beat note whose frequency is proportional to the path length. This method has also been applied in laser ranging. [Dupuy et al., 2001,Dupuy and Lescure, 2002] propose a FMCW laser range-finder for diffuse reflectorless targets up to 20 m. The architecture is well defined and analyzed although performance results are not provided. The authors discuss the use of this method instead of CW phase measurements in systems where the crosstalk between the emitter and the receiver is relevant. The proposal uses the receiver APD as a mixer by modulating its polarization with the local reference. This way, the generated photocurrent is the beat note at a much lower frequency, reducing noise addition in the transimpedance amplifier. The same concept is applied in [Nakamura et al., 2000], where it is referred to as OFDR[50], as the non-coherent equivalent to CFDR, previously addressed in the coherent detection methods in [Wang et al., 2001]. In this case, the research effort is focused on achieving a very efficient emission using FSF[51] laser source to generate a wideband frequency comb with very high chirp rate. The reported measurements over 18.5 km yield a resolution of 2 cm.

Ranging with spread spectrum signals is a very extended technique in the RF domain, applied, for example, as the fundamental measuring systems of all the GNSSs. This method relies on measuring the propagation delay with correlation-based receivers over PRN modulated signals. Its main advantages in RF, such as narrowband interference rejection and high resistance to eavesdropping, do not usually apply for optical ranging and its implementation is more complex. [Kwak and Lee, 2004] applies spread spectrum optical ranging for low accuracy inter-vehicle distance measurement because of its inherent CDMA capabilities. [Esteban et al., 2009, Esteban Delgado et al., 2009] apply it for inter-satellite ranging within the LISA project, design to provide sub-meter absolute distance measurements over the 5 million km links between the LISA spacecrafts. The ranging signal is a 1024 long PRN at 1.5 MHz modulated using 1% of the power of the interferometer laser link. Apart from providing ranging information used to correct the interferometric measurements, the system also provides inter-satellite communication at 97 kbit/s with data modulated on the PRN using DSSS.

2.3.1 Conclusions on optical ranging

The following conclusions can be drawn from the review of the state of the art in optical ranging:

- Coherent detection techniques yields much higher precision, but the required stability in

[50] Optical Frequency Domain Reflectometry
[51] Frequency-Shifted Feedback

the set-ups to maintain adequate coherency and achieve good beam interference prevents its practical application to indoor localization.

- Most direct detection applications are laser-based. The use of laser emitters instead of LEDs implies an inherent high relationship between emitter power and bandwidth. Both parameters are related with the achieved accuracy. The localization scope, where the emitted radiation must reach several receivers simultaneously, requires using a wide radiation pattern. This, together with safety issues, forces the use of LED-based emitters, where a careful optimization in the device selection, aiming at maximizing power and bandwidth, will be fundamental to achieve high accuracy. This includes also the photodetector device, where sensible area and time response should also be carefully balanced.

- Similarly, most ranging applications use directional emission. Again, due to the coverage requirements of the application, the needed wide emitting patterns create a particular coverage-SNR trade-off which is not typical in optical ranging. This trade-off implies a careful selection of the emitter in terms of total power and radiation pattern. In addition, if optics are considered for the receivers, their design should also take into account the trade-off between the virtual increase in sensible area and the receiver FoV.

- Taking into account typical dimensions in indoor environments and the strong accuracy related trade-offs previously commented, using a PoA approach is initially more adequate to maximize the integrated information in the measurement bandwidth. Pulsed measurements would allow increasing ranges, i.e., using fewer receivers to cover certain area, but providing poorer results given the relatively small integration time allowed by the dynamic constrains of the application. Besides, this method would require very fast devices for good accuracy, what would be strongly limited without using laser emitters. Moreover, the pulsed method requires very fast electronics while the design efforts in a PoA alternative could be focused on the time stability of the conditioning circuits, what is easier to achieve under smaller bandwidth constrains. The principal limitation of applying PoA would lie in being able to reach the minimum required signal quality level to perform the measurements in the dynamic conditions of the application while reaching acceptable coverage. However, multi-point LED emitters and APD receivers could be used to relax this limit and increase coverage if the time-stability of a design using those components is not severely reduced in comparison with a link based on a single LED and PiN photodiodes.

- The application of PRN ranging can be interesting due to its easy multiplexing capabilities by CDMA although, initially, considering the power spectrum of typical spreading sequences, the distortion due to the strong bandwidth limitation of the LED-based link would affect the achievable accuracy more severely than in a phase-based method, yielding poorer performance under the same conditions.

2.4 Multipath mitigation

Multipath propagation is a term used in several technological areas related to communications and non-contact measurement, and refers to the propagation of a signal between a transmitter and a detector by more than one path, usually of different length. This, assuming a LTI[52] channel, makes the signal reaching the detector to be formed by the superimposition of several differently delayed and attenuated replicas of the same signal. The degradation in the received signal due to this propagation is usually referred to as multipath interference. This is a phenomenon that usually affects systems that operate with electromagnetic waves (typically in the RF and optical bands), although it is also present in US systems.

Multipath propagation requires the existence of different propagation paths. This can occur due to the reflection of the signal in objects in the environment in wireless propagation, different propagation modes in optical fibers or signal reflections in high frequency wired communications.

Note that, in this context, the term interference does not strictly refers to physical wave interference, for which coherence along the propagation path is required. Multipath interference is used to refer to the perturbation of a received signal on interest, typically the one traveling through the LOS path between transmitter and receiver, by one or several delayed replicas of itself that reach the receiver by other propagation paths. A good sample of this is the case that affects the optical ranging system addresses in this work, in which non-coherent IR signals are used for DToA ranging, and the multipath interferences occur over the intensity modulated optical carriers.

Multipath interferences are a typical source of error in communications, mainly (but not only) through wireless channels, some ranging technologies applied to localization and some interferometric measurements.

- Communications: Wireless RF channels and free-space optical channels are subject to the effect of multipath, what usually causes a reduction of the communication quality by increasing intersymbol interferences. The signal received by the LOS path is not necessarily the signal of interests that is interfered, since the goal of these systems is to maximize the quality of the received symbols to avoid communication errors. Multipath interferences can also occur in NLOS transmissions, in which the symbols are distorted because of the arrival of several signals with different delays. Multipath also appears in fiber-optics communications when multi-mode fibers are used, what creates different propagation lengths for the different components inside the fiber. High frequency wired electrical links can also suffer from multipath if signal reflections occur in the wire due to bad impedance matching; standard input and output impedance values, such as the extended 50 Ω connection, are used in high frequency wired connections to avoid this effect.

- Ranging / localization: Multipath is also a relevant source of error in many non-contact ranging systems. It typically affects ranging applied to localization since this kind of distance measurements, in opposition to other ranging systems such as laser EDM[53] in

[52] Linear Time-Invariant
[53] Electronic Distance Measurement

geodetic instruments, are performed between points whose relative location is unknown. This requires that both the emission and reception systems should cover wide angles, what enables the reception of signals coming from different directions. Typical examples of systems affected by multipath in this category are GNSSs operating in dense man-made environments, where typical construction materials of buildings are good reflectors of the microwave ranging signals coming from the satellites. Also ToA-based ranging systems for indoor localization, such as UWB or optical systems, where surfaces from walls, furniture and people create high density multipath environments. US systems, although initially affected by multipath, can solve most situations (except for very short NLOS-to-LOS path differences) using time-resolved methods, given typical delays in indoor environments and the slow propagation speed of acoustic waves. The multipath problem in ranging, unlike communication systems, is mainly referred to the degradation of the information of only the first component that reaches the receiver, as the goal of these systems is to measure the LOS distance between two points.

- Interferometry: The performance of some interferometric measurements is limited by spurious interferences caused by scattered light or spatial leakage. These phenomena can be classified as multipath effects because they imply the propagation between a source and a receiver by a non-desired paths with higher delays.

A review of the different approaches that have been devised for multipath mitigation is presented in the next subsections. Only those fields that are somehow related to this work, and can therefore provide useful ideas to address the particular multipath problem in IR DToA-based indoor localization, will be covered. Works related to multipath effects on communications are not analyzed since they primarily focus on reducing intersymbol interference, mainly by pursuing the coherent integration of the information that reaches the receiver by differently delayed paths, which is not useful for LOS distance estimation. Subsection 2.4.1 is focused on the multipath problem and its mitigation in localization, mainly regarding GNSS, which is the scope of most multipath-related literature. UWB, whose ToA-ranging architectures are often similar to those used in optical systems, are also addressed. There is no research in optical multipath mitigation for indoor localization, being one of the motivations for this work. Subsection 2.4.2 addresses multipath in interferometric ranging. The specific multipath problems that affect interferometry are briefly explained and the research on multipath separation and delay-based multiplexing are analyzed.

2.4.1 Multipath in localization

GNSS

The vast majority of the research on multipath modeling and mitigation is related to GNSSs. A great number of the solutions proposed for the problem of multipath in more than two decades have been developed in this context.

The initial approaches to this problem regarding the signal processing level were focused on the features of the correlation or discrimination functions [Braasch, 2001]. The effect of the

multipath contributions can be mitigated by proper design of the tracking loops used in these architectures. Some proposals achieve multipath rejection by forming modified discrimination functions using reduced Early-Late spacings as in the narrow correlator approach [Van Dierendonck et al., 1992], or by combining different early and late correlation outputs, as implemented in strobe and edge correlators [Veitsel et al., 1998] and high resolution correlators [McGraw and Braasch, 1999]. Other approaches try to reduce the impact of multipath in the actual correlation functions, before forming the discriminator, by operating the incoming signals with specifically designed references or gating signals. Interesting examples of this technique can be found in [Nunes, 2007] and [Wu and Dempster, 2011], where specific gating functions are developed for the modern BOC[54] signals. Among the new emerging signal structures, BOC signals, where a square sub-carrier modulation is applied to the PRN sequence, have been selected for Galileo[55], modernized GPS and GLONASS[56] partly because of their inherent multipath rejection. The adaptation of previous mitigation techniques to theses signals will probably yield interesting results in the near future. All these discriminator or correlator-based techniques are, in general, simple architectures which do not require high computational power in comparison with the more modern solutions explained next. In addition, their operation does not require any a priori knowledge about the number of multipath components and is more independent from it. They show, however, less robustness against noise than more standard Early-Late tracking loops, and reduce the effective SNR significantly when applied for carrier phase correction. These techniques are fundamentally based on enhancing the estimation of the dominant component, what can create high measurement errors when some multipath component power is higher than the LOS power, what can typically happen in indoor environments.

Research in the last 15 years has been more focused, though not only, on multipath estimation derived from the original concept of the MEDLL[57] [van Nee, 1992, Sanchez-Fernandez et al., 2007]. These techniques are not based on enhancing the resolution for the dominant component but on performing multi-parameter estimations of the composed received signal, what generally requires some a priori knowledge of the approximate multipath situation. The original MEDLL concept has evolved into different improved variants during the last years, such as the Multipath Mitigation Technology [Weill, 2002], the Vision Correlator [Fenton and Jones, 2005], the CADLL[58] [Chen et al., 2011], and the Enhanced CADLL [Chen and Dovis, 2011]. The main advantage of these methods is that they are able to estimate both code and carrier phases for the LOS and multipath components simultaneously while performing close to the theoretical noise-affected precision bounds. This, however, requires high sampling rates and parallelization for tracking the different components, what implies a high number of correlators. Due to this, these techniques are generally more complex and have higher power and computational needs. In addition, the required SNR levels for proper operation are higher than in the correlator/discriminator-based methods. This can be achieved using longer integration times, but it limits the implementation of this solutions to static applications where these integration

[54] Binary Offset Carrier
[55] A GNSS under development by the European Union and the European Space Agency
[56] A GNSS operated by the Russian Aerospace Defense Forces
[57] Multipath Estimating Delay-Locked Loop
[58] Coupled Amplitude Delay-Locked Loop

times are allowed. Some other estimation approaches such as the Teager-Kaiser operator [Lohan et al., 2006] or MUSIC[59] [Li and Pahlavan, 2004] have been proposed; their application for multipath separation is, however, still far from a practical implementation due to the complexity of the required set-up, including the use of antenna arrays. There is also a wide variety of works based on canceling multipath at the reception level, using special antenna designs such as choke-rings or multi-array antennas. These works, however, have not been investigated because of not being applicable for the optical problem addressed in this thesis.

All these works are mainly focused on the correction of typical multipath situations in outdoor scenarios such as urban environments. A study specifically focused in indoor GNSS multipath mitigation was develop by [Dragunas and Borre, 2010]. This work selects two deconvolution-based algorithms, POCS[60] and DA[61], as good candidates for indoor multipath mitigation, and investigates them in depth. The research concludes that the algorithms cannot be directly applied for adequate indoor mitigation, requiring further research as well as higher SNR levels.

Although not particularly useful in GNSS, it is worth mentioning the RAKE receiver [Bottomley et al., 2000] as the classical approach to reduce multipath effects in wireless communications. A rake receiver is formed by several fingers that demodulate the received signal with different delays, and integrates the demodulated information. They are not focused on separating the LOS component, which is the pursued function in ToA systems, but on maximizing the quality of the recovered information by effectively integrating the information received by different propagation channels.

UWB

UWB is the second localization-related field where multipath has been widely addressed and, in this case, specifically focusing on indoor environments. As seen in the indoor positioning section 2.1 of this chapter, UWB technology is one of the best candidates for the development of high accuracy indoor localization. This has motivated some research groups to try to improve UWB ToA ranging by reducing its main error contributions, what, given the signal reflection properties, includes multipath. In addition, the high time resolution inherent to UWB derived from its high bandwidth enables time-resolved multipaths, what makes research in this line even more attractive given its potentially good results.

Part of the UWB literature regarding multipath is focused on location estimation making use of the information received by NLOS paths, such as [Luo and Law, 2012] or [Van de Velde and Steendam, 2012]. The relevant contributions for this thesis are, however, those works focused on analyzing or mitigating multipath in the measuring system level. [Dardari et al., 2009] studies the main accuracy limitations in ToA UWB ranging. Multipath, LOS blockage, clock drifts and interferences are analyzed, and the fundamental accuracy bounds are derived in both ideal propagation conditions and multipath scenarios. A brief study on RSS model-based UWB ranging is also provided, and the performance of some typical ToA estimators regarding the aforementioned error sources is compared. The evaluated practical estimators are a matched

[59] Multiple Signal Classification
[60] Projection onto Convex Sets
[61] Deconvolution Approach

filter with simple threshold approach and several searching methods on an energy detector output (simple thresholding, Max, P-Max, JBSF[62] and SBS[63]). The numerical evaluation shows that, in multipath scenarios, the matched filter approach reaches better accuracy for high SNR and equal for low SNR compared to the simple threshold energy detector. Comparing only the energy detector search methods, simple threshold and JBSF show the minimum error levels for most SNR values. This document is an excellent reference for the understanding and derivation of correlation-based ToA-ranging accuracy limits, not only applicable to UWB signals.

Most of the research in UWB ranging in multipath environments is focused either on mitigating the impact of the NLOS components in the detection of the LOS delay at the measuring system level, or on identifying and classifying NLOS channels, whose parameters are usually applied for a subsequent multipath mitigation. An example of the latter can be found in [Wu et al., 2007], where an algorithm for multipath mitigation in energy detection-ToA, when the LOS is blocked and reaches the receiver strongly attenuated after through-wall propagation, is proposed. A loss model is applied to estimate the excess attenuation suffered by the LOS component, derived from the delay and energy of LOS and reflected (but no obstructed) multipaths. The information of the excess attenuation is used to correct the multipath error. The results are compared with thresholded energy detection in situations where the LOS path is obstructed by one and more than one walls. Multipath errors are reduced by more than 50% in most tests cases.

An interesting example of mitigation at the measuring system level can be found in [Zhang et al., 2009], where a specific ToA-ranging architecture with improved multipath behavior is proposed. The method is based on two stages: an initial noise and interference suppression is applied, based on time-frequency processing which selects the frequency sub-bands with good signal-to-noise and signal-to-interference ratios. First-pulse detection is then applied on the selected sub-bands to obtain multipath-reduced time windows, used for DToA in a subsequent phase measurement. The results are compared with a matched filter peak detection estimator, yielding better performance under low SNR conditions and in the presence of interferences and most strong multipath situations. Multipath error is reduced by one order of magnitude on average except for short wall-reflected multipaths. The results in good conditions, with high SNR and not strong interferences or multipath, are slightly worse (although still comparable) than the ones achieved with the standard time-domain method.

Other

The problem of multipath has not been extensively studied in other localization-related areas, however, some interesting works can be found addressing diverse topics. A specially interesting work for this thesis is [Kurz et al., 2008], who propose a multipath detection and mitigation receiver architecture for pseudolite systems. The proposal is formed by two subsystems. First, a RAIM[64] algorithm is applied. RAIM algorithms are usually implemented at the localization level in GNSSs, whose function is to detect multipath-affected channels so that they are discarded in the computation of the target position when enough signals from other satellites are

[62] Jump Back and Search Forward
[63] Serial Backward Search
[64] Receiver Autonomous Integrity Monitoring

available. The second module is a multi tap correlator-based delay tracking stage that monitors potentially-affected channels taking into account the information provided by the RAIM. When enough measurements are available, the potentially affected channels are discarded; on the contrary, they are processed by the multi tap correlator which provides certain multipath rejection. The specific implementation of the multi tap correlator in the test prototype is based on high resolution correlators [McGraw and Braasch, 1999], whose performance is demonstrated in this work tracking both GPS L1-C/A and Galileo BOC(1,1) signals. The experimental test of the proposal for practical performance evaluation is suggested for future contributions.

Other works like [Alsindi and Pahlavan, 2004] and [Casas et al., 2006] are focused on the optimization of ToA and location estimators in dense multipath environments. Similarly to specific UWB localization algorithms, these are not of interest for this work, primarily focused on the correction of multipath at the measurement system level.

2.4.2 Multipath in interferometry

Scattered light, spatial leakage, cross leakage between arms or doubly-reflected signals in the optical set-ups of interferometers can cause multipath interferences in the detected signals, which lead to nonlinearities between the true and measured displacements known as cyclic errors. A technique known as digitally enhanced interferometry has been developed for reducing these errors, as well as simplifying measurement set-ups by multiplexing the optical path so that differently delayed signals can be measured using a single optical arrangement and detector. Analyzing the research on this method, specifically in its heterodyne version, is of high interest to the present thesis because of the similarities in the specific features of the signal processing stages.

The basis of this method is to modulate the probe beam, after it has been separated from the reference one, with a PRN sequence using an electro-optic modulator. The modulation causes 0 or π rad phase shifts in the optical signal, i.e., the PRN modulates the laser beam in a BPSK scheme. The probe beam then propagates through the measurement arm and is recombined with the reference beam, and the interference signal is measured in the photodetector. When this method is applied to heterodyne interferometry, which is the case of interest for this thesis, the detected signal in multipath-free conditions is a sine signal, whose frequency is the heterodyne tone used to frequency shift the reference beam and whose phase is shifted by the PRN sequence in positions that depend on the probe beam ToF. In standard heterodyne interferometry, if multipath interferences occur in the measurement arm, or more than one target is measured in the same optical path, the received signal would be a superimposition of sine signals of the same frequency, that form a new sine signal where no individual delays could be distinguished. With this method, however, the received signal is the sum of the PRN-modulated sines, whose phase shifts are different for each component due to their different delays. The composed received signal can then be demodulated by multiplying it with the ± 1 sequence of the PRN. Only the sinusoidal components multiplied with a time-aligned version of the PRN will be recovered, while the ones not time-aligned will maintain the original π phase shifts plus the ones caused but the non-coherent demodulation in different positions. A narrowband phase measurement carried

out in the heterodyne frequency band after this demodulation will only extract the phase from the coherently demodulated sine signal, while other components remain as a nearly-white noise floor. This process rejects most part of the multipath effects caused by spurious interferences or signals from other targets by translating their power into an increase of the noise floor that can be time averaged. Different components can be extracted from the same beam in case several delayed signals are to be measured by applying an adequately delayed PRN for demodulating each component.

This method was first described in [Lay et al., 2007], where it is referred to as coherent ranged-gated metrology. In this work the method is applied for simplifying the optical set-up in laser displacement metrology. Standard schemes require the use of several optical heads for adequate isolation of the probe and reference beams. Applying the described technique, the partially-reflective tip of the optical fiber used to emit the probe laser beam towards the target is used as a reference surface, and both returning beams are measured with the same photodetector and separated, based on their delay, in the PRN demodulation after digitization. This method provides a great simplification of the optical set-up, implemented using a single optical head where a traditional set-up for a similar displacement measurement would require 4 heads. Practical measurements with the proposed method in a single optical head set-up, for one retro-reflective target displaced with a piezoelectric transducer, are provided. A rejection rate of 1/120 between the reference and the probe beams is achieved. Apart from the simplified set-up, the effect of cyclic errors that would normally limit the measurement accuracy is also mitigated, and the noise increment from the non-coherently demodulated sines remain as the dominant error contribution, which, in opposition to multipath errors, can be averaged with time.

[Shaddock, 2007] applies this method to measure the separation of three partially reflective mirrors in a single optical path. The receiver recovers every component of interest by demodulating the received signal with different expected delays. The delay is approximately known for each mirror since small displacement in the μm level are measured. The demodulation delay does not have to be very accurate while the error is much smaller than the chip time of the PRN, given that this error causes a small power reduction but has no impact in the measured phase. For achieving good rejection between components, a delay of one full chip time is required. In this case, a 50 MHz chip rate is used, hence the targets must be separated by 3 m so that the round trip between two targets is a full chip length (6 m). Equal chip and heterodyne frequencies are used to achieve better suppression by averaging the measured phases in full code epochs. The proposal is numerically simulated and a cross-talk error between targets of 30 μrad is measured, which agrees with the expected value that depends on the inverse of the number of averaged chips. The authors also discuss the advantages of using a single detector scheme, so that delays and noise contributions in the signal conditioning and digitization stages are common for all the targets, consequently improving performance and simplifying calibration procedures.

[de Vine et al., 2009] apply this method for pm level displacement of an optical cavity 3.75 m long (80 MHz chip rate is used for the PRN). The system is evaluated with an FPGA implementation of the signal processing stage, and the results are compared with an independent and simultaneous readout based on Pound-Drever-Hall locking for reference. An accuracy of 5

pm/$\sqrt{\text{Hz}}$ at 1 Hz is achieved.

[Isleif et al., 2014] present a high speed implementation of this method for multiplexing the measurement system for closely spaced targets. Chip and sampling rates of 1.25 GHz are used, what allows to simultaneously measure the displacement of targets separated 36 cm. A two-mirror configuration (one semi-transparent) is used, in which the reflected signals from each mirror plus several round trip signals are measured. An accuracy of 3 pm/$\sqrt{\text{Hz}}$ at 10 Hz and 1 nm/$\sqrt{\text{Hz}}$ at 1 mHz is achieved. An excess of noise is observed at low frequencies, which the authors associate to clock noise coupling caused by the bandwidth limitation of the test set-up, although suggest further investigations in this line.

2.4.3 Conclusions on multipath mitigation

The following conclusions can be drawn from the review of the state of the art in multipath mitigation:

- UWB systems usually deal with multipath with a time-resolved approach, relying on the high time resolution provided by its bandwidth. This methods cannot be applied to the current optical problem given the strong bandwidth limitation of the LED-based link.
- Multipath estimation methods developed for GNSS require some a priori information of the expected multipath situation and are optimized for a small number of dominant components. This is not the case in the current multipath problem, given the highly diffuse optical multipath propagation in indoor environments.
- The mitigation methods from GNSS-based modified correlation techniques could be studied for the given problem using high sampling rates, although they have a complex implementation and the optical bandwidth limitation would limit their efficiency.
- Interferometric methods using PRN modulations are initially adequate for the addressed problem since, although the whole system is completely different, the electronic measuring stages are very similar given typical heterodyne beat notes in the MHz and tens of MHz ranges. However, this method requires an approximate knowledge of the ToA of the received signals for coherent demodulation, which is not known in the present problem.
- This required delay information for the PRN demodulation of the interferometric approach could be achieved applying spread spectrum synchronization techniques, given the properties of the PRN-modulated signals. This implies the use of correlation-based receivers which, in turn, allows applying some of the GNSS correlation-based mitigation techniques for further multipath rejection in the delay measurement.

Chapter 3

Problem statement and proposed solution

This chapter focuses in the definition of the particular problem addressed by this thesis and a general description of the proposed solution that is studied in detail in following chapters. The general requirements of the IR-based positioning system that contextualizes this work are detailed in section 3.1, conditioning the particular requirements of the ranging system defined to fulfill them. Current technological limits and necessary working conditions related to the practical implementation of the system are also addressed in this section. The multipath problem, detected as a critical error source in the current localization approach, is explained under the particular characteristics of IR ranging in section 3.2. A general description of the proposed method and ranging architecture, defined to mitigate this critical source of error while meeting the necessary requirements, are provided in section 3.3, where the parts of the study, developed during the rest of the document, are detailed.

3.1 Global analysis

This work contributes to the applicability of IR-based DToA ranging for indoor localization by trying to overcome the most relevant limitations of this technique detected in the previous research described in section 2.2. This improvement is addressed by defining a new ranging architecture that eliminates or reduces the main drawbacks of the previous proposals. The basic considerations for the localization system are maintained from the previous work, this is, the basis of the method is still to provide localization by means of distance estimations obtained from near-IR signals. In addition, taking into account that the system is mainly conceived for robotics or small mobile targets localization, the general architecture, where the emitter is boarded in the target and the receivers are placed in the environment, is also kept. This way the target is not loaded with large and high-power consuming hardware, while all the signal processing is carried out in the fixed set-up in the environment. In the probable case that the position information is used for navigation, it can be easily provided by the environment by some adequate RF communication link with the robot.

3.1.1 General requirements

The proposed localization technology is conceived aiming at high accuracy and speed considering typical results in indoor localization. The fundamental application fields of the proposal are mobile robotics, machine guidance and intelligent transport, where cm-to-dm accuracies and sub-second update rates are required for correct and safe navigation. The term "mobile robot" is used in the rest of the document to refer to any kind of autonomous or guided mobile unit located by the system. The general requirements of the ranging system defined for this technology are derived from this context:

- Accuracy: navigation of mobile robots or autonomous vehicles in indoor environments requires that the location of the target is known with relatively high accuracy in comparison with other indoor localization technologies conceived for human navigation or LBSs. Mobile robotics in indoor environments range from small service robots to heavy transport vehicles such as forklifts. In all cases, taking into account typical dimensions of indoor environments, the position of the robot should be known with an accuracy in the cm level or better to allow proper navigation without collisions with humans, surrounding objects or other robots. As demonstrated in previous works on accurate IR-based localization [Martín-Gorostiza et al., 2011, Martín-Gorostiza, 2011], the error in the estimated ranges propagates into errors 2 to 3 times higher when calculating the position of the target from them with the proposed sensor distribution. Taking this into account, the aimed accuracy of the ranging system, understanding accuracy in this context as the total typical error combining the dominant error sources, should be in the mm to cm level.

- Speed: navigation speed of indoor mobile robots in certain applications, such as those related to transport in industrial environments, can also be rather high compared to other localization services. Target speeds up to 1 m/s or even higher may be required in the most demanding cases of near future applications, such as, for example, fully-automated warehouses. The positioning system should be able to meet these requirements, being able to keep track of the current position of the target without accumulating an unacceptable error, and provide this information at a high enough update-rate so that the navigation systems can work properly. The impact of these in the ranging system are: 1) the final bandwidth of the distance estimations should be high enough so that the accumulated error caused by variations in the measured ranges are kept below the accuracy requirements, creating a relevant trade-off between static and dynamic-related errors; 2) the digital system where the signal processing is carried out must be able to work properly under the signal sampling constrains, maintaining a real-time operation to provide measurements with an adequate update-rate.

- Coverage: as in any other localization system, an area as large as possible should be covered minimizing the deployed infrastructure to reduce initial installation and maintenance costs. In the present system ranges are estimated from optical signals propagating in free-space in the LOS path between the emitter boarded on the target and receivers placed on an elevated horizontal plane (typically the ceiling of the environment). Maximizing coverage

in this configuration means reducing the number of deployed receivers as much as possible. From the ranging system point of view, this means spreading the emitted optical radiation in the widest possible solid angle, while also maximizing the field of view of the receivers, so that enough power simultaneously reaches a minimum number of receivers so that the position equations can be solved with an adequate accuracy.

- Multiagent: The ability of providing service simultaneously to a number of users with little or no performance reduction is a key feature in most localization systems. In the particular case of the technology addressed in this work, it involves several targets, each one having its own emitter, being localized by the same infrastructure. This is, their signals reaching simultaneously the same receivers. Thus, the ranging system must be able to process several received signals in parallel, defining some method that allows the system to make the difference between them in a coherent and continuous way.

- Viability: Apart from the aforementioned requirements, some general considerations that make the system feasible in a practical level must be considered. These requirements are ultimately related to minimizing the cost of the system. This means, in one hand, reducing the hardware costs and simplifying the necessary processing units as much as possible. In the other hand, reducing maintenance, which is related to avoiding or minimizing any calibration processes needed for the proper long-term operation of the system.

The first three requirements represent the most relevant trade-off of the positioning system. In a high-level point of view, relative to the positioning system, both coverage and speed cannot be improved without penalizing precision. This is explained by the translation of this trade-off to the low-level, relative to the measuring system. These trade-offs on both levels are depicted in figures 3.1 and 3.2 respectively. Coverage is related with the emission and reception angle of the optoelectronic devices or the optical systems applied to them. Precision is related to the final SNR of the signals used to carry out the estimation. This is itself related, in one hand, with the amount of received power in certain receiver and, in the other hand, with the amount of noise integrated in the final bandwidth of the estimation. Speed is also related with the estimation bandwidth, given that the response time of the measurement system, hence the amount of accumulated dynamic error for a given target speed, is ultimately determined by this bandwidth.

If the system coverage wants to be increased to reduce the number of deployed receivers, the emitted radiation pattern should be widen as much as possible. This, for a given total emitted power for certain device, means reducing the amount of power per solid angle, i.e., the power reaching any receiver. This would reduce SNR, so the precision of the system would be penalized. In the other hand, if the maximum allowable speed of the target wants to be increased, guaranteeing that the dynamic error in its tracking does not surpasses certain level, the estimation bandwidth should be increased. A higher bandwidth improves the response time of the measurement system, reducing dynamic errors; however, it also means integrating a higher amount of noise spectrum in the measurement, reducing SNR, hence precision.

Most of the requirements commented above, as well as the trade-offs relating them, affected the previous version of the ranging system developed for the proposed IR LPS, described in

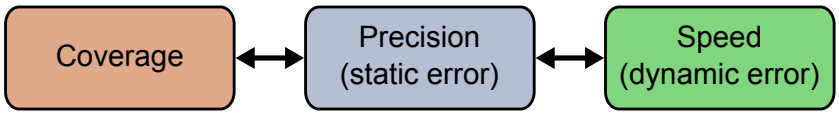

Figure 3.1: Trade-offs in the positioning system level

Figure 3.2: Trade-offs in the ranging system level

[Martín-Gorostiza, 2011] and detailed in section 2.2, and were already addressed in its design. The main motivation of this study is the improvement of this previous version of the system by solving its main drawbacks and adding the possibility of simultaneously locating several targets.

3.1.2 Specific problems

The main issues to be specifically addressed by this study, while fulfilling all the other general requirements, are:

- Reducing calibration requisites that affect the analog processing stages of the previous ranging proposal.
- Adding multiplexing capabilities to the ranging system so that several targets can be simultaneously tracked without reduction of performance.
- Reducing the effect of multipath interferences so that the system performance meets the accuracy requirements more independently from the particular environment geometry and reflective properties.

Calibration: The previous proposal of the system, as shown in section 2.2 relied on analog processing to extract the phase information. Digitization was performed in the late stages of the measurement process, after analog signal demodulation. This implies that a careful calibration of the demodulation stage was required to maintain the accuracy requirements. The need of calibration in every individual demodulator was an important drawback from the viability point of view: maintenance tasks are required more often to recalibrate the system, and scalability is also penalized since calibration tasks are proportional to the system extension, increasing both installation and maintenance costs.

In the digital domain, most of the parameters that required calibration in analog processing, such as amplitude imbalances, DC offsets or quadrature errors of the I/Q demodulator [Martín-Gorostiza et al., 2009], are not present or can be neglected in relation to other error sources. Due to this, the main approach to solve the calibration issues is aiming to carry out all the signal processing in the digital domain by, independently of the proposed system, bringing digitization as close as possible to the sensor output. This way, calibration tasks will be strongly

reduced or even completely discarded. On the other hand, special attention should be given to the performance and errors added in the digitization stage since, being applied shortly after low-level signal conditioning, its influence in the overall system performance becomes more relevant. Independently of the selected ranging technique, some general requirements regarding the digitization stage in relation to the received signal quality are defined in section 3.1.4, aiming to define the minimum requisites that the digitization system should fulfill so that its effect can be neglected compared to other error sources of the system that cannot be reduced given the current technological limits.

Multiuser: Multiuser is a key feature for most localization systems, which was not fully solved by the previous version of the ranging architecture. The previous design allowed multiplexing the channel by FDMA[1], however, this would imply adapting the receivers for a wider frequency range, what impeded their optimization to a particular working frequency to achieve better phase stability, and therefore higher accuracy. On the other hand, ranging precision is strongly related with working frequency, hence, applying FDMA would also mean having different performance depending on the particular frequency assigned to each user.

The possibility of providing multiuser localization without reduction of performance has been considered in the definition of the proposed ranging architecture by applying CDMA, as will be seen in section 3.3.

Multipath: Multipath interferences were identified as the main accuracy-limiting factor of the previous design. Providing a ranging solution that reduces this effect is, therefore, a key issue in fulfilling the aforementioned accuracy requirement. The particular multipath problem in this context requires a specific modeling and further development of its geometrical dependencies before addressing its mitigation; thus, section 3.2 is specifically dedicated to it, while its reduction has been taken as one of the main design goals in the definition of the ranging proposal.

3.1.3 Current technological limits

Some practical considerations regarding current realistic signal and noise levels considering a feasible IR link built with up-to-date optoelectronic devices, as well as achievable timing accuracy that defines the frequency errors bounds between emitter and receivers, are addressed next.

3.1.3.1 IR link and signal conditioning

The IR link features critically define the whole ranging system performance. Received power and working frequency are set by the link, depending on the emitter and receiver devices and electronics, and the noise addition in the conditioning stage. The constrains related to them are defined assuming a non-coherent link. This implies the use of an emitter system based on an IR LED and a receiver based on a standard photodiode. In case the cost requirement of the system are relaxed, the receiver could be replaced by an APD, adding optical gain that would increase the received power while maintaining frequency and coverage parameters. Apart from

[1] Frequency Division Multiple Access

increasing costs, the use of an APD would make the whole receiving infrastructure more complex by adding the need of high-voltage power supply in the receivers, since APDs usually require polarization levels in the other of tens of volts, or even above one hundred volts, while standard photodiodes can work properly with supplies in the volt level.

- Emitter: The relevant features related to the emitter are the total emitted power, the frequency response and the emission pattern that defines how the total optical flux is distributed. The emission pattern is not addressed as a constrain here because it can be usually adapted to the coverage requirements by adding some simple optical system. As commented in the system requirements section, emitted power and frequency response of LEDs are inversely related. High output devices are larger due to its inherent manufacturing requirements and thermal dissipation issues. This implies that the parasitic effects that limit their frequency response become larger, reducing the maximum working frequency allowable with that devices.

- Receiver: The relevant features of the receiver are the sensible area and the frequency response. Similarly to the emitter, both parameters are inversely related. Larger devices that cover a wider solid angle, thus increasing their received power, show a larger parasitic capacitance, reducing their frequency response. On the other hand, if optics are used to increase the effective sensible area of the receiver without affecting its frequency response, the achievable area is inversely related to the field of view covered by the optical system; hence setting a new trade-off between SNR and coverage.

- Conditioning stage: The main feature of the conditioning stage that limits the system performance is the amount of noise added to the received signal. The conditioning stage converts the photocurrent generated by the receiver photodiode into a voltage, and amplifies and filters to adequate the signal for digitization before processing. The generated photocurrent is very small, reaching the nanoampere level. This implies applying a very high transimpedance gain to produce a signal with an acceptable voltage level for the digitizer input. This high gain also amplifies the noise contributions generated in the photodiode and the transimpedance amplifier itself, setting them as the dominant noise contribution of the system. The relevant parameter that encompasses these noise contributions, assuming a flat frequency response in the signal bandwidth, is the noise density in the output of the conditioning stage. This noise density, together with the electrical power of the signal in that point, define the SNR in the input of the digitizer and, ultimately, the SNR available for the subsequent signal processing. Phase stability and frequency response of the conditioning stage are also relevant for the system performance, increasing uncertainty, distortion and total power losses. However, with a proper low level electronic design, which is not in the scope of this work, these contributions can be neglected when compared to the limitations imposed by the previous parameters.

A simple calculation of the SNR level in the output of the conditioning stage is given next. After defining a realistic IR link and conditioning stage that maximizes the aforementioned parameters, the expectable minimum SNR level in a practical indoor configuration is estimated.

The received optical power P_o in certain receiver, assuming a Lambertian (n=1) emitter and that the boresights of emitter and receiver are in the same direction, is given by

$$P_o = I_e \frac{A_s}{d^2} \cos^2(\theta) f(\lambda) \tag{3.1}$$

with I_e being the radiant intensity in the normal direction to the emitter surface, A_s being the sensible area of the photodetector, d being the propagation path length, θ being the emission and reception angle to the vertical and $f(\lambda)$ being the absorption of an optical filter in the receiver as a function of wavelength.

A standard photodiode conditioning stage is defined, formed by a transimpedance amplifier followed by a voltage amplifier, whose frequency response is assumed to be flat in the signal bandwidth.

The received electrical power P_r at the output of the low-level conditioning stage is given by

$$P_r = (P_o \mathcal{R} G_f G_v)^2 \tag{3.2}$$

with $\mathcal{R}$ being the responsivity of the photodetector at the peak emission wavelength, G_f being the gain of the transimpedance amplifier and G_v being the voltage gain before digitization, both considered flat in the signal bandwidth.

The SNR in the output of the conditioning stage, i.e., the input of the digitizer, is

$$\text{SNR} = \frac{P_r}{N_0/2} \tag{3.3}$$

where $N_0/2$ is the double-side noise power spectral density in that point of the circuit.

A practical selection of an available IR LED and photodiode has been carried out, following the criterion of maximizing the relation between transmitted power and available bandwidth in the link. Table 3.1 shows the device parameters corresponding to an example of a practical selection of up-to-date IR-LED and Silicon-PIN photodiode to implement a 870 nm link with 25 MHz chip-rate using simple optics on both devices. The gains and noise contribution in the conditioning stage are also included, taken from a realistic design for indoor ranging applications, evolved from the design developed in [Martín-Gorostiza et al., 2011] for the previous version of the positioning system explained in section 2.2.

Considering these parameters, the achievable SNR is calculated for the worst case of a practical configuration in an typical indoor environment. Let assume the receivers are placed in the ceiling of the environment, being 2.5 m high; and the emitter is boarded on a target 0.35 cm high. Assuming the maximum allowable disorientation between emitter and receiver boresights is set to their half-intensity angle, i.e., $\theta = 60^o$, the maximum horizontal distance between emitter and receiver would be approximately 3.7 m, yielding a propagation path $d = 4.28$ m. The described situation is depicted in figure 3.3.

In the described configuration, the received optical power would be approximately 2 nW. Considering the conditioning stage parameters, this optical power yields an electrical power in the output of the voltage amplifier of approximately 14 μW, what, taking into account the noise

Table 3.1: Parameters of the emitter (IR-LED: Hamamatsu L12170), receiver (Silicon-PIN photodiode: OSI BPX-65R) and conditioning stage selected as a practical example to implement an IR link for 25 MHz chip-rate

	Parameter (Symbol)	Value	Units
Emitter	Total radian flux (Φ_e)	113	mW
	Radiant intensity (I_e)	36	mW/sr
	Peak emission wavelength (λ_p)	870	nm
	Half-intensity angle ($\alpha_{1/2}$)	60	^{o}
	Cut-off frequency ($f_{c_{Tx}}$)	50	MHz
Receiver	Sensible area (A_s)	4	mm^2
	Responsivity @ 870 nm ($\mathcal{R}$)	0.57	A/W
	Cut-off frequency ($f_{c_{Rx}}$)	160	MHz
	Transimpedance gain (G_f)	33	kΩ
	Voltage gain (G_v)	100	V/V
	Noise spectral density ($N_0/2$)	$1.34{\cdot}10^{-11}$	W/Hz
	Optical filter @ 870 nm ($f(\lambda)$)	1	W/W

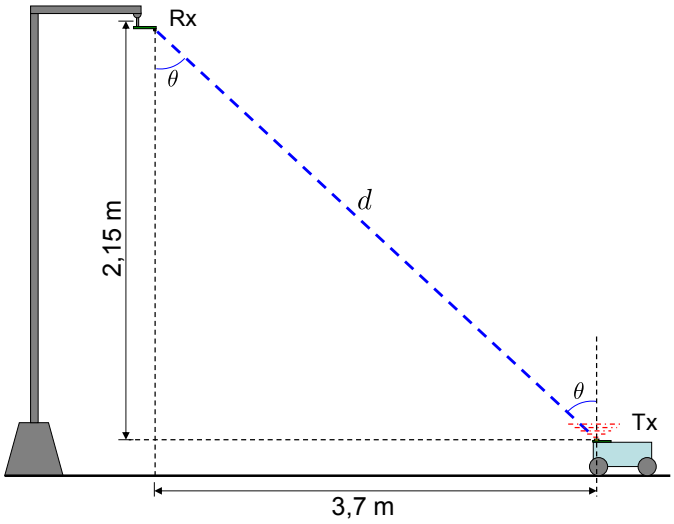

Figure 3.3: Link configuration used for the expected minimum SNR calculation

power spectral density in the same point of the circuit, yields an SNR of 60.1 dBHz.

On the other hand, in the most favorable situation when the target is exactly under certain receiver, the received optical power is approximately 31 nW, which means in turn an electrical power of 3.4 mW, yielding an SNR of 84.1 dBHz.

The minimum and maximum SNR levels in the same conditions, maintaining a maximum horizontal distance of 3.7 m and varying the ceiling height form 2.5 m to 8 m is shown in figure 3.4.

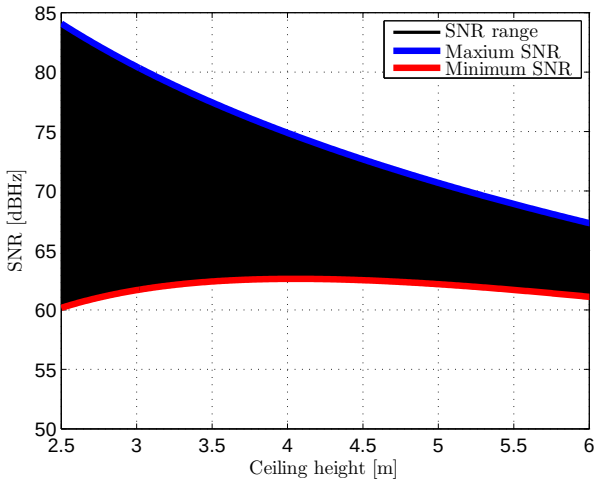

Figure 3.4: SNR range as a function of ceiling height using the defined IR link when the maximum horizontal separation between emitter and receiver is 3.7 m

A complete test set-up will be defined in the results section to evaluate the whole system performance, however, these SNR values can be taken as realistic signal quality limits. An SNR range of $[60 - 85]$ dBHz will be generally assumed for bounding the error analysis in following chapters.

The maximum horizontal separation between emitter and receiver has a strong impact for the general features of the localization system, since it defines the coverage per receiver, and consequently the number of deployed sensors required to cover certain area. The value of 3.7 m calculated for the half angle when ceiling is 2.5 m high will be taken as a reference for this study. However, to illustrate the dependence of SNR with this parameter, the SNR range calculated in the same conditions as in figure 3.4, when the maximum horizontal distance between emitter and receiver is either 1 m shorter (2.7 m) or 1 m larger, is respectively depicted in figures 3.5.a and 3.5.b.

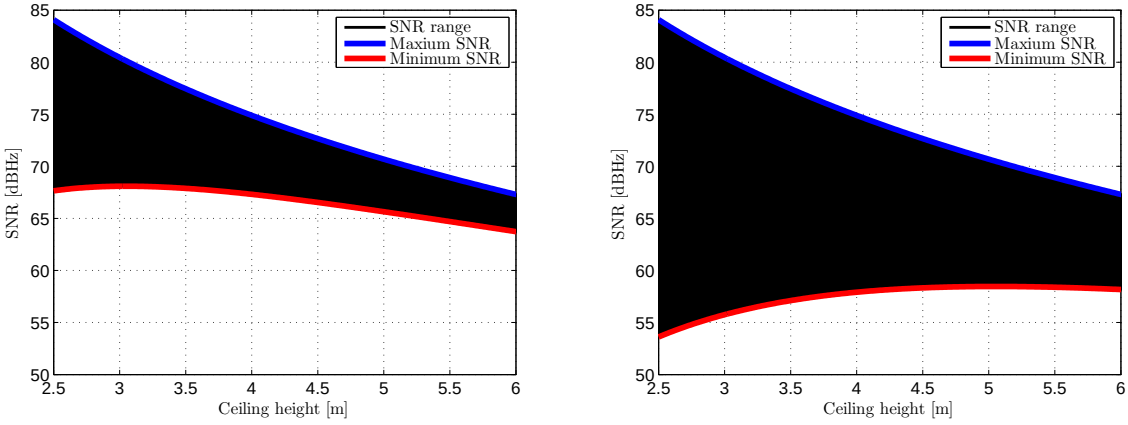

(a) Maximum horizontal separation: 2.7 m

(b) Maximum horizontal separation: 4.7 m

Figure 3.5: SNR range as a function of ceiling height using the defined IR link for two different maximum horizontal separations between emitter and receiver

3.1.3.2 Signal generation

The emitter boarded on the target to locate is independent from the rest of the infrastructure formed by the receivers and signal processing. This implies an inherent asynchronous behavior between emitter and receivers, leading to frequency errors between the timing systems in both subsystems. The general conception of the ranging system is based on differential measurements between pairs of receivers. This difference solves the lack of synchronism between emitter and receivers, however, any process carried out in a single receiver which implies the generation of local signals before calculating differences, is subject to frequency errors in relation to the received signal generated in the emitter. Due to this, the dynamics of these non-differential processing in every receiver must be adapted to tracking delay variations in the received signal not only related to the target displacement but also to the apparent delay variation caused by frequency errors.

The delay variation caused by these error is modeled next to be used in subsequent chapters and define a realistic maximum delay rate of change considering up-to-date oscillators.

The emitter produces a signal with fundamental frequency $f_{c_{Tx}}$. This signal reaches the receiver and, regardless of the method, its delay in relation to a locally generated replica is calculated. The local replica is generated with fundamental frequency $f_{c_{Rx}}$. If both clocks were ideal: $f_{c_{Tx}} = f_{c_{Rx}} = f_c$, where f_c is the design fundamental frequency of the transmitted signal.

The frequency tolerance provided by oscillators manufacturers is given by ϵ_{CLK} expressed in ppm, as the maximum relative frequency difference between the real frequency f_{CLK} in relation to the nominal frequency f_{CLK_N} is

$$\epsilon_{\mathrm{CLK}} = \frac{\left| f_{\mathrm{CLK}} - f_{\mathrm{CLK}_N} \right|}{f_{\mathrm{CLK}_N}} 10^6 \tag{3.4}$$

with certain probability, usually higher than 99%. Taking the worst case, the real frequency of the oscillator is

$$f_{\mathrm{CLK}} = f_{\mathrm{CLK}_N} \pm \frac{\epsilon_{\mathrm{CLK}}}{10^6} f_{\mathrm{CLK}_N} \tag{3.5}$$

Assuming for simplicity that the emitter clock is ideal ($f_{c_{Tx}} = f_c$), and adding its error to the receiver clock assuming both are maximum and of opposite sign, the worst case frequency difference in relation to the design frequency is

$$f_{c_{Rx}} = f_c \pm 2\frac{\epsilon_{\mathrm{CLK}}}{10^6} f_c \tag{3.6}$$

The apparent rate of change of the delay caused by this frequency difference is

$$\Delta_\tau^{\mathrm{CLK}} = 1 - \frac{f_c}{f_{c_{Rx}}} \tag{3.7}$$

which, replacing the worst-case value for the receiver clock, yields

$$\Delta_\tau^{\mathrm{CLK}} = 1 - \frac{1}{1 \pm 2\frac{\epsilon_{\mathrm{CLK}}}{10^6}} \approx \pm 2\frac{\epsilon_{\mathrm{CLK}}}{10^6} \tag{3.8}$$

As shown in the previous section on the IR link performance, current achievable bandwidths are in the range of tens of MHz. Up-to-date high performance TCXOs[2] working in that frequency range can reach an overall stability, after proper load calibration and considering aging and non-compensated temperature variations below 0.1ppm. Nevertheless, a value of 1ppm, easier and cheaper to achieve, will be considered in the analyses. The consequences of using more accurate timing will be commented in the results discussion.

This clock error, assuming the worst case defined above, would cause an apparent delay rate of change of approximately 2 μs/s. The dynamic of any process in the receivers that requires tracking the delay of its incoming signal, instead of the differential delay only affected by target displacements, must be adapted to this delay rate of change. The calculated value will be used in the rest of the document to bound the necessary requirements in the dynamics of the receiver processing stage.

3.1.4 Working conditions and requirements

Regarding the digitization stage and digital signal processing hardware, current technological limits are beyond the application requirements. Due to this, this section aims to define an adequate scaling of the digitizing and processing hardware so that the system can operate properly, avoiding any relevant performance reduction in relation to the main error sources of the system while minimizing the cost of these stages.

3.1.4.1 Digitization

The effect of digitization is briefly analyzed, to define some approximate minimum requirements and considerations related to the resolution, sampling frequency and simultaneity of the digitizer.

Resolution

The applied criterion to define the necessary resolution is that the quantization noise can be neglected against the input signal AWGN[3] contribution. This will be defined in terms of a worst case SNR.

Assuming that the worst received power level in certain scenario is $P_{r_{\min}}$, the worst case SNR for that scenario would be

$$\mathrm{SNR}_{\min} = \frac{P_{r_{\min}}}{N_0/2} \tag{3.9}$$

where N_0 is the double-side noise power density of the AWGN contribution contained in the received signal before digitization.

The SNR defined by quantization noise for that minimum received power is

$$\mathrm{SNR}_{\mathrm{Q}} = \frac{P_{r_{\min}}}{N_Q} \tag{3.10}$$

[2] Temperature-Controlled Crystal Oscillators
[3] Additive White Gaussian Noise

with N_Q being the noise density due to quantization noise

$$N_Q = \frac{\sigma_Q^2}{f_s/2} \tag{3.11}$$

which depends on the total quantization noise variance σ_Q^2 and the quantization noise bandwidth $f_s/2$ defined by the sampling frequency. σ_Q^2 can be modeled as the variance of a uniform probability distribution with limits $[-Q/2,\ Q/2]$

$$\sigma_Q^2 = \frac{Q^2}{12} \tag{3.12}$$

where Q is the quantization step defined by the digitizer SPAN and resolution

$$Q = \frac{\text{SPAN}}{2^{n_{\text{ADC}}}} \tag{3.13}$$

with n_{ADC} being the number of bits of the digitizer ADC[4]. The SPAN should be adapted to the maximum voltage value to be digitized. Assuming that the difference between maximum and minimum received power in certain scenario is of 2 orders of magnitude (which is the approximate value for the link set-up given in 3.1.3.1), the maximum received power would be $100P_{r_{\min}}$. The maximum voltage range in the input of the digitizer, considering signal structure, would be

$$v_{max} = \sqrt{2 \cdot 100P_{r_{\min}}} \tag{3.14}$$

The digitizer SPAN should be adjusted to that range, which, adding a margin of $2v_{max}$ to avoid saturation due to noise, and taking into account signal bipolarity, yields

$$\text{SPAN} = 4v_{max} = 4\sqrt{2 \cdot 100P_{r_{\min}}} \tag{3.15}$$

Replacing in the above expressions, noise power density due to quantization is

$$N_Q = \frac{\left(4\sqrt{2 \cdot 100P_{r_{\min}}}\right)^2}{\left(2^{n_{\text{ADC}}}\right)^2 f_s/2} = \frac{6400P_{r_{\min}}}{2^{2n_{\text{ADC}}} f_s} \tag{3.16}$$

so the SNR defined by quantization noise in the worst case, i.e., for the minimum received power, is

$$\text{SNR}_Q = \frac{P_{r_{\min}}}{\left(\frac{6400P_{r_{\min}}}{2^{2n_{\text{ADC}}} f_s}\right)} = \frac{2^{2n_{\text{ADC}}} f_s}{6400} \tag{3.17}$$

The goal is being able to neglect quantization noise introduced by digitization in the worst case scenario. The chosen criteria to fulfill this is that the ratio between this minimum SNR due to digitization and the minimum SNR due to noise is, at least, of 2 orders of magnitude (20 dB), this is

$$\frac{\text{SNR}_{\text{Q}}}{\text{SNR}_{\text{min}}} > 100 \tag{3.18}$$

[4]Analog-to-Digital Converter

Replacing

$$\frac{\left(\frac{2^{2n_{\mathrm{ADC}}} f_s}{6400}\right)}{\mathrm{SNR}_{\mathrm{min}}} > 100 \tag{3.19}$$

what yields

$$2^{2n_{\mathrm{ADC}}} f_s > 6.4 \cdot 10^5 \mathrm{SNR}_{\mathrm{min}} \tag{3.20}$$

Considering that the signal is bandlimited to the channel bandwidth (BW_{IR}), a minimum sampling frequency $f_s = 2BW_{IR}$ should be used to avoid aliasing. The minimum resolution of the ADC to fulfill the defined criterion is

$$n_{\mathrm{ADC}} > \frac{\log\left(\frac{6.4 \cdot 10^5 \mathrm{SNR}_{\mathrm{min}}}{2BW_{IR}}\right)}{2\log\left(2\right)} \tag{3.21}$$

This relation, though approximate, is useful to define some minimum digitizer requirements in terms of noise addition. The main assumption about the scenario is considering 2 orders of magnitude between maximum and minimum received power, which is a reasonable assumption taking into account the power levels calculated for the practical scenario and implementation of the IR link defined in section 3.1.3. Should this relation be higher, the digitizer requirements would become more strict due to the higher difference between the necessary SPAN and the minimum signal level to be converted.

As an example to illustrate the calculated relationship, defining a received signal with $f_c = 25$ MHz over a 50 MHz optical channel sampled at the Nyquist frequency. The minimum number of ADC bits as a function of the minimum SNR level is shown in figure 3.6.

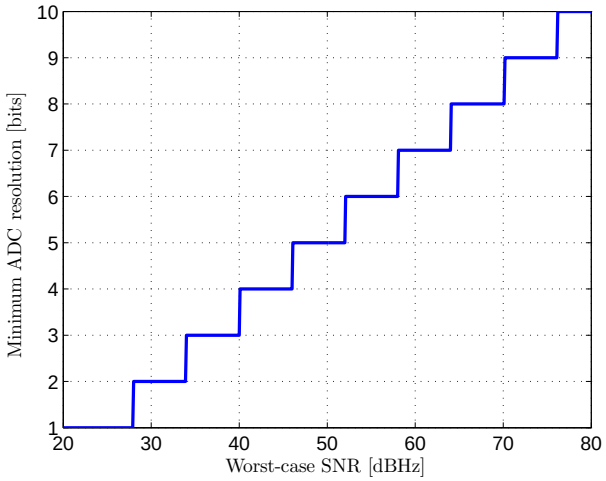

Figure 3.6: Minimum number of ADC bits as a function of the analog signal minimum SNR level ($BW_{IR} = 50$ MHz, $f_c = 25$ MHz, $f_s = 100$ MHz)

The number of ADC bits shown in the figure for every worst-case SNR would guarantee, with the defined criterion, that the effect of quantization noise over the total noise stays approximately around 1%. For the minimum expected SNR level of approximately 60 dBHz, calculated in 3.1.3, the required digitizer resolution would be 7 bits. Using a higher resolution would increase the digitizer price hardly increase performance, since quantization noise would be negligible against

conditioning electronics noise. On the other hand, using a smaller resolution would have a relevant impact on precision, generating quantization noise levels that could not be neglected anymore when compared to conditioning electronics noise.

Sampling frequency

The required sampling frequency is addressed here from a simple theoretical point of view. There are some practical implications relating sampling frequency to very specific stages of the system. These will be addressed in the particular sections in 4.2.2 and 5.2.2.

The basic condition to be fulfilled is the Nyquist-Shannon theorem in relation to the signal bandwidth so that the digital sequence introduced in the processing stage provides an adequate representation of the analog received signal. This is, if the analog signal bandwidth is BW_S, the sampling frequency should be higher than 2 times the signal bandwidth ($f_s > 2BW_S$). On the other hand, in case that the full signal bandwidth is higher than the IR link bandwidth ($BW_S > BW_{IR}$), i.e., the received signal is partially distorted by design, the minimum sampling frequency should be chosen to provide an adequate representation of the signal falling into the available link bandwidth ($f_s > 2BW_{IR}$).

An adequate anti-aliasing filter in $f_s/2$ should be applied in any case to the received signal before digitization to avoid increasing the noise level in the digital signal caused by noise overlapping.

As part of the background research of this thesis, investigations were carried out aiming to reduce the sampling requirements of the previous IR-PoA localization proposal by applying sub-Nyquist techniques. These can be found in [Salido-Monzú, 2011, Salido-Monzú et al., 2012]. This work was later extended and generalized to apply to any narrowband phase measuring system and has been submitted as [Salido-Monzú et al., 2015].

Simultaneity

Since the final estimation is based on differential measurements between pairs of receivers, the quality of sampling simultaneity between digitized signals has a direct impact on the final estimation error. The first and most relevant consideration in this sense is that, to cancel the errors caused by the asynchronous emitter-receiver processing by using differential observations, the time-base of the processed received signals must be common. This implies applying a digitization process with a common timing system for all the channels corresponding to potential receivers to be paired.

Achieving accurate enough sampling synchronism using digitizers spatially separated without a wired connection, e.g., broadcasting an optical or RF synchronization signal, is a very complex task for such a demanding application in terms of differential errors. This approach would add some other relevant effects that require a very specific study and will not be considered in this work. This work assumes the use of a digitization system in which all the channels share a good quality wired connection, hence a common timing system based on a single master clock.

A simultaneous digitization is not strictly required as long as the delay between sampling times in different channels is stable enough and can be calibrated. The main consideration to

be taken into account for scaling the digitization requirements is related to jitter effects in the sampling time.

Sampling jitter is defined as a temporal dispersion of the sampling instant in relation to its average value. This effect can be periodic, usually caused by interferences in the timing signal of the sampling system, or random, caused by the fluctuations in the aperture instant of the sampler due to noise contained in the timing signal. Periodic jitter is not considered here because it usually depends on external and environmental factors and cannot be specified by the manufacturer. On the other hand, random jitter is usually defined by noise addition in the digitizer electronics, and its maximum values are usually provided by manufacturers of high performance digitizers.

Random jitter can be modeled as an increment in the additive noise of the digitized signal. This jitter can itself be divided into two different contributions. When the noise addition that causes the jitter affects the timing signal generation and signal paths common to all channels, its effect is highly correlated between channel, hence canceled when differential measurements are carried out, so its effect is not considered for this application. On the other hand, some jitter effects are not common to all channels, generally because they are caused by noise contributions introduced in the specific timing signal path for one channel. This kind of inter-channel jitter does introduce a noise increment in the signals which is uncorrelated between channels, thus increasing the error in the differential measurements.

When sampling pure tones, jitter appears as an additive noise contribution in the digitized signal. The digitized signal is assumed to be sampled with equally-spaced intervals, when this is not the case due to jitter, the value of a particular sample has an error in relation to the value that it should have if the sampling instant was perfectly placed. Assuming that jitter is caused by AWGN, which is usually a reasonable assumption given the noise sources in the digitizer electronics, the apparent additive noise in the digitized signal is also AWGN, whose power depends on the jitter power and the amplitude and frequency of the digitized tone. Higher frequencies and amplitudes translate certain time jitter into higher amplitude errors due to the faster rate of change of the signal. The study of the maximum admissible jitter is carried out under the assumption of digitizing pure tones. This assumption will not be strictly true since, as will be seen in following sections, a modulation including pure tones and PRN signals will be used in the proposal. However, regardless of the particular parameters of the signal to be defined in following sections, it will generally imply the digitization of a sine-like signal, even if phase-shifted by a PRN code, hence having a similar translation between time jitter and additive noise as if it was a pure tone.

Defining the inter-channel jitter standard deviation between two channels as δ_{jitter}, the additive noise power introduced by it, as a function of the signal power P_r and frequency f_r, is

$$P_{\text{jitter}} = P_r \left(2\pi f_r \delta_{\text{jitter}}\right)^2 \tag{3.22}$$

This power is uniformly distributed in the Nyquist bandwidth $f_s/2$, so the noise density

N_{jitter} caused by jitter is

$$N_{\text{jitter}} = \frac{P_r \left(2\pi f_r \delta_{\text{jitter}}\right)^2}{f_s/2} \tag{3.23}$$

so the SNR defined by jitter is

$$\text{SNR}_{\text{jitter}} = \frac{f_s/2}{\left(2\pi f_r \delta_{\text{jitter}}\right)^2} \tag{3.24}$$

The criterion used to defined the maximum admissible jitter level is the same used for the ADC resolution, this is, that the SNR caused by it is two orders or magnitude higher than the minimum SNR level set by the the dominant noise source of the system, addition in the conditioning stage of the receivers, in the worst case. This is

$$\frac{\text{SNR}_{\text{jitter}}}{\text{SNR}_{\text{min}}} > 100 \tag{3.25}$$

so the expression of the admissible standard deviation of the ADC inter-channel jitter that fulfills this criterion is

$$\delta_{\text{jitter}} < \sqrt{\frac{f_s}{800 \left(\pi f_r\right)^2 \text{SNR}_{\text{min}}}} \tag{3.26}$$

It can be observed that the maximum admissible jitter depends on the minimum SNR in the analog signal before digitization and the relationship between sampling and tone frequencies. To provide an illustrative numerical result, the worst case will be considered for the frequencies relationship. This worst case would imply that the sampling frequency is set to fulfill the Nyquist theorem for the IR channel bandwidth, and the tone frequency is equal to it, this is $f_s = 2f_r$. Considering this relationship, the jitter must fulfill

$$\delta_{\text{jitter}} < \sqrt{\frac{1}{400\pi^2 f_r \text{SNR}_{\text{min}}}} \tag{3.27}$$

Figure 3.7 shows the maximum admissible standard deviation for the inter-channel jitter as a function of the minimum SNR level in the analog signal for different signal frequencies.

The maximum jitter standard deviation shown in the figure for every worst-case SNR would guarantee, with the defined criterion, that the effect of sampling jitter over the total noise stays approximately around 1%. Again, considering the practical implementation of the IR link defined in 3.1.3, were a minimum SNR of approximately 60 dBHz at 25 MHz chip rate was calculated, the standard deviation of the inter-channel jitter for the selected digitizer should be smaller than 3 ns.

3.1.4.2 Signal processing

The basic requirement for the hardware carrying out the signal processing is that it is able to work in real-time i.e., continuously processing the digitized signal at the sampling rate without accumulating unacceptable delays. The processing is rather demanding since a high signal bandwidth has to be maintained during most of the measuring process for tracking the delay variations caused by the asynchronous emitter-receiver processing. This does not allow reducing

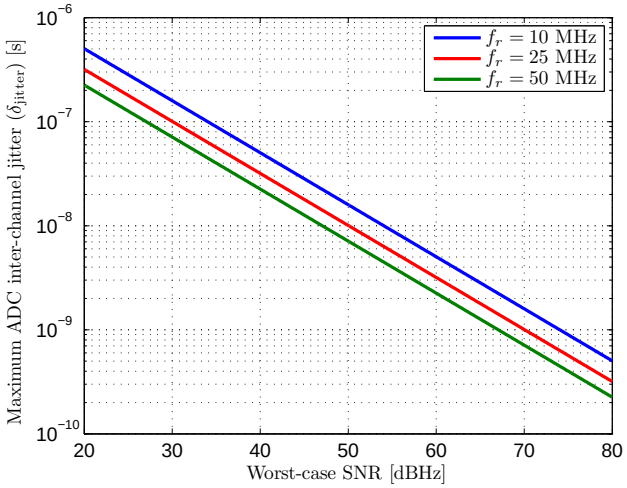

Figure 3.7: Maximum ADC inter-channel jitter standard deviation δ_{jitter} as a function of the analog signal minimum SNR level for different signal frequencies f_r ($f_s = 2f_r$)

the data-rates until the final stages of the measurement process, when differential measurements are carried out, canceling fast delay variations caused by frequency errors therefore allowing much smaller processing bandwidths. The consequence of this asynchronous delay tracking, independently of the particular method, is that most of the signal processing must be carried out, at least, at the digitizer sampling rate, and downsampling to reduce data-rates can only be performed on the final estimation data.

3.2 The multipath problem

As explained in 2.4, multipath interferences can be a relevant error source in communications and ranging systems based on different technologies. In the particular case of optical ranging, it does not usually appear as a relevant problem since most systems are formed by either focused detectors or non-spatially spread emissions. In the case of focused systems, such as standard reflective telemeters, the laser spot reflected in the target is spread by the diffusive properties of the surfaces. However, the receiver is aligned with the emission, making it possible to use wide optics that, apart from virtually widening the sensible area of the detection device, define a very narrow field of view centered on the reflected spot. This narrow field of view prevents most NLOS radiation from being detected. In the case of point-to-point ranging for industrial applications, something similar happens, as the propagation path is usually known a priori. In those cases, apart from using narrow fields of view in the detectors, collimated laser emissions are normally applied, and no NLOS radiation is present in the channel.

An optical ranging system to be used in the proposed IR LPS is, however, severely affected by multipath. The LOS path is not defined a priori, since the target position is unknown. Due to this, a wide emission should be used to ensure that it reaches several receivers simultaneously and wide reception patterns are also necessary so that the LOS radiation emitted from the target is detected in a large area of possible positions. This configuration causes that a large number of NLOS paths are present in the receivers positions, and that these paths are detected by those

receivers. Figure 3.8 shows an example of two possible multipath situations in the system if specular reflection were assumed in all the surfaces .

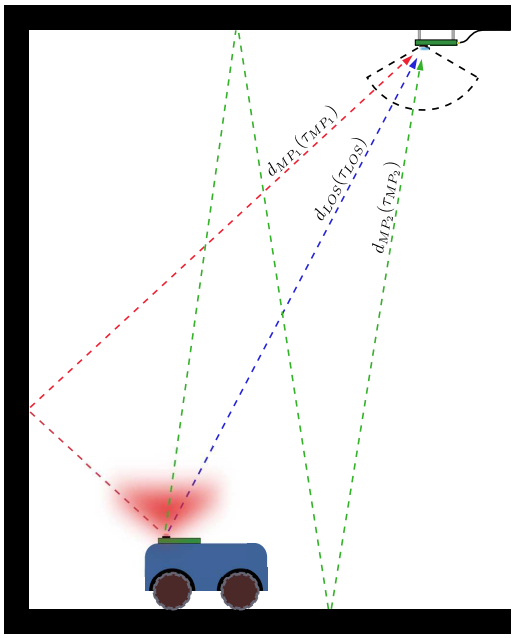

Figure 3.8: Example of possible multipath situations in the ranging system

The figure represents two typical multipath situations that affect the system. The LOS path, represented in blue, is defined by its propagation delay (τ_{LOS}), depending on the path length, and the power received through this path (P_{LOS}). This is the signal of interest, containing the desirable information for the range estimation. The red arrow represents a NLOS propagation caused by the reflection in a nearby surface. The green arrow represents another NLOS propagation, reaching the receiver after the double reflection in the ceiling and floor of the environment. Both multipath situations are defined by their respective received powers $\left(P_{\text{MP}_1},\ P_{\text{MP}_2}\right)$ and propagation delays $\left(\tau_{\text{MP}_1},\ \tau_{\text{MP}_2}\right)$.

The amount of multipath error caused by the NLOS signals that reach the receiver, for a given ranging technique, depends on the power and delay relationships between LOS and NLOS signals. Both multipath situations in the example, considering the absorbed and diffused energy in the reflections, and the extremely narrow solid angle of the emission covered by the receivers, would contribute with a very small power compared to that of the LOS path. When high accuracy measurements are required, this small power can, however, contribute to relevant errors in the estimated ranges.

Note that the example shows specular reflection in all surfaces. In a general, more realistic case, due to the diffusive properties of most surfaces, a very large number of paths with similar trajectories would reach the receiver, each of them having, however, a much smaller power compared to the specular assumption. This will generally imply, as will be seen in the next section, that the estimated multipath error if a specular model is assumed can be considered a worst case situation under the same room geometry. Several test were carried out to measure the error in the estimation when varying the distance of emitter and receivers to nearby walls and ceiling in [Pallarés-Puerto, 2010]. Those tests demonstrated that the overall effect of those

NLOS paths contribute to a non-negligible multipath error, reaching values in the dm level while the precision of the system due to noise is in the cm level. Thus, multipath error should be reduced by redesigning the ranging architecture so that the accuracy requirements of the positioning system can be met.

3.2.1 Multipath propagation models

In order to provide quantitative power and delay relationships between a LOS and NLOS paths to be used in the theoretical analysis and the results chapter (6), two multipath propagation models are defined depending on the parameters of a simple environment configuration. The basic difference between both models depends on the assumptions made on the reflection of the optical signals in the relevant surfaces of the environment:

- Specular reflection: the first, simpler model, is based on the assumption of perfect specular reflection on all the surfaces, only including an absorption factor in every reflection. This way, a dominant component from one single NLOS path reaches every receiver for any given target position. This model is a less realistic approach to real multipath effects, since typical surfaces in indoor environments have diffusive or partially diffusive properties. This approach, however, provide a useful simplification for the theoretical investigations of the multipath effects in the system performance. The results obtained using this model can be analyzed considering the effect of only two components (one LOS path and one NLOS path) in the received signal whose delay and power relationship can be investigated, instead of the sum of a very high number of similarly attenuated and delayed multipath replicas.

- Diffuse reflection: The second model represents a more realistic approach to optical multipath propagation. It is based on the assumption of diffusive reflections, dividing the implied surfaces on a fine simulation grid so that a multi-ray approximation can be used, integrating in individual rays all the power contained in the solid angles covered by every element of the grid. This model considers, depending on the surface, either an isotropic reflection pattern or a Lambertian pattern whose direction of maximum radiation is that of the specular reflection angle. This model is mainly used to generate the test signals for the measurements in the results chapter to obtain more realistic conclusions on the multipath error and the mitigation capabilities of the proposal.

The extensive validation of these models is a complex task that requires a deep specific study, including intensive optical tests, which is not the goal of this work. The results yielded by the more realistic diffuse approach applied to the PoA multipath error model, explained later in this section, have been compared with the multipath errors measured with the previous version of the system, based on direct differential PoA with sinusoidal intensity modulated signals. The comparison could be performed only in a coarse general way, since the environment where previous measurements where taken was irregular and complex, not specifically prepared for multipath tests. It could be concluded, however, that the diffuse reflection model can be considered an

acceptable preliminary approximation for real multipath effects in terms of magnitude of the error depending on the fundamental geometrical parameters of the scenario.

The scenario in which both reflection models are applied considers only the ceiling and floor surfaces of the environment, give that this is the general multipath situation for the system. The tests with the previous version of the system performed in [Pallarés-Puerto, 2010] showed that the effect of wall reflections on multipath error is dominant when either the emitter or the receiver is close ($\approx$ 1 m) to the given wall. The ceiling-floor multipath effect, however, is present in the general system operation and represents the general multipath problem of the system. It should also be noted that wall-reflected multipath components can generally be avoided rather easily by hard-limiting the viewing angle of those receivers close to walls or other vertical surfaces, so that they do not cover them in their field of view, since those angles of arrival could never belong to a real LOS path. This way, all multipath components coming from that direction could be avoided without reducing the system performance. This approach, however, cannot be applied to ceiling-floor reflection since, both in the specular assumption or a more realistic diffuse model, most components will reach the receivers with angles that could belong to a real LOS path for a different target position and, therefore, they cannot be eliminated by reducing the coverage of the receivers in specific areas.

3.2.1.1 Specular model

Figure 3.9 shows a diagram of the scenario defined for the model, where the specular ceiling-floor reflection is depicted.

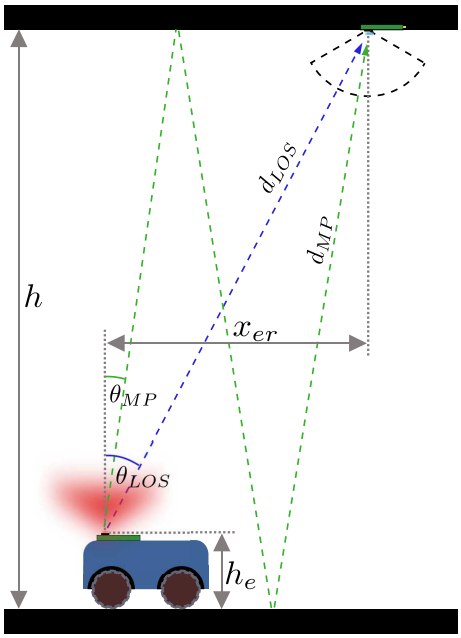

Figure 3.9: Ceiling-floor reflection diagram with the geometric parameters used in the model

The emitter is boarded on the robot and its height in relation to the floor level is h_e. The receiver is assumed to be placed directly at the ceiling level. The ceiling height is h and the horizontal distance between the emitter and the receiver is x_{er}.

The LOS path length d_{LOS} as a function of the geometry parameters of the set-up is

$$d_{\text{LOS}} = \sqrt{(h - h_e)^2 + x_{er}^2} \tag{3.28}$$

and the LOS emission-reception angle ϕ_{LOS} is

$$\theta_{\text{LOS}} = \text{atan}\left(\frac{|x_{er}|}{h - h_e}\right) \tag{3.29}$$

The NLOS path length d_{MP} is

$$d_{\text{MP}} = \sqrt{\left(\frac{x_{er}\,(h - h_e)}{3h - h_e}\right)^2 + (h - h_e)^2} + 2\sqrt{\left(\frac{x_{er} h}{3h - h_e}\right)^2 + h^2} \tag{3.30}$$

and the NLOS emission-reception angle ϕ_{MP} is

$$\theta_{\text{MP}} = \text{atan}\left(\frac{|x_{er}|}{3h - h_e}\right) \tag{3.31}$$

The corresponding propagation delays associated to those paths are

$$\begin{aligned} \tau_{\text{LOS}} &= \frac{d_{\text{LOS}}}{c} \\ \tau_{\text{MP}} &= \frac{d_{\text{MP}}}{c} \end{aligned} \tag{3.32}$$

where c is the propagation speed of the optical signals, approximate to the propagation speed in vacuum ($3 \cdot 10^8$ m/s). And the corresponding received optical powers, assuming a Lambertian emitter, are given by

$$\begin{aligned} P_{\text{LOS}} &= I_e \frac{A_s}{d_{\text{LOS}}^2} \cos^2(\theta_{\text{LOS}}) \\ P_{\text{MP}} &= I_e \frac{A_s}{d_{\text{MP}}^2} \cos^2(\theta_{\text{MP}}) \end{aligned} \tag{3.33}$$

with I_e being the radiant intensity in the normal direction to the emitter surface and A_s being the sensible area of the photodetector.

3.2.1.2 Diffuse model

As previously commented, this model considers a diffuse reflection on each surface. Consequently, there is not a single possible NLOS propagation path, but an arbitrarily high number of paths depending on the resolution of the simulation grid. The diffuse model yields, for certain geometric configuration, and emitter and receiver positions, a dataset formed by a high number of received components, where each n component is defined by its power P_{MP_n} and delay τ_{MP_n}.

The explanation and mathematical formulation of the diffuse reflection model for multipath is, due its length, documented in the internal report [Lázaro-Galilea et al., 2015].

3.2.2 PoA multipath error model

A model for the multipath error in standard PoA ranging is derived next. The concept of standard PoA is used in this work to refer to a system where simple sinusoidal signals are used for ranging, alike the previous implementation of the IR LPS that serves as background for this work. Multipath errors in a PoA system of these characteristics can, therefore, be modeled from the resulting phase yielded by the interference between several sinusoidal components of the same frequency.

In a generic multipath scenario, a received signal $s(t)$ can be defined as a LOS contribution affected by L multipath components with their respective powers $\left(P_{\text{LOS}},\ P_{\text{MP}_n}\right)$ and delays $\left(\tau_{\text{LOS}},\ \tau_{\text{MP}_n}\right)$

$$s(t) = \sqrt{2P_{\text{LOS}}}\sin\left(2\pi f_r t + \phi_{\text{LOS}}\right) + \sum_{n=1}^{L}\left[\sqrt{2P_{\text{MP}_n}}\sin\left(2\pi f_r t + \phi_{\text{MP}_n}\right)\right] \tag{3.34}$$

where f_r is the modulation frequency of the emitted sinusoidal signal, and the relationships between delays and phases are $\phi = 2\pi X$ with X being the fractional part of τf_r.

This composed input signal is a sum of sinusoidal components of the same frequency. This sum results in a sinusoidal component of the same frequency whose power P_T and phase ϕ_T depends on the power and phase relationships between all the components, being

$$s(t) = \sqrt{2P_T}\sin\left(2\pi f_r t + \phi_T\right) \tag{3.35}$$

Let define the input signal as phasors for easier operation

$$\begin{aligned} S &= \sqrt{2P_{\text{LOS}}}_{\angle\phi_{\text{LOS}}} + \sum_{n=1}^{L}\left[\sqrt{2P_{\text{MP}_n}}_{\angle\phi_{\text{MP}_n}}\right] \\ &= \left\{\sqrt{2P_{\text{LOS}}}\cos\left(\phi_{\text{LOS}}\right) + \sum_{n=1}^{L}\left[\sqrt{2P_{\text{MP}_\text{n}}}\cos\left(\phi_{\text{MP}_\text{n}}\right)\right]\right\} \\ &+ i\left\{\sqrt{2P_{\text{LOS}}}\sin\left(\phi_{\text{LOS}}\right) + \sum_{n=1}^{L}\left[\sqrt{2P_{\text{MP}_\text{n}}}\sin\left(\phi_{\text{MP}_\text{n}}\right)\right]\right\} \end{aligned} \tag{3.36}$$

Identifying terms with $a + ib$ and taking into account that

$$|a + ib| = \sqrt{a^2 + b^2} \tag{3.37}$$

and

$$\angle(a + ib) = \operatorname{atan}\left(\frac{b}{a}\right) \tag{3.38}$$

the total power and phase are obtained, being

$$P_T = \frac{1}{2}\left\{\sqrt{2P_{\text{LOS}}}\cos\left(\phi_{\text{LOS}}\right) + \sum_{n=1}^{L}\left[\sqrt{2P_{\text{MP}_\text{n}}}\cos\left(\phi_{\text{MP}_\text{n}}\right)\right]\right\}^2 + \frac{1}{2}\left\{\sqrt{2P_{\text{LOS}}}\sin\left(\phi_{\text{LOS}}\right) + \sum_{n=1}^{L}\left[\sqrt{2P_{\text{MP}_\text{n}}}\sin\left(\phi_{\text{MP}_\text{n}}\right)\right]\right\}^2 \tag{3.39}$$

and

$$\phi_T = \text{atan}\left\{\frac{\sqrt{2P_{\text{LOS}}}\sin\left(\phi_{\text{LOS}}\right) + \sum_{n=1}^{L}\left[\sqrt{2P_{\text{MP}_\text{n}}}\sin\left(\phi_{\text{MP}_\text{n}}\right)\right]}{\sqrt{2P_{\text{LOS}}}\cos\left(\phi_{\text{LOS}}\right) + \sum_{n=1}^{L}\left[\sqrt{2P_{\text{MP}_\text{n}}}\cos\left(\phi_{\text{MP}_\text{n}}\right)\right]}\right\} \tag{3.40}$$

ϕ_T is the multipath-affected phase for that received signal. The multipath error $\epsilon_{\hat{d}_{\text{MP}}}$ in the PoA measurement $\hat{d}$ obtained from that signal is the distance that corresponds to the deviation of this phase to the original LOS phase, being

$$\epsilon_{\hat{d}_{\text{MP}}} = \frac{c}{2\pi f_r}\left(\phi_T - \phi_{\text{LOS}}\right) \tag{3.41}$$

This model for multipath error is PoA is validated in section 5.3.2 of chapter 5 by comparison with measurements using the phasemeter implementation for the proposed system.

3.2.3 Computed PoA error with multipath propagation models

The previous PoA model is used next to compute the errors yielded as a function of room height h and emitter-receiver horizontal distance x_{er} depending on what multipath propagation model is used to calculate the power and delay relationships between the LOS and NLOS components that reach the receiver.

The computed error when the specular model is used are shown in figure 3.10.a, while the results for the diffuse model are shown in figure 3.10.b.

The computed results show that the multipath error due to ceiling-floor reflection depends fundamentally on the vertical distance, becoming more critical for low-ceiling environments. A larger horizontal separation increases this error when the vertical distance is low and shows no effect for high-ceiling environments.

Figure 3.11 show the same results depicted together for comparison. It can be seen that, although the tendencies with ceiling height and horizontal separation are similar, the specular model yields much higher errors, above 50 cm in the worst case for a ceiling of 2.5 m when emitter and receiver are separated 3.5 m horizontally; while the maximum error for the diffuse model, associated to the same position, is approximately 4 cm.

The specular and diffuse approaches will be also compared in section 6.5.2.3 of chapter 6 from the measured errors obtained with the proposed system prototype and test set-up when the multipath effects in the input signals are generated using both models.

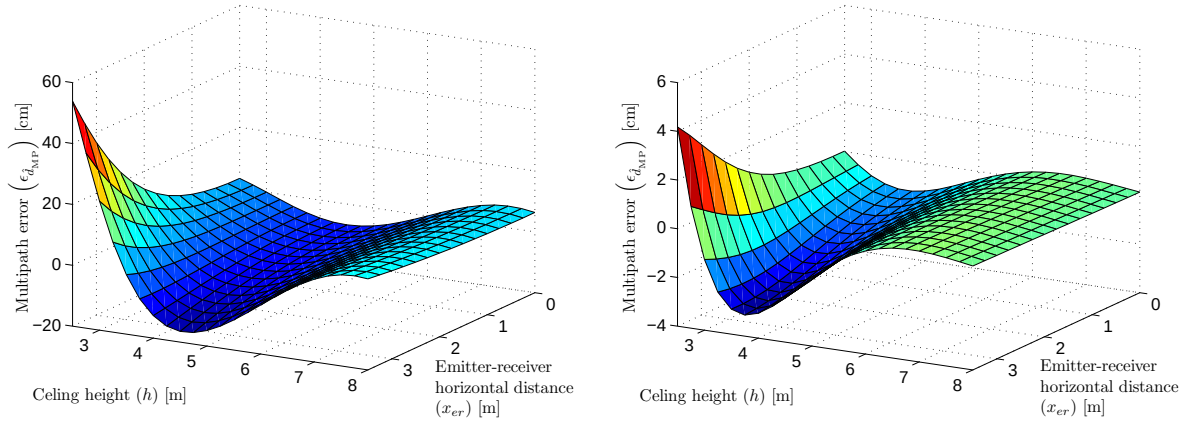

(a) Specular model (b) Diffuse model

Figure 3.10: Computed multipath errors in PoA as a function of room height h and emitter-receiver horizontal distance x_{er} for specular and diffuse multipath propagation models

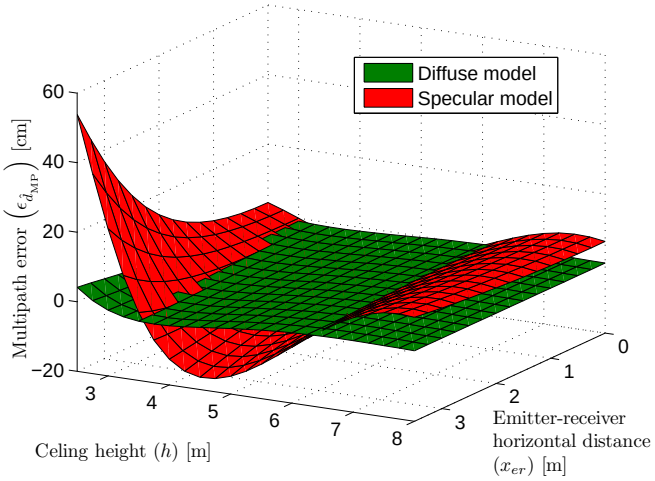

Figure 3.11: Comparison of computed multipath errors in PoA as a function of room height h and emitter-receiver horizontal distance x_{er} for both multipath propagation models

3.3 Proposed ranging method

A new definition of the ranging system is proposed in this thesis aiming to meet the system requirements by reducing the critical effect of multipath on accuracy while allowing precise ranging and effective multiuser operation, and not requiring complex calibration and maintenance processes that increase cost and reproducibility.

3.3.1 Method basis

The ranging proposal is formed by a composition of three different techniques. Phase-based ranging, similar to the previous version of the system, is used together with spread spectrum techniques to reduce the effect of multipath. The general idea behind the ranging scheme is to add PRN modulation to the sinusoidal signal used for phase-based ranging. The properties

of the coherent[5] and non-coherent PRN demodulation, carried out in the receiver, are used to reduce the power of multipath components before the phase estimation, which, in turn, provides better accuracy under limited bandwidth conditions. An initial delay estimation of the PRN modulated signal is necessary to carry out the demodulation, which is performed using typical RF synchronization methods.

A brief clarification should be made here on the terminology used during the rest of the document to refer to the PRN modulation applied to the sinusoidal signal. The explanations related to the modulation and demodulation schemes, as well as the various effects caused by these processes in the signals spectra, will refer to spread spectrum terminology during all the document, by analogy to RF-related literature. There are, however, some reasons that may reasonably lead to the conclusion that the use of spread spectrum terminology, more specifically, DSSS, is not appropriate for the PRN-based modulation used in this proposal, hence this clarification.

In standard DSSS schemes, the PRN modulates a data signal, typically formed by a binary sequence of much lower frequency than the spreading code. It is said that the modulation spreads the data into a much wider bandwidth than its original spectrum. The signal modulated by the PRN sequence in the proposed architecture is a pure sine tone instead of a data signal. In addition, as will be seen later in this chapter, the design of the signal structure to optimize the performance of the proposed architecture under the strict bandwidth limitations of the optical channel requires that the sinusoidal signal and the PRN code used to modulate it are of similar frequency. From a DSSS point of view, the data signal modulated by the PRN in this system is a sinusoidal signal of similar frequency, what greatly differs from standard DSSS data signals. The signal of interest, i.e., the "data" to be recovered in the receivers, is a sinusoidal signal, whose phase (including the phase-shift added due to the propagation delay) is the information of interest. This terminology does not seem initially appropriate for the selected modulation scheme but has been used for convenience, for a clearer interpretation of the effect caused in the sinusoidal signal power spectrum when modulated by the PRN.

One of the principal advantages of using DSSS, apart from allowing effective multiplexing and reducing the effect of narrowband interferences, is the inherent multipath rejection. The power of the data contained in signals that arrive through NLOS paths, thus having longer propagation delays, is not despread (or at least not so efficiently), what reduces the magnitude of the interference with the data contained in the LOS signal, increasing the quality of the received information in multipath-affected scenarios. The proposed system takes advantage of this property of the PRN modulation to reduce multipath interferences in the sinusoidal signal used for ranging, where, similarly to DSSS data transmissions, the effect of other sine components that arrive through NLOS paths is reduced.

On the other hand, the spreading and despreading effect caused by the modulation on the "data" spectrum is also useful to explain the processes that affect the signal spectrum. This can be understood as a very specific spreading and despreading process, where the power contained in the very narrowband of the sinusoidal signals is spread in all the optical channel bandwidth

[5]The concept of coherency, when related to the PRN modulation, is used in all the document to refer to the phase alignment/misalignment between the signals involved in the demodulation process.

by the PRN modulation, to be despread back to the original sine frequency in the receivers before the phase measurement.

In some cases, the reader may also find similarities in the mathematical modeling of the modulation process with a BPSK scheme. Given that the PRN modulates a sinusoidal signal, the mathematical expressions of the process are equivalent to a PRN being modulated in a RF carrier by BPSK. It should be noted that the sinusoidal signal is not the carrier but the "message" to be transmitted for ranging, and the PRN-modulated sine, i.e., the spread spectrum signal, is actually transmitted though an optical near-IR carrier using IMDD over a DC component. Note that, in opposition to typical RF transmission models, the optical carrier will be omitted in all the expression since its effect in the actual signals processed by the system is transparent to the emitter and receivers due to the optical downconversion performed by the optoelectronic devices. The DC component used in the IMDD will also be generally omitted as it is only added in the drivers just before the emitters excitation and later eliminated in the low-level conditioning after the photodetectors.

3.3.1.1 Spread spectrum modulation

As explained in section 2.4.2, PRN modulation has been used in interferometry to differentiate sinusoidal heterodyne signals reaching a single receiver based on their delays. The main idea behind this technique is that, if a spread spectrum signal is coherently demodulated, i.e., the local reference used for its demodulation is sufficiently aligned with it, the spread spectrum modulation is undone, despreading most of its power to its original narrower band. On the other hand, when the signal is non-coherently demodulated, it maintains a spread spectrum, keeping a very small amount of power in the original narrowband. This property can be used to enhance the power ratio between sinusoidal components contained in spread spectrum signals with different delays simultaneously reaching a receiver, depending on the delay of the local replica used to demodulate the composed received signal.

Figure 3.12 shows a time representation of the signals involved in the DSSS demodulation process. The top plot represents the bandlimited normalized received signal in blue, together with the spreading sequence contained in its modulation, shown in red. The received signal is formed by a sinusoidal component whose phase is shifted by the spreading sequence. The received signal is demodulated with a local code replica of the spreading sequence. This local replica is represented in the second plot in red. The demodulated signals are shown in the bottom plots. Figure 3.12.a shows the demodulated signal when the alignment error between the delay of the received signal and the local replica is 0.1 chips while figure 3.12.b shows the demodulation result for 0.5 chips alignment error. Comparing both demodulated signals, it can be seen that the bottom plot of figure 3.12.a is a closer representation of the sinusoidal modulation contained in the received signal. This is, a smallest alignment error, hence a more coherent demodulation, implies more power is folded back to the sine narrowband. This can also be seen in figure 3.13, where the power spectra of all the involved signals is depicted in its corresponding color. The sync-shaped spectrum of the spreading sequence and the emitted signal can be seen in the top plot. The power spectra of both demodulated signals are shown below. In the first case most of

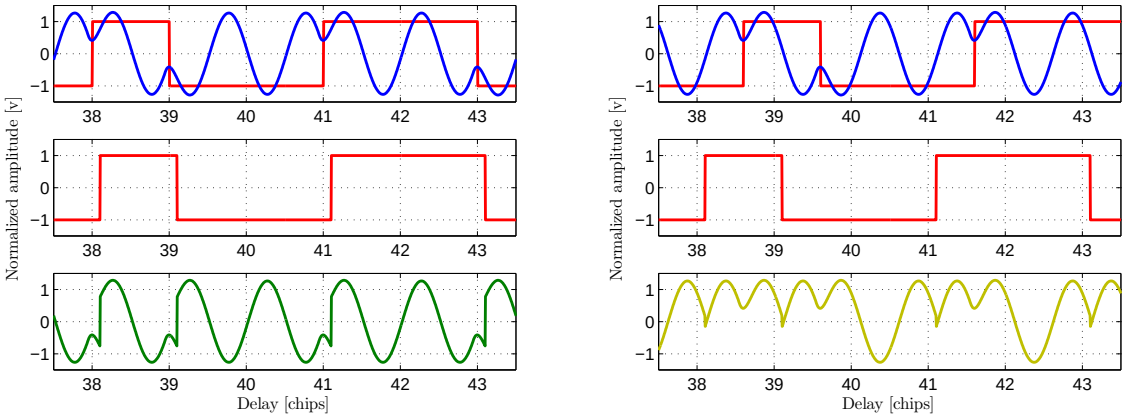

(a) DSSS demodulation with 0.1 chips alignment error (b) DSSS demodulation with 0.5 chips alignment error

Figure 3.12: Time representation of the signals involved in the DSSS demodulation for two different local replica alignment errors. Top: emitted signal and spreading code. Middle: local code. Bottom: demodulated signal ($f_c = f_r = 25$ MHz, $BW_{IR} = 50$ MHz, 255 chips M-sequence)

the signal power, approximately 80%, is recovered in the narrowband. In the other case, when the demodulation alignment error is higher, a higher amount of power stays spread over a wide range of frequencies and harmonics of the sine component, reducing the despread power in the narrowband to approximately 40% of the full signal power.

The previous example can be considered an arbitrary multipath situation. Let assume the received signal in figure 3.12.a is the LOS component and the received signal in figure 3.12.b is a multipath component, with certain attenuation and delayed 0.6 chips in relation to the LOS component. A delay estimation of the incoming signal would be carried out to generate the local replica for demodulation, yielding an estimation affected by multipath, but closer to the LOS delay true-value given its higher power. In the example, the local replica would be generated 0.1 chips later than the LOS delay and 0.5 chips earlier than the multipath delay. The local replica generated with this estimated delay would be the despreading sequence shown in red. The full received signal is demodulated with this local replica, yielding a demodulated signal which is the superimposition of both green and yellow signals. The final distance estimation is carried out by the phasemeter on the sine narrowband, where the multipath component power has been reduced in relation to the LOS power, yielding a phase estimation where the effect of multipath has been mitigated in relation to the original received signal.

Figure 3.14 shows the power spectrum of the demodulated signal for different delays in the alignment of the local replica from 0 (perfect alignment) to 1 chip duration (T_c). It can be clearly seen how the amount of despread power in the sine band is reduced when the local replica alignment error is increased. A spread spectrum signal is yielded for any alignment above 1 chip duration between any particular component and the local replica. This completely cancels the contribution of that component as a multipath error in the final range estimation. For smaller alignment errors some part of the component power is despread while the rest appears as a spread spectrum signal or distortion harmonics.

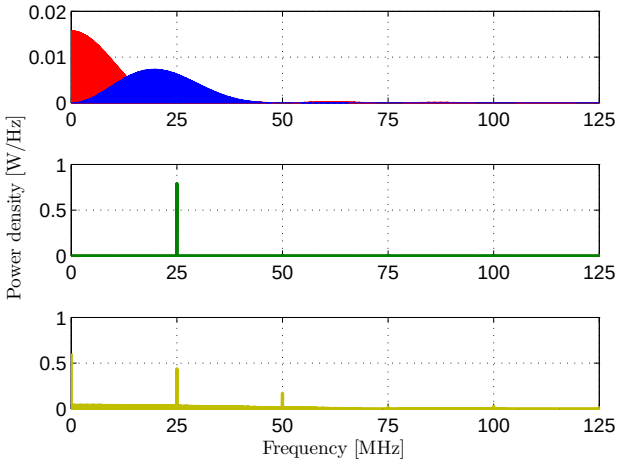

Figure 3.13: Power spectrum of the signals involved in the DSSS demodulation for two different local replica alignment errors. Top: Received signal and spreading code. Middle: demodulated signal with 0.1 chips alignment error. Bottom: demodulated signal with 0.5 chips alignment error ($f_c = f_r = 25$ MHz, $BW_{IR} = 50$ MHz, 255 chips M-sequence)

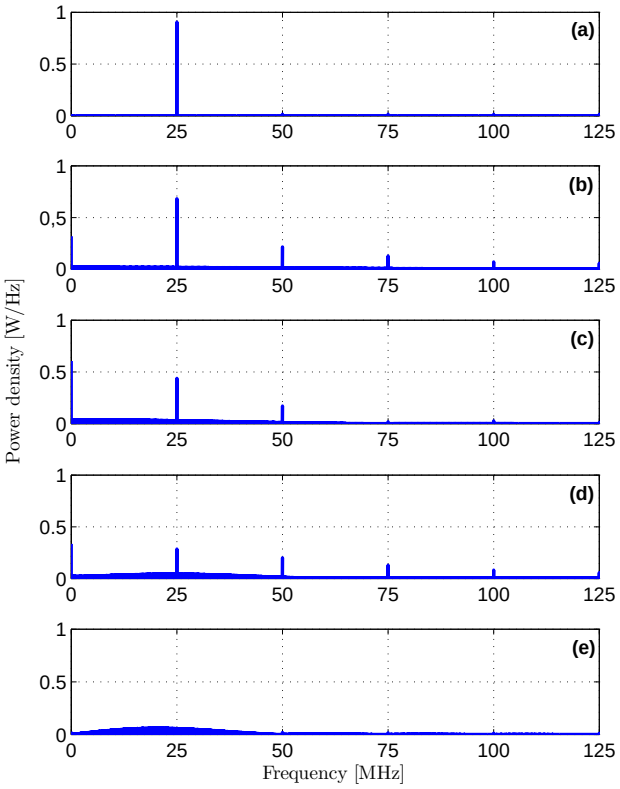

Figure 3.14: Power spectrum of demodulated signal for different local replica alignment errors: ((a)=0, (b)=0.25T_c, (c)=0.5T_c, (d)=0.75T_c, (e)=T_c) ($f_c = f_r = 25$ MHz, $BW_{IR} = 50$ MHz, 255 chips M-sequence)

3.3.1.2 Delay estimation

Generating the local replica for demodulation requires an estimation of the delay of the received signal. This received signal, being a single LOS component or, more generally, a composition of a dominant LOS component plus several multipath components, will present spread spectrum properties. Estimating and tracking the delay of a spread spectrum signal is a common task, mainly applied in RF technology. Synchronization stages are used for data demodulation in communication systems and for distance estimation in spread spectrum ranging systems, typically applied in GNSSs.

The properties of the particular spread spectrum signals proposed in this work, that will be defined next, differ from those typically used in RF communications and ranging. Theses differences are conditioned both by the adaptation of spread spectrum technology to optical carriers and by the specific signal definition to enhance ranging accuracy and multipath mitigation. Thus, the general structure of delay estimation stages classically applied in RF can be used to carry out the required delay estimation for generating the local replica, although the specific architecture and optimization of the stage should be adapted to the signals defined for this work, not being directly translatable from the RF domain. This delay estimations are usually performed by delay tracking loops that exploit the correlation properties of the spread spectrum signals, thus, the correlation properties of the defined signal are a key element in the adaptation and optimization of the selected tracking loop.

In this first approach to the proposed method, a baseband early-late delay-lock loop with narrow early-late spacing has been selected, being a simple and extended technique that shows a good balance between reduced complexity, accuracy and multipath behavior. Note that this stage could be optimized, since a wide variety of tracking loops has been developed during the years both for communications and GNSS applications, adapted to different signal properties and requirements, however, the aim of this study is to analyze the general feasibility of the proposal, so a simple but effective approach has been selected, leaving its optimization for future contributions.

3.3.1.3 Phase estimation

Finally, a method to extract the phase of the despread sinusoidal signal must be defined. Several techniques can be used to estimate the argument of sinusoidal signals, such as quadrature detectors [Walker, 2008], sine wave fitting [Ramos et al., 2004], cross-correlation [Liang et al., 2012] or those based on the frequency-domain analysis of the signal [Agrež, 2008]. The performance of these methods is rather similar in terms of noise behavior, however, two considerations should be made for its selection: (i) the selected method should be able to carry out the estimation on real-time considering the system timing constrains, i.e., the processing should be kept as simple as possible, and (ii) the selected method must be able to perform the estimation without having accurate information of the signal frequency, since, due to frequency errors between emitter and receiver, an asynchronous or frequency-locking demodulation of the sine signals is required.

An I/Q based demodulation, followed by an arctangent estimation after differentiation be-

tween two received signals has been selected to extract the phase information since, being simple to implement, it can easily operate in real-time and only requires a coarse a priori knowledge of the expected frequency of the received signal without the need of any frequency-locking mechanism.

3.3.2 Proposed ranging architecture

The proposed architecture relies on phase-based estimation, yielding more precise results under strict BW limitations, while providing multipath mitigation capabilities by using spread spectrum techniques. The structure of the full ranging system is shown in figure 3.15.

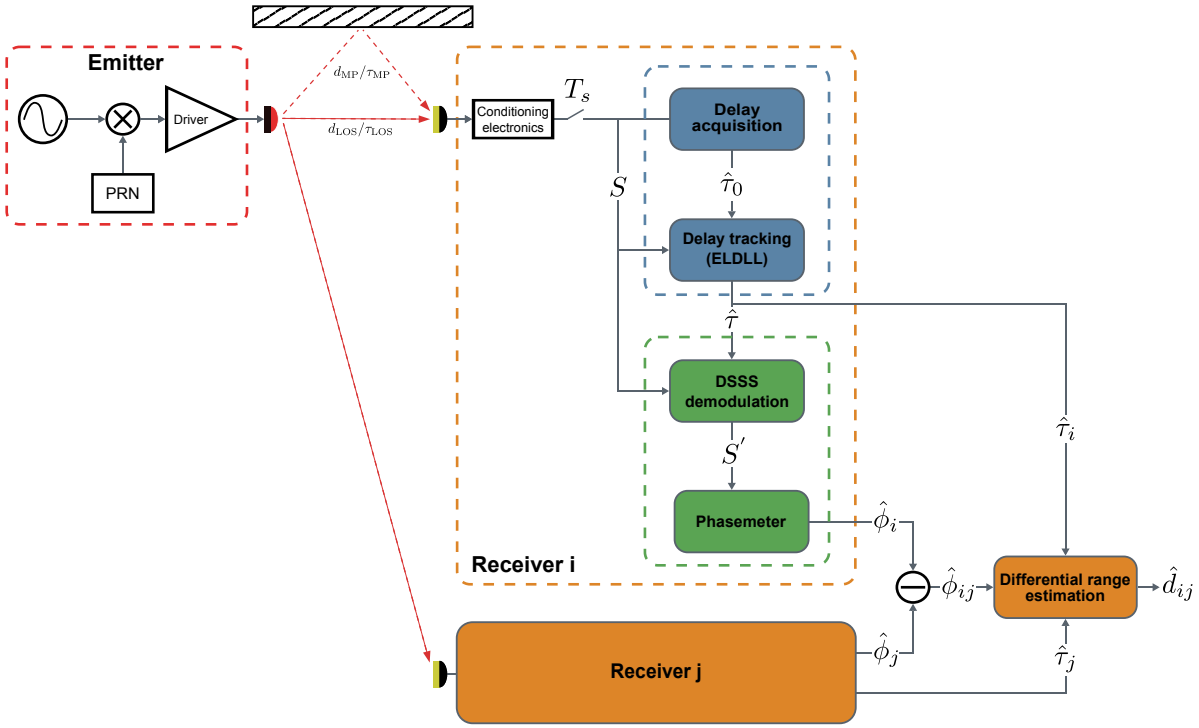

Figure 3.15: General diagram of the ranging architecture

The emitted signal is defined by a double modulation of the IR optical carrier. Before driving the emitter, a sinusoidally signal is multiplied by a PRN sequence by DSSS. This process spreads the narrowband power of the sinusoidal signal over a wide range of frequencies defined by the PRN sequence. This double modulated signal will be referred to as spread spectrum signal for the rest of the document. This signal is emitted and reaches the receiver after propagating through the LOS path and an arbitrary number of NLOS paths.

The composed spread spectrum received signal, after low-level conditioning and digitization, is fed into the synchronization stage, formed by the blue blocks in the figure. The synchronization stage exploits the correlation properties of received signal to provide a delay estimation of the composed received signal. The synchronization stage is formed by an acquisition stage and a tracking stage. The acquisition stage provides an initial delay coarse estimation $\hat{\tau}_0$, achieved by sweeping possible delay candidates in the local replica of the expected signal and evaluating the

calculated correlation values. Once the initial delay is available, the tracking stage, formed by a base-band ELDLL, is locked with the incoming signal using the coarsely estimated delay, keeping track of the variations in the delay of the incoming signal to provide a continuous estimation $\hat{\tau}$.

The synchronization stage formed by the two aforementioned processes is explained and studied in detail in chapter 4, where the effect of noise, dynamic errors and multipath on tracking accuracy are analyzed.

The estimated delay $\hat{\tau}$ is used by the DSSS demodulation stage to generate a local in-phase replica of the PRN signal contained in the received signal S. The local replica is multiplied with the incoming signal to partly undo the DSSS modulation applied in the emitter. This DSSS demodulation despreads part of the power of the received signal back to the original sinusoidal modulation band, yielding a partly recovered version of the sinusoidal signal, while the rest of the power, non-coherently demodulated, stays spread. An I/Q-based phase estimation is then carried out on the demodulated signal S' on a narrowband around the expected sinusoidal frequency. The estimated phase corresponding to that particular receiver $\hat{\phi}_i$ is then subtracted with an equivalent one, $\hat{\phi}_j$, coming from another receiver, simultaneously digitized and processed, yielding the estimated differential phase $\hat{\phi}_{ij}$ between both receivers. Finally, the differential phase is converted into a differential range estimation taking into account the applied sine frequency and propagation speed, where cycle ambiguities in the phase estimation are solved using the delay estimations $\hat{\tau}_i$ and $\hat{\tau}_j$ provided by the synchronization stages of both receivers.

The demodulation and phase-based ranging stages formed by the two aforementioned processes are explained and studied in detail in chapter 5, where the amount of recovered power as a function of demodulation alignment error is modeled and the effect of noise, dynamic errors and multipath on the phasemeter are analyzed.

The multipath mitigation capabilities of the system depend on the DSSS demodulation process. If the estimated delay $\hat{\tau}$, used to define the phase of the local code replica for demodulation, is closer to the LOS component than to any multipath component, a more coherent demodulation is applied to it. A higher amount of power is folded back into its original sine frequency for the LOS component than for the rest of the signals reaching the receiver, as the amount of despread power in the demodulated signal S' depends on this coherence. This provides the demodulated signal with a relative power enhancement of the LOS component in the sinusoidal modulation band, so that the multipath error in the phase estimation carried out in this band is reduced.

The delay tracked by the synchronization stage corresponds to the full received signal, this is, affected by multipath if present. The amount of multipath error is defined by the relative power and delays of all the components of the received signal. Due to the high absorption upon signal reflections, typical optical multipath situations present a highly dominant LOS component in terms of relative power. Except for severe multipath situations, the estimated delay affected by multipath is closer to the LOS delay true-value than to the delay of any multipath component. This causes that the DSSS demodulation process is, in most situations, more coherent for the LOS component, so that certain level of multipath power reduction can be generally expected.

Note that the estimated phase, where multipath error has been reduced, could be fed back to

the DSSS demodulation stage to improve the accuracy of the estimated delay $\hat{\tau}$, so that its error in relation to the LOS component is reduced. This would yield more LOS power recovered for the phase estimation, and therefore a higher level of multipath mitigation in the loop. However, this work aims to provide a complete analysis of the first and most simple approach to the proposal, where this feedback is not considered.

Apart from reducing multipath errors, the use of spread spectrum modulation provides a very convenient solution for multiplexing the optical channel. CDMA can be easily applied by assigning different spreading sequences to different users, as long as the cross-correlation properties between them are good, which is not hard to achieve. This way, parallelizing the signal processing in the receivers to support several expected spreading sequences (similarly to GNSS receivers for different satellites), the multiuser feature of the localization system is easily implemented.

In addition, the proposal is conceived to be fully implemented in the digital domain after signal conditioning in the sensor. This way, most calibration issues are solved, except for an initial process after installation regarding the calibration of propagation paths for every sensor, which does not imply complex measurements and needs no periodical recalibration.

3.3.2.1 Signal structure

The signal structure designed for the proposed method is formalized next in order to analyze its fundamental properties to be used in the following chapters.

The emitted signal with the double (sinusoidal + PRN) modulation, omitting the optical carrier and the DC component, is

$$m(t) = \sqrt{2P_{tx}}r(t)c(t) \tag{3.42}$$

where P_{tx} is the emitted power. The sinusoidal signal $r\,(t)$ is

$$r\,(t) = \sin\left(2\pi f_r t + \phi_0\right) \tag{3.43}$$

where f_r is its modulation frequency and ϕ_0 its constant phase in relation to the spreading sequence phase. The spreading signal $c\,(t)$ is

$$c\,(t) = \sum_{n=0}^{\infty} p\,(t - nT_f) \tag{3.44}$$

where $p(t)$ is a non-return-to-zero (NRZ) PRN sequence periodically repeated with a frame period $T_f = NT_c$, with N being the number of chips of the particular PRN sequence and $f_c = 1/T_c$ its chip-rate.

The PRN sequence $p(t)$ is

$$p(t) = \sum_{k=0}^{N-1} C_k \Pi\left(\frac{t - kT_c}{T_c}\right) \tag{3.45}$$

where $C_k \in \{\pm 1\}$ is the value of every chip k of the NRZ PRN and

$$\Pi\left(\frac{t}{T_c}\right) = \begin{cases} 1 & \text{if } \ 0 \leq t \leq T_c \\ 0 & \text{else} \end{cases} \tag{3.46}$$

The parameters that define the emitted signal are the sine frequency f_r, the chip-rate f_c, the phase relationship between them determined by ϕ_0 and the particular PRN sequence that sets the individual chip values C_k and frame period T_f. The definition of the signal structure through a proper selection of these parameters is fundamental for the performance of the system.

Some considerations should be taken into account for this selection. In the first place, maximizing the use of the available optical bandwidth in terms of power, by increasing SNR and reducing distortion in the received signals, is related with the precision of both synchronization and phase estimation stages. Secondly, the precision of the delay estimation in the synchronization stage is related with the chip-rate and the precision of the phase estimation in the phasemeter after demodulation is related with the sine frequency, so both of them should be also maximized. This creates a trade-off in the frequency selection since, given certain optical bandwidth, the use of high frequencies would increase precision under similar SNR conditions, but reduce SNR and increase distortion since a larger portion of the power spectrum of the original signal would surpass the channel bandwidth.

Taking this trade-off into account, both frequencies has been defined equal to half the optical channel bandwidth (BW_{IR}), this is,

$$f_r = f_c = \frac{BW_{IR}}{2} \tag{3.47}$$

This way, the main lobe of the sync-shaped signal spectrum lies centered in the channel bandwidth, containing more than 90% of the signal power. A more efficient use of the channel bandwidth could be achieved by an adequate pulse shaping, allowing certain compensation of the distortion introduced by the bandlimited channel. However, as the aim of this work is analyzing the general feasibility of the proposal, a simple approach has been selected.

The phase relationship between the sinusoidal signal and the spreading sequence is defined using $\phi_0 = 0$ in the sine form of the sinusoidal modulation. This way, the phase inversions caused by the DSSS modulation are applied in the zero crossing points of the sinusoidal signal, minimizing distortion in the symbol transitions.

The defined signal with these parameters, rewriting $f_r = 1/T_c$, is

$$m(t) = \sqrt{2P_{tx}}\sin\left(\frac{2\pi t}{T_c}\right)\sum_{n=0}^{\infty}\sum_{k=0}^{N-1} C_k \Pi\left(\frac{t - kT_c - nT_f}{T_c}\right) \tag{3.48}$$

An time representation of this signal is that shown in the examples in figure 3.12.

3.3.2.2 Signal analysis

The power spectrum and autocorrelation function of the defined signal are calculated in this section, to be used in the rest of the document.

Power spectrum

The power spectrum of the spreading sequence $c(t)$, assuming the use of N chips long MLS[6], is

$$|C(f)|^2 = \left(\frac{N+1}{N^2}\right) \sum_{m=-\infty}^{\infty} \operatorname{sinc}^2\left(\frac{m}{N}\right) \delta\left(f - \frac{m}{NT_c}\right) \tag{3.49}$$

depicted in figure 3.16.

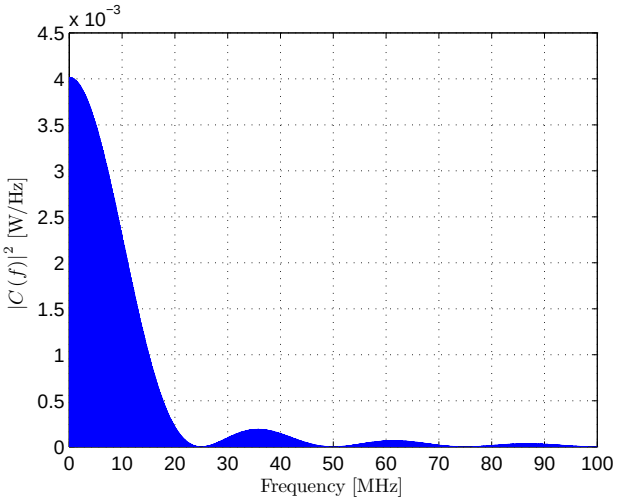

Figure 3.16: Power spectrum $|C(f)|^2$ of the PRN sequence $c(t)$ ($N = 255$ chips, $T_c = 40$ ns)

After modulating the sinusoidal signal, its spectrum is shifted by the sine frequency, so the power spectrum of the emitted signal $m(t)$ is

$$\begin{aligned} |M(f)|^2 = \frac{P_{tx}}{2}\left(\frac{N+1}{N^2}\right) \Bigg[& \sum_{m=-\infty}^{\infty} \operatorname{sinc}^2\left(\frac{m}{N}\right) \delta\left(f - \frac{1}{T_c} - \frac{m}{NT_c}\right) \\ & + \sum_{m=-\infty}^{\infty} \operatorname{sinc}^2\left(\frac{m}{N}\right) \delta\left(f + \frac{1}{T_c} - \frac{m}{NT_c}\right) \Bigg] \end{aligned} \tag{3.50}$$

depicted in figure 3.17.

The spreading sequence is a finite length PRN periodically repeated. Therefore, its spectrum is not continuous in frequency, but formed by line components separated f_c/N. The longer the PRN sequence is, the smaller the separation between line components. In the figures and most experiments in subsequent chapters, 25 MHz chip-rate and 255 MLS are used, its spectrum formed by line components with an approximate separation of 98 kHz. It should also be noted that the spectrum of the modulated signal $m(t)$ does not contains power in the sine modulation frequency, as can be seen in the detail of its spectrum in figure 3.18.

[6]Maximum Length Sequence

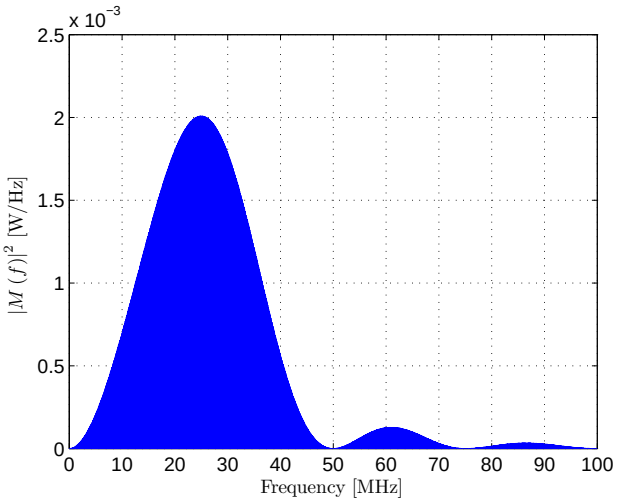

Figure 3.17: Power spectrum $|M(f)|^2$ of the emitted signal $m(t)$ ($N = 255$ chips, $T_c = 40$ ns, $P_{tx} = 1$ W)

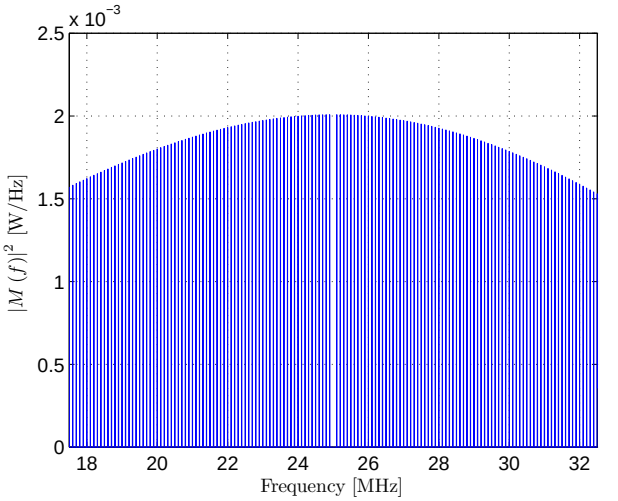

Figure 3.18: Power spectrum $|M(f)|^2$ of the emitted signal $m(t)$ (detail around the sine frequency) ($N = 255$ chips, $T_c = 40$ ns, $P_{tx} = 1$ W)

The calculated power spectra correspond to the non-bandlimited signal. The received signal is affected by the IR channel bandwidth limitation. This limitation reduces the power of the received signal and distorts it by attenuating high frequency components. Both effects are considered in the experimental results in following chapters. Signal distortion, however, is not included in the theoretical analyses. Preliminary test comparing theoretical and experimental results in the tracking and demodulation stages showed that distortion has a small effect on the various performance indicators, and its inclusion highly increased the complexity of some developments. The total power reduction is considered by adding an attenuation factor to the non-bandlimited received power. This factor is calculated assuming a first-order low-pass channel. This is an appropriate approximation since the dominant frequency limitation in the optical link is defined by the response time of the emitter or receiver optoelectronic device and this frequency response is typically defined by a parasitic capacitance.

Figure 3.19 shows the power spectrum of the bandlimited received signal, compared with its non-bandlimited spectrum. The frequency response and 3dB cut-off frequency of the filter modeling the channel response are also shown. Given the selected signal structure, designed for maximizing accuracy by balancing high received power and high working frequencies, the main lobe of its sync-shaped spectrum is contained in the 3dB bandwidth of the channel. The total power contained in this signal is 88% of the non-bandlimited total power.

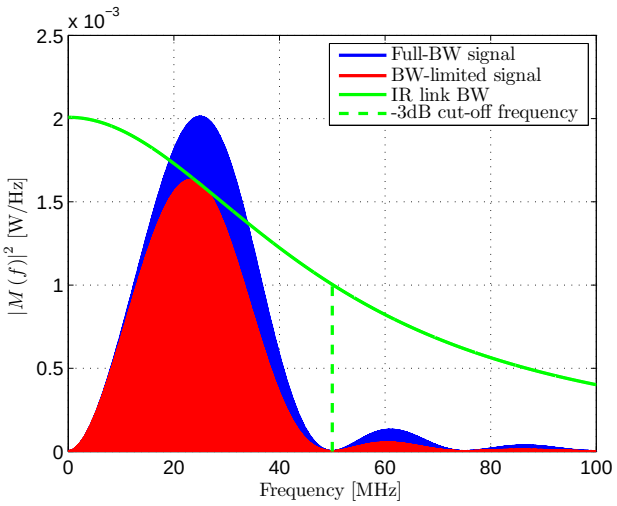

Figure 3.19: Effect of IR link bandwidth (BW_{IR}) on the power spectrum $|M(f)|^2$ of the emitted signal $m(t)$ ($N = 255$ chips, $T_c = 40$ ns, $P_{tx} = 1$ W)

Autocorrelation function

The autocorrelation function of $m(t)$ is calculated next, being fundamental for the performance study of the tracking stage.

The phase relationship ϕ_0 between the sine signal and the PRN sequence is constant. Assuming that this phase is random and uniform in $[0, T_c]$, and that the PRN has a discrete random phase uniform in $[0, N-1]$, both random variables being independent, the defined signal can be considered stationary and its autocorrelation function can be written as

$$R_m(\tau) = \sum_{n=-\infty}^{\infty} R_c(n)\, R_q(\tau - nT_c) \tag{3.51}$$

where $R_c(n)$ is the autocorrelation function of the PRN sequence C_k

$$R_c(n) = \begin{cases} 1 & \text{if} \quad n = 0 \\ -\frac{1}{N} & \text{if} \quad n \neq 0 \end{cases} \tag{3.52}$$

and $R_q(\tau)$ is the symbol autocorrelation. This symbol, including the sine signal in its definition, is

$$q(t) = \Pi\left(\frac{t}{T_c}\right) \sin\left(\frac{2\pi t}{T_c}\right) \tag{3.53}$$

and its autocorrelation is

$$R_q(\tau) = \begin{cases} \frac{1}{2}\left(1 - \frac{|\tau|}{Tc}\right)\cos\left(\frac{2\pi\tau}{T_c}\right) + \frac{1}{2\pi}\sin\left(\frac{2\pi|\tau|}{T_c}\right) & \text{if} \quad |\tau| < T_c \\ 0 & \text{if} \quad |\tau| \geq T_c \end{cases} \tag{3.54}$$

The calculated autocorrelation in ±2 chips around the correlation peak in 0 delay is depicted in figure 3.20 for a signal generated with $N = 255$ chips.

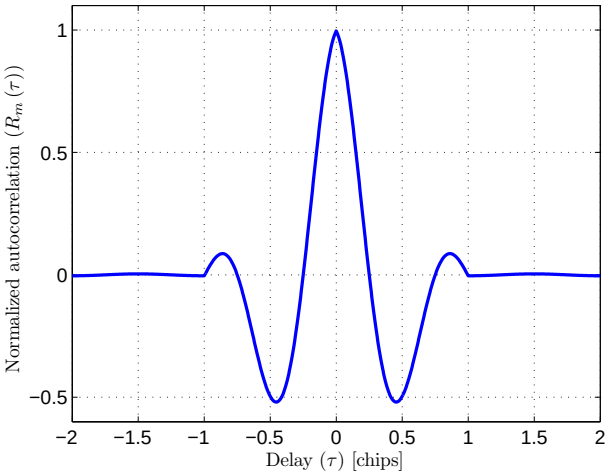

Figure 3.20: Normalized autocorrelation function $R_m(\tau)$ of the signal $m(t)$ for $N = 255$ chips

As can be seen in the derived expression of the signals autocorrelation, the length of the applied PRN conditions the magnitude of the correlation for $|\tau| \geq T_c$, as can be seen in figure 3.21, where the autocorrelation between ±10 chips around the peak is shown for signals generated using different spreading sequence lengths.

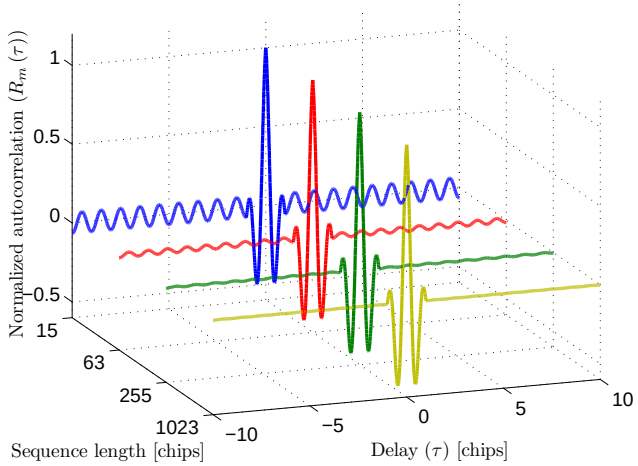

Figure 3.21: Normalized autocorrelation function $R_m(\tau)$ of the signal $m(t)$ for several sequence lengths $N = (15,\ 63,\ 255,\ 1023)$ chips

3.3.2.3 Comments on multiplexing

Providing a solution which allows multiuser operation was a design constrain for the proposed solution and it has been taken into account on its definition. However, studying this feature in depth is not the goal of this work and will not be addressed in the rest of the document, leaving its implementation and optimization for future works. This section provides some general comments and tests on how multiuser operation could be achieved with the proposed architecture by applying standard multiplexing techniques based on CDMA.

As commented previously, the use of spreading sequences provide a very suitable solution for multiplexing by using a standard CDMA scheme applied to ranging. This approach is very similar to the one used in GNSS for differentiating satellites, where every satellite is assigned a different PRN sequence and the GNSS receiver tries to acquire and track all the expected sequences. In the case of the proposed system, every target would be assigned a specific sequence and the receivers signal processing would be parallelized as many times as targets to be located, by operating its synchronization and demodulation stages with replicas of every assigned code and its associated spread signal.

The implementation of this technique is almost immediate and does not require any hardware adaptation apart from parallelizing the receivers for the expected signals and loading every emitter signal generation system with the signal spread by its assigned sequence. Some considerations should be made, however, in the selection of the particular sequences used for multiplexing.

Two basic considerations should be taken in to account in the selection of the specific sequences: 1) having a good autocorrelation in the spread signals, meaning a high autocorrelation peak for zero delay and low values for any other delays, and 2) having good cross-correlation properties, meaning that the cross-correlation between the signals spread with the assigned codes should be as low as possible, independently of the delay, to minimize interferences when several targets are operating simultaneously.

The initial proposal for the signal structure in the proposed system is based on MLSs, as this is the simpler approach in terms of available resources for the theoretical study. The selection of the most adequate spreading sequence for both good tracking performance and good multiplexing capabilities requires an specific study which is proposed as future works, which should carefully consider the autocorrelation and cross-correlation properties of the signal constructed with the selected spreading sequence.

A simple multiplexing test based on simulation has been performed to provide a preliminary demonstration of the potential multiuser capabilities of the proposal.

Four different versions of the signal defined for the proposed system have been built using 4 MLSs 1023 chips long. The selected MLSs have been chosen randomly from the available set derived from a 10 bit LFSR[7], meaning that their cross-correlation properties are not particularly optimized. A signal formed by the addition of these four components has been built, simulating the signal formed in one receiver when the components coming from 4 different target, each

[7]Linear Feedback Shift Register

having an specific assigned code, are reaching it with the same power. This composed signal is shown in figure 3.22.

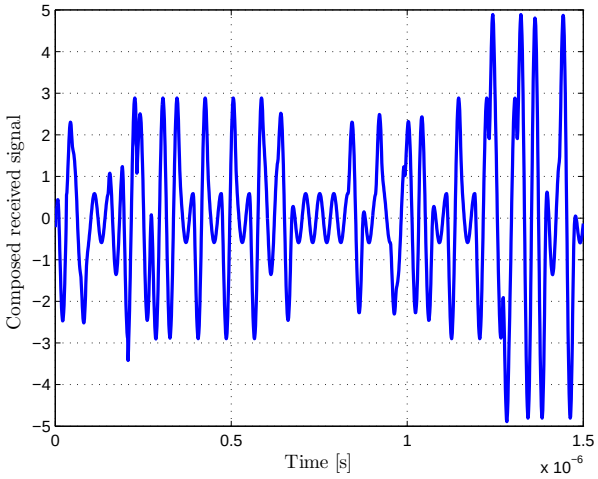

Figure 3.22: Signal formed by the addition of 4 different signals with equal power and random delays coming from 4 targets with different assigned MLSs

This test simulates the system, from the point of view of a single receiver, measuring four simultaneously operating targets. The receivers should be adapted to that multiplexing by having four parallel signal processing stages, each operating with local replicas of the expected spread signals (for synchronization) and spreading codes (for demodulation). A partial version of the local replicas used in the correlators of each synchronization stage are shown in figure 3.23.

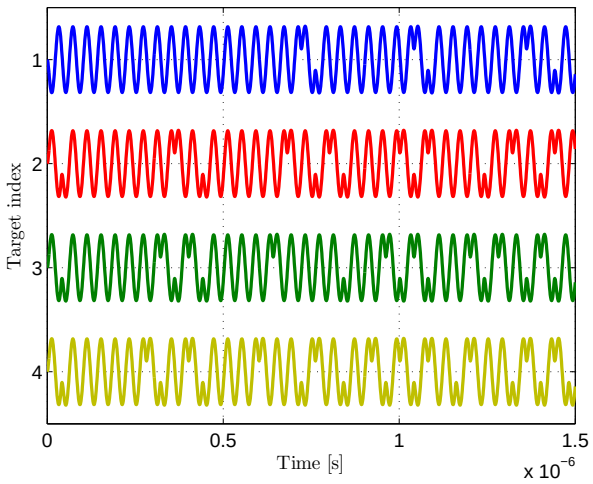

Figure 3.23: Detail of the local replicas of the expected signals (formed with 4 different MLSs 1023 chips long) used in the correlators of the processing stag for every target

The operation of the synchronization stage associated to every target, both in its acquisition and tracking sub-stages, is basically based on the correlation between the received signal and the local replica of its expected signal; so the amount of interference in the resulting correlations is the fundamental parameter that determine the performance of the system in multiuser operation.

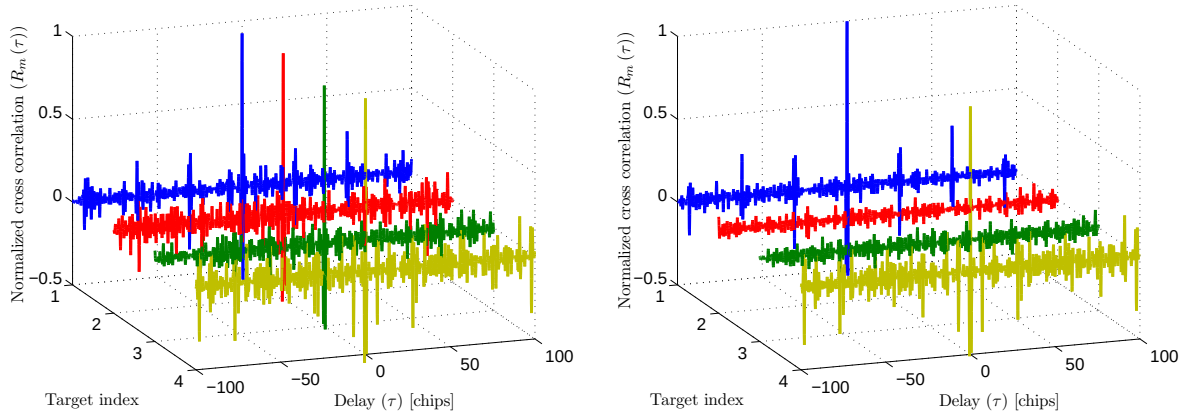

(a) 4 simultaneous targets

(b) Targets 1 and 4

Figure 3.24: Correlation results between ±100 chips of the composed received signal with every locally expected signal associated to every target. (Spreading signals are MLSs 1023 chips long)

Figure 3.24.a shows the correlation results between ±100 chips for every expected signal, i.e., the function obtained in every receiver by correlating the composed received signal of figure 3.22 with the locally expected signals of figure 3.23. Figure 3.24.b shows the same results when targets 2 and 3 are missing.

The figures show that every correlation output, despite being contaminated by the signals coming from other targets with relatively high power, presents a clearly detectable correlation peak corresponding to the expected target when it is present, a no other correlation peaks of similar height that could lead to a wrong delay estimation. On the other hand, when the expected target in certain correlator is missing there is no high value in its output that could lead to a false detection.

This test does not aim to demonstrate the multiplexing behavior of the proposed system, which should be studied carefully by considering the effect of multiuser interferences in the performance of every stage; but does show the potential multiplexing capabilities of the proposal in a simple qualitative approach.

3.3.3 Required analyses

The general structure of the proposed ranging system has been designed in the high level and the selected signal structure has been defined to optimize system performance following some general criteria, and characterized by deriving its power spectrum and autocorrelation function. The specific definition and performance study of the different stages that form the ranging system and its overall behavior are analyzed in following chapters, mainly addressing the following topics:

- **Delay tracking**: The full specific design of the delay tracking stage, based on an ELDLL, has to be defined, and its parameters: early-late spacing and loop bandwidth, have to be

selected. After the stage is fully described, its performance, i.e., estimated delay errors regarding noise, delay variation and multipath, has to be analyzed and validated.

- **DSSS demodulation**: The properties of the demodulated signal as a function of the input signal and local replica alignment has to be defined. This implies analyzing the amount of despread and non-despread power in the band where the subsequent phase estimation is carried out- These powers are calculated as a function of the delays of every component reaching the receiver and the delay used to generate the local replica for demodulation, being the delay estimated by the previous tracking stage.

- **Phase estimation**: The full specific design of the phasemeter, based on I/Q demodulation, has to be defined, and the final estimation bandwidth has to be selected. After the stage is fully described, its performance, i.e., estimated differential phase/distance errors regarding noise, distance variation and multipath, has to be analyzed and validated.

3.3.3.1 Comments on the validation measurements

Along the rest of the document, the terms "simulation" and "emulation" are used to refer to the method employed to collect the measured data for the validation and evaluation of the proposal. The test set-up is explained in detail in section 6.3 of the results chapter, however, measurements are also provided in chapters 4 and 5 for the individual validation of the theoretical analyses derived for every stage. All these validation measurements have been performed using Simulink discrete-time implementations of every stage of the system. These Simulink diagrams and the top-level systems that joint them are provided in appendix A. The reader will often find results defined as "simulation" and "emulation". In both cases the Simulink implementations are used to process the measurements, and these terms address the method used to obtain the input signals introduced in the processing stages, being:

- Simulation: this implies that the signals introduced in the processing stage are directly generated in the digital domain. The different effects such as bandlimited wideband noise, emitter and receiver/AAF[8] bandwidth, delay variation and multipath are added to the signals upon generation.

- Emulation: this implies that the signals have been generated using a system that emulates more closely a practical IR link, using a wired connection between high performance AFGs[9] and a 5 GS/s simultaneous oscilloscope. The main differences between these signals and the all-digital ones is the lack of synchronism between both instruments and the real digitization after the wired analog transmission. This implies a more realistic signal processing since the local replicas in the receiver processing are not frequency locked with the incoming signal. Multipath components, if present, are added to the original signal before D/A[10] conversion in the AFG. The effect of the optical bandwidth is introduced by digital filtering after digitization, prior to downsampling to the emulated sampling rate;

[8] Anti-Aliasing Filter
[9] Arbitrary Function Generators
[10] Digital-to-Analog

and the adequate noise density in every case is introduced by adding an external bandlimited AWGN source in the analog channel. The set-up used to obtain the emulation signals is further explained in section 6.3.

3.4 Summary and conclusions

This chapter provides an analysis of the problem addressed in this thesis and a global description of the method proposed to solve it.

The analysis of the problem has been first addressed in broad sense, considering the general requirements and conditions that affect this work. The localization solution that contextualizes this ranging problem is conceived for mobile units localization. This specific application context requires sub-dm accuracies and sub-second update rates to allow the correct and safe guidance or navigation of the mobile units. Apart from this performance requirements, the system should be able to provide efficient multiuser operation and minimize cost and scalability problems to the extent possible. The current technological limits regarding available devices to build an adequate optical link and the quality of the signal timing in emitter and receivers have also bee studied. A balanced 870 nm link that enables operation at 25 MHz chip rate has been defined. The expected signal quality achievable with this link in a practical location configuration, where the receivers are 2.15 m above the emitter horizontal plane and the maximum horizontal separation with the emitter is 3.7 meters, have been calculated. The analysis concludes that an SNR range between 60 dBHz and 85 dBHz can be expected in the defined scenario. The evaluation of the dependence of SNR with vertical and horizontal separation between emitter and receivers show that the minimum value of 60 dBHz can be reached with the defined link, for a wide range of vertical distances up to 6 m if the horizontal separation is kept below 3.7 m. The apparent delay variation between the time bases in emitter and receivers has been calculated considering an accuracy of 1ppm in the signal generation of every system, yielding a delay rate of change of approximately 2 μs/s. Some considerations regarding sampling rate and signal processing requirements are also discussed and the resolution requirements of the digitizer are analyzed. An expression of the required number of bits in the ADCs that guarantees that the contribution of quantization noise over the total noise is smaller than 1% is derived, assuming that SNR can take values with a maximum difference of two orders of magnitue. This evaluation concludes that 7 bits are required for the minimum SNR of 60 dBHz calculated previously.

The particular multipath problem in optical ranging for indoor localization with the proposed configuration has also been addressed. Multipath reflections in walls are not considered for this study, since they can be generally avoided by limiting the receivers FoV so that they do not cover any wall. The main multipath problem of this system, given that it cannot be avoided in a similar way as the wall reflections, is due to the double ceiling-floor reflections. Previous works demonstrated that this contribution is present in most measurement scenarios and is the principal multipath situation to be addressed in this proposal. Two multipath propagation models (one assuming specular reflection in all surfaces and other assuming Lambertian and isotropic diffuse reflections) have been defined for this situation to provide estimations of the received delay and power levels for the multipath components depending on the parameters of

the scenario. These estimations are used to generate the emulated received signals in multipath conditions in the results chapter. A multipath error model for PoA single-frequency ranging has also been derived to be also used in the results chapter for comparison with the measured errors.

The proposed ranging method to address the multipath problem while fulfilling the other application requirements has been explained. The proposal uses the properties of coherent spread spectrum demodulation for enhancing the power of the LOS component in relation to the multipaths components regarding the phase-based differential distance estimation. The signal synchronization required for coherent demodulation is achieved using delay tracking techniques typical from RF communications and ranging. The whole architecture proposed for the implementation of this method has been described. The signal synchronization is performed by a delay acquisition stage and a baseband ELDLL tracking stage, described and analyzed in depth in chapter 4. The differential phase measurement is performed by a dual asynchronous I/Q demodulator which, together with the spread spectrum demodulation, is analyzed in depth in chapter 5. The signal structure has been formalized using MLS sequences spreading a pure sinusoidal component. Its frequency and phase parameters have been selected aiming to maximize accuracy in both delay and phase estimations by a balanced used of the available bandwidth, increasing chip rate and sinusoidal modulation frequencies while avoiding significant signal distortion and attenuation. The analysis concludes that an efficient and simple solution can be achieved by setting both frequencies to half the available IR channel bandwidth, meaning that the main lobe of the sync-shaped spread spectrum signal lies centered in the channel bandwidth. This selection provides a good balance in terms of accuracy and low-complexity in the generation and analysis of the proposed signal. The use of pulse shaping techniques to make better use of bandwidth has been left for future contributions. Finally, the autocorrelation function and the power spectrum of the proposed signal are calculated to be used in the following chapters.

Chapter 4

Signal synchronization

The synchronization stage of the proposed ranging architecture is analyzed in this chapter. The functions, operation, and performance study of this stage are explained in detail.

The main functions and general architecture are summarized in section 4.1. The rest of the chapter is divided into two main blocks, focusing on each of the two processes necessary to carry out the signal synchronization. The initial delay acquisition stage (coarse synchronization) is presented in section 4.2, while section 4.3 is centered on the delay tracking stage (fine synchronization). In both sections, specific functions and operation are explained in detail, and relevant performance parameters are analyzed and validated to extract conclusions about the expected performance under realistic constrains, and dominant trade-offs and limitations.

4.1 Introduction

The proposed ranging method requires every receiver to achieve and maintain synchronization with the incoming signal. This synchronization is based on the estimation of the relative delay of the incoming signal, including the effect, if present, of multipath components. This delay estimate, exploiting the correlation properties of the received signal, is necessary for:

- Generating a local replica of the PRN code contained in the received signal with an adequate phase. The local PRN replica is used in the DSSS demodulation stage to despread the signal power back to the original sine frequency so that the narrowband phase estimation can be carried out. The accuracy of the delay estimation regarding the LOS component of the received signal should stay below 1 chip time of the PRN code so that some fraction of the LOS component power is coherently demodulated.
- Providing an absolute differential range estimation, after differentiation with an equivalent estimate from another receiver. This absolute differential range estimation allows solving the cycle uncertainties in the phase-based range estimate caused by the sine signal wavelength being a fraction of the full range to be measured.

A simplified diagram of the complete synchronization stage is shown in figure 4.1. The digitized input signal $s(t)$ is fed into both acquisition and tracking stages. The acquisition

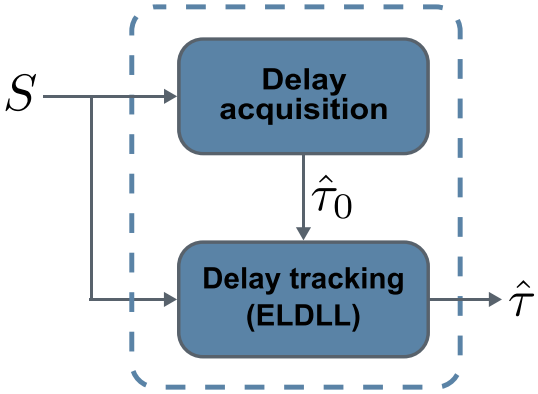

Figure 4.1: Simple diagram of the synchronization stage

stage provides a coarse delay estimation ($\hat{\tau}_0$) by sweeping all possible phases of the expected signal with certain resolution in the local replica phases. $\hat{\tau}_0$ is used by the tracking stage to start operating in a locked state, consequently, the acquisition stage only operates on system initialization or after a loss of lock has been detected. The error of the coarse estimation must stay below the locked operation range of the tracking stage. The tracking stage, based on a base-band Early-Late delay-locked loop (ELDLL), provides a continuous delay estimation ($\hat{\tau}$) of the input signal. This estimation will be used by the DSSS demodulator, explained in section 5.2 of chapter 5, to generate the local replica of the PRN code used for despreading.

It is noteworthy that the true value of the delay to be estimated by this stage in a multipath-free situation, where

$$s(t) = \sqrt{2P_{\mathrm{LOS}}}m\left(t - \tau_{\mathrm{LOS}}\right) + n\left(t\right) \tag{4.1}$$

would be the delay of the LOS signal (τ_{LOS}). However, if multipath components are present in the input signal,

$$s(t) = \sqrt{2P_{\mathrm{LOS}}}m\left(t - \tau_{\mathrm{LOS}}\right) + \sum_{i=1}^{N}\left[\sqrt{2P_{\mathrm{MP_i}}}m\left(t - \tau_{\mathrm{MP_i}}\right)\right] + n\left(t\right) \tag{4.2}$$

the delay to be estimated depends on the composition of LOS and NLOS signal components. In this case, the mean value of the delay estimation in static conditions will tend to that which maximizes the value of the correlation function between the composed input signal and the local replica. The position of this maximum depends on the respective delays ($\tau_{\mathrm{LOS}}, \tau_{\mathrm{MP_i}}$) and relative powers ($P_{\mathrm{LOS}}, P_{\mathrm{MP_i}}$) of all received signal components (LOS and NLOS), and the bandwidth of the optical link (BW_{IR}).

4.2 Delay acquisition

The delay acquisition stage function is providing a coarse delay estimation so that the tracking loop can start (or re-start in case of lose lock) operating in a locked state. This means providing a delay estimation whose error is within the margin where the discriminator of the tracking loop, explained in section 4.3, contains useful information to allow proper operation. This error

margin depends on the signal structure, defined in section 3.3.2.1, and the Early-Late correlators spacing (Δ) in the tracking loop, whose optimization is addressed in section 4.2.1.

This stage is divided in two sequential processes. First, a search of delay candidates is carried out. This search is based on calculating the different correlation values of the input signal with the local replica by sweeping all possible phases of the local replica with certain resolution. Once this search process is finished, all the correlation results are analyzed for detection of the presence of a valid input signal. If detection is achieved, the phase of the local replica providing the higher correlation value is the coarse delay estimate $\hat{\tau}_0$.

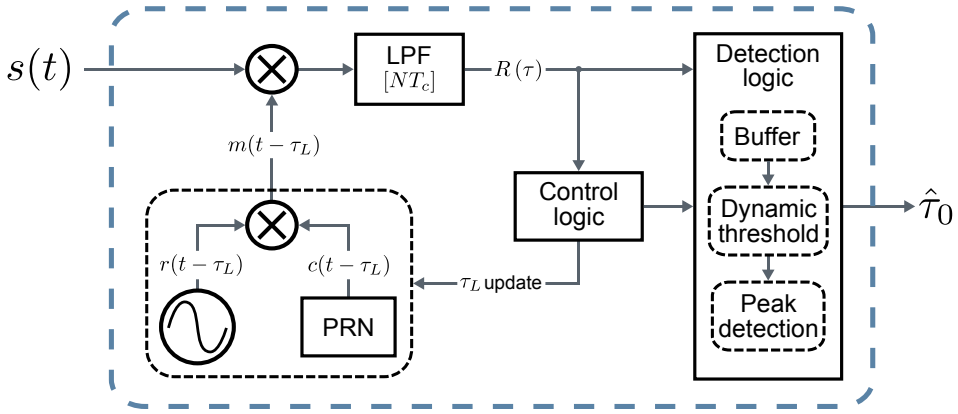

Figure 4.2: Diagram of the delay acquisition stage

The structure of the acquisition stage is shown in figure 4.2. The incoming signal $s(t)$ is correlated with the local replica of the expected signal $m(t)$, generated with certain phase τ_L. The correlation period NT_c is defined by the number of symbols to be correlated (N) and the symbol duration (T_c).The resulting correlation result for that particular phase ($R(-\tau_L)$) is buffered and the control logic updates the local phase τ_L, with resolution Δ_{τ_L}. Once the correlation values with all possible phases of the local replica has been calculated and buffered, the detection logic stars operating. The whole range of stored correlation values is analyzed to define a threshold based on the average of all values. This threshold is used by the peak detector to determine the presence of a valid signal. In case of a successful detection, the local phase τ_L associated to the maximum value of the detected peak is output to the tracking stage as the best delay estimate ($\hat{\tau}_0$).

The calculated correlation is

$$R(\tau) = R(-\tau_L) = \frac{1}{NT_c}\int_0^{NT_c} s(t)m(t-\tau_L)d\tau_L \tag{4.3}$$

where τ is the relative delay between both signals. When a generic input signal $s(t)$ is considered, $\tau = -\tau_L$.

In an ideal case, considering a noise-free and multipath-free situation, with unlimited optical channel bandwidth, the received signal would be an attenuated and delayed version of the local expected signal

$$s(t) = \sqrt{2P_{\text{LOS}}}m(t-\tau_{\text{LOS}}) \tag{4.4}$$

and the calculated correlation would correspond to the autocorrelation function of $m(t)$, $R_m(\tau)$,

whose expression, calculated in section 3.3.2.2, is shown in equation (3.51). In this case, the relative delay between both signals is $\tau = \tau_{\text{LOS}} - \tau_L$

$$R(\tau) = R_m(\tau_{\text{LOS}} - \tau_L) = \frac{1}{NT_c}\int_0^{NT_c} \sqrt{2P_{\text{LOS}}}m(t-\tau_{\text{LOS}})m(t-\tau_L)d\tau_L \tag{4.5}$$

discretized by the resolution of the local phase sweep.

An example of this ideal correlation function with a correlation length of 255 chips is shown in figure 4.3.a. A detail of this correlation, centered around the peak, is shown in figure 4.3.b. Both functions are normalized to the received power P_{LOS} and centered in the position of the maximum peak value, this is, the delay true value to be estimated by the acquisition stage corresponds to the 0 value of the relative delay $(\tau_{\text{LOS}} - \tau_L)$.

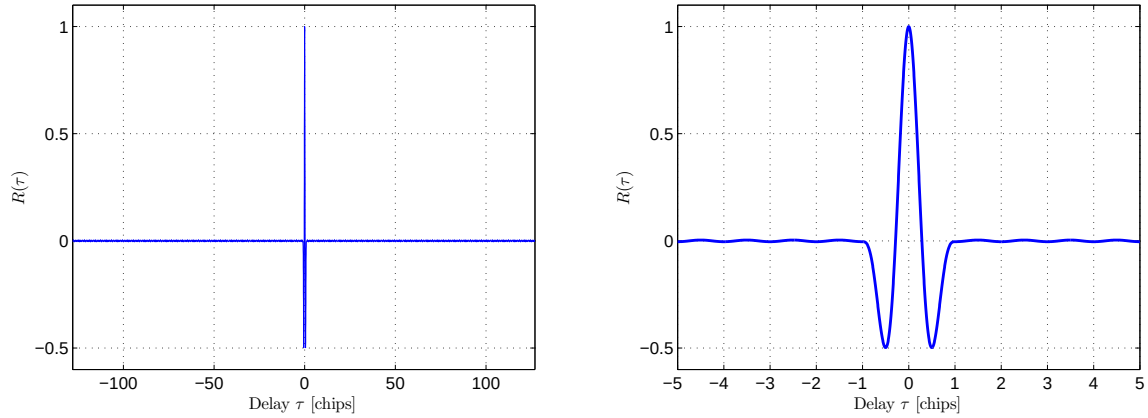

(a) Full correlation (N=255 chips)

(b) Detail around correlation peak

Figure 4.3: Correlation function $R(\tau)$ of simulated signals for ideal input (multipath-free, noise-free, unlimited channel bandwidth, $f_c = 25$ MHz, unlimited local phase resolution)

In a real case considering most dominant effects on the received signal, this is, noise, multipath components and the effect of channel bandwidth defined by its impulse response $h(t)$, the received signal would be

$$s(t) = \left[\sqrt{2P_{\text{LOS}}}m(t-\tau_{\text{LOS}}) + \sum_{i=1}^{N}\left[\sqrt{2P_{\text{MP}_i}}m\left(t-\tau_{\text{MP}_i}\right)\right]\right] * h(t) + n(t) \tag{4.6}$$

An example of the normalized correlation yielded by a more realistic signal, including noise effect and channel bandwidth, is shown in figure 4.4.a. The correlation result is discretized by the resolution of the local phase sweep (Δ_{τ_L}). Figure 4.4.b shows a detail of the former one centered around the delay true value. Note that the channel bandwidth limitation, apart from reducing the total signal power in the band, as shown in section 3.3.2.2, introduces a time offset due to its phase response which should be compensated by calibration. This constant time offset can be easily corrected. Aiming at simplifying the interpretation of figures, it will be canceled in subsequent correlation examples unless it is important for the particular discussion.

The effect of the relevant non-idealities on the estimated delay, as well as the limited phase

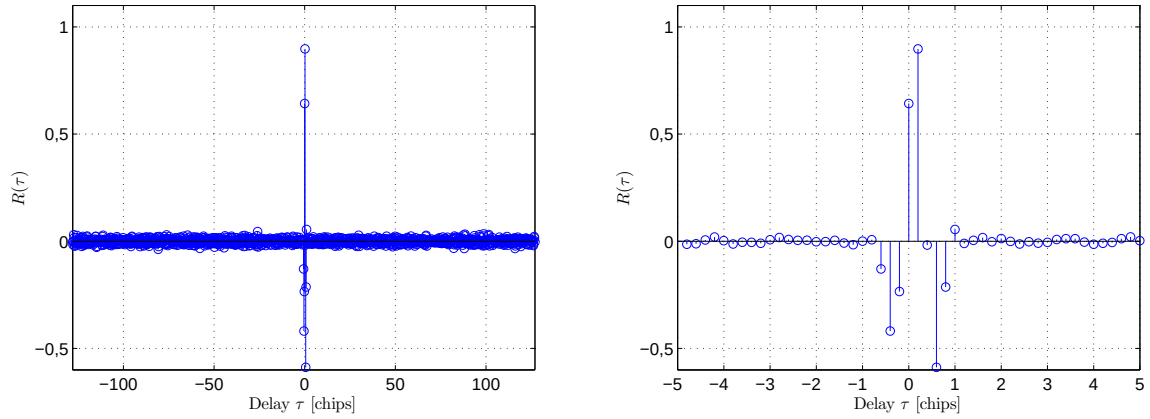

(a) Full correlation (N=255 chips)

(b) Detail around correlation peak

Figure 4.4: Correlation function $R(\tau)$ of simulated signals for real input (multipath-free, SNR = 85 dBHz, $f_c = 25$ MHz, $\Delta_{\tau_L}/T_c = 0.2$ chips)

resolution of the local replica, will be addressed next in the corresponding sections.

The main design trade-off in the coarse acquisition process, for a given signal structure and power, noise and channel bandwidth limitations, is related with the total error in the estimation and the mean acquisition time. Using higher resolution in the local phase implies a smaller estimation error due to a less severe discretization of the measured correlation, at the cost of increasing the mean acquisition time. In the same way, using higher correlation lengths would reduce the error added by noise while increasing acquisition time. In both cases, a higher acquisition time would yield a poorer dynamic behavior, meaning an increase of the error caused by movement of the target and frequency errors between emitter and receiver while acquisition is achieved. The study related to this trade-off aims at balancing static and dynamic errors in the estimation by optimizing acquisition time adjusting the local phase resolution and correlation length. This optimization is addressed in section 4.2.6, once the main error sources are explained and analyzed.

The performance study of the acquisition stage is divided into three main performance indicators. First, precision is analyzed by studying the estimation variance cause by noise and resolution in the local replica possible phases. The accuracy of the estimation is then analyzed considering the accumulated error caused by dynamic effects such as real movement of the target and frequency errors between emitter and receiver. Finally, the mean acquisition time is calculated as a function of the correlation length and local phase resolution. The total error, considering the trade-off between all parameters, is presented at the end of the section, where the optimization of those for certain general requirements and limitations is addressed.

The precision of the estimated delay τ_0 is mainly defined by two phenomena: the effect of noise in the input signal and the limited resolution in the local replica phase.

4.2.1 Effect of noise

The effect of noise in the input signal is the main precision-limiting factor of the delay acquisition. Noise added to the incoming signal causes variations in the position of the maximum peak of its correlation with the local replica. Figure 4.5 shows a comparison of the correlation of $R(-\tau_L)$ in noise-free conditions with SNR = 85 dBHz. The displacement of the correlation peak can be clearly seen in the detail.

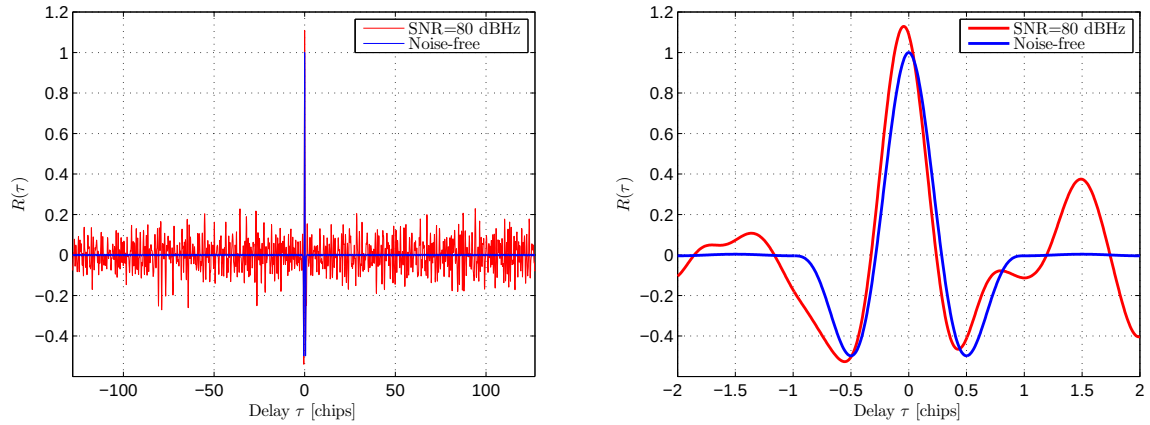

(a) Full correlation (N=255 chips)

(b) Detail around correlation peak

Figure 4.5: Correlation function $R(-\tau_L)$ of simulated signals. Ideal and affected by noise (SNR = 80 dBHz, multipath-free, $f_c = 25$ MHz, $\Delta_{\tau_L}/T_c = 0.005$ chips)

AWGN with double-sided power spectral density $N_0/2$, bandlimited taking into account the optical channel bandwidth, is considered for the study. This is an appropriate consideration since the main noise addition occurs in the low-level conditioning stage of the receivers, where the photocurrent generated by the photodiode is converted into a voltage. Thermal and shot noise processes, which can be properly approximate to AWGN sources, are clearly dominant at this stage. The band limitation in the optical channel cut-off frequency is imposed by the AAF after signal conditioning to maximize SNR in the digitized sequence.

Comments on SNR threshold effect

The variance of a correlation-based delay estimation as a function of SNR is subject to what is usually described as threshold effect. The threshold effect defines two different regions of SNR, plus a transition region joining them, in which the error of the estimation should be analyzed independently. In the first region, when SNR is below certain threshold, there is not enough information in the correlation function to carry out the estimation. This happens when noise influence is more relevant than signal information in the correlation result, meaning that values of the correlation defined by noisy contributions are generally higher than the signal correlation peak. In this region the position of the detected correlation peaks will be uniformly distributed over the whole correlation delay range, providing no information about the true value of the delay. In the opposite region, when SNR is higher than certain threshold, signal information is dominant in the correlation result. A clear peak can be detected in this region and the effect of noise causes a jitter in the position of this maximum, higher for smaller SNR, but following

a zero-mean distribution centered in the delay true value. This is the desirable working region so the estimation can be carried out. In this range, CRLB[1] is widely used to analyze accuracy limits in correlation-based delay estimations working above the proper SNR threshold.

Figure 4.6 shows an example of this effect for the typical error of τ_0. The figure shows simulated results of the standard deviation of the correlation peak maximum as a function of SNR. Observing the figure, two clear SNR ranges, joined by the transition region, can be seen for every correlation length.

When SNR goes below certain SNR, approximately 70 dBHz for $N = 63$ chips and 55 dBHz for $N = 4096$ chips, the standard deviation of the estimation reaches a stable value independently on SNR. This is the range where there is no practical information of the signal in the correlation result. The particular value reached by the simulated standard deviation is related with the whole range of possible delay values, i.e., the full length of the correlation (NT_c). This can be seen in the figure, where standard deviations in this region are higher for longer correlation times.

In the other hand, above approximately 83 dBHz for $N = 63$ chips and 66 dBHz for $N = 4096$ chips, the standard deviation starts showing a clear dependency with SNR. This is the working region of the estimation, which is analyzed below.

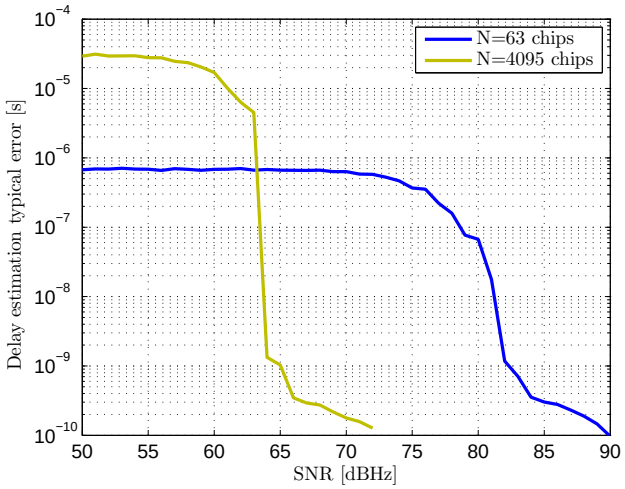

Figure 4.6: Example of threshold effect on the coarse acquisition delay estimation (τ_0) for 2 correlation lengths ($f_c = 25$ MHz)

Theoretical precision bound

CRLB will be used to define a lower bound to the attainable accuracy in the estimation as a function of SNR [Weiss and Weinstein, 1983, Weinstein and Weiss, 1984]. The delay estimation based on correlations with a replica of the expected signal and maximum search is an unbiased ML estimate of the delay true value [Dardari et al., 2009]. Its performance theoretically reaching CRLB for high SNR values where the correlation maximum can still be disguised from the noisy correlation background. The minimum achievable variance in the estimation error for a single

[1] Cramér-Rao Lower Bound

symbol satisfies

$$\sigma^2_{\hat{\tau}_{pm}} \geq \text{CRLB} = \frac{N_0/2}{(2\pi)^2 \beta^2 E_p} \tag{4.7}$$

where $E_p = P_r T_c$ is the symbol energy and β, usually called effective bandwidth, is

$$\beta^2 = \frac{\int_{-\infty}^{\infty} f^2 |M(f)|^2 df}{\int_{-\infty}^{\infty} |M(f)|^2 df} \tag{4.8}$$

which depends on the spectrum $P_m(f)$ of the symbol $p_m(t)$ that forms the signal $m(t)$, defined and modeled in section 3.3.2.1 of chapter 3.

β^2 has been calculated for different optical channel bandwidths (BW_{IR}). As explained and justified in section 3.3.2.1, the symbol structure is defined by the channel bandwidth, with $1/T_c = BW_{IR}/2$. Taking this into account, the integral has been numerically calculated with

$$|P_m(f)|^2 = \frac{T_c^2}{4}\left[\text{sinc}^2\left[(f - f_r)\, T_c\right] + \text{sinc}^2\left[(f + f_r)\, T_c\right]\right] \tag{4.9}$$

Figure 4.7 depicts the results of the calculation. It can be seen that, for the given symbol, β^2 shows a linear relationship with BW_{IR}, i.e., with the sine and chip frequencies f_r and f_c, which can be very closely approximate to

$$\beta^2 \approx \frac{1.05}{T_c} \tag{4.10}$$

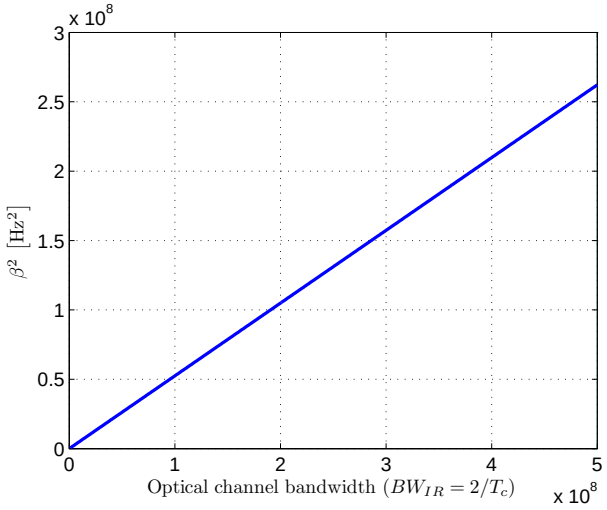

Figure 4.7: Squared efficient bandwidth (β^2) as a function of channel bandwidth (BW_{IR})

Adding the integration of N symbols, the typical error of the delay estimation in the coarse acquisition stage ($\hat{\tau}_0$) would be approximately lower bounded by

$$\sigma_{\hat{\tau}_0} \geq \frac{T_c}{2\pi 1.05}\sqrt{\frac{N_0/2}{N P_r T_c}} \tag{4.11}$$

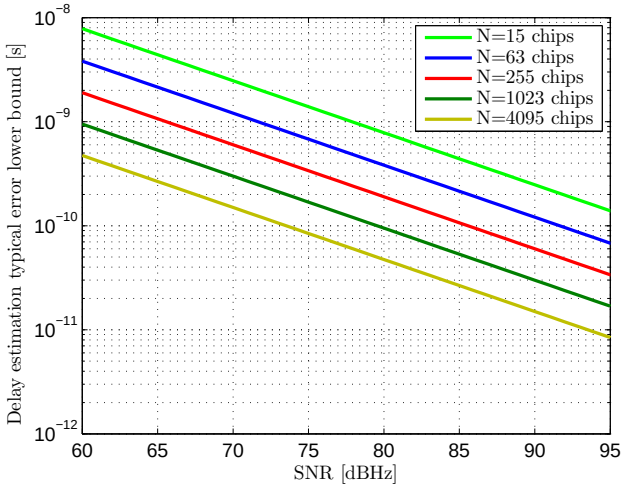

Figure 4.8: Lower bound of the delay estimation error as a function of SNR for different correlation lengths (N) ($f_c = 25$ MHz)

Defining the signal to noise density ratio as

$$\text{SNR} = \frac{P_r}{N_0/2} \tag{4.12}$$

and simplifying

$$\sigma_{\hat{\tau}_0} \geq \frac{1}{2.1\pi}\sqrt{\frac{T_c}{N\text{SNR}}} \tag{4.13}$$

As expected, the lower bound of the estimation error is smaller for higher SNR, higher chip-rates ($f_c = 1/T_c$) and longer observation times.

Figure 4.8 shows the lower bound of the estimation error calculated as a function of SNR for different correlation lengths and 50 MHz optical channel bandwidth. This channel bandwidth defines a chip-rate of 25 MHz. Observation times associated to every correlation length are shown in table 4.1.

Table 4.1: Observation times in figure 4.8 as a function of correlation length for 25 MHz chip-rate

Correlation length	**Observation time**
N=15 chips	0.6 μs
N=63 chips	2.5 μs
N=255 chips	10.2 μs
N=1023 chips	40.9 μs
N=4095 chips	163.8 μs

Measured precision in the presence of AWGN

The calculated lower bound is compared in this section with simulations of the standard deviation in the estimated position of the correlation peak.

Figure 4.9 shows the results shown in figures 4.6 and 4.8, comparing simulations and the calculated CRLB. It can be seen how the simulation results, above the minimum SNR defined by the threshold effect, show a dependency with SNR which is coherent with CRLB. The computing and memory load of these simulations, covering a very wide SNR range, are very demanding. Due to this, sampling frequency in the synthetic signals generated for simulation could not be set higher than $f_s = 10$ GS/s. This sampling frequency introduces an error in the results that can be modeled as a uniform distribution with variance $T_s^2/12$, where $T_s = 1/f_s$. For $f_s = 10$ GS/s, this error would be approximately 300 ps, i.e., non-negligible compared to the error caused by noise. The combination of both effects causes an absorption of the noise related error by the sampling resolution, yielding smaller total errors. Finer simulations are shown next using a sampling frequency of 25 GS/s, where the computing and memory limitations have been solved by focusing only in the region coherent with CRLB.

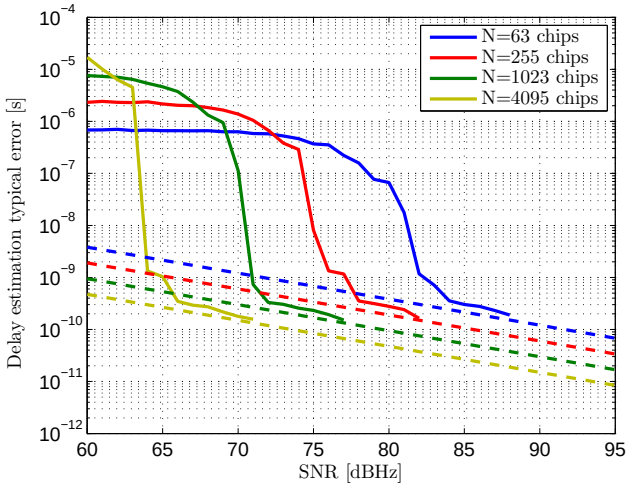

Figure 4.9: Delay estimation error caused by AWGN as a function of input SNR for different correlation lengths (N). Lower bound (dashed) and simulations (solid) ($f_c = 25$ MHz)

Figure 4.10 shows finer simulations, with increased sampling rate so that the effect of time quantification of the sampled digital signals is much smaller than that of caused by noise and can be neglected. The simulations for every correlation length has been carried from the minimum SNR determined by the previously explained threshold effect, i.e., the range in which the results can be properly compared with CRLB.

The results, although limited in range, show that the standard deviations obtained by simulation of the peak detection process strongly agree with the expected precision defined by the CRLB, specifically calculated for the designed symbol.

4.2.2 Effect of local phase resolution

The resolution Δ_{τ_L} of the local replica phase τ_L is the minimum update step defined in the local signal generator. This generator has been implemented with a memory containing the expected signal $m(t)$, which outputs samples at the sampling rate of the receiver (f_s), to be correlated with the digitized input signal. It is possible, however, to define this memory with

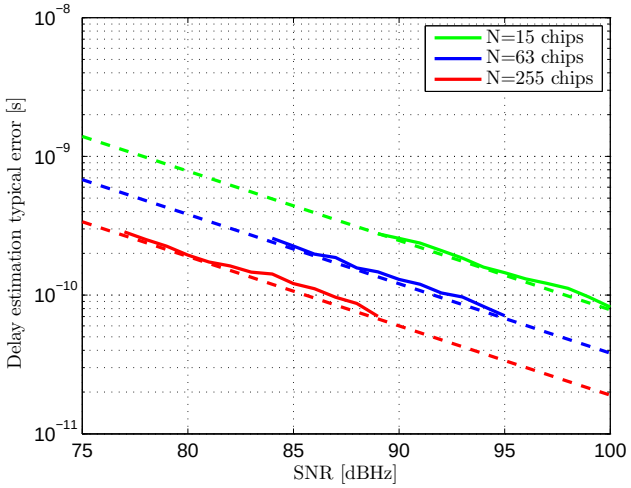

Figure 4.10: Delay estimation error caused by AWGN as a function of input SNR for different correlation lengths (N). Lower bound (dashed) and simulations (solid) ($f_c = 25$ MHz)

higher resolution than f_s, i.e., a higher number of stored samples per symbol than those of the received signal. If the received signal has

$$N_s = f_s/f_c \tag{4.14}$$

samples per symbol, and the memory contains

$$N_L = kN_s \tag{4.15}$$

with $k \in \mathbb{N}^*$, samples per symbol, the possible phases of the local replica are defined by N_L with subsample resolution

$$\Delta_{\tau_L} = T_s/k \tag{4.16}$$

seconds, where k can be made arbitrarily high at the cost of increasing both memory size and acquisition time in the same proportion. The size in samples of this memory implementing the local replica generator would be the frame period of the received signal ($T_f = NT_c$) times the receiver sampling rate (f_s) times k. The effect of $\Delta\tau_L$ on the acquisition time is described in section 4.2.5.

As explained in the introduction of section 4.2, a correlation value is calculated for every τ_L value, which is updated with $\Delta\tau_L$ steps, until all possible phase values are sweep. Consequently, the calculated correlation $R(\tau)$ will be discretized with $\Delta\tau_L$ sample period.

Figures 4.11 to 4.14 show correlation results applying different local phase resolutions from 0.05 chips to 0.5 chips. The correlation delay associated to the maximum value is taken as delay estimate $\hat{\tau}_0$, while the origin of the correlation delay axis is the delay true value (τ_{LOS} in the multipath-free case used in the figures). The figures clearly depict how the uncertainty of the estimation increases for lower resolutions in the local replica phase.

This uncertainty can be modeled as a quantification of the correlation delay time base. The delay true value has equal probability to be found between $[-\Delta_{\tau_L}/2,\ \Delta_{\tau_L}/2]$ of the estimated

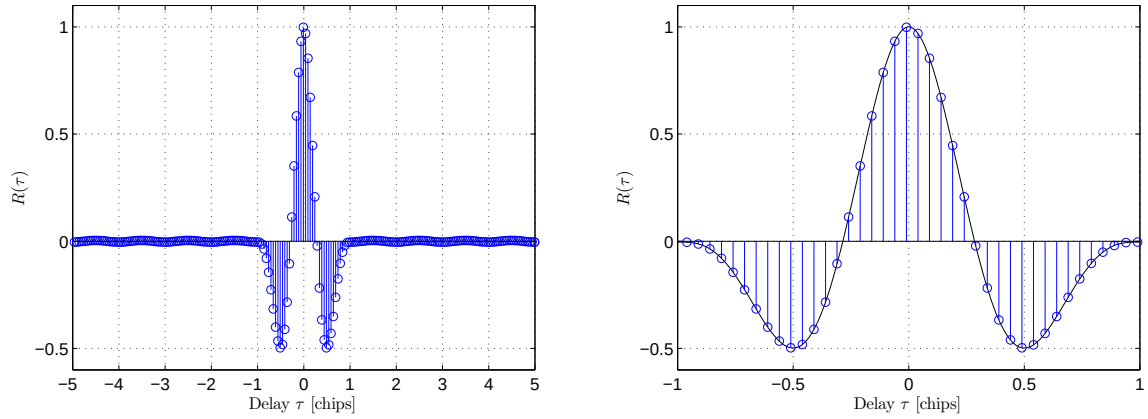

(a) (b)

Figure 4.11: Correlation function $R(\tau)$ of simulated signals with $\Delta_{\tau_L} = 2$ ns ($\Delta_{\tau_L}/T_c = 0.05$ chips) (multipath-free, noise-free, $f_c = 25$ MHz)

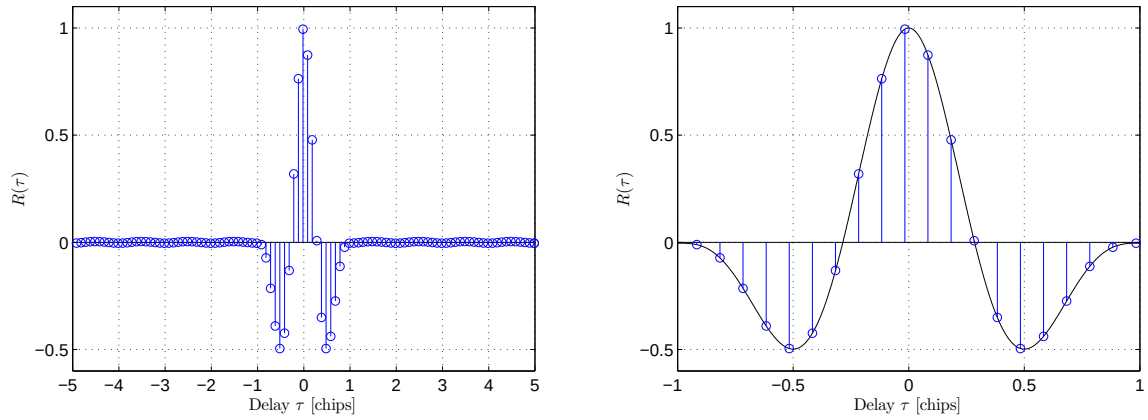

(a) (b)

Figure 4.12: Correlation function $R(\tau)$ of simulated signals with $\Delta_{\tau_L} = 4$ ns ($\Delta_{\tau_L}/T_c = 0.1$ chips) (multipath-free, noise-free, $f_c = 25$ MHz)

delay $\hat{\tau}_0$. This is, the probability density function of the error in the delay estimation follows a uniform distribution with limits $[-\Delta_{\tau_L}/2,\ \Delta_{\tau_L}/2]$, defining a zero-mean error with variance

$$\sigma^2_{\hat{\tau}_0} = \frac{\Delta^2_{\tau_L}}{12} \tag{4.17}$$

The typical error in the delay estimation as a function of the local phase resolution for a chip-rate of 25 MHz is depicted in figure 4.15. The red circles correspond to the particular cases used in the examples above.

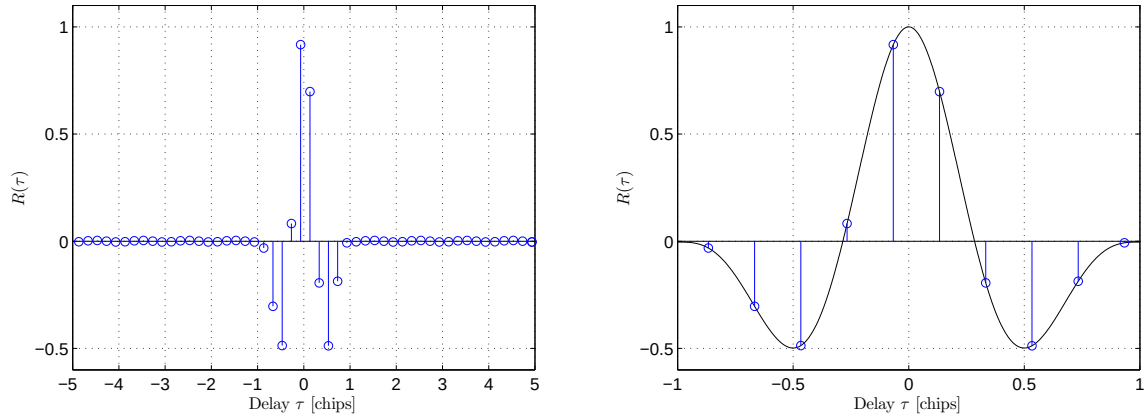

(a) (b)

Figure 4.13: Correlation function $R(\tau)$ of simulated signals with $\Delta_{\tau_L} = 8$ ns ($\Delta_{\tau_L}/T_c = 0.2$ chips) (multipath-free, noise-free, $f_c = 25$ MHz)

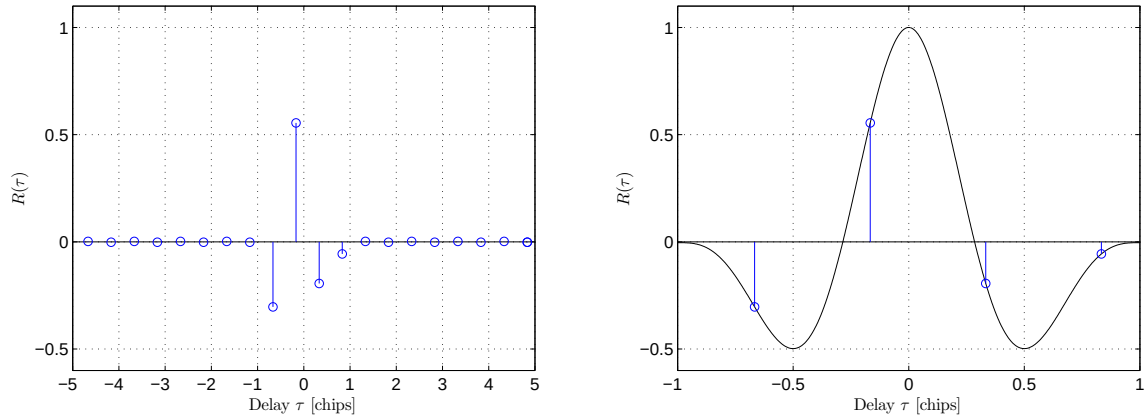

(a) (b)

Figure 4.14: Correlation function $R(\tau)$ of simulated signals with $\Delta_{\tau_L} = 20$ ns ($\Delta_{\tau_L}/T_c = 0.5$ chips) (multipath-free, noise-free, $f_c = 25$ MHz)

4.2.3 Effect of Multipath

The ranging system is subject to three main accuracy-related error sources: multipath and dynamic errors associated to real movement of the target and frequency errors between emitter and receivers.

The presence of multipath components in the received signal introduces an error in the estimation of the LOS delay true value. The function of the acquisition stage is providing a coarse delay estimate so that the tracking loop can start operating in a locked state. The tracking stage operates with the complete input signal, fully affected by multipath, i.e., the tracked delay is that of the composed input signal, since multipath mitigation is carried out in the subsequent range estimation stage, explained in 5. Consequently, the admissible delay error that allows proper locking of the tracking loop are related to the full signal delay, determined, as explained in the multipath problem section (3.2) of chapter 3, by the LOS and multipath

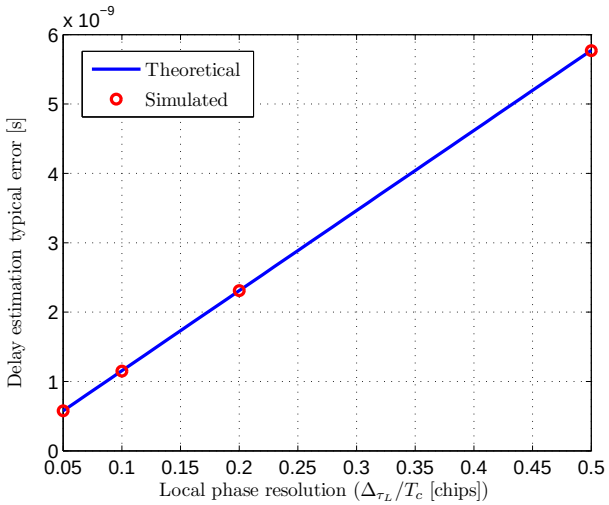

Figure 4.15: Delay estimation typical error as a function of the local replica phase resolution. Theoretical and measured on simulated signals ($f_c = 25$ MHz)

particular delays and relative powers. It is therefore not necessary to analyze the multipath related errors in the acquisition stage.

4.2.4 Dynamic error

The dynamic error of the acquisition stage is caused by:

- Movement of the target causing variations of the received signal delay true value. The maximum rate of change of the delay depends on the environment geometry and the maximum target speed defined in section 3.1.1.

- Frequency errors due to the fully unsynchronized operation between emitter and receivers, causing a constant frequency difference between the input signal and the locally generated replica. This frequency difference appears in the delay estimation as a constant delay variation, whose rate of change depends on the signal frequency and the accuracy of the emitter and receiver reference clocks.

The error in the acquisition stage should stay below the operating range of the tracking loop taking into account all precision-related error sources analyzed above plus the effect of delay drifts accumulated before acquisition is achieved. The acquisition process is based on sweeping all possible delay candidates before analyzing the presence of valid signal and estimating its delay. The accumulated error, caused by delay drifts before acquisition is complete, depends on the delay rate of change and the acquisition time. Long acquisition times allow longer integration in the correlations hence higher noise rejection, and better resolution in the local replica phase. In the other hand, short acquisition times reduce the accumulated dynamic errors. This trade-off is studied in section 4.2.6, after acquisition time is defined in section 4.2.5, and the total dynamic error is defined in this section.

4.2.4.1 Movement of the target

As defined in the general system requirements in 3.1.1, the system must be able to track variations of the target position allowing a maximum target speed of 1 m/s over the floor. The maximum rate of change of the delay as a function of robot speed depends on the relative position between emitter and receivers. The maximum delay variation ($\Delta_\tau^{\text{target}}$) seen by one receiver happens when the target is moving directly towards or against that receiver. In the proposed setups receivers are generally placed in the ceiling of the environment, so the rate of change would be the projection over the LOS of the speed vector of the target moving on the floor, i.e., any rate of change seen by the receiver would be smaller than $\Delta_\tau^{\text{target}}$. This value is taking as a general worst case for the study.

Considering a target moving directly towards a receiver at V_{target} m/s, the delay variation seen by the receiver is

$$\Delta_\tau^{\text{target}} = \frac{V_{\text{target}}}{c} \tag{4.18}$$

where c is the propagation speed of the optical signal, approximate to the propagation speed in vacuum ($3 \cdot 10^8$ m/s).

4.2.4.2 Frequency errors

Clock synchronization between emitter and receiver defines a common time-base for the signals generated in both systems. When a periodic correlation is calculated between the received signal and the local replica in these circumstances and static conditions, the output correlation peaks appear at a constant correlation delay. If there is not such synchronization, the frequency difference between both signals to be correlated causes a drift in the correlation peak position, appearing as a variation in the estimated delay.

The maximum apparent delay variation caused by frequency errors was calculated in 3.1.3.2, yielding

$$\Delta_\tau^{\text{CLK}} = 1 - \frac{1}{1 \pm 2\frac{\epsilon_{\text{CLK}}}{10^6}} \approx \pm 2\frac{\epsilon_{\text{CLK}}}{10^6} \tag{4.19}$$

where ϵ_{CLK} is the emitter and receiver clocks accuracy in ppm.

4.2.4.3 Total dynamic error

The total dynamic error caused by the joint contribution of both sources is

$$\Delta_\tau = \Delta_\tau^{\text{target}} \pm \Delta_\tau^{\text{CLK}} \tag{4.20}$$

which, in the worst case, when the delay variation of both error sources takes the same sign, yields a maximum delay rate of change of

$$\Delta_\tau = \frac{V_{\text{target}}}{c} + 2\frac{\epsilon_{\text{CLK}}}{10^6} \tag{4.21}$$

To give a quantitative idea about the magnitude of this error, an example with realistic values is calculated. The target is moving at its maximum speed over the floor ($V_{\text{target}} = 1$ m/s). Emitter and receiver systems generate their respective signals based on a master clock of 25 MHz with frequency tolerance of 1 ppm. The rate of change of the delay would be

$$\Delta_\tau = 3 \ [\text{ns/s}] + 2 \ [\mu\text{s/s}] \tag{4.22}$$

Observing the numerical result, the effect of the movement of the target is 3 orders of magnitude smaller than the effect of frequency errors. Movement of the target is therefore negligible, and system dynamics should be adapted to the limitations imposed by timing errors. Note that even if more accurate timing was achieved by using more accurate clocks, frequency errors would still be clearly dominant. To illustrate this, consider that a clock with a frequency tolerance of 0.05ppm would yield a delay variation of 100 ns/s, still more than 30 times faster than the effect of the target displacement.

In case of the acquisition stage, the problem associated to this dynamic contribution is the error accumulation before the acquisition process is finished. As commented, the stage calculates correlation values with different phase candidates in the local replica. Once all candidates has been sweep, the whole data set is analyzed for detection and estimation. Only after this process, the coarse estimation is known and output to the tracking stage. The time elapsed since the better candidate correlation is calculated and the end of the acquisition process defines the amount of accumulated error. This error is

$$\epsilon_{\hat{\tau}_0} = (t_{\text{acq}} - t_{\text{det}})\, \Delta_\tau \tag{4.23}$$

where acquisition time (t_{acq}) is the full duration of the candidates sweep, and detection time (t_{det}) is the time when the better candidate correlation was calculated. Acquisition time is a constant value depending on correlations length and resolution of the phase sweep. It is defined and calculated in the next section. Detection time is variable, its probability being uniformly distribute over the whole acquisition duration, as it depends on the arbitrary time difference between emitter and receiver startups. The worst case for dynamic error accumulation is that the better phase candidate is used in the first update of the local phase, this is, after only one correlation. The maximum search is always performed over a whole epoch and has a fix duration, so this is the situation that maximizes the elapsed time between the coarse delay measurement and its use to initialize tracking, i.e., the accumulated error would be maximum when the tracking stage starts operating. The maximum accumulated error in that case is

$$\epsilon_{\hat{\tau}_0} = (t_{\text{acq}} - NT_c)\, \Delta_\tau \tag{4.24}$$

where NT_c is the time length of one correlation.

4.2.5 Acquisition time

The duration of the acquisition process is directly related to its performance. Precision errors due to noise and resolution in the replica phase can be reduced by increasing the integration time of the correlations (NT_c) and reducing the update steps of the local replica phase (Δ_{τ_L}) respectively.

Total acquisition time is the duration of every correlation (NT_c) times the number of correlations to be calculated (N_{corr}). The number of correlations to be calculated depends on the number of chips per frame (N_f) of the received signal and the number of phase candidates per chip (T_c/Δ_{τ_L}).

$$t_{\text{acq}} = NT_c N_{\text{corr}} = NT_c N_f \frac{T_c}{\Delta_{\tau_L}} \tag{4.25}$$

To reduce line components in the signal spectrum, the emitted signal is design in such a way that the frame period T_f matches the integration time used in the receiver correlators, i.e., the number of chips per frame (N_f) is equal to the number of chips integrated in every correlation (N). The acquisition time is then

$$t_{\text{acq}} = \frac{N^2 T_c^2}{\Delta_{\tau_L}} \tag{4.26}$$

As commented, longer acquisition times allow better precision in the coarse delay estimation. However, as seen in the previous sections, error due to accumulation of dynamic effects depends directly on acquisition time. It is, therefore, necessary to optimize it in order to achieve the requirement of the next stage, i.e., a total error that stays within the locked margin of the tracking loop. This trade-off is analyzed in the next section.

4.2.6 Total error

The admissible error in the coarse delay estimation so that the tracking loop can start operating is ±0.5 chips. This is the margin where the discriminator of the tracking loop contains proper information to maintain a locked state. This margin depends on the discriminator features, which are studied in the following section (4.3).

The maximum error of the coarse delay estimation includes precision-related errors and the dynamic error accumulated during the whole acquisition duration. This maximum error (ϵ_T) will be defined by the sum of variances of noise contributions (σ^2_{noise}) and local phase resolution contributions (σ^2_{phase}) plus the worst-case accumulated error due to dynamic effects ($\epsilon_{\hat{\tau}_0}$). In order to guarantee a correct initialization of the tracking loop in most situations, 3 standard deviations of the total precision-related errors are considered.

$$\epsilon_T = 3\sqrt{\sigma^2_{noise} + \sigma^2_{phase}} + \epsilon_{\hat{\tau}_0} \tag{4.27}$$

σ^2_{noise} is defined in section 4.2.1. The achieved expression of CRLB in equation (4.13) is used as an approximation to the effect of noise. σ^2_{phase} has been defined in equation (4.17) in

section 4.2.2, and the accumulated dynamic error is summarized is defined in section 4.2.4, as a function of the acquisition time summarized in equation (4.26) of section 4.2.5.

Replacing the corresponding expressions for every contribution, the total error is

$$\epsilon_T = 3\sqrt{\frac{1}{(2.1\pi)^2}\frac{T_c}{N\mathrm{SNR}} + \frac{\Delta_{\tau_L}^2}{12}} + \left(\frac{N^2T_c^2}{\Delta_{\tau_L}} - NT_c\right)\Delta_\tau \tag{4.28}$$

The optimization of the total error is carried out by selecting the best combination of correlation length (N) and local phase resolution (Δ_{τ_L}) for a given chip-rate. Worst-case SNR is considered so that correct locking can be guaranteed in most situations.

An example of the optimization is given for 25 MHz chip-rate and range of worst-case SNR from 20 dBHz to 80 dBHz. A rate of change of the delay caused by dynamic errors of 2 μs/s is considered. This rate of change was calculated in section 4.2.4.3 for a clock accuracy in of 1ppm in both emitter and receiver. The minimum correlation length considered is 15 chips, given that non-realistic SNR levels would be necessary to yield admissible errors with shorter correlations. The minimum number of phase candidates per chip considered for the definition of the local phase resolution is 0.5 chips, since peak detection cannot be guaranteed above this number.

Figure 4.16 depicts the total error as a function of correlation length and local phase resolution for different SNR levels. The minimum error value that optimizes both parameters is marked with a red dot.

By observing the figures it can be seen that, under low-SNR conditions, noise contributions dominate the total error and long correlations are necessary to reduce it. In figure 4.16.a, with SNR=20 dBHz, the minimum achievable total error is approximately 425 ns, with 735 chips correlation length and local phase resolution of 2 phase candidates per chip. In the opposite case show in figure 4.16.d, with SNR=80 dBHz, noise in non-dominant and the error is dominated by the resolution of the phase sweep. The minimum error for this case is approximately 3 ns, achieved with 15 chips correlation length and a phase resolution of 20 candidates per chip.

Figure 4.17 shows the optimal parameters for the whole SNR range. The projection of the curve over the floor plane is also included in a thinner line to provide clearer 3D visualization.

The total error level achieved with the optimal correlation length and phase resolution for every SNR is shown in figure 4.18. The admissible error level of ± 0.5 chips (20 ns) for the 25 MHz chip-rate used in the optimization is depicted in red. It can be seen that, to fulfill the requirements of the tracking stage, a minimum worst-case SNR of 56 dBHz is necessary.

The acquisition time associated to optimal correlation lengths and phase resolutions for every SNR is shown in figure 4.19.

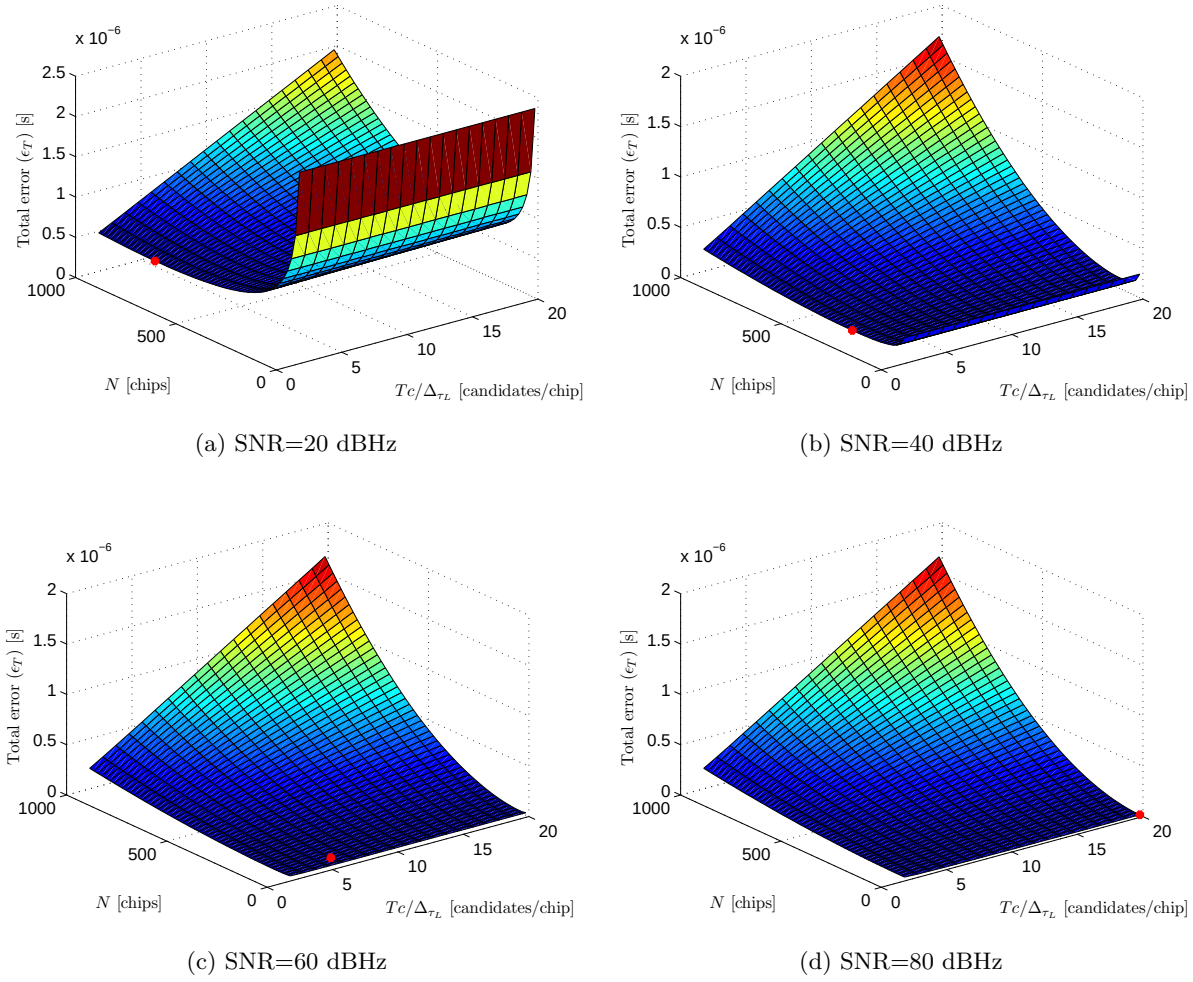

(a) SNR=20 dBHz

(b) SNR=40 dBHz

(c) SNR=60 dBHz

(d) SNR=80 dBHz

Figure 4.16: Total error as a function of correlation length and local phase resolution ($f_c = 25$ MHz, $\Delta_\tau = 2$ μs/s)

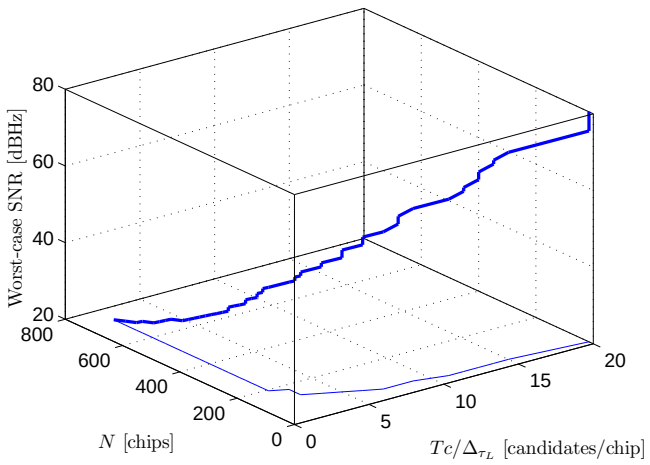

Figure 4.17: Correlation length and local phase resolution values that minimize total error as a function of SNR ($f_c = 25$ MHz)

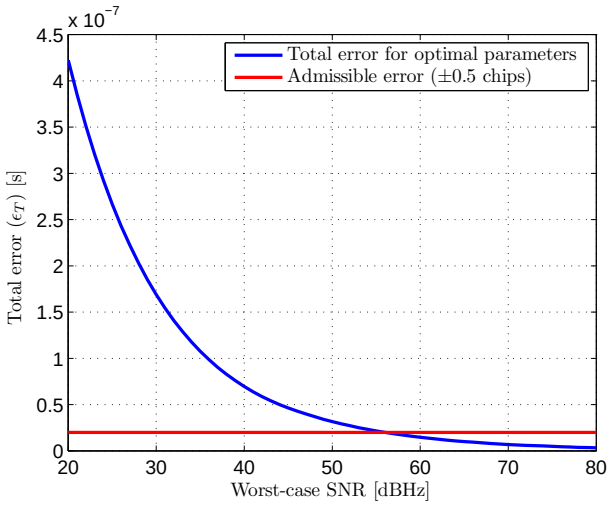

Figure 4.18: Total error for optimal parameters as a function of SNR (f_c =25 MHz)

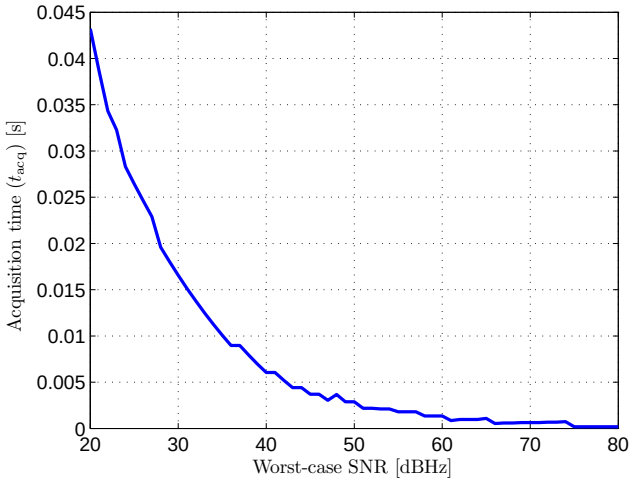

Figure 4.19: Acquisition time for optimal parameters as a function of SNR (f_c =25 MHz)

4.3 Delay tracking

The delay tracking stage function is to provide a continuous estimation of the delay of the incoming signal. This delay estimation is used by the next stage, explained in chapter 5, to generate the local replica of the expected PRN sequence. This replica is used to carry out a partially-coherent DSSS demodulation process. The tracked delay is also used in the final differential ranging stage to solve the cycle uncertainty of the phase-based range estimation.

The attainable accuracy in the tracking stage is essentially affected by the same effects conditioning the accuracy of the coarse acquisition explained above. There is, however, one important difference: the phase resolution of the local replica generated for tracking does not have an influence on system dynamics, since no candidates search is carried out. This relaxes the trade-off between precision-related errors and accumulated dynamic errors, allowing higher global accuracy in the estimation.

The delay tracking is based on a base-band early-late delay-locked loop (ELDLL). This kind

of tracking loops, once locked, correlate the incoming signal with slightly advanced and delayed versions of the local replica to obtain information about the alignment error with the incoming signal. This information is used to correct the local phase in order to keep tracking and provide a continuous delay estimation.

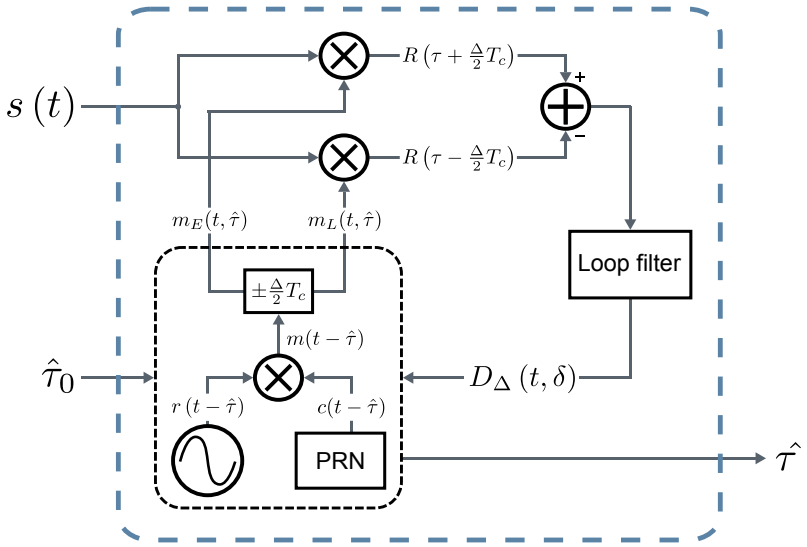

Figure 4.20: Diagram of the delay tracking stage

The structure of the tracking stage is shown in figure 4.20. Once the coarse delay estimation $\hat{\tau}_0$ is available, it is used to initialize the local replicas generator. Two versions of the expected received signal are output with an initial phase defined by $\hat{\tau}_0$, which, after closing the loop, will be replaced by the actual estimated tracked delay $\hat{\tau}$.

These signals are

$$m_{_E}(t,\hat{\tau}) = m\left(t - \hat{\tau} + \frac{\Delta}{2}T_c\right) \tag{4.29}$$

$$m_{_L}(t,\hat{\tau}) = m\left(t - \hat{\tau} - \frac{\Delta}{2}T_c\right) \tag{4.30}$$

i.e., the respective early and late versions of the prompt replica. The delay of these two signals in relation to the actual delay estimation is determined by the early-late spacing, defined in Δ chips.

$m_{_E}(t,\hat{\tau})$ and $m_{_L}(t,\hat{\tau})$ are multiplied with the incoming signal $s(t)$. Note that the outputs of the multipliers are not actual correlations as no integration is applied to them before the subtraction. However, for simplicity and not affecting the results, they are treated as correlations both in the figure and following explanations. The resulting correlation values correspond to the $\Delta/2$ advanced and delayed values of the correlation of $s(t)$ with the prompt local replica $m(t-\hat{\tau})$. When a generic signal $s(t)$ is considered, the relative delay τ between both signals is $-\hat{\tau}$, and

$$R(\tau) = R(-\hat{\tau}) = \frac{1}{T_{_{W_L}}}\int_0^{T_{W_L}} s(t)m(t-\hat{\tau})d\hat{\tau} \tag{4.31}$$

where $T_{_{W_L}}$ is the integration time defined by the loop filter.

Assuming an ideal multipath-free and noise-free situation, where

$$s(t) = \sqrt{2P_{\text{LOS}}}m\left(t - \tau_{\text{LOS}}\right) \tag{4.32}$$

the relative delay is $\tau = \tau_{\text{LOS}} - \hat{\tau}$, yielding the prompt correlation

$$R\left(\tau\right) = \frac{1}{T_{W_L}}\int_0^{T_{W_L}} \sqrt{2P_{\text{LOS}}}m\left(t - \tau_{\text{LOS}}\right)m(t - \hat{\tau})d\hat{\tau} = \sqrt{2P_{\text{LOS}}}R_m\left(\tau_{\text{LOS}} - \hat{\tau}\right) \tag{4.33}$$

and, therefore, the early and late correlation values would be

$$R_{_E} = R\left(\tau + \frac{\Delta}{2}T_c\right) = \sqrt{2P_{\text{LOS}}}R_m\left(\tau_{\text{LOS}} - \hat{\tau} + \frac{\Delta}{2}T_c\right) \tag{4.34}$$

$$R_{_L} = R\left(\tau - \frac{\Delta}{2}T_c\right) = \sqrt{2P_{\text{LOS}}}R_m\left(\tau_{\text{LOS}} - \hat{\tau} - \frac{\Delta}{2}T_c\right) \tag{4.35}$$

To illustrate this, assuming no error in the delay estimation, i.e., $(\tau_{\text{LOS}} - \hat{\tau}) = 0$, the calculated correlation samples would correspond to those shown in figure 4.21. The prompt sample, which is not actually calculated, is also shown in the figure. This sample would correspond to the correlation value calculated with the estimated delay $\hat{\tau}$, this is,

$$R_{_P} = R\left(\tau\right) = \sqrt{2P_{\text{LOS}}}R_m\left(\tau_{\text{LOS}} - \hat{\tau}\right) \tag{4.36}$$

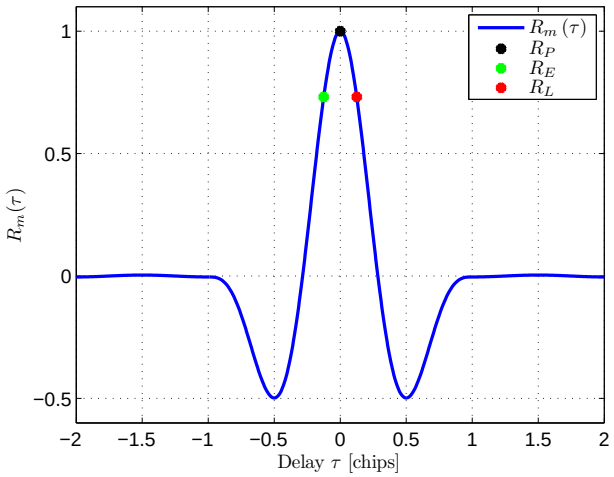

Figure 4.21: Normalized early and late samples for ideal input (multipath-free, noise-free) and perfect alignment $(\tau_{\text{LOS}} - \hat{\tau} = 0)$ with $\Delta = 0.25$ chips

As shown in 3.3.2.2, $R_m(t)$ is a symmetrical function in ideal conditions and, even distorted by a limited channel BW in $2f_c$, it stays strongly symmetrical. Due to this property, the values of the late and early samples tend to be equal when the estimation error tends to 0.

In case there is an error in the estimation, e.g., ± 0.05 chips, the late and early samples would correspond to those shown in figures 4.22.a and 4.22.b.

It can be seen that, depending on the sign of the delay, early and late samples tend to grow

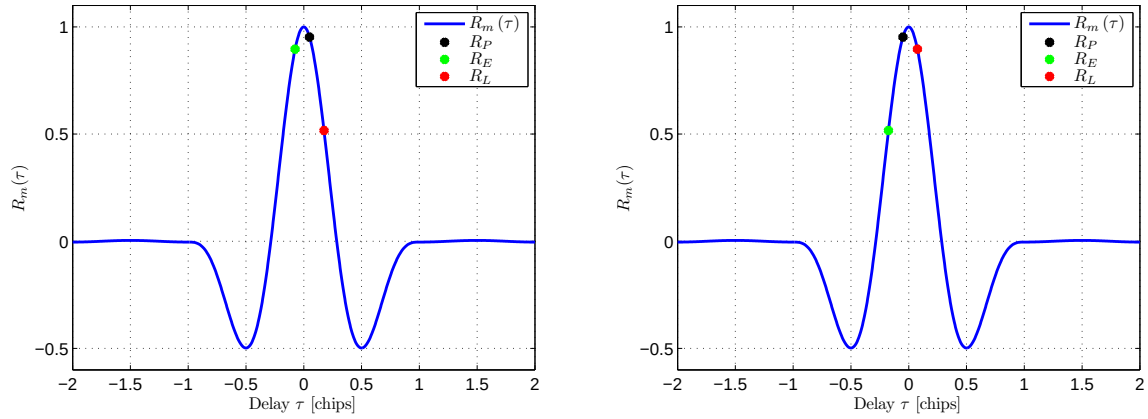

(a) −0.05 chips estimation error

(b) +0.05 chips estimation error

Figure 4.22: Normalized early and late samples for ideal input (multipath-free, noise-free) with ±0.05 chips estimation errors with $\Delta = 0.25$ chips

with different sign. This is the property used by the ELDLL to keep tracking of the estimation error and correct it.

The discriminator function $D_\Delta(t, \delta)$ is built by filtering the subtraction of the early and late outputs. This discriminator will take positive values when the estimation error is $(\tau_{\text{LOS}} - \hat{\tau}) < 0$, i.e., the estimated delay is higher than the actual delay and the prompt local replica is said to be 'late'. In this case, the early replica yields a higher value when correlated with the incoming signal. On the other hand, when the estimated delay is smaller than the actual delay, the estimation error is $(\tau_{\text{LOS}} - \hat{\tau}) > 0$, the prompt local replica would be 'early' and the delay of the late replica will be closer to that of the incoming signal, causing the discriminator to take negative values.

Assuming that the involved signals are ergodic, i.e., the time average of the loop filter equals the statistical one, the normalized discriminator output as a function of the normalized tracking error δ can be approximate to the subtraction of the early and late correlations

$$D_\Delta(t, \tau) = R\left(\tau + \frac{\Delta}{2}T_c\right) - R\left(\tau - \frac{\Delta}{2}T_c\right) \tag{4.37}$$

which, assuming again a multipath-free and noise-free input as modeled in equation (4.32), yields

$$D_\Delta(t, \tau_{\text{LOS}}, \hat{\tau}) = \sqrt{2P_{\text{LOS}}}\left[R_m\left(\tau_{\text{LOS}} - \hat{\tau} + \frac{\Delta}{2}T_c\right) - R_m\left(\tau_{\text{LOS}} - \hat{\tau} - \frac{\Delta}{2}T_c\right)\right] \tag{4.38}$$

which, expressed as a function of the normalized error δ

$$\delta = \frac{\tau_{\text{LOS}} - \hat{\tau}}{T_c} \tag{4.39}$$

and normalizing to the received amplitude, yields

$$D_\Delta(t, \delta) = \left[R_m\left(\delta T_c + \frac{\Delta}{2}T_c\right) - R_m\left(\delta T_c - \frac{\Delta}{2}T_c\right)\right] \tag{4.40}$$

this is, the subtraction of the early and late values of the expected signal autocorrelation.

Figure 4.23 shows the discriminator function for an early-late spacing of $\Delta = 0.25$ chips. The discriminator values associated to the estimation errors shown in figures 4.21, 4.22.a and 4.22.b are depicted.

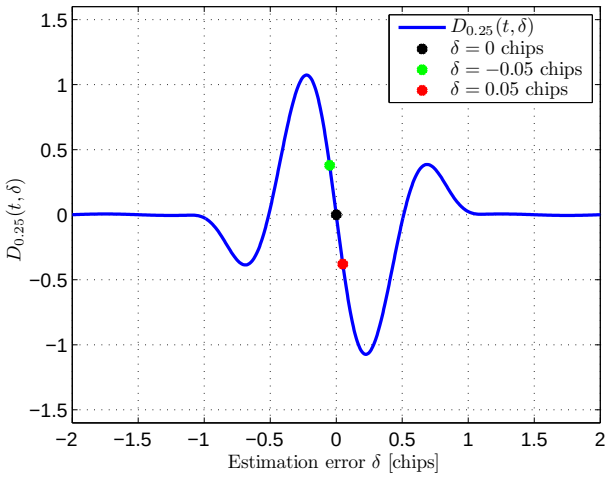

Figure 4.23: Normalized discriminator $D_\Delta(t,\delta)$ for ideal input (multipath-free, noise-free) with $\Delta = 0.25$ chips. Discriminator values for estimation error δ =[-0.05, 0, 0.05] chips

The shape of the discriminator is strongly dependent on the spacing Δ. The selection of an adequate spacing for the proposed system is addressed in section 4.3.1.1. Observing the examples, it is clear that the discriminator can be used as an error signal for the estimation, that can drive a feedback loop aiming at continuously driving this error to 0. The discriminator output drives the local replicas generator by correcting the delay applied to the generated signals. The estimated delay $\hat{\tau}$ is extracted from the current value of this delay. The loop filter applied to the early-late subtraction defines the loop bandwidth (W_L), thus the amount of error caused by noise and varying delays, by limiting the loop bandwidth as much as the system dynamics allow it.

The effect of non-idealities, such as the presence of noise, multipath and dynamic tracking errors, are modeled and validated next. The performance of the tracking stage is basically defined by the effect of noise and phase resolution on precision; and the effect of multipath and dynamic errors on accuracy.

The precision of the tracking estimate is affected by similar dominating phenomena than those conditioning the acquisition stage. This is, noise and local phase resolution. However, both effects must be considered differently. From the noise point of view, the error study is not based on CRLB, but on loop tracking variance analysis, strongly dependent on the discriminator function used as an error signal to close the loop. On the other hand, the effect of local phase resolution, though being similar to the acquisition stage in terms of reduction of precision, as analyzed in section 4.2.2, does not impose a trade-off with accumulated dynamic error is this case. This allows reducing its effect as much as HW resources allow it. This is an issue related to the practical implementation of the system, dependent on the particular HW platform, and will not be addressed in this work.

4.3.1 Effect of noise

The study of the effect of noise on the tracking jitter has been carried out following standard baseband DLL[2] analysis [Peterson et al., 1995]. These analyses are typically carried out in the RF context, for spread spectrum ranging and synchronization of communication systems, where the typical spreading signal is a PRN sequence. In this case, the analysis has been adapted to the discriminator $D_\Delta(t,\delta)$ formed by the signal defined for the proposed ranging architecture ($m(t)$).

The discriminator output in the presence of AWGN is explicitly analyzed here for the proposed signal structure. Once it is adequately characterized, the resulting tracking jitter yielded by linear loop analysis of the baseband DLL, that can be found in spread spectrum literature, will be applied considering the particular discriminator characteristics.

The resulting tracking jitter depends on the discriminator shape, defined by the early-late spacing. The tracking jitter is calculated as a function of this spacing to evaluate its influence. The effect of early-late spacing on multipath error is briefly discussed at the end of this section. Finally, taking into account the tracking jitter analysis and the impact on multipath error, an adequate early-late spacing value will be selected to provide a good balance between noise behavior and multipath rejection.

The received signal with power P_r in multipath-free conditions is

$$s(t) = \sqrt{2P_r}\, m(t - \tau_{\text{LOS}}) + n(t) \tag{4.41}$$

where $n(t)$ is an AWGN contribution bandlimited by the anti-aliasing filter to the optical channel bandwidth BW_{IR}, having two-sided power spectral density $N_0/2$.

Defining the output of the discriminator as $D(t, \tau_{\text{LOS}}, \hat{\tau})$ for this input, expressed as a function of time and the true and estimated delays in static conditions

$$D(t, \tau_{\text{LOS}}, \hat{\tau}) = \sqrt{2P_r} D_\Delta(t,\delta) + n_f(t) \tag{4.42}$$

where $D_\Delta(t,\delta)$ is the ideal normalized discriminator defined in equation (4.40), and $n_f(t)$ is the noise signal after the loop filter.

The jitter power caused by $n_f(t)$ can be calculated by integrating the noise power spectral density before the loop filter in the loop noise bandwidth W_L. The noise signal before the loop filter is

$$n'(t,\Delta) = n(t)\left[m\left(t - \hat{\tau} + \frac{\Delta}{2}T_c\right) - m\left(t - \hat{\tau} - \frac{\Delta}{2}T_c\right)\right] \tag{4.43}$$

The power spectrum of $n'(t)$ is calculated from its autocorrelation function. Considering $\hat{\tau}$ as a

[2]Delay-Locked Loop

random variable, $n^{'}(t)$ can be considered stationary and

$$\begin{aligned} R_{n'}(\tau,\Delta) =& E\left\{n(t)\,n(t+\tau)\left[m\left(t-\hat{\tau}+\frac{\Delta}{2}T_c\right)-m\left(t-\hat{\tau}-\frac{\Delta}{2}T_c\right)\right]\right. \\ &\left.\times\left[m\left(t+\tau-\hat{\tau}+\frac{\Delta}{2}T_c\right)-m\left(t+\tau-\hat{\tau}-\frac{\Delta}{2}T_c\right)\right]\right\} \end{aligned} \tag{4.44}$$

Since $n(t)$ is independent from the expected signal $m(t)$, the expected value can be factored as

$$\begin{aligned} R_{n'}(\tau,\Delta) =& E\left[n(t)\,n(t+\tau)\right]E\left\{\left[m\left(t-\hat{\tau}+\frac{\Delta}{2}T_c\right)-m\left(t-\hat{\tau}-\frac{\Delta}{2}T_c\right)\right]\right. \\ &\left.\times\left[m\left(t+\tau-\hat{\tau}+\frac{\Delta}{2}T_c\right)-m\left(t+\tau-\hat{\tau}-\frac{\Delta}{2}T_c\right)\right]\right\} \end{aligned} \tag{4.45}$$

The autocorrelation function of the input noise is a delta function whose amplitude is its power spectral density

$$E\left[n(t)\,n(t+\tau)\right]=\frac{N_0}{2}\delta(\tau) \tag{4.46}$$

Taking into account that the noise autocorrelation is zero for any $\tau \neq 0$

$$R_{n'}(\tau,\Delta)=\frac{N_0}{2}\delta(\tau)\left[2R_m(0)-2R_m(\Delta T_c)\right] \tag{4.47}$$

The two-sided power spectral density of $n^{'}(t,\Delta)$ is the Fourier transform of its autocorrelation, being

$$S_{n'}(f,\Delta)=\frac{N_0}{2}\left[2R_m(0)-2R_m(\Delta T_c)\right] \tag{4.48}$$

The tracking jitter obtained by linear baseband DLL analysis, easily found in spread spectrum literature [Peterson et al., 1995], can now be applied considering the calculated noise power spectral density. The variance of the normalized estimation error is

$$\sigma_\delta^2=\frac{S_{n'}(f,\Delta)\,W_L}{2K_d^2} \tag{4.49}$$

where W_L is the two-sided closed-loop noise bandwidth set by the loop filter, calculated as

$$W_L=\int_{-\infty}^{\infty}|H(j2\pi f)|df \tag{4.50}$$

where $H(s)$ is the closed-loop transfer function of the tracking loop; and K_d is the discriminator gain that depends on the signal power and the sensibility of the discriminator

$$K_d=\sqrt{\frac{P_r}{2}}\left.\frac{\partial D_\Delta(t,\delta)}{\partial\delta}\right|_{\delta=0} \tag{4.51}$$

This analysis is valid for values of δ around zero, when the estimation error is small, assuming the discriminator has a linear behavior in that range approximate to its slope in the origin.

Finally, undoing the normalization to the chip duration T_c, the tracking variance is

$$\sigma_{\hat{\tau}}^2 = T_c^2 \frac{S_{n'}(f,\Delta)\, W_L}{P_r \left(\frac{\partial D_\Delta(t,\delta)}{\partial \delta}\Big|_{\delta=0} \right)^2} \tag{4.52}$$

4.3.1.1 Early-late spacing

As can be seen in equation (4.52), both the sensibility of the discriminator $\frac{\partial D_\Delta(t,\delta)}{\partial \delta}\Big|_{\delta=0}$ and the noise power spectral density $S_{n'}(f,\Delta)$ depend on the selected early-late spacing Δ. Figure 4.24 shows various discriminators for different early-late spacings between 0.1 chips and 1 chip, where the variation of the discriminator slope with Δ can be clearly seen.

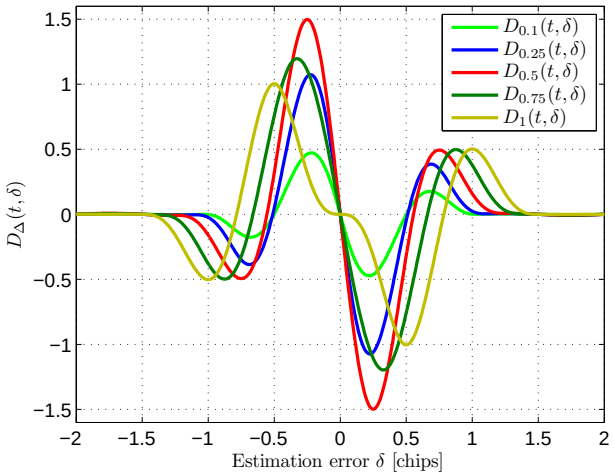

Figure 4.24: Normalized discriminators $D_\Delta(t,\delta)$ for ideal input (multipath-free, noise-free) for different early-late spacing (Δ)

The dependence of both the sensibility and transfered noise with Δ is shown in figure 4.25, where the noise power spectral density is normalized to the input noise power spectral density $N_0/2$.

The absolute value of the discriminator slope is maximum when Δ is approximately 0.42 chips. However, this spacing maximizes noise transfer in the loop, which is reduced for smaller spacings due to the higher correlation between noise components in the early and late outputs.

Figure 4.26 shows the tracking jitter as a function of Δ, calculated for a noise bandwidth W_L of 100 kHz, a chip-rate f_c of 25 MHz and a SNR of 75 dBHz, where SNR is defined as

$$\text{SNR} = \frac{P_r}{N_0/2} \tag{4.53}$$

As can be seen in figure 4.26, the value of Δ that minimizes tracking jitter is around 0.35 chips, although a stable low value is achieved between 0.1 and 0.6 chips.

Effect of early-late spacing on multipath error

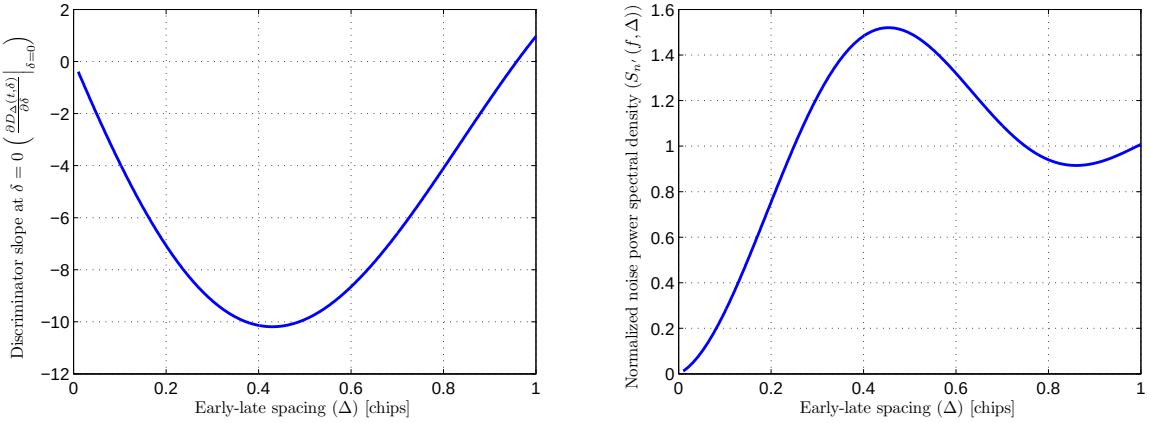

(a) Discriminator slope at $\delta = 0$ (b) Normalized noise power spectral density

Figure 4.25: Discriminator slope at $\delta = 0$ $\left(\frac{\partial D_\Delta(t,\delta)}{\partial \delta}\Big|_{\delta=0}\right)$ and normalized noise power spectral density $(S_{n'}(f,\Delta))$ as a function of early-late spacing (Δ)

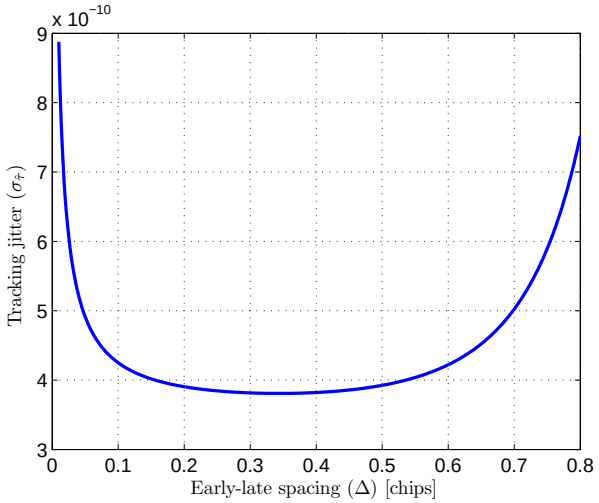

Figure 4.26: Tracking jitter $(\sigma_{\hat{\tau}})$ as a function of early-late spacing (Δ) (SNR=75 dBHz, W_L = 100 kHz, $f_c = 25$ MHz)

There is extensive literature on spread spectrum ranging based on similar early-late processing, mainly related to GNSS receivers. In this context it has been demonstrated that narrower correlation spacing yields higher multipath rejection [Van Dierendonck et al., 1992, McGraw and Braasch, 1999, Braasch and DiBenedetto, 2001]. Multipath error is studied in section 4.3.3, however, a simple simulation of the multipath error depending on the early-late spacing has been carried out, aiming at providing a qualitative confirmation that the tendency studied for RF spread spectrum ranging can also be applied to the proposed system. Figure 4.27 shows the simulated multipath error for a single multipath component with 10% the power of the LOS component, as a function of the delay between NLOS and LOS signals. Observing the figure, the tendendy of multipath error to increase with early-late spacing can be clearly appreciated.

Taking into account the tracking jitter analysis and the multipath error simulations, an early-late spacing of 0.25 chips is selected and considered from now on in the performance study.

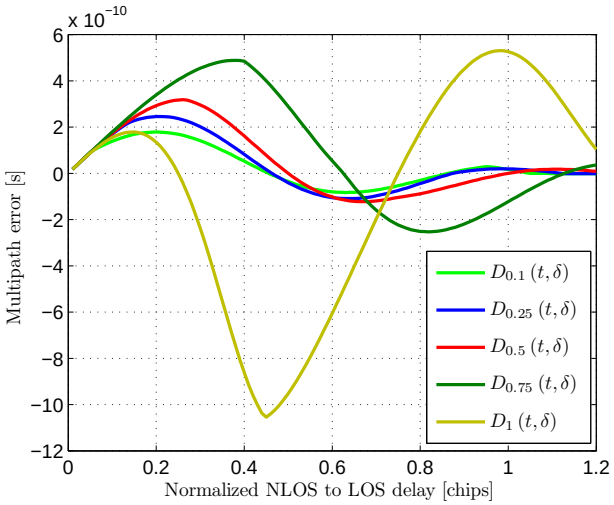

Figure 4.27: Simulated multipath error as a function of NLOS-to-LOS delay for different early-late spacings (Δ). NLOS component power is 10% of LOS component power

This value provides a good balance between noise behavior and multipath rejection while, being a simple fraction of a chip-time, presents little hardware complexity in the implementation of the corresponding delays.

Having selected an adequate value for the early-late spacing, the discriminator slope at the origin and the transfered noise power spectral density can be calculated for $\Delta = 0.25$ chips, yielding an expected tracking variance

$$\sigma_{\hat{\tau}}^2 = T_c^2 \frac{W_L}{64\text{SNR}} \tag{4.54}$$

4.3.1.2 Measured tracking jitter

The resulting tracking typical errors obtained from the theoretical analysis for a range of SNR between 60 dBHz and 95 dBHz and three different loop bandwidths are shown in figure 4.28. The theoretical results are compared with simulations using synthetic input signals and the digitized analog signals obtained from the IR link emulation (see 3.3.3.1), under the same SNR conditions and loop filter configuration in the Simulink model of the system.

The measured tracking jitter, both for simulated and digitized analog inputs, are very similar to the expected results. Higher differences can be observed for high SNR and low loop bandwidths since the noise related error in those cases is smaller. In these situations, other error sources such as the quantization effect of digitization and the time-discretization of the signals start showing a non-negligible effect compared to the noise-related source.

The expected tracking jitter for the signal quality limits defined in 3.1.3.1, where the SNR goes from 60 dBHz to 85 dBHz using a chip rate of 25 MHz, goes from 500 ps to 30 ps for a 10 kHz loop bandwidth. When higher loop bandwidths are selected to minimize total error due to more demanding dynamics (higher asynchronism), the achieved precision goes from 1.5 ns to 90 ps for 100 kHz bandwidth and 5 ns to 300 ps for 1 MHz bandwidth.

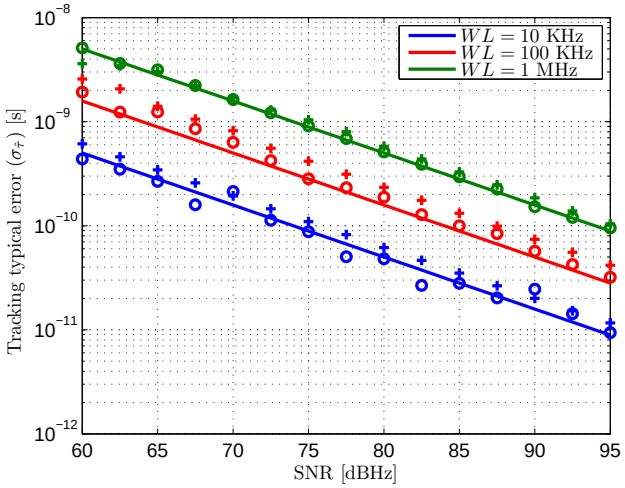

Figure 4.28: Tracking jitter caused by AWGN as a function of input SNR for different loop bandwidths (W_L). Theoretical (solid), simulation (crosses) and IR link analog emulation (circles) ($f_c = 25$ MHz)

4.3.2 Dynamic error

The dynamic error sources affecting the tracking stage are the same than those affecting the acquisition stage, analyzed in section 4.2.4 for a multipath-free scenario. These are the real displacement of the target where the emitter is boarded and frequency errors due to the lack of synchronization between emitter and receivers. The performance of the acquisition stage was severely limited by the accumulation of dynamic errors, given the relatively long of estimation process necessary to sweep all possible phase candidates. The tracking stage performance is, however, less affected by these dynamics than the acquisition stage, because the estimation process is much faster. The dynamics of the tracking stage are limited by the loop bandwidth, chosen as a trade-off between reducing noise and keeping a low probability of losing lock. A small loop bandwidth would reduce tracking jitter because of integrating a smaller noise bandwidth. However, its slow dynamic response would reduce the capacity of the tracking loop to follow variations in the input delay, increasing the possibility of losing lock because of reaching tracking errors outside the lock range of the discriminator.

Similarly to the calculations in 4.2.4, the maximum delay rate of change for the sum of the effect of target movement and frequency errors, considering the worst case in terms of sign of the variation, is

$$\Delta_\tau \approx \frac{V_{\text{target}}}{c} + 2\frac{\epsilon_{\text{CLK}}}{10^6} \tag{4.55}$$

The error of the closed-loop transfer function in tracking a linear delay variation whose slope is Δ_τ defines the dynamic error of the tracking stage. In the most simple case, if the loop filter is a simple first order low-pass with 3dB cut-off frequency f_h, the closed-loop transfer function is

$$H(s) = \frac{2\pi f_h K_d}{S + 2\pi f_h (1 + K_d)} \tag{4.56}$$

where K_d is the discriminator gain defined in (4.51).

The function defining the linear delay variation is

$$x_r(t) = \Delta_\tau t \tag{4.57}$$

and the estimated delay for this input considering the closed-loop impulse response is

$$y_r(t) = h(t) * x_r(t) \tag{4.58}$$

so the tracking error would be

$$\epsilon_{\hat{\tau}} = x_r(t) - y_r(t) \tag{4.59}$$

The input linear delay variation can be represented as the integral of the step function

$$u_s(t) = \begin{cases} 0 & \text{if } t < 0 \\ \Delta_\tau & \text{if } t > 0 \end{cases} \tag{4.60}$$

so that

$$x_r(t) = \int_0^t u_s(t)dt \tag{4.61}$$

The response of the tracking loop to that step function considering the closed-loop transfer function defined in (4.56) is

$$y_s(t) = \Delta_\tau \left(1 - e^{-t2\pi f_h(1+K_d)}\right) \tag{4.62}$$

and the response to the ramp function can be calculated as the integral of the step response as

$$\begin{aligned} y_r(t) &= \int_0^t y_s(t)dt \\ &= \int_0^t \Delta_\tau \left(1 - e^{-t2\pi f_h(1+K_d)}\right) dt \\ &= \Delta_\tau \left[t - \frac{1}{2\pi f_h(1+K_d)} \left(1 - e^{-t2\pi f_h(1+K_d)}\right)\right] \end{aligned} \tag{4.63}$$

When $t >> \frac{1}{2\pi f_h(1+K_d)}$, the exponential term becomes negligible and

$$y_r(t) \approx \Delta_\tau \left(t - \frac{1}{2\pi f_h(1+K_d)}\right) \tag{4.64}$$

so the tracking error is

$$\epsilon_{\hat{\tau}} = x_r(t) - y_r(t) = \frac{\Delta_\tau}{2\pi f_h(1+K_d)} \tag{4.65}$$

To provide an easier comparison with the noise-related results, the tracking error can be rewritten considering the noise bandwidth of the first order loop

$$W_L = \frac{\pi}{2} f_h(1+K_d) \tag{4.66}$$

yielding

$$\epsilon_{\hat{\tau}} = \frac{\Delta_\tau}{4W_L} \tag{4.67}$$

The dynamic error results used to validate the theoretical expected values are shown next. The dynamic error is measured indirectly due to hardware limitations of the test set-up. The phase modulation of the function generator used for generating the IR link emulation analog signal does not allow generating arbitrarily fine delay changes on the signals introduced in the processing architecture. Instead, delay steps of approximately 18 ps are introduced into the emitted signal with the adequate period to generate the average delay variations defined for the tests. The output of the system is obtained for this input signal with different loop filters. Since the closed-loop frequency response of the system is known to be of first order, the input and output signals are used to carry out a system identification in order to calculate the closed-loop cut-off frequency of the system. Finally, the identified value for every loop filter is used to calculate the tracking error applying (4.65), where the identified value would correspond to the theoretical closed-loop cut-off frequency $f_h\,(1+K_d)$. Figure 4.29 shows the input signal delay true value and the system outputs for different loop bandwidths when the introduced average delay rate of change is 1 μs/s.

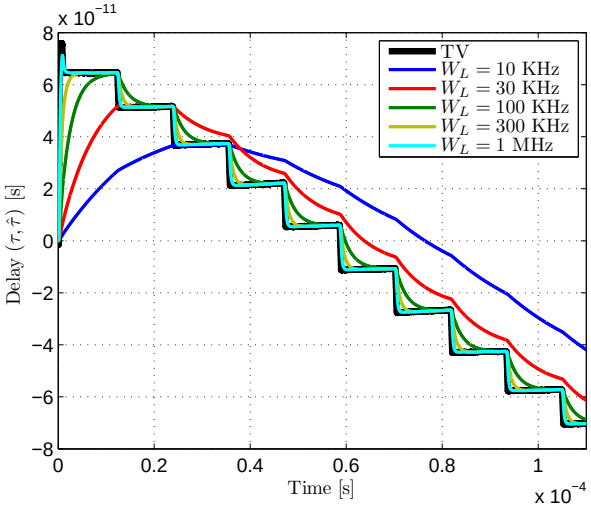

Figure 4.29: Delay true value and measured delay with different loop bandwidths for a delay rate of change (Δ_τ) of 1 μs/s

Figure 4.30 shows the tracking error as a function of loop bandwidth for two different delay rates of change. The theoretical results are shown in solid lines while the measured error for the bandwidths depicted in figure 4.29 are shown in circles.

The delay errors, measured indirectly by system identification of the known closed-loop cut-off frequency, agree with the theoretical expected results for the test values of Δ_τ. Slight differences can be observed for the highest rate of change, caused by higher inaccuracies in the faster phase modulation of the generated signals.

A practical value of the expected total delay rate of change was calculated in section 4.2.4.3. The delay variation is practically defined by the lack of synchronism between the emitter and receiver timing systems, imposing much more demanding dynamic constrains than the displacement of the target. The estimated delay rate of change for differential clock errors of 2ppm is 2 μs/s. The optimum loop bandwidth is chosen as a trade-off between noise filtering and dynamic effects. This optimum bandwidth, as well as as the dynamic and total error associated to it, is

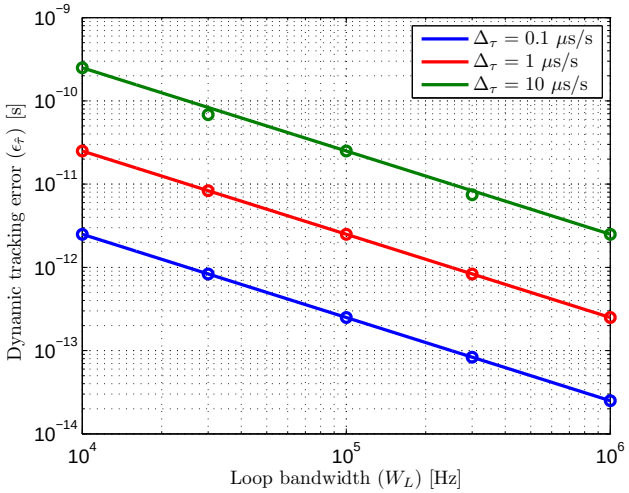

Figure 4.30: Dynamic error as a function of loop bandwidth (W_L) for two delay rates of change (Δ_τ). Theoretical (solid) and IR link analog emulation (circles) ($f_c = 25$ MHz)

calculated in section 4.3.4 for this expected delay rate of change and two other cases presenting more demanding dynamics (20 μs/s and 200 μs/s).

4.3.3 Multipath error

The basis of the delay tracking operation is the existence of an error signal, the discriminator output, that provides information about the delay estimation error, so it can be constantly corrected. In the previous sections, a multipath-free input was considered. Under these circumstances, after proper calibration of the constant delays imposed by the receiver circuitry, the discriminator value is zero when the delay error is zero, being a valid signal to correct the estimation. However, when multipath components are present in the input signal of the tracking loop, the discriminator output is modified by those, causing the discriminator zero-crossing to have an unknown offset in relation to the point where the estimation error $\tau_{\text{LOS}} - \hat{\tau}$ is zero. The magnitude of this error depends on the particular delays and power relations of all the components forming the incoming signal. These delays and power relations depend on the position of the target and the particular environment geometry and properties, causing, therefore, an unknown multipath error.

The multipath error has been studied by an analysis of the discriminator output in the presence of a NLOS component added to the LOS component. The zero-crossing point of the discriminator has been analyzed in the discriminator affected by multipath for different delays and power relations between both components. The resulting conclusions are then compared with simulations in the Simulink model of the receiver architecture, measuring the noise-free estimation error in the presence of an input signal subject to multipath.

For simplicity, one single multipath component has been considered in the theoretical study. The received signal affected by one multipath component is defined as

$$s(t) = \sqrt{2P_{\text{LOS}}}\, m\left(t - \tau_{\text{LOS}}\right) + \sqrt{2P_{\text{MP}}}\, m\left(t - \tau_{\text{MP}}\right) \tag{4.68}$$

With this input signal, the output of the early and late correlators, shown in equations (4.34) and (4.35) for multipath-free conditions, is formed by the addition of two versions of the expected signal autocorrelation for two different delays and powers. This correlations, applying the early-late spacing of 0.25 chips calculated in 4.3.1.1, are

$$R_E = \sqrt{2P_{\text{LOS}}} R_m \left(\tau_{\text{LOS}} - \hat{\tau} + \frac{T_c}{8} \right) + \sqrt{2P_{\text{MP}}} R_m \left(\tau_{\text{MP}} - \hat{\tau} + \frac{T_c}{8} \right) \tag{4.69}$$

$$R_L = \sqrt{2P_{\text{LOS}}} R_m \left(\tau_{\text{LOS}} - \hat{\tau} - \frac{T_c}{8} \right) + \sqrt{2P_{\text{MP}}} R_m \left(\tau_{\text{MP}} - \hat{\tau} - \frac{T_c}{8} \right) \tag{4.70}$$

The discriminator output formed by this early and late correlations is

$$\begin{aligned} D_{0.25}(t, \delta) = & \sqrt{2P_{\text{LOS}}} \left[R_m \left(\delta T_c + \frac{T_c}{8} \right) - R_m \left(\delta T_c - \frac{T_c}{8} \right) \right] \\ & + \sqrt{2P_{\text{MP}}} \left\{ R_m \left[(\delta + \delta_{\text{MP}}) T_c + \frac{T_c}{8} \right] - R_m \left[(\delta + \delta_{\text{MP}}) T_c - \frac{T_c}{8} \right] \right\} \end{aligned} \tag{4.71}$$

where δ is the estimation error $(\tau_{\text{LOS}} - \hat{\tau})$ normalized to T_c and

$$\delta_{\text{MP}} = \frac{\tau_{\text{MP}} - \tau_{\text{LOS}}}{T_c} \tag{4.72}$$

i.e., the normalized difference between NLOS and LOS delays.

The normalized multipath error ϵ_{MP} for some given P_{LOS}, P_{MP} and δ_{MP} is the value of δ in the linear region of the discriminator that makes

$$D_{0.25}(t, \delta)|_{\delta = \epsilon_{\text{MP}}} = 0 \tag{4.73}$$

Figure 4.31 shows the discriminator functions associated to a LOS path and a NLOS path, together with the composed discriminator formed by both. The optical power ratio between NLOS and LOS is 25% and the NLOS to LOS delay is 10 ns ($\delta_{\text{MP}} = 0.25$ chips at 25 MHz chip-rate). It can be seen how the zero-crossing point of the composed discriminator presents an offset compared to the multipath-free discriminator. This offset is the the normalized multipath error (ϵ_{MP}) caused by the NLOS path.

The multipath error has been computed using this model, considering the expression (3.51) for the autocorrelation calculated in 3.3.2.2. The amplitude of the multipath component has been set to different values between 1% and 50% of the LOS component amplitude, sweeping delays $(\tau_{\text{MP}} - \tau_{\text{LOS}})$ from 0.01 to 1.2 chips. The resulting errors are shown in figure 4.32. Observing the results, it can be seen that maximum multipath errors are caused by multipath to LOS delays around 0.25 chips, moving closer to 0.3 chips for stronger multipath components. The maxium error value, for a multipath power of 50% the LOS power, is a 6.5% of a chip duration, approximately 2.6 ns for a chip-rate of 25 MHz.

The achieved results based on the model have been compared for validation with simulations of the discriminator obtained by the addition of two signals with the selected relative powers and 6 different delay values from 0.2 chips to 1.2 chips. The results are shown in figure 4.33. The errors obtained by simulations are slightly higher than those yielded by the model for most

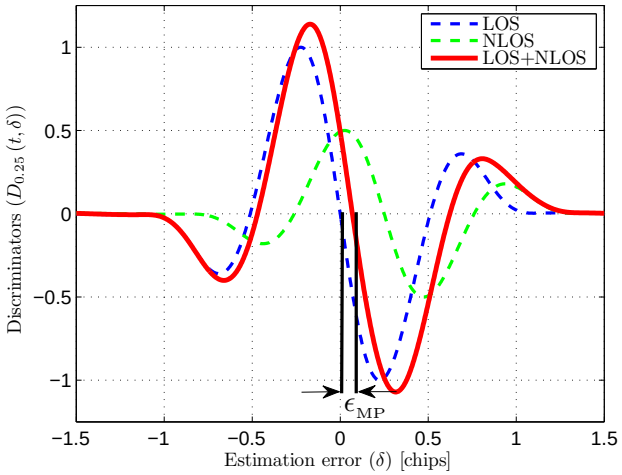

Figure 4.31: Discriminator functions associated to LOS, NLOS and composed signal (NLOS-to-LOS optical power ratio = 25%)

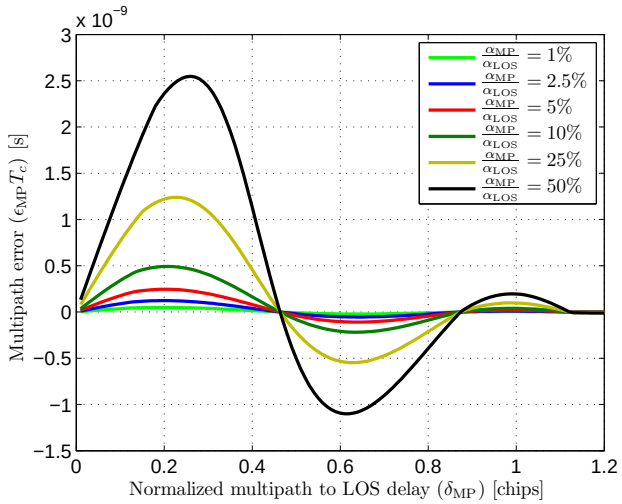

Figure 4.32: Multipath error ($\epsilon_{MP}T_c$) as a function of the delay between LOS and NLOS components for different relative amplitudes (f_c = 25 MHz)

delays; their dependency with magnitude and multipath-to-LOS delay, however, is reasonably similar between both results. The model will therefore be considered as a valid approximation to compute the expected multipath error in the tracking stage when one dominant NLOS component is present. Its validity to represent the behavior affected by multiple NLOS contributions will be checked in the results chapter in the tests where the diffuse multipath model is employed to generate the input signal affected by a high number of NLOS contributions.

4.3.4 Loop bandwidth

The dominant error sources affecting the tracking stage have already been defined and analyzed, comparing the theoretical expected errors with simulations and measurements using the set-up emulating the optical link. The precision of the estimated delay is defined by its behavior in the presence of AWGN, studied in section 4.3.1. The accuracy of the estimation, i.e., non-zero mean

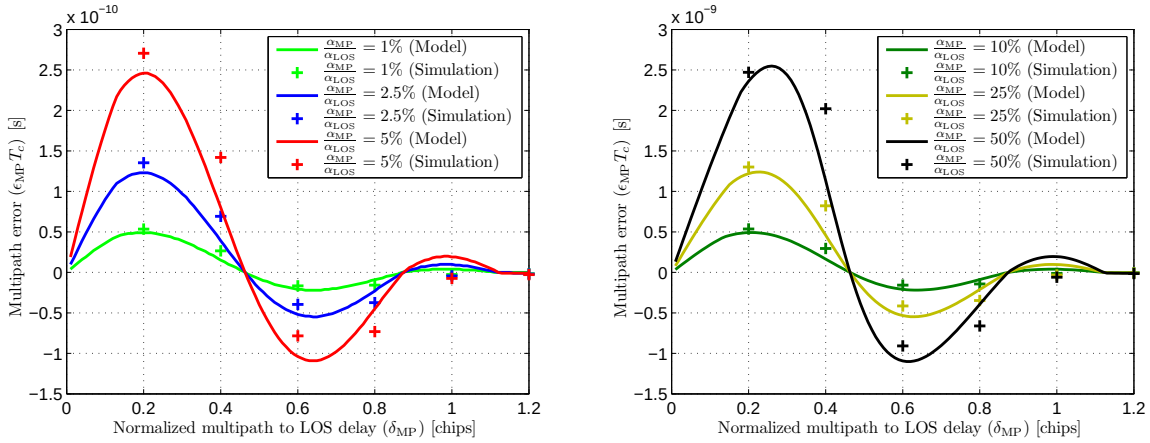

(a) $\frac{\sqrt{2P_{MP}}}{\sqrt{2P_{LOS}}} = (1\%,\ 2.5\%,\ 5\%)$ (b) $\frac{\sqrt{2P_{MP}}}{\sqrt{2P_{LOS}}} = (10\%,\ 25\%,\ 50\%)$

Figure 4.33: Multipath error ($\epsilon_{MP}T_c$) for different relative powers and delays between LOS and NLOS components, based on modeled discriminator (solid) and simulations (crosses)

errors that cannot be reduced by increasing observation time, is mainly affected by dynamic errors dominated by the lack of synchronism between emitter and receiver, analyzed in section 4.3.2, and the presence of multipath components in the input signal, studied in section 4.3.3.

The effect of multipath in relation to the DLL architecture basically depends on the chosen early-late spacing. Applying different correlator spacings changes the discriminator characteristics, and consequently the impact of multipath components on the estimation. As explained in section 4.3.1.1, the early-late spacing of 0.25 chips used in all the performance study has been selected taking into account the trade-off between multipath error and noise performance. Therefore, once the DLL architecture is defined, the multipath error does not impose any constrain related to the design parameters selection of the tracking stage, its magnitude being only dependent on the amount of multipath components present in the input signal, and their power and delay relations with the LOS component.

Considering this, the only trade-off in the system parameters is the selection of the adequate loop filter that defines the closed-loop bandwidth (W_L), linking noise-related errors and dynamic errors. Using a small loop bandwidth reduces integration of the noise spectra, yielding smaller estimation errors under certain input signal SNR. On the other hand, a small loop bandwidth has a poorer dynamic behavior, so the error in the tracking of varying delays, mainly due to clocks asynchronism, would be increased.

The tracking typical error in the presence of AWGN was analyzed in section 4.3.1, and its relation with the loop bandwidth W_L and input SNR is given by equation (4.54). The dynamic error was studied in section 4.3.2 and it is related with the loop bandwidth W_L and the expected delay rate of change Δ_τ by equation (4.66). Considering both contributions, the total typical error defined as the addition of the noise-related typical error (1σ) and the dynamic error is

$$\epsilon_T = \frac{T_c}{8}\sqrt{\frac{W_L}{\text{SNR}}} + \frac{\Delta_\tau}{4W_L} \tag{4.74}$$

The optimum W_L is the value that, for a given chip-rate under certain SNR and delay rate of change, minimizes the total error.

Calculating the extremes of the total error curve as a function of W_L

$$\frac{\partial \epsilon_T}{\partial W_L} = 0 \tag{4.75}$$

which is

$$\frac{T_c}{16}\sqrt{\frac{1}{W_L \cdot \mathrm{SNR}}} - \frac{\Delta_\tau}{4W_L^2} = 0 \tag{4.76}$$

yielding

$$W_L = \sqrt[3]{\frac{16\Delta_\tau^2 \mathrm{SNR}}{T_c^2}} \tag{4.77}$$

The total error as a function of input SNR and loop bandwidth is shown in figures 4.34, 4.35 and 4.36 for different delay rates of change. The minimum error for every SNR value is depicted in a red line. The error shown in 4.34 has been computed for variation of the delay of 2 μs/s, calculated as a maximum estimated value in section 4.2.4.3. This delay variation is dominated the by emitter-receiver lack of synchronism, calculated for a differential clock error of 2ppm over 25 MHz clocks. Figures 4.35 and 4.36 show the total error considering the master clocks of both systems would be 10 times and 100 times less accurate, yielding differential clock errors of 20ppm and 200ppm. These values define maximum delay rates of change of approximately 20 μs/s and 200 μs/s respectively.

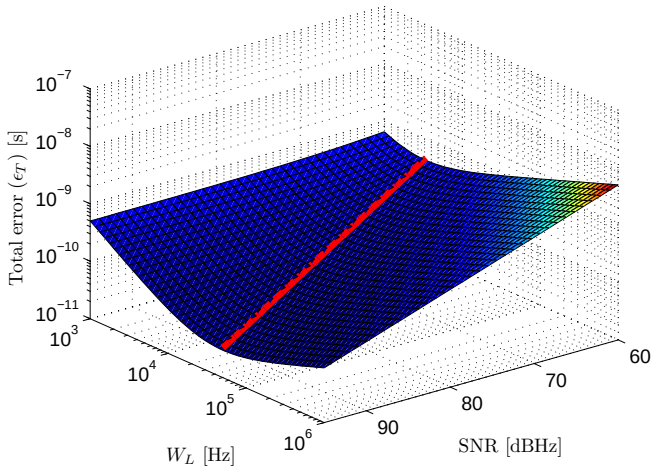

Figure 4.34: Total error and total minimum error (red) as a function of input SNR and loop bandwidth W_L for a delay rate of change Δ_τ of 2 μs/s

Observing the figures, it can be seen that when the loop bandwidth is too small, the error increases, dominated by dynamic effects, due to the slow response of the system. On the other hand, when the loop bandwidth is too large, the error is dominated by noise, since a higher amount of noise spectra is integrated in the loop, causing a very reduced noise filtering. The optimum value of the loop bandwidth for every SNR is higher when the delay rate of change is higher, as faster system dynamics are necessary to yield the same dynamic error, as shown in

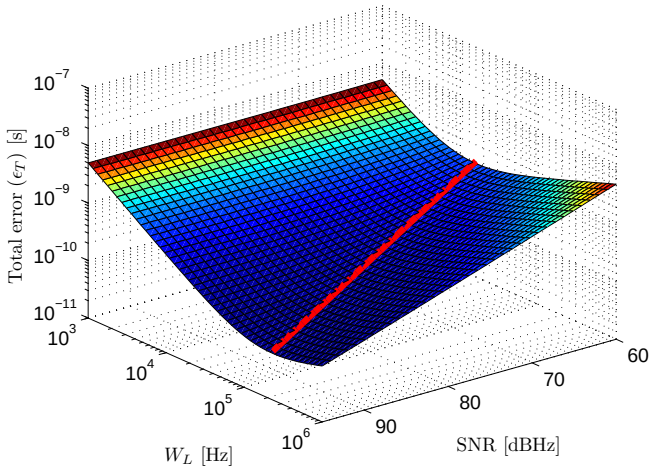

Figure 4.35: Total error and total minimum error (red) as a function of input SNR and loop bandwidth W_L for a delay rate of change Δ_τ of 20 μs/s

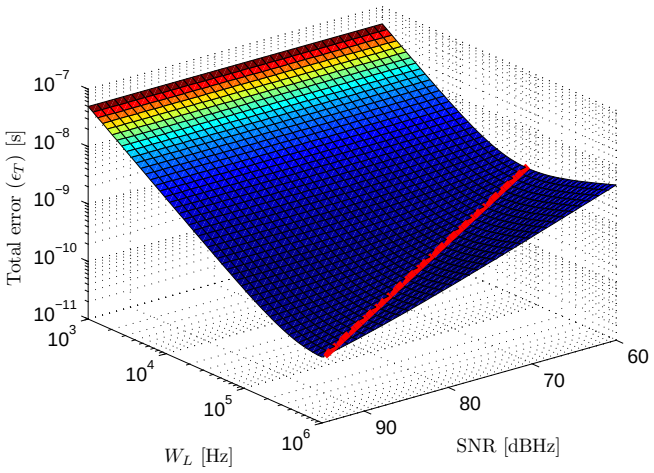

Figure 4.36: Total error and total minimum error (red) as a function of input SNR and loop bandwidth W_L for a delay rate of change Δ_τ of 200 μs/s

figure 4.30 of section 4.3.2.

The loop bandwidth that minimizes the total error for the three delay rates of change (Δ_τ = 2 μs/s, 20 μs/s, 200 μs/s) is shown in figure 4.37.

In a practical case, the selected value for W_L would be the one associated to the minimum expected SNR, in order to guarantee a maximum error level in all situations. Figure 4.38 shows the minimum error yielded by the optimum loop bandwidths as a function of SNR. Solid lines represent the error if the loop bandwidth is optimized for the 60 dBHz worst case SNR of the test IR link defined in 3.1.3.1. It can be seen that when SNR is increased the total error stops decreasing with it since it becomes dominated by dynamic effects. Dashed lines represent the minimum error that would be achieved for every SNR if the loop bandwidth was optimized to that particular SNR.

Under the assumption that the worst case SNR in the scenario is 60 dBHz, the loop filter

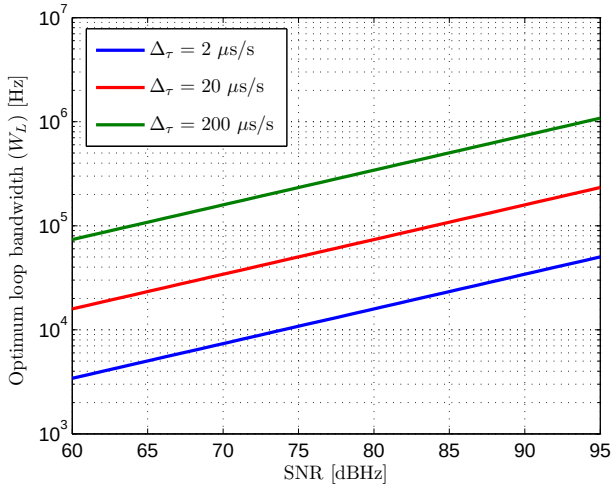

Figure 4.37: Loop bandwidth W_L that minimizes the total error ϵ_T as a function of input SNR for three different delay rates of change Δ_τ

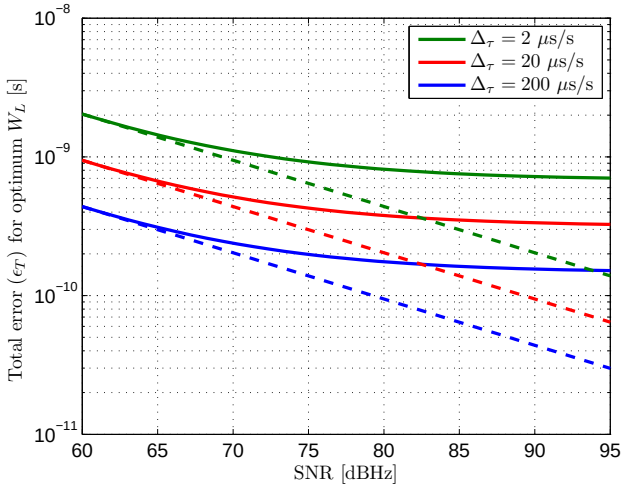

Figure 4.38: Total error ϵ_T for optimum loop bandwidth W_L as a function of input SNR for three different delay rates of change Δ_τ. Solid: Error with optimum bandwidth (3.5 kHz, 15 kHz and 70 kHz) for worst-case SNR (60 dBHz). Dashed: Error with optimum bandwidth for every SNR

should be defined so that the loop bandwidth is approximately 3.5 kHz if the expected maximum delay rate of change is 2 μs/s. This would yield a total typical estimation error, cause by both input noise and dynamic errors, of approximately 400 ps in the worst-case SNR. In case a higher clock error is assumed, expecting a delay rate of change up to 20 μs/s, the selected bandwidth would be approximately 15 kHz. In this case, the total typical error for the worst-case SNR would be approximately 950 ps. Finally, if the expected delay rate of change is 200 μs/s, a bandwidth of 70 kHz would be optimal, yielding a total error of approximately 2 ns. These total errors, considering a chip-rate of 25 MHz, correspond to an approximate 1%, 2.4% and 5% of a chip time.

The previous results represent the error considering the joint effect of noise addition in the input signal and tracking error of a varying delay. The multipath error, depending on the

particular situation and environment geometry and reflective properties, is added to this error, defining the total error of the delay estimation ($\hat{\tau}$) in the tracking stage.

As an example, let consider the worst results for the estimated multipath error shown in section 4.3.3. This particular multipath situation would add an error of approximately 2.6 ns to the previous results, increasing the total error a 6.5% of a chip time.

4.4 Summary and conclusions

The signal synchronization for the proposed ranging method has been analyzed in this chapter. The synchronization subsystem uses the correlation properties of the baseband received signal to provide a continuous estimation of its delay. This delay is used by the DSSS demodulator, explained in the next chapter, for partially-coherent demodulation of the received signal. The signal synchronization is performed by a delay acquisition stage whose output is used for locked-initialization of a delay tracking stage. The behavior of both stages affected by their main error contributions has been studied, and theoretical expressions of their expected performance have been derived and validated.

Unlike the phasemeter addressed in the next chapter, the signal synchronization provides a non-differential delay estimation. Due to this, the frequency errors caused by the emitter-receiver asynchronous operation are not canceled. The delay variation caused by these errors must be supported by the synchronization stages and considered as a source of dynamic error in the estimations. The rate of change of this delay, assuming emitter and receiver master clocks with an accuracy of 1ppm, is approximately 3 orders of magnitude faster than the true delay variation caused by target displacement up to 1 m/s. This makes frequency errors the dominant dynamic error source for signal synchronization.

The delay acquisition is based on a maximum search in the computed correlation after sweeping possible delay candidates for the received signal. The errors caused by noise, system dynamics and resolution of the delay sweep have been studied. The acquisition time has been calculated depending on the delay sweep resolution and length of the epochs of the received signal. The total error in the estimated delay, that depends on the acquisition time due to possible accumulated dynamic errors, is calculated. This value is used to optimize the epoch duration and sweep resolution so that adequate locking is guaranteed for the next stage for a given chip rate, target speed and minimum SNR level. Multipath effects do not affect this stage since the delay of the complete received signal, including multipath if present, is required for locking of the tracking loop.

The delay tracking is based on an ELDLL with narrow correlator spacing. The tracking loop provides fine tracking of the received signal delay using the feedback from the early and late correlations with an oversampled local replica to continuously correct the delay estimation. The effect of noise, system dynamics and multipath has been studied. The effect of the early-late spacing in the loop sensitivity and noise transfer has been analyzed. The study shows that the tracking jitter is minimum and of similar value for a spacing between 0.2 and 0.5 chips. On the other hand, extensive studies in GNSS multipath mitigation show that rejection rates are

higher for narrower correlator spacings, what has been proved by simulation with the proposed architecture and signals. An early-late separation of 0.25 chips has been selected as a good trade-off solution between tracking jitter, multipath rejection and implementation complexity for the local signals generator. The loop bandwidth has been optimized for balancing noise-related and dynamic-related errors. An expression of the optimum value has been derived as a function of the expected target speed and minimum SNR level for a given chip rate. This analysis concludes that a loop bandwidth of 3.5 kHz is adequate for tracking the aforementioned delay variations caused by asynchronism when the minimum expected SNR is 60 dBHz.

The contributions of this chapter have been published in [Salido-Monzú et al., 2014].

Chapter 5

Range estimation

This chapter is focused on the range estimation of the proposed system. The three stages that form this process are explained and analyzed to obtain and validate its theoretically expected performance, and to define the main design trade-offs.

The general architecture and functions of the range estimation are summarized in section 5.1. Sections 5.2, 5.3 and 5.4 are centered in its three different stages respectively: DSSS demodulation, phase measurement and differential range estimation. Their particular functions and operation are explained and modeled, validated through measurements with the test set-up.

5.1 Introduction

The ultimate goal of the ranging architecture is to provide an estimation of the differential distance between an emitter and two different receivers. The synchronization stage analyzed in 4 provides a delay estimation of the received signal. This estimation, affected by multipath components if present, is used by the DSSS demodulator to despread part of the power of the received signal into the narrow band of the sinusoidal modulation, where a phase measurement is carried out. The estimated phase, subtracted with an equivalent one from another receiver, is used to calculate the final differential distance, where cycle ambiguities of the phase-based measurement are solved using the delay tracked by the previous stage.

Figure 5.1 shows a simple diagram of the ranging architecture, containing the synchronization stage and the three processes addressed in this chapter:

- DSSS demodulation: This stage uses the estimated delay $\hat{\tau}$ to generate a local replica of the spreading sequence contained in the received signal. This local replica is used to demodulate the received signal S, despreading part of its power back to the original band of the sinusoidal modulation. The amount of despread power on the demodulated signal S' depends on the coherence of the demodulation process, i.e., the alignment between the delay of every component (LOS and NLOS) of the received signal and the local replica.
- Phasemeter: This stage carries out a phase measurement on the demodulated signal in a narrowband around the expected sine signal frequency. The phasemeter is formed by an

asynchronous I/Q demodulator and an arctangent estimation, outputting a low frequency signal $\hat{\phi}_i$ that contains the phase information. This signal is finally subtracted with an equivalent one coming from another receiver (ϕ_j) to obtain the differential estimated phase $\hat{\phi}_{ij}$.

- Differential range estimation: Finally, this stage converts the differential phase into the differential distance d_{ij} taking into account the sine signal frequency, and solves, if necessary, the cycle ambiguities of the phase measurement using the estimated delays $\hat{\tau}_i$ and $\hat{\tau}_j$.

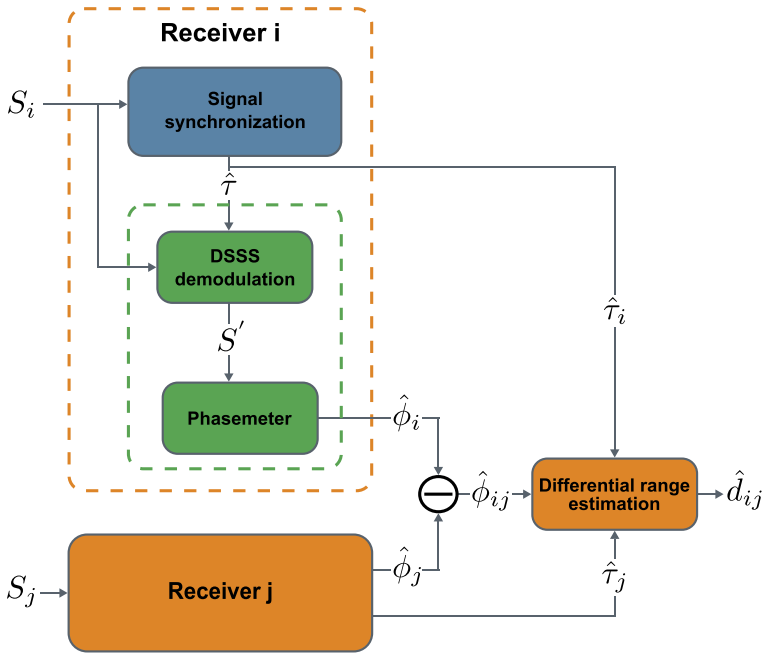

Figure 5.1: Simple diagram of a differential receiver architecture

5.2 DSSS demodulation

The function of the DSSS demodulation stage is to despread the power of the components in the received signal which are coherent with the estimated delay $\hat{\tau}$. Once $\hat{\tau}$ is available after the initial acquisition, a local replica of the spreading signal $c(t)$, whose phase is defined by $\hat{\tau}$, this is, $c(t-\hat{\tau})$, is generated. This local replica is multiplied with the received signal $s(t)$, outputting a partially despread version of it $\left(s'(t)\right)$. A diagram of this stage is shown in figure 5.2.

The ideal operation of this stage implies despreading all the power of the LOS component of the input signal, while keeping the multipath components power spread, so that its effect in the subsequent phase measurement on the sinusoidal modulation narrowband appears as a pseudorandom noise contribution, no longer causing multipath interferences. This ideal situation implies two conditions: 1) the estimated delay is error-free so that the local replica is perfectly aligned with the LOS component and an ideally coherent demodulation is applied to it and 2)

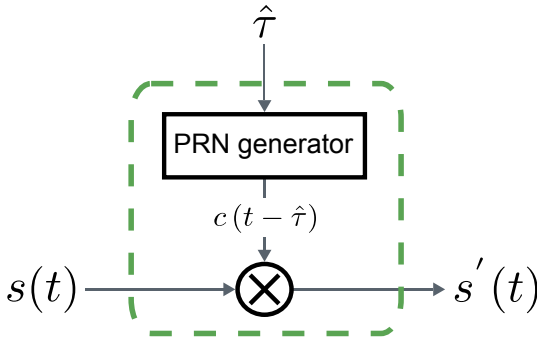

Figure 5.2: Diagram of the DSSS demodulation stage

all multipath components are delayed more than 1 chip in relation to the estimated delay so that a completely non-coherent demodulation is applied to them.

In any real situation, assuming the estimated delay error in relation to the LOS delay is smaller than 1 chip (a condition that will generally be fulfilled but in extremely severe multipath situations), only part of the power of the LOS component is despread. On the other hand, some multipath components whose delay in relation to the estimated delay is smaller than 1 chip are partially despread. In this case, taking input noise into account, the resulting demodulated signal in the band of interest of the phasemeter is formed, from a qualitative point of view, by 5 contributions:

- (1): A non-random contribution from the despread power of the LOS component, being the signal of interest.
- (2): A zero-mean pseudorandom contribution from the non-despread power of the LOS component, caused by the alignment error between its delay and the estimated delay.
- (3): A non-random contribution from the despread power of any multipath component whose delay in relation to the estimated delay is smaller than 1 chip, being the residual multipath interference for the subsequent measurement.
- (4): A zero-mean pseudorandom contribution from the non-despread power of the multipath components.
- (5): A zero-mean random contribution from the noise component of the input signal after demodulation.

The power relationships between these contributions define the performance of the subsequent phase measurement. The SNR in the band of interest around the sine signal frequency is defined by the relationship between the sum of the despread contributions (1) and (3) and the sum of the non-despread and noise contributions (2), (4) and (5), determining the variance of the estimation. On the other hand, the amount of multipath interference in the phase measurement is defined by the relationship between the despread LOS contribution (1) and the despread multipath contribution (3).

The amount of despread power for every component as a function of its error in relation to the estimated delay, as well as the effect of demodulation on the input noise, are modeled in the next section.

The despreading process of the sinusoidal signal power into its original band depending on the demodulation alignment is fundamental for the system operation, since both the adequate LOS signal recovery for measuring and the multipath rejection depend on it. The following figures show examples of this process for different significant delays between certain received component and the local PRN, computed for the signal parameters used in all the document, i.e., 25 MHz chip rate and sine frequency, and a channel bandwidth of 50 MHz. These examples are intended to show, in a qualitative approach, the consequences of different demodulation alignments on the resulting signal. The component referred in the figures as received signal could either represent a LOS component or a multipath component. In the first case, the despread power would belong to the contribution previously defined as (1), being the signal of interest. In the second case, if the examples are understood as referring to a multipath component, the despread power would belong to the contribution previously defined as (3), being an undesirable recovered contribution and remaining in the subsequent phase estimation as multipath power increasing the final error.

Figures 5.3.a show the signals involved in the demodulation process for an ideal alignment, i.e., when the error between the received component and the local reference is 0. The rest of the figures: 5.3.b, 5.3.c, 5.3.d, 5.3.e and 5.3.f, show the involved signals when the demodulation error is 0.2, 0.4, 0.6, 0.8 and 1 chip respectively. The top plot in all the figures represent a received component, depicted in blue, whose delay is equal for all the examples. The PRN in-phase PRN used to modulate the sine signal is also depicted in thin dashed red lines. The local reference for demodulation, whose delay changes in every figure from 0 to 1 chips, is also depicted in the top plot in thick red lines. The medium plot shows the resulting signal after demodulating with the corresponding delay, and the bottom plot show the power spectrum computed for this signal, where the effect of different demodulation errors on the amount of despread power can be clearly seen.

Observing the power spectra in all the figures, one can see how the despread power in the sine frequency band becomes smaller for higher demodulation errors up to 1 chip. In figure 5.3.a the alignment between the received signal and the local reference is perfect, and all the possible power is despread to the narrowband around 25 MHz. Note that an ideal sine signal recovery is not possible due to the distortion caused on the received signal by the bandwidth limitation of the optical channel. Observing the rest of the figures (note the scale reduction in the power spectrum plots), the reduction of despread power for higher alignment errors can be seen. All the power which is not folded back to 25 MHz is divided between a spread frequency distribution similar to the one of the original received signal, shown in the signal analysis section 3.3.2.2, and harmonics of the sine frequency at multiples of 25 MHz. The spread distribution can only be appreciated in the last two figures, 5.3.e and 5.3.f. 5.3.f shows the demodulation result when the alignment error is 1 full chip. As can be observed, most of the power maintains a spread spectrum distribution in this case, which is also the resulting behavior for any demodulation error higher than 1 chip.

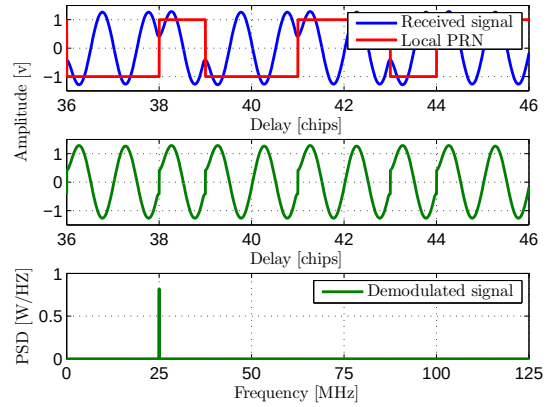

(a) $\hat{\tau} - \tau = 0$ chips

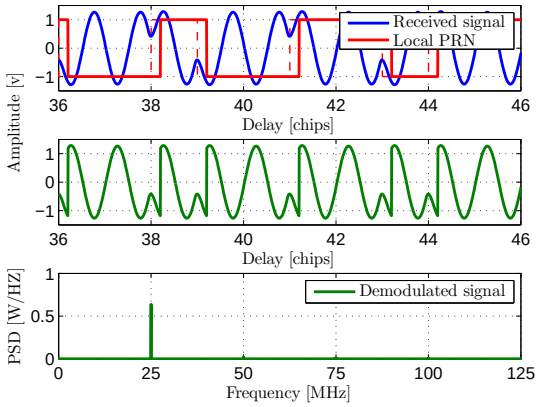

(b) $\hat{\tau} - \tau = 0.2$ chips

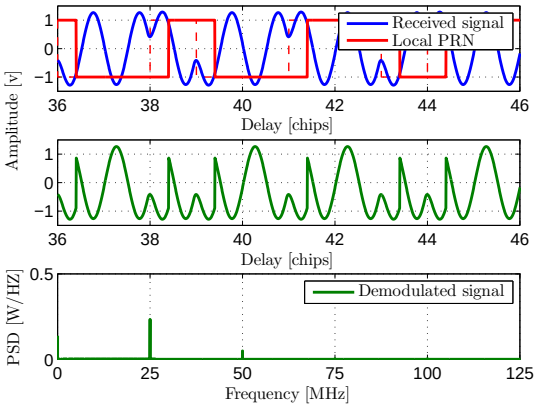

(c) $\hat{\tau} - \tau = 0.4$ chips

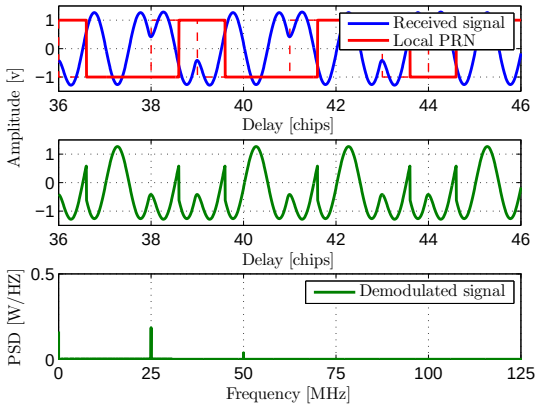

(d) $\hat{\tau} - \tau = 0.6$ chips

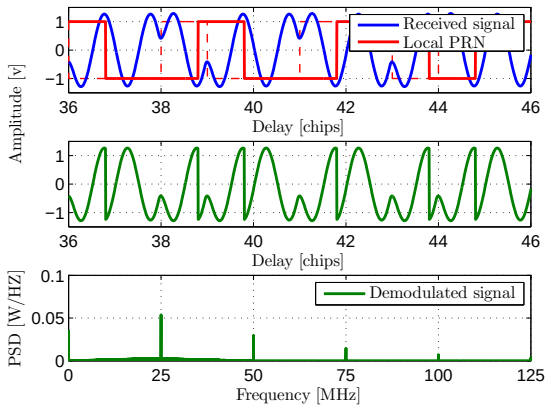

(e) $\hat{\tau} - \tau = 0.8$ chips

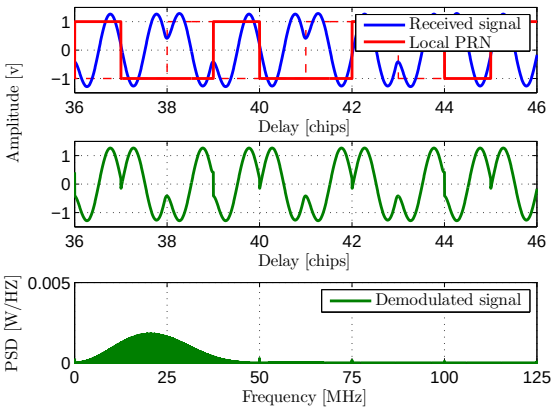

(f) $\hat{\tau} - \tau = 1$ chip

Figure 5.3: Signals involved in the demodulation process for different demodulation delays. Top: Received signal and local PRN, medium: demodulated signal, bottom: power spectrum of demodulated signal. (Input signal power before channel bandwidth limitation is 1 W)

5.2.1 Demodulation model

In an ideal multipath-free and noise-free situation, the received signal with delay τ_{LOS} is

$$s(t) = \sqrt{2P_{\text{LOS}}}m(t - \tau_{\text{LOS}}) \tag{5.1}$$

where P_{LOS} is the power of the LOS component and $m(t)$ is the normalized emitted signal formed by the sinusoidal signal $r(t)$ and the spreading signal $c(t)$, as defined in 3.3.2.1. The demodulated signal for this input is

$$s'(t) = \sqrt{2P_{\text{LOS}}}m(t - \tau_{\text{LOS}})\,c(t - \hat{\tau}) = \sqrt{2P_{\text{LOS}}}r(t - \tau_{\text{LOS}})\,c(t - \tau_{\text{LOS}})\,c(t - \hat{\tau}) \tag{5.2}$$

If there is no error in the delay estimated by the synchronization stage, i.e., $\hat{\tau} = \tau_{\text{LOS}}$

$$c(t - \tau_{\text{LOS}})\,c(t - \hat{\tau}) = 1 \tag{5.3}$$

and

$$s'(t) = \sqrt{2P_{\text{LOS}}}r(t - \tau_{\text{LOS}}) \tag{5.4}$$

this is, all the signal power is folded back to the sine signal frequency, meaning a perfect recovery of the sinusoidal signal.

In a real situation, when noise and an arbitrary number L of multipath components are present in the received signal and the estimated delay is also affected by both so that $\hat{\tau} \neq \tau_{\text{LOS}}$, the demodulated signal is

$$s'(t) = \left\{\sqrt{2P_{\text{LOS}}}m(t - \tau_{\text{LOS}}) + \sum_{i=1}^{L}\left[\sqrt{2P_{\text{MP}_i}}m\left(t - \tau_{\text{MP}_i}\right)\right] + n(t)\right\}c(t - \hat{\tau}) \tag{5.5}$$

where P_{MP_i} are the powers of the NLOS components, τ_{MP_i} are their corresponding delays, always higher than τ_{LOS}, and $n(t)$ is the composition of all noise contributions, defined as a zero-mean AWGN signal with variance σ_n^2.

The demodulated signal can be divided into three components, associated to the three components of the received signal: a LOS-related component, a sum of multipath-related components and a noise-related component. Replacing the emitted signal by the product of the sine signal $r(t)$ and the spreading sequence $c(t)$, and defining the demodulated noise

$$n'(t) = n(t)\,c(t - \hat{\tau}) \tag{5.6}$$

the demodulated signal is

$$\begin{aligned} s'(t) = {} & \sqrt{2P_{\text{LOS}}}r(t - \tau_{\text{LOS}})\,c(t - \tau_{\text{LOS}})\,c(t - \hat{\tau}) \\ & + \sum_{i=1}^{L}\left[\sqrt{2P_{\text{MP}_i}}r\left(t - \tau_{\text{MP}_i}\right)c\left(t - \tau_{\text{MP}_i}\right)\right]c(t - \hat{\tau}) \\ & + n'(t) \end{aligned} \tag{5.7}$$

Focusing on the noise contribution in the first place. The expected value of the demodulated noise $n^{'}(t)$ is

$$E\left[n^{'}(t)\right] = E\left[n(t)\, c(t-\hat{\tau})\right] \tag{5.8}$$

which can be factorized since the local replica is independent from the noise signal, yielding

$$E\left[n^{'}(t)\right] = E\left[c(t-\hat{\tau})\right] E\left[n(t)\right] = 0 \tag{5.9}$$

since the expected value of the NRZ spreading sequence is 0; and its variance

$$\sigma^2_{n'} = E\left[n^2(t)\, c^2(t-\hat{\tau})\right] - E\left[n(t)\, c(t-\hat{\tau})\right] = E\left[n^2(t)\right] = \sigma^2_n \tag{5.10}$$

since $c^2(t-\hat{\tau}) = 1$. So the mean and variance of the original input noise $n(t)$ are preserved.

Defining the generic product of the spreading sequence with different phases, where τ could either represent τ_{LOS} or τ_{MP_i}

$$g(t, \tau - \hat{\tau}) = c(t-\tau)\, c(t-\hat{\tau}) \tag{5.11}$$

and rewriting the demodulated signal

$$\begin{aligned} s^{'}(t) = {} & \sqrt{2P_{\text{LOS}}}\, r(t-\tau_{\text{LOS}})\, g(t, \tau_{\text{LOS}} - \hat{\tau}) \\ & + \sum_{i=1}^{L} \left[\sqrt{2P_{\text{MP}_i}}\, r\left(t-\tau_{\text{MP}_i}\right) g\left(t, \tau_{\text{MP}_i} - \hat{\tau}\right)\right] \\ & + n^{'}(t) \end{aligned} \tag{5.12}$$

$g(t, \tau - \hat{\tau})$ determine the amount of despread and non-despread power of every component. The amount of despread power in the sinusoidal modulation band is directly related to the power spectral distribution of $g(t, \tau - \hat{\tau})$ in the appropriate band.

The calculation of the power spectrum of $g(t, \tau - \hat{\tau})$ when the applied PRN is a MLS can be found in the literature [Peterson et al., 1995]. The final expression for the power spectrum is used here, being

$$\begin{aligned} |G(f, \tau - \hat{\tau})|^2 = {} & \left[1 - \left(1 + \frac{1}{N}\right) \frac{|\tau - \hat{\tau}|}{T_c}\right]^2 \delta(f) \\ & + \left(1 + \frac{1}{N}\right) \left(\frac{|\tau - \hat{\tau}|}{T_c}\right)^2 \sum_{n=-\infty}^{\infty} \text{sinc}^2\left(n \frac{|\tau - \hat{\tau}|}{T_c}\right) \delta\left(f - \frac{n}{T_c}\right) \\ & + \left(\frac{N+1}{N^2}\right) \left(\frac{|\tau - \hat{\tau}|}{T_c}\right)^2 \sum_{m=-\infty}^{\infty} \text{sinc}^2\left(\frac{m}{N} \frac{|\tau - \hat{\tau}|}{T_c}\right) \delta\left(f - \frac{m}{N T_c}\right) \end{aligned} \tag{5.13}$$

where n and m in the sums take all integer values except for 0.

This expression is valid for $|\tau - \hat{\tau}| \leq T_c$. When the delay is higher, the resulting signal $g(t, \tau - \hat{\tau})$ can be understood as the product of two different m-sequences, which is a spreading sequence itself. The specific power spectrum of this signal depends on the particular phase relationship between both sequences, but will generally keep a sinc shape distribution, which

will be approximate to the power spectrum of the original PRN (3.49), calculated in 3.3.2.2.

$$|G(f,\tau-\hat{\tau})|^2 = \left(\frac{N+1}{N^2}\right)\sum_{m=-\infty}^{\infty}\operatorname{sinc}^2\left(\frac{m}{N}\right)\delta\left(f-\frac{m}{NT_c}\right) \tag{5.14}$$

Figure 5.4 depicts the partial alignment $(\hat{\tau}-\tau)$, where C_k and C_{k-b} are the specific chips from the sequence, and $b=0$ when $(\hat{\tau}-\tau)\leq T_c$.

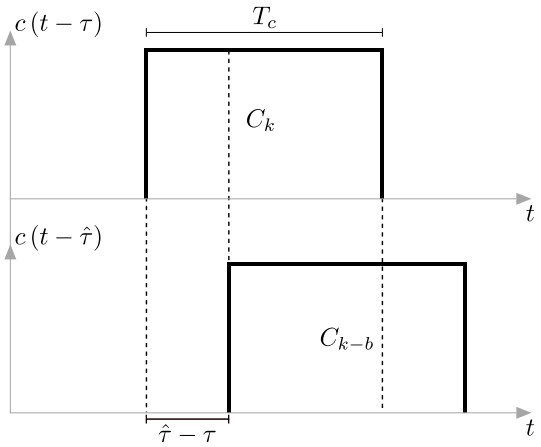

Figure 5.4: Definition of partial alignments between $c(t-\tau)$ and $c(t-\hat{\tau})$

The product of $g(t,\tau-\hat{\tau})$ with the sine signal $r(t-\tau)$, assuming unity power, shifts the previous power spectra to the sinusoidal modulation frequency $1/T_c$, yielding

$$\begin{aligned}
|R(f)*G(f,\tau-\hat{\tau})|^2 = \frac{1}{2}\Bigg\{ & \left[1-\left(1+\frac{1}{N}\right)\frac{|\tau-\hat{\tau}|}{T_c}\right]^2\delta\left(f-\frac{1}{T_c}\right) \\
& +\left(1+\frac{1}{N}\right)\left(\frac{|\tau-\hat{\tau}|}{T_c}\right)^2\sum_{n=-\infty}^{\infty}\operatorname{sinc}^2\left(n\frac{|\tau-\hat{\tau}|}{T_c}\right)\delta\left(f-\frac{1}{T_c}-\frac{n}{T_c}\right) \\
& +\left(\frac{N+1}{N^2}\right)\left(\frac{|\tau-\hat{\tau}|}{T_c}\right)^2\sum_{m=-\infty}^{\infty}\operatorname{sinc}^2\left(\frac{m}{N}\frac{|\tau-\hat{\tau}|}{T_c}\right)\delta\left(f-\frac{1}{T_c}-\frac{m}{NT_c}\right) \\
& +\left[1-\left(1+\frac{1}{N}\right)\frac{|\tau-\hat{\tau}|}{T_c}\right]^2\delta\left(f+\frac{1}{T_c}\right) \\
& +\left(1+\frac{1}{N}\right)\left(\frac{|\tau-\hat{\tau}|}{T_c}\right)^2\sum_{n=-\infty}^{\infty}\operatorname{sinc}^2\left(n\frac{|\tau-\hat{\tau}|}{T_c}\right)\delta\left(f+\frac{1}{T_c}-\frac{n}{T_c}\right) \\
& +\left(\frac{N+1}{N^2}\right)\left(\frac{|\tau-\hat{\tau}|}{T_c}\right)^2\sum_{m=-\infty}^{\infty}\operatorname{sinc}^2\left(\frac{m}{N}\frac{|\tau-\hat{\tau}|}{T_c}\right)\delta\left(f+\frac{1}{T_c}-\frac{m}{NT_c}\right)\Bigg\}
\end{aligned} \tag{5.15}$$

for $|\tau-\hat{\tau}|\leq T_c$, where, again, n and m in the sums take all integer values except for 0.

On the other hand, when $|\tau-\hat{\tau}|>T_c$

$$|R(f)*G(f,\tau-\hat{\tau})|^2 = \frac{1}{2}\left(\frac{N+1}{N^2}\right)\sum_{m=-\infty}^{\infty}\operatorname{sinc}^2\left(\frac{m}{N}\right)\delta\left(f-\frac{1}{T_c}-\frac{m}{NT_c}\right) \tag{5.16}$$

This power spectra, particularized on the narrowband of interest for the phase measurement

around the sinusoidal modulation frequency, defines the amount of despread power of the sine signal. Whether this despread power is desirable or not depends on the particular component under study being LOS or NLOS.

For a given received power P_r, corresponding to any LOS or NLOS component, the power of the despread sine signal $P_r^{'}$ corresponding to that component, after demodulating it with an error $|\tau - \hat{\tau}|$, is

$$P_r^{'} = P_r \left| R\left(f\right) * G\left(f, \tau - \hat{\tau}\right) \right|^2_{f=\frac{1}{T_c}} \tag{5.17}$$

When certain component is demodulated with $|\tau - \hat{\tau}| > T_c$, it does not contribute with any despread power to the phasemeter, and its contribution to the noise floor in the phase estimation is null due to the line component spectrum of the signal, approximate to (5.16). As shown in 3.3.2.2, the spectrum of the periodically repeated PRN modulated signal is not continuous but concentrates its power in line components separated $1/NT_c$, where N is the sequence length in chips. The measurement bandwidth of the phasemeter around the sine frequency is in the order of tens or hundreds of Hz, depending on the application speed requirements. In a worst case situation, which requires very high bandwidth estimations for tracking very fast targets, the final measurement bandwidth would not surpass 1 kHz, as will be seen in the end of this chapter in section 5.3.4. The code required for producing line components which could lie in this bandwidth would be 25000 chips long, when practical code lengths for an adequate system operation are of some hundreds of chips. It is, therefore, practically impossible that the demodulated signal power when $|\tau - \hat{\tau}| > T_c$ affects the phase estimation.

The demodulation of components with $|\tau - \hat{\tau}| \leq T_c$ is the situation of interest for this application, since this will generally be the case for the LOS component and the most critical multipath components. In this case, inspecting the resulting power spectrum in equation 5.15, three different contributions can be distinguished. The expression is formed by the addition of 6 different components, being actually 3 different components shifted by $\pm 1/T_c$:

- (A): The first and fourth components of the sum are deltas at the sine frequency $1/T_c$, which define the despread power that will be used by the phasemeter.
- (B): The second and fifth components of the sum are deltas at multiples of $1/T_c$, which are the distortion harmonics caused by the non-aligned demodulation that could be appreciated in the examples shown in figure 5.3.
- (C): The third and sixth components of the sum represent the residual spread distributed spectrum that increases its power for higher demodulation delays, having a similar appearance to the original spectrum formed by line components every $1/NT_c$.

The following figure 5.5 show computations of the modeled spectrum for different demodulation delays between 0.25 and 1 chips, where the three aforementioned components of the expression (5.15) (A, B and C) are depicted in different colors. the evolution of the three components as a function of the demodulation delay can be seen.

One can see how most of the power is concentrated in $\pm 1/T_c$ for small demodulation errors, meaning that most of the signal is despread to the sine frequency, while higher errors divide

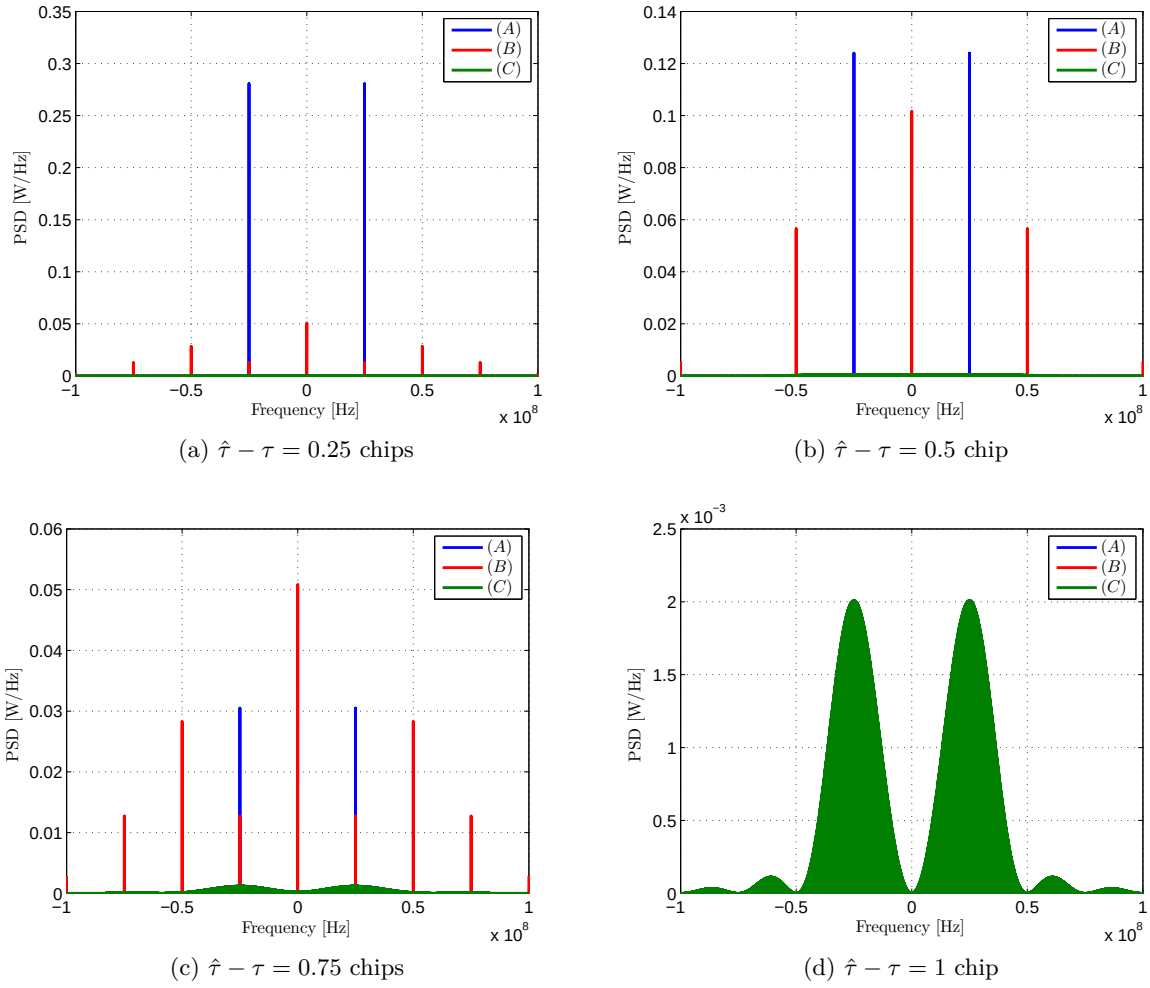

(a) $\hat{\tau} - \tau = 0.25$ chips

(b) $\hat{\tau} - \tau = 0.5$ chip

(c) $\hat{\tau} - \tau = 0.75$ chips

(d) $\hat{\tau} - \tau = 1$ chip

Figure 5.5: Modeled power spectrum of $R(f) * G(f, \tau - \hat{\tau})$ for two different demodulation delays. (Input signal power before channel bandwidth limitation is 1 W)

this power between other harmonics and the spread distribution, and the recovered power for the phase estimation is reduced. Note that the harmonics belonging to (B) centered in $-1/T_c$ interfere in the positive band of interest for the phasemeter centered in $1/T_c$ and vice versa, potentially introducing an error in the phase estimation associated to the demodulation delay. This error, however, has not been observed in the measurements and its deeper study is left for future works.

As defined in (5.17), the band of these spectra that will affect the phase estimation is that around the sine frequency at $1/T_c$, being 25 MHz. The modeled spectrum has been compared with simulations and emulations of the demodulation process for validation. Both digitally generated signals and analog signals from the IR-link emulation have been demodulated with different delays between ± 1 chips. The power of the demodulated signals has been measured in a band of ± 1 kHz around 25 MHz and compared with the results yielded by the model. These tests, alike the previous examples, have been performed using input signals of 1 W before the channel bandwidth limitation, which, as shown in 3.3.2.2, reduces the total signal power by approximately 0.5 dB when considering a first order channel response with -3dB cut-off

frequency in $2/T_c$.

Figure 5.6 shows the results of the test, compared to the recovered power given by the model in the band of interest.

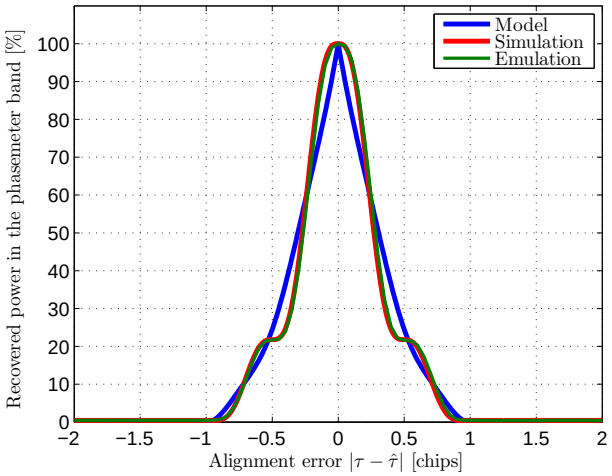

Figure 5.6: Rate of recovered power of the sine component as a function of alignment error $(\tau - \hat{\tau})$ (255 chips MLS, $f_c = 25$ MHz)

The results from the simulation and emulation test are very similar; they, however, show visible differences with the expected recovered power yielded by the theoretical model. These differences are very likely caused by the distortion introduced by the channel bandwidth limitation. The theoretical model, as can be seen in its derivation above, does not consider the distortion in the signal spectrum caused by the channel frequency response, but only takes into account its effect on the the total signal power. On the other hand, both the simulation and the emulation tests do introduce the filtering effect of the channel on the received signal, as it would occur in a real situation, causing a small distortion of the higher frequency components of the received signal which is very probably the reason behind the differences that can be seen in figure 5.6.

Although this effect is clearly visible, the consequences of applying the derived model in the total error model used for estimating the expected system performance is not very significant. The maximum deviation in the recovered power comparing the model with the measurements is smaller than 15% in the worst case. Taking into account the dependances of the system performance with power, derived in the study of the phasemeter in the next section, an error of that magnitude in the power estimation of certain component would imply an error smaller than 10% in any case regarding the calculations of both the precision in the presence of noise and the multipath error. Therefore, the demodulation model will be considered as a valid approximation to be used in the error model for comparing the measurements with the expected system performance in the results chapter of this work, and the inclusion of signal distortion in the model is postpone for future contributions on the system optimization in which a more accurate error model may be required.

For simplicity in the model used for the results, the expression of the recovered power in the

band around $1/T_c$ will be redefined as a function that depends on the demodulation error, being

$$F\left(|\tau-\hat{\tau}|\right)^2 = \left|R\left(f\right) * G\left(f,\tau-\hat{\tau}\right)\right|^2_{f=\frac{1}{T_c}} \tag{5.18}$$

for $|\tau-\hat{\tau}| \leq T_c$. This function, considering also the null effect for the phasemeter of the signals demodulated with delays higher than 1 chip, can be expanded to

$$F\left(|\tau-\hat{\tau}|\right)^2 = \begin{cases} \left|R\left(f\right) * G\left(f,\tau-\hat{\tau}\right)\right|^2_{f=\frac{1}{T_c}} & \text{if} \quad |\tau-\hat{\tau}| \leq T_c \\ 0 & \text{if} \quad |\tau-\hat{\tau}| > T_c \end{cases} \tag{5.19}$$

so that, in general, when the delay estimated by the synchronization stage is $\hat{\tau}$, the power recovered in the phasemeter band for a LOS component whose input power is P_{LOS_0} would be

$$P_{\mathrm{LOS}} = P_{\mathrm{LOS}_0} F\left(|\tau_{\mathrm{LOS}}-\hat{\tau}|\right)^2 \tag{5.20}$$

and, equivalently, the power recovered for a multipath component whose input power is P_{MP_0}, when demodulated with the same estimated delay $\hat{\tau}$, would be

$$P_{\mathrm{MP}} = P_{\mathrm{MP}_0} F\left(|\tau_{\mathrm{MP}}-\hat{\tau}|\right)^2 \tag{5.21}$$

This powers are used as inputs for the error model of the phasemeter regarding the effect of noise and multipath in the estimations. Note that the multipath mitigation capability of the system mainly relies on the demodulation process, which determines the attenuation applied to every received component before the phase estimation, hence the magnitude of its effect on the final measurement.

5.2.2 Effect of sampling rate

A deep study on the effect of sampling rate on the different processes that form the proposed architecture was not the goal of this thesis, aiming at reaching fundamental conclusions about the system feasibility by considering a continuous-time approach for simplicity in most of the analyses. The test system developed for the tests is, however, implemented in the digital domain for practical reasons. In most of the measurements the use of highly oversampled signals allowed a sufficient approximation to the continuous-time models as to achieve valid results. However, in some cases, due to hardware limitations of the test set-up, this is not possible and the effect of the signals discretization has to be considered for a proper understanding of the results yielded by those tests. This is the case of the effect of the discretized demodulation on the estimated phases. Due to the highly demanding computation required for the Simulink implementation of the system, it is not possible to use a high enough sampling rate as to neglect the digitization. Consequently, the impact of sampling on the final estimated phase has been briefly studied to allow a correct interpretation of the measurements in the results chapter.

The tests performed to evaluate the resolution limits associated to sampling rate in the demodulation are based on measuring the differential phase when the input signals delay is

varying linearly at the same speed for both receivers. The differential phase should stay constant since the delay speed of change is the same for both signals, however, this variation causes the tracking stage in every receiver to constantly update the delay used in the demodulation, so that varying demodulation delays are applied for every signal. This test has been performed in noise-free conditions with all-digital signals to avoid introducing any other effects, using different sampling rates in the input signals. The first results showed that the resolution in the measured phase also depends on the sampling rate used for generating the local PRN for demodulation, so this parameter was also introduced in the test for evaluation. Figure 5.7 shows an example of the measured phases for several differential phase true values when the local signals are generated with 1 GS/s and four different sampling rates are used in the input signals. Observing the figure, the phase steps caused by the discretized demodulation can be seen, as well as their dependence with sampling rate.

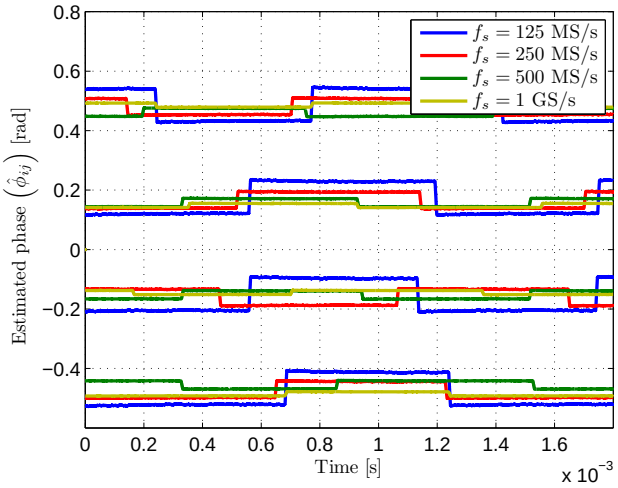

Figure 5.7: Example of measured phases with varying delay in both receivers for different sampling rates. Local PRN for demodulation is generated with $f_{s_{\text{local}}} = 1$ GS/s

The magnitude of theses steps has been measured and averaged for every combination of sampling rate and resolution of the local signal. The results are shown in figure 5.8.a, where the X-axis is the sampling rate of the input signal and every color corresponds to a different local PRN resolution. Note that local signal resolution is always equal or higher than the sampling rate, given that the former is the actual practical limitation. Increasing local signal resolution also implies the use of higher hardware resources, either in the memory or numerical controlled oscillator used for generating it. This is, however, generally much less demanding than increasing sampling rate in the digitizer. Figure 5.8.b shows the same results converted into distances for a more direct interpretation of the expected effects that will appear in the results chapter.

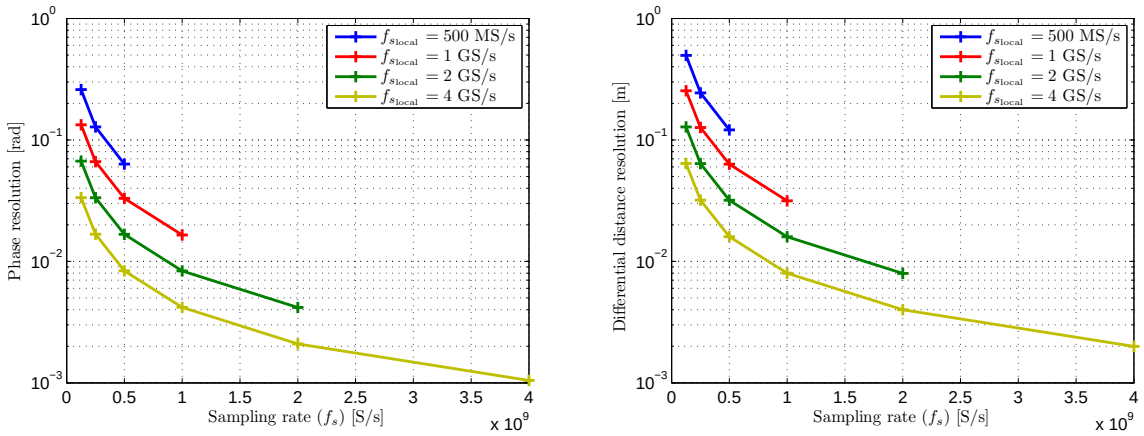

(a) Phase resolution

(b) Differential distance resolution

Figure 5.8: Phase and differential distance resolution due to discretized demodulation for different sampling (f_s) and local signal ($f_{s_{\text{local}}}$) rates

5.3 Phasemeter

This stage carries out a phase measurement on the demodulated signal $s^{'}(t)$ in a narrowband around the expected sinusoidal modulation frequency. The phasemeter is based on asynchronous I/Q demodulation and an arctangent estimator. Its output $\hat{\phi}$, subtracted with an equivalent one from another receiver, provides the differential phase estimation to be converted into a range difference.

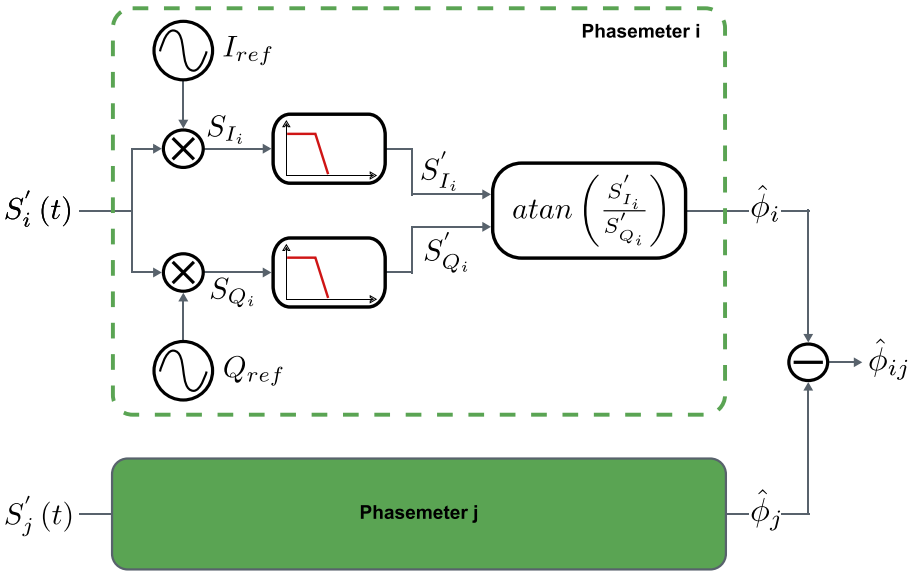

Figure 5.9: Diagram of the phasemeter

Figure 5.9 shows a diagram of the phasemeter. The demodulated signal in receiver i $\left(s_i^{'}(t)\right)$ is multiplied with the I and Q reference signals

$$\begin{aligned} I_{\text{ref}}(t) &= \cos(2\pi f_{\text{ref}} t) \\ Q_{\text{ref}}(t) &= \sin(2\pi f_{\text{ref}} t) \end{aligned} \tag{5.22}$$

generated with frequency $f_{\text{ref}} = f_r - \Delta_f$, with $f_r = 1/T_c$ being the true value of the sinusoidal modulation frequency of the received signal and Δ_f representing a small frequency deviation caused by the lack of synchronism between emitter and receiver.

Assuming a noise-free ideally despread input signal whose power is P_i and whose delay is τ_i in static conditions

$$s_i^{'}(t) = \sqrt{2P_i} r(t - \tau_i) = \sqrt{2P_i} \sin(2\pi f_r t + \phi_i) \tag{5.23}$$

where ϕ_i is $2\pi X$ with X being the fractional part of $\tau_i f_r$.

The product splits its power into two components, being the sum and subtraction of their frequencies.

$$\begin{aligned} s_{I_i}(t) &= \sqrt{\frac{P_i}{2}} \{\sin[2\pi\Delta_f t + \phi_i] + \sin[2\pi(2f_r - \Delta_f)t + \phi_i]\} \\ s_{Q_i}(t) &= \sqrt{\frac{P_i}{2}} \{\cos[2\pi\Delta_f t + \phi_i] - \cos[2\pi(2f_r - \Delta_f)t + \phi_i]\} \end{aligned} \tag{5.24}$$

which, after low pass filtering

$$\begin{aligned} s_{I_i}^{'}(t) &= \frac{\alpha_i}{2} \sin(2\pi\Delta_f t + \phi_i) \\ s_{Q_i}^{'}(t) &= \frac{\alpha_i}{2} \cos(2\pi\Delta_f t + \phi_i) \end{aligned} \tag{5.25}$$

Finally, applying the arctangent operator

$$\hat{\phi}_i(t) = \frac{s_{I_i}^{'}(t)}{s_{Q_i}^{'}(t)} = 2\pi\Delta_f t + \phi_i \tag{5.26}$$

which is a sawtooth signal between $\pm\frac{\pi}{2}$ whose slope $2\pi\Delta_f$ is defined by the frequency deviation between the input signal and the I/Q references. The expected slope is in the order of tens of Hz if 1ppm accurate clocks generating 25 MHz signals are used. The operation of ranging system is, however, independent from it, since the estimated phase coming from another receiver will be affected by the same frequency error, so that it will be canceled in the subtraction, yielding

$$\hat{\phi}_{ij}(t) = 2\pi\Delta_f t + \phi_i - 2\pi\Delta_f t - \phi_j = \phi_i - \phi_j \tag{5.27}$$

Figure 5.10 shows an example of these outputs when the input signals are noise-free and the frequency error in the reference signals is 50 Hz. The differential phase $\hat{\phi}_{ij}$, depicted in green, is the signal introduced into the differential range estimation stage to be filtered and converted into a differential distance.

5.3.1 Effect of noise

A model of the phase measurement in the presence of AWGN is developed and validated next to calculate the propagation of noise in the demodulated signal into the measured phase.

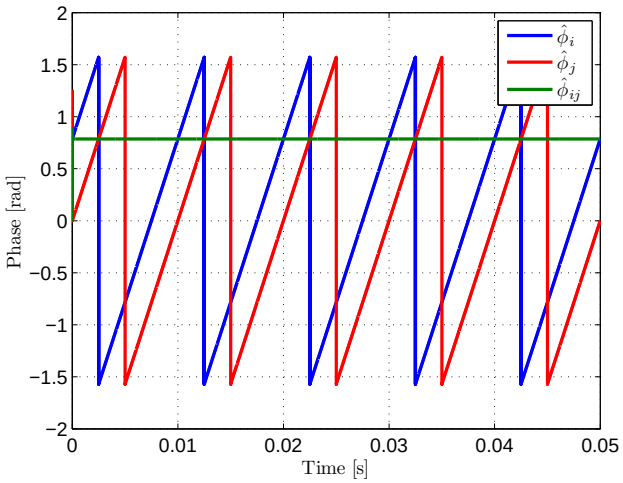

Figure 5.10: Noise-free single phase $\left(\hat{\phi}_i,\ \hat{\phi}_j\right)$ and differential phase $\hat{\phi}_{ij}$ outputs. $\phi_i - \phi_j = pi/4$ rad, $\Delta_f = 50$ Hz

Defining a demodulated signal in receiver i in static conditions whose despread power is P_i, containing an AWGN contribution $n_i(t)$ with double-side power spectral density $N_0/2$

$$s_i^{'}(t) = \sqrt{2P_i}\sin\left(2\pi f_r t + \phi_i\right) + n_i(t) \tag{5.28}$$

This noise contribution is essentially dependent on the noise contained in the input signal. The line spectrum of the non-despread components, as concluded in the demodulated signal study in section 5.2.1, does not contribute to any power increment in the phasemeter band for practical spreading sequence lengths.

The signals after the mixing with the references and filtering of the resulting high frequency components are

$$\begin{aligned} S_{I_i}^{'}(t) &= \sqrt{\frac{P_i}{2}}\sin\left(2\pi\Delta_f t + \phi_i\right) + n_i^{'}(t)\sin\left(2\pi f_{\text{ref}} t\right) \\ S_{Q_i}^{'}(t) &= \sqrt{\frac{P_i}{2}}\cos\left(2\pi\Delta_f t + \phi_i\right) + n_i^{'}(t)\cos\left(2\pi f_{\text{ref}} t\right) \end{aligned} \tag{5.29}$$

where $n_i^{'}(t)$ is the equivalent noise signal after low-pass filtering.

Defining the noise signal normalized to the amplitude of the signal component

$$n_{iN}^{'}(t) = \frac{n_i^{'}(t)}{\sqrt{P_i/2}} \tag{5.30}$$

and forming a signal composed by the I/Q components as

$$d_i(t) = e^{-j\left(2\pi\Delta_f t + \phi_i\right)} + n_{iN}^{'}(t)\, e^{j2\pi f_{\text{ref}} t} \tag{5.31}$$

The estimated differential phase for these composed signals, considering receivers i and j, is

$$\hat{\phi}_{ij}(t) = \angle[d_i(t)] - \angle[d_j(t)] = \angle\left[\frac{d_i(t)}{d_j(t)}\right] \tag{5.32}$$

$$\hat{\phi}_{ij}(t) = \angle\left[\frac{e^{-j\left(2\pi\Delta_f t+\phi_i\right)} + n_{iN}^{'}(t)\, e^{j2\pi f_{\text{ref}} t}}{e^{-j\left(2\pi\Delta_f t+\phi_j\right)} + n_{jN}^{'}(t)\, e^{j2\pi f_{\text{ref}} t}}\right] \tag{5.33}$$

$$\hat{\phi}_{ij}(t) = \angle\left[e^{j(\phi_i-\phi_j)}\frac{1 + n_{1N}^{'}(t)\, e^{j\left[2\pi\left(f_{\text{ref}}+\Delta_f\right)t+\phi_i\right]}}{1 + n_{jN}^{'}(t)\, e^{j\left[2\pi\left(f_{\text{ref}}+\Delta_f\right)t+\phi_j\right]}}\right] \tag{5.34}$$

$$\hat{\phi}_{ij}(t) = \phi_i - \phi_j + \Delta_{n_{iN}}(t) - \Delta_{n_{jN}}(t) \tag{5.35}$$

where

$$\begin{aligned}\Delta_{n_{iN}}(t) &= \angle\left[1 + n_{iN}^{'}(t)\, e^{j\left[2\pi\left(f_{\text{ref}}+\Delta_f\right)t+\phi_i\right]}\right]\\ \Delta_{n_{jN}}(t) &= \angle\left[1 + n_{jN}^{'}(t)\, e^{j\left[2\pi\left(f_{\text{ref}}+\Delta_f\right)t+\phi_j\right]}\right]\end{aligned} \tag{5.36}$$

Developing the expression of the noise residuals for every receiver

$$\Delta_{n_{iN}}(t) = \operatorname{atan}\left[\frac{n_{iN}^{'}(t)\sin\left[2\pi\left(f_{\text{ref}}+\Delta_f\right)t+\phi_i\right]}{1 + n_{iN}^{'}(t)\sin\left[2\pi\left(f_{\text{ref}}+\Delta_f\right)t+\phi_i\right]}\right] \tag{5.37}$$

which, considering noise instant values are much smaller than the unit, can be approximate to

$$\Delta_{n_{iN}}(t) \approx \operatorname{atan}\left[n_{iN}^{'}(t)\sin\left[2\pi\left(f_{\text{ref}}+\Delta_f\right)t+\phi_i\right]\right] \tag{5.38}$$

Approximating $\operatorname{atan}(x)$ to x, considering the argument is very small

$$\Delta_{n_{iN}}(t) \approx n_{iN}^{'}(t)\sin\left[2\pi\left(f_{\text{ref}}+\Delta_f\right)t+\phi_i\right] \tag{5.39}$$

Applying the same development for the residuals from receiver j, the estimated phase is

$$\hat{\phi}_{ij}(t) \approx \phi_j - \phi_i + n_{iN}^{'}(t)\sin\left[2\pi\left(f_{\text{ref}}+\Delta_f\right)t+\phi_i\right] - n_{jN}^{'}(t)\sin\left[2\pi\left(f_{\text{ref}}+\Delta_f\right)t+\phi_j\right] \tag{5.40}$$

Finally

$$\hat{\phi}_{ij}(t) \approx \phi_i - \phi_j + n_{iN}^{'}(t)\sin\left(2\pi f_r t+\phi_i\right) - n_{jN}^{'}(t)\sin\left(2\pi f_r t+\phi_j\right) \tag{5.41}$$

It can be observed that, as expected, if both noise contributions are completely correlated and both phase true values are equal, the error in the estimation is canceled.

Finally, the estimated phase typical error can be calculated as the sum of two independent

random variables weighted by the cosine functions as

$$\sigma_{\hat{\phi}_{ij}} \approx \sqrt{\frac{\sigma_{n_{iN}}^2}{2} + \frac{\sigma_{n_{jN}}^2}{2}} \tag{5.42}$$

where $\sigma_{n_{iN}}$ and $\sigma_{n_{jN}}$ are the standard deviations of the normalized noise signal defined in (5.30). Undoing the normalization

$$\sigma_{\hat{\phi}_{ij}} \approx \sqrt{\frac{\left(\frac{\sigma_n}{\sqrt{P_i/2}}\right)^2}{2} + \frac{\left(\frac{\sigma_n}{\sqrt{P_j/2}}\right)^2}{2}} = \sqrt{\frac{\sigma_n^2}{P_i} + \frac{\sigma_n^2}{P_j}} \tag{5.43}$$

where σ_n is the standard deviation of noise, considered equal in both demodulated signals $s_i^{'}(t)$ and $s_j^{'}(t)$, integrated in the measurement bandwidth. Calculating these standard deviation taking into account the noise power spectral density $N_0/2$ and the noise equivalent bandwidth (W_N) defined by the final filtering stage applied in the differential range estimation

$$\sigma_n = \sqrt{\frac{N_0}{2} W_N} \tag{5.44}$$

so the standard deviation of the final differential phase estimation can be approximate to

$$\sigma_{\hat{\phi}_{ij}} \approx \sqrt{\frac{\frac{N_0}{2}W_N}{P_i} + \frac{\frac{N_0}{2}W_N}{P_j}} \tag{5.45}$$

which, defining the demodulated signals SNR as

$$\begin{aligned} \mathrm{SNR}_i &= \frac{P_i}{N_0/2} \\ \mathrm{SNR}_j &= \frac{P_j}{N_0/2} \end{aligned} \tag{5.46}$$

yields

$$\sigma_{\hat{\phi}_{ij}} \approx \sqrt{W_N \left(\frac{1}{\mathrm{SNR}_i} + \frac{1}{\mathrm{SNR}_j}\right)} \tag{5.47}$$

It can be seen that the final approximation for the estimation typical error is related with the square root of the inverse of the combined SNR of both demodulated signals.

Figure 5.11 shows an example of the estimated single and differential phases for two different SNR combinations between both receivers. No filtering has been applied to the differential phase $\hat{\phi}_{ij}$ so the estimation bandwidth W_N is set in this case by the internal low-pass filter applied for removing the double frequency component of the mixing, defining a value for W_N of approximately 160 kHz.

The model for the phase measurement under AWGN has been validated with measurements on a digital implementation of the phasemeter using a high sampling rate so that the effect of digitization can be neglected in relation to the effect of input noise.

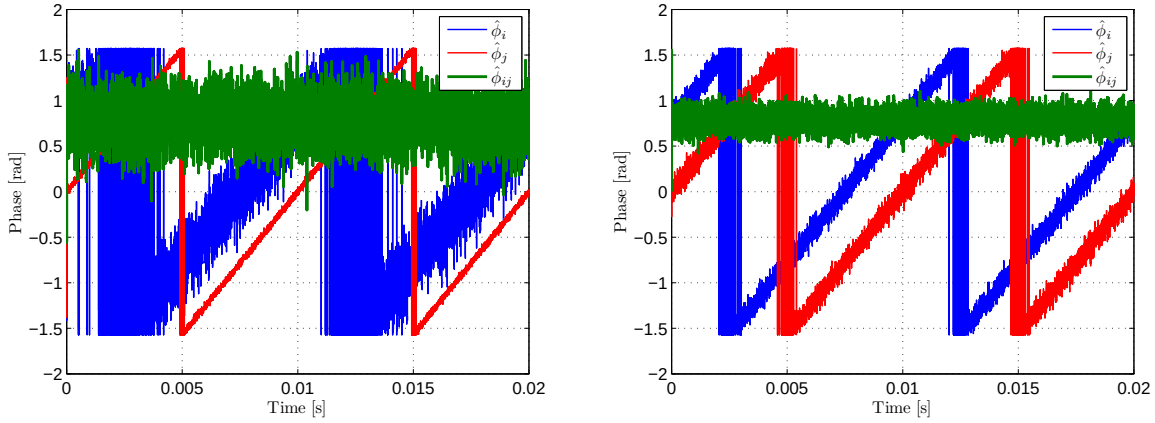

(a) $\text{SNR}_i = 65$ dBHz, $\text{SNR}_j = 85$ dBHz (b) $\text{SNR}_i = 75$ dBHz, $\text{SNR}_j = 75$ dBHz

Figure 5.11: Single phases $\left(\hat{\phi}_i,\ \hat{\phi}_j\right)$ and differential phase $\hat{\phi}_{ij}$. $\phi_i - \phi_j = pi/4$ rad, $\Delta_f = 50$ Hz, $W_N \approx 160$ Hz

Equally to the delay estimations addressed in 4, the phase measurement is subject to threshold effect. This defines a minimum SNR level so that there is enough signal information in relation to the noise level and the estimation provides a significant result. The model for the phase typical error developed above defines the theoretically expected behavior of the estimation above that minimum SNR level. Figure 5.12 shows the phase typical error and mean error as a function of SNR comparing the theoretical expected results with results from simulations. The SNR values correspond to one receiver while the input signal of the other receiver is noise-free. This way, the differential SNR if defined by the former one and equal to it.

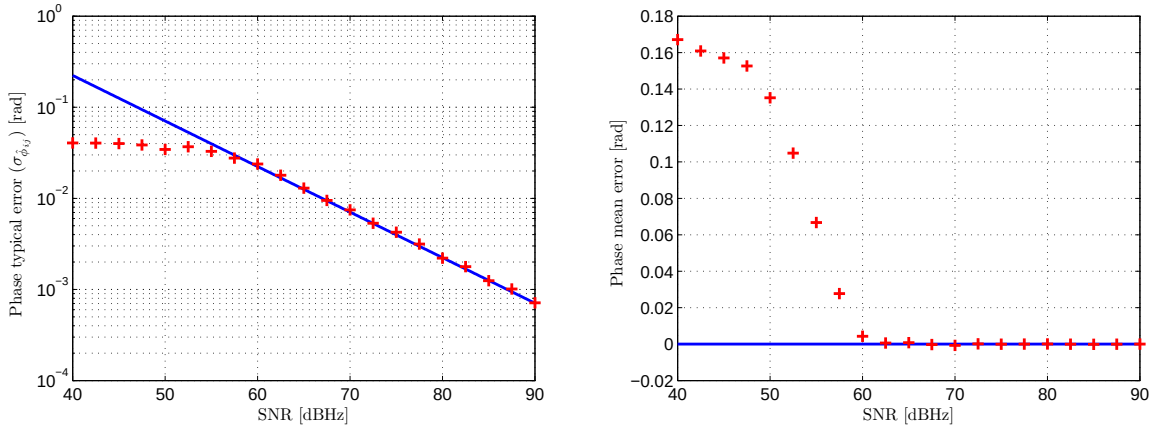

(a) Phase typical error (b) Phase mean error

Figure 5.12: Threshold effect. Phase typical $\left(\sigma_{\hat{\tau}_{ij}}\right)$ and mean error as a function of SNR. Theoretical (solid) and simulations (crosses) ($W_N = 500$ Hz)

As can be seen in the figure, a minimum SNR of approximately 60 dBHz is necessary for the phasemeter to provide a proper estimation. When SNR goes below 60 dBHz the mean error starts growing and the standard deviation of the estimation no longer relates to the theoretically expected value.

The theoretical values obtained with the model has been compared with the simulation results for three different W_N. The noise equivalent bandwidth is defined by the filtering stage applied over the final estimation. In the most simple case, implementing this filter as a first order low-pass with 3 dB cut-off frequency f_{LP}

$$W_N = \frac{\pi}{2} f_{\text{LP}} \tag{5.48}$$

The selected W_N used for validation are 1 kHz, 500 Hz and 250 Hz. Figure 5.13 shows the theoretical and simulation results as a function of the SNR of one of the input signals, while the other remains noise-free.

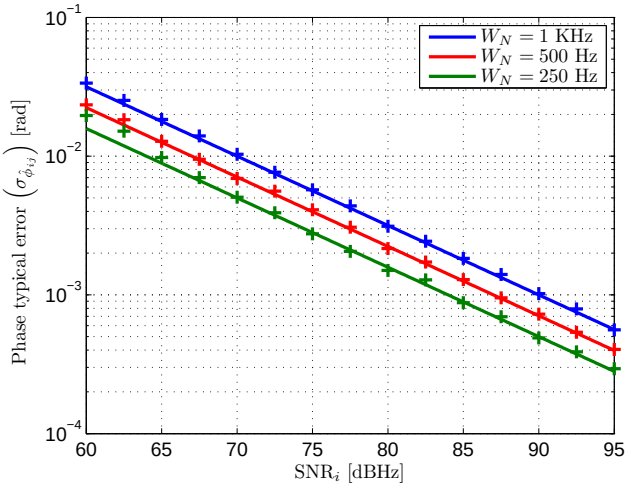

Figure 5.13: Phase typical error $\left(\sigma_{\hat{\tau}_{ij}}\right)$ for different noise equivalent bandwidths as a function of SNR of one input signal while the other input is noise-free. Theoretical (solid) and simulations (crosses)

Figure 5.14 shows the validation results in a more realistic situation, in which the SNR of every receiver depends on the position of the target. The test has been carried out defining complementary SNR levels in every receiver. This approximately represents a situation where the target is moving horizontally from one receiver to the other, i.e., when the SNR of one input signals is increased because of the target getting closer to it, the other is decreased in a related proportion.

As can be seen in the results, the model yields an adequate estimation of the phase typical error as long as the individual SNR level of every receiver is above 60 dBHz.

5.3.2 Multipath error

The phase error when the input signal is affected by multipath can be approximate to a multipath problem in standard PoA where the input components are the despread LOS and NLOS contributions, since the phase estimation is performed on a narrowband only affected the recovered sinusoidal power.

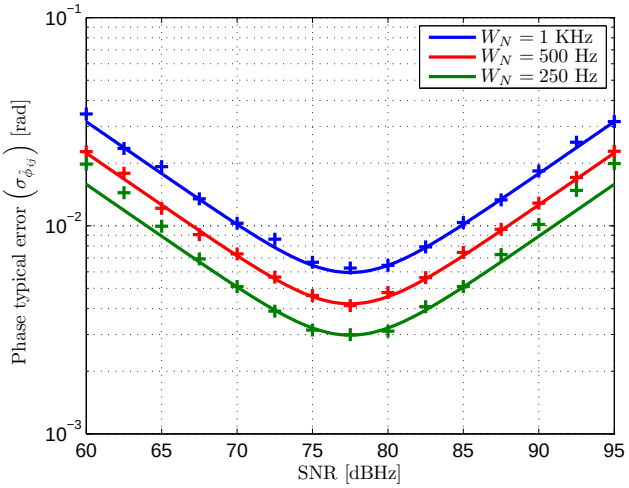

Figure 5.14: Phase typical error $\left(\sigma_{\hat{\tau}_{ij}}\right)$ for different noise equivalent bandwidths as a function of SNR of one input signal (SNR_i =[60 dBHz, 95 dBHz]) while the other input signal SNR is its complementary value (SNR_j =[95 dBHz, 60 dBHz]). Theoretical (solid) and simulations (crosses)

A noise-free demodulated signal in static conditions affected by L multipath components, defined by their respective powers $\left(P_{\text{LOS}},\ P_{\text{MP}_n}\right)$ and delays $\left(\tau_{\text{LOS}},\ \tau_{\text{MP}_n}\right)$, would be

$$\begin{aligned} s^{'}(t) &= \sqrt{2P_{\text{LOS}}}r\left(t-\tau_{\text{LOS}}\right)+\sum_{n=1}^{L}\left[\sqrt{2P_{\text{MP}_n}}r\left(t-\tau_{\text{MP}_n}\right)\right] \\ &= \sqrt{2P_{\text{LOS}}}\sin\left(2\pi f_r t+\phi_{\text{LOS}}\right)+\sum_{n=1}^{L}\left[\sqrt{2P_{\text{MP}_n}}\sin\left(2\pi f_r t+\phi_{\text{MP}_n}\right)\right] \end{aligned} \tag{5.49}$$

where the relationships between delays and phases are $\phi = 2\pi X$ with X being the fractional part of τf_r.

The total phase ϕ_T for this signal, i.e., the multipath-affected phase, can be obtained following the same derivation used in 3.2.2 for modeling the PoA multipath error, where the final expression for this phase as a function of the power and delay of each component is shown in equation (3.39). This total phase ϕ_T is the multipath-affected phase in one receiver. The multipath error in that receiver is the deviation of this phase to the original LOS phase ($\phi_T - \phi_{\text{LOS}}$).

The differential multipath error can be defined considering the errors for both receivers, being

$$\epsilon_{\hat{\phi}_{\text{MP}ij}} = \phi_{T_i} - \phi_{\text{LOS}_i} - \phi_{T_j} + \phi_{\text{LOS}_j} \tag{5.50}$$

The derived error for one receiver, considering a single multipath component, has been computed using the expression for the total phase ϕ_T in equation (3.39). The results have been compared for validation with measurements carried out for certain multipath phases with simulated input signals using the phasemeter implementation of the proposed architecture. The amplitude of the multipath component has been set to different values between 1% and 50% of the LOS component amplitude, meaning the multipath power is between a 0.01% and a 25%

of the LOS power. The phase difference between multipath and LOS components has been sweeped between 0 and 2π rad.

Figure 5.15 shows the resulting multipath errors, where the model results are shown in solid lines and the results with simulated inputs are represented with crosses. The strong agreement between both results is clear. It can be seen that the effect of multipath maximizes for phase differences which are close to $\pi/2$ rad and $3\pi/2$ rad when the relative multipath power is small, as can be seen in figure 5.15.a. However, when multipath power is a relevant fraction of the LOS power, as depicted in 5.15.b, the phase difference that maximizes the error gets closer to 2 rad and 4 rad, as can be seen in the 25% and 50% cases. The maximum error for the computed cases, yielded by a multipath component whose amplitude is a 50% of the LOS amplitude, when the phase difference is either 2.2 or 4.2 rad, is approximately 0.53 rad.

The model has been validated using one multipath component, however, it is also valid for multiple NLOS contributions as their joint effect can always be modeled as one single dominant component.

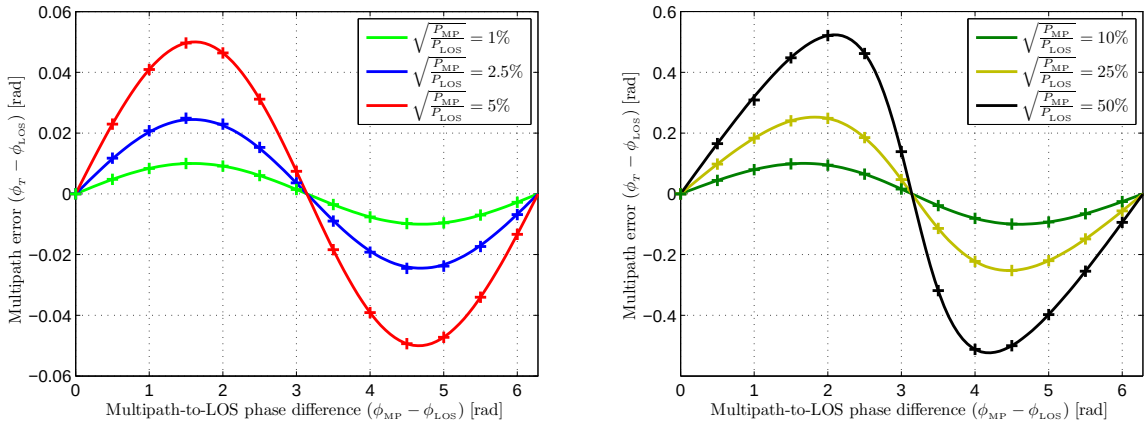

(a) $\sqrt{\frac{P_{MP}}{P_{LOS}}} = (1\%,\ 2.5\%,\ 5\%)$ (b) $\sqrt{\frac{P_{MP}}{P_{LOS}}} = (10\%,\ 25\%,\ 50\%)$

Figure 5.15: Multipath error ($\phi_T - \phi_{LOS}$) as a function of the phase difference between LOS and NLOS components for different relative amplitudes. Theoretical (solid) and simulations (crosses)

5.3.3 Dynamic error

The dynamic behavior of the phasemeter defines the final dynamic error of the ranging architecture. This behavior is defined by the output filter of the phasemeter, setting the final estimation and noise equivalent bandwidths.

The dynamic error sources that affect the phasemeter are the same affecting the synchronization stages addressed in chapter 4, this is, movement of the target and frequency errors between emitter and receivers caused by the lack of synchronism. The output of every single-phase

measurement in noise-free non-static conditions is

$$\begin{aligned}\hat{\phi}_i(t) &= 2\pi\Delta_f t + \phi_i(t) + \phi_{\text{CLK}}(t)\\ \hat{\phi}_j(t) &= 2\pi\Delta_f t + \phi_j(t) + \phi_{\text{CLK}}(t)\end{aligned} \tag{5.51}$$

where $\phi_i(t)$ and $\phi_j(t)$ are the time varying phases of each received signal depending on the variation of the target position and $\phi_{\text{CLK}}(t)$ is the phase variation caused by frequency errors.

The effect of frequency error does not cause any error in the differential phase estimation since it is common for both receivers, hence canceled in the subtraction

$$\hat{\phi}_{ij}(t) = \hat{\phi}_i(t) - \hat{\phi}_j(t) = \phi_i(t) - \phi_j(t) \tag{5.52}$$

The individual phase variations are defined considering a worst case in terms of speed of change of the received phase in the differential measurement. This situation implies a target moving at its maximum speed in the straight line joining two receivers. This situation is unreal because it would mean that the target moves in the horizontal plane where the receivers are placed. It is useful, however, to define a maximum dynamic error independently of the positioning cell configuration.

If the target changes its position at V_{target} m/s, moving closer to receiver i while moving away from receiver j, the differential phase is

$$\hat{\phi}_{ij}(t) = \phi_{i_0} + \frac{2\pi V_{\text{target}} f_r}{c} t - \phi_{j_0} + \frac{2\pi V_{\text{target}} f_r}{c} t \tag{5.53}$$

where ϕ_{i_0} and ϕ_{j_0} are the respective initial phases for receiver, f_r is the sinusoidal modulation frequency and c is the propagation speed of the optical signals, approximate to its propagation speed in vacuum ($3 \cdot 10^8$ m/s).

So the maximum differential phase variation that has to be tracked by the phasemeter is

$$\Delta_{\phi_{ij}} = \frac{4\pi V_{\text{target}} f_r}{c} \tag{5.54}$$

Considering the same practical values used in chapter 4, i.e., a maximum target speed of 1 m/s and a modulation frequency of 25 MHz, the differential phase variation would be approximately 1.05 rad/s.

Following the same development carried out in the dynamic error section for the delay tracking stage (4.3.2), the differential phase tracking error, assuming the output filter of the phasemeter is a first order low-pass with 3 dB cut-off frequency f_{LP}, is

$$\epsilon_{\hat{\phi}_{ij}} = \frac{\Delta_{\phi_{ij}}}{2\pi f_{\text{LP}}} = \frac{2 V_{\text{target}} f_r}{c f_{\text{LP}}} \tag{5.55}$$

For easier comparison with the noise-related results, the dynamic error can be rewritten considering the noise equivalent bandwidth W_N defined by the first order low-pass filter as

shown in (5.48), yielding

$$\epsilon_{\hat{\phi}_{ij}} = \frac{\pi V_{\text{target}} f_r}{c W_N} \tag{5.56}$$

The theoretical results has been compared with simulations with the digital implementation of the phasemeter. Input signal with time-varying phases have been introduced in the phasemeter and its output compared with the theoretical expected results. Figure 5.16 shows the output signals of the phasemeter, together with the differential phase true value, for different output filters, i.e., different noise equivalent bandwidths, when the phase rate of change is that of a target moving at 1 m/s in the configuration described above.

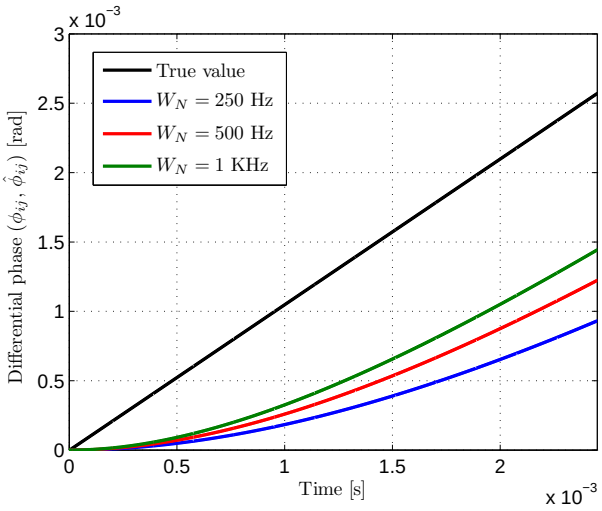

Figure 5.16: Differential phase true value (ϕ_{ij}) and measured phase $\left(\hat{\phi}_{ij}\right)$ as a function of time for different noise equivalent bandwidths (W_N) ($f_r = 25$ MHz, $V_{\text{target}} = 1$ m/s)

Figure 5.17 shows a comparison between the theoretical expected dynamic error and the measured error in the simulations. It can be seen that the simulation results strongly agree with the theoretical estimation.

5.3.4 Measurement bandwidth

The main design parameter that affects the phasemeter is the final measurement bandwidth W_N, which affect both noise-related and dynamics-related errors. A smaller bandwidth provides stronger noise filtering integrating less noise power in the estimation, however, it also makes the system time response slower, increasing dynamic errors when the target is moving.

Equivalently to the tracking-loop bandwidth selection in 4.3.4, the measurement bandwidth W_N is selected for balancing noise-related errors $\sigma_{\hat{\phi}_{ij}}$ and dynamic errors $\epsilon_{\hat{\phi}_{ij}}$. $\sigma_{\hat{\phi}_{ij}}$ links SNR and W_N, as defined in equation 5.47, while $\epsilon_{\hat{\phi}_{ij}}$ links target speed V_{target} and W_N.

Both errors are balanced by minimizing their multipath-free joint contribution, which has been defined considering one standard deviation of the noise-related error. This multipath-free total error is

$$\epsilon_T = \sqrt{W_N \left(\frac{1}{\text{SNR}_i} + \frac{1}{\text{SNR}_j} \right)} + \frac{\pi V_{\text{target}} f_r}{c W_N} \tag{5.57}$$

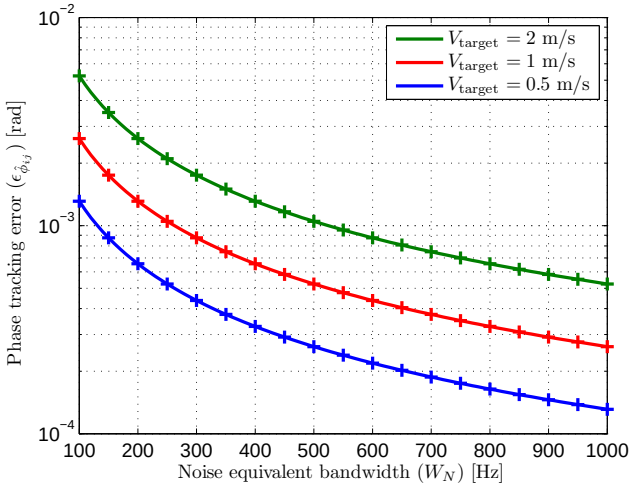

Figure 5.17: Dynamic error $\left(\epsilon_{\hat{\phi}_{ij}}\right)$ as a function of noise equivalent bandwidth (W_N) for different target speeds (different phase rates of change) (f_r = 25 MHz). Theoretical (solid) and simulations (crosses)

Figure 5.18 shows the total error as a function of the measurement bandwidth W_N for three different target speeds (0.5 m/s, 1 m/s and 2 m/s) and two different signal quality situations considering the SNR range defined in 3.1.3.1: the worst case for the combined SNR, this is, when the target is under one receiver and the SNR in the other one is minimum (SNR_i = 85 dBHz, SNR_j = 60 dBHz); and the best case for the combined SNR, this is, when the target is in the middle point between both receivers ($\text{SNR}_i = \text{SNR}_j$ = 75 dBHz).

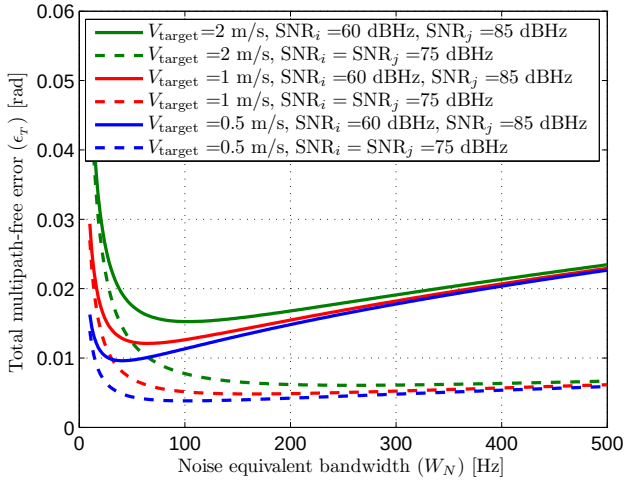

Figure 5.18: Total error as a function of noise equivalent bandwidth (W_N) for two different SNR values in both receivers

The figure shows how the optimum value for W_N depends on the target speed and specific SNR levels the system is operating with. When the combined SNR is higher, noise-contributions are smaller and a higher bandwidth is allowed for better tracking of varying phases. Equivalently, when the allowed target speed is smaller, system dynamics can be slower, thus allowing smaller bandwidths for increasing noise filtering.

The expression of W_N that minimizes the total error, defined as the addition of both contributions, is

$$W_N = \sqrt[3]{\frac{4\pi^2 V_{\text{target}}^2 f_r^2}{c^2\left(\frac{1}{\text{SNR}_i}+\frac{1}{\text{SNR}_j}\right)}} \tag{5.58}$$

In practical terms, the criterion for selecting the final bandwidth depends on the priorities defined for a particular application, penalizing either static or dynamic performance; however, it would be generally advisable to select a final bandwidth that balances both contributions in the worst case, i.e., when the combined SNR is minimum, as in the solid lines in figure 5.18. This would imply, for a maximum target speed of 1 m/s, setting W_N to approximately 60 Hz, what would yield a maximum total multipath-free error of approximately 1.2 cm.

5.4 Differential range estimation

The final differential range estimation stage carries out the conversion from phase to distance taking into account the wavelength of the sine signal, solves the ambiguities of the phase-based measurement and implements the final filtering stage of the estimation.

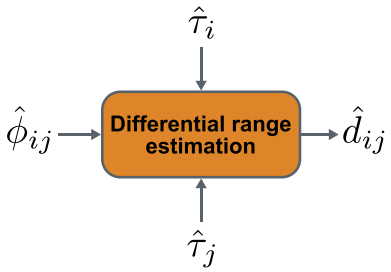

Figure 5.19: Diagram of the differential range estimation

The stage receives the differential phase $\hat{\phi}_{ij}$ and low pass filter it. This filter, as commented in section 5.3, sets the final measurement bandwidth and noise equivalent bandwidth, defining the system dynamic response and performance in the presence of AWGN. The estimated phase is then converted into distance by

$$\hat{d}_{ij} = \frac{c}{2\pi f_r}\hat{\phi}_{ij} \tag{5.59}$$

where c is the optical signal free-space propagation speed, approximate to its speed in vacuum ($3 \cdot 10^8$ m/s), and f_r is the sine signal frequency.

The phase-based measurement is based on an arctangent estimation, whose output is defined in $\pm\pi$ radians. When half of the wavelength defined by the sine signal frequency is smaller than the maximum differential range to be measured, cycle ambiguities occur in the differential phase estimation, since a phase difference of x radians produces the same output as any phase difference of $n\pi + x$ radians, with $n \in \mathbb{N}^*$.

This does not becomes an issue considering current practical IR links. A currently feasible link defines bandwidths in the order of tens of MHz and the spatial distribution of receivers to achieve good SNR levels implies differential ranges below 2.5 m. As a practical example, let

consider the up-to-date IR link defined in 3.1.3.1. A modulation frequency of 25 MHz sets a wavelength of 12 m, so that the maximum unambiguous range would be 6 m. The positioning cell defined for this link to achieve a minimum SNR level of 60 dBHz allows placing the receivers 3.7 m apart from each other and 2.15 m above the horizontal target place. In this configuration, the maximum distance to a receiver is 4.28 m, and the maximum differential range is 2.13 m, well below the half wavelength of the sine signal. However, as optical devices technology increases, higher bandwidths can be reached to increase precision, setting smaller wavelengths hence smaller unambiguous ranges. At the same time, the increase in transmitted power allows defining larger positioning cells, where the maximum differential ranges are increased. Under this circumstances, the ambiguities can be solved using the information of the estimated delays in the synchronization stage. The unambiguous range of this estimations are defined by periodicity of the spreading sequences, i.e., their frame periods. Even if small frame periods are used, the unambiguous range of the delay estimations are much larger than those of the phase-based measurement. As an example, let consider a very small PRN of 15 chips with a chip-rate of 25 MHz. The periodicity of this estimation is 600 ns. This periodicity defines an unambiguous range of 180 m, in contrast to the 6 m of the phase measurement.

5.5 Summary and conclusions

In this chapter, the DSSS demodulation stage and the phasemeter that extracts the differential phase information for ranging have been addressed. The DSSS demodulator uses the information from the estimated delay, provided by the synchronization subsystem (addressed in the previous chapter), to partially despread the power of the received signal. The delay estimated by the previous stage is, except for very severe multipath situations, closer to the LOS delay than to any NLOS delay, so the demodulation provides enhancement of the LOS-NLOS power ratio in the despread signals in most situations. The phasemeter operates in a narrowband where only the despread power is contained, therefore, multipath error is reduced in the differential PoA measurement.

The effect of the DSSS demodulation on the LOS, multipath and noise components has been analyzed. The despread power for every non-noisy component of the received signal as a function of its demodulation error has been studied and validated. The analysis concludes that demodulated components whose demodulation error is higher than 1 chip time remain completely spread, not contributing to the subsequent phase measurement. The approximate expression of the despread power for smaller demodulation errors has been derived. The study also concludes that the noise component of the received signal, considered flat in the signal bandwidth, preserves its mean and variance after demodulation. The effect of sampling frequency on the phase of the demodulated signal has also been studied, showing a non-negligible phase error depending on the sampling rate. This error has been experimentally quantified for a proper understanding of the global results and its analytical study is left for future contributions.

The differential phasemeter operates on a narrowband where only the power despread in the previous stage is contained, together with the noise contribution after demodulation. It is based on I/Q demodulation and does not require frequency locking with the received signal as frequency

errors are canceled in the differential computation. The effect of noise and system dynamics have been analyzed and validated, deriving expressions of the measured differential range affected by them. The system dynamics that affect this stage, unlike the signal synchronization, are determined by the target displacement, since frequency errors between emitter and receivers are common to both receivers and also canceled in the differential computations. This allows using smaller bandwidth that in the tracking stage to provide higher noise absorption. Multipath error has also been analyzed using the PoA multipath error model derived in chapter 3. This model has been validated with simulation results using one multipath component. An expression of the final measurement bandwidth that balances noise-related and dynamics-related contributions has also been derived as a function of the SNR of both input channels, target speed and chip rate. The analysis concludes that, when the minimum expected SNR is 60 dBHz, a final estimation bandwidth of 60 Hz is adequate for tracking moving targets up to 1 m/s.

Part of the contributions of this chapter have been published in [Salido-Monzú et al., 2013].

Chapter 6

Results

The results that demonstrate the global performance of the proposed ranging architecture are shown, explained and analyzed in this chapter.

The global error model that put together the performance analyses from previous chapters is presented and explained in section 6.1. The operation of the digital implementation of the system, whose Simulink schemes are provided in appendix A, is clarified with an example in section 6.2, supported by captures of the internal signals involved in the measurement process. The test set-up used to perform the measurements is explained in section 6.3. The expected results obtained with the model are compared with actual measurements of the global system performance in section 6.4, where global system accuracy is measured and analyzed in realistic conditions, and the validity of the theoretical model of the system is verified. Finally, section 6.5 is particularly focused on the achieved results regarding the multipath mitigation capabilities of the system compared with a standard PoA ranging model evaluated under equivalent conditions.

6.1 Error model

An error model of the whole ranging system has been developed based on the theoretical analysis carried out in chapters 4 and 5. The model considers the main parameters that affect the operation of the different stages of the system and how the errors in the output of each stage propagate to the subsequent ones. A diagram of the error model is depicted in figure 6.1.

The model is divided into the three stages that operate simultaneously in the system after initialization. The signal synchronization stage, formed by the ELDLL, was designed and analyzed in chapter 4. The DSSS demodulation and the phasemeter and differential range estimation were addressed in chapter 5. The inputs to the model are related to:

- Input signal: containing all the parameters that define the received signal in every receiver, being: received power P_{LOS_0} and delay τ_{LOS} of the LOS component, received powers $P_{\mathrm{MP}_{0n}}$ and delays τ_{MP_n} NLOS components and double-side power spectral density $N_0/2$ of the AWGN contribution.

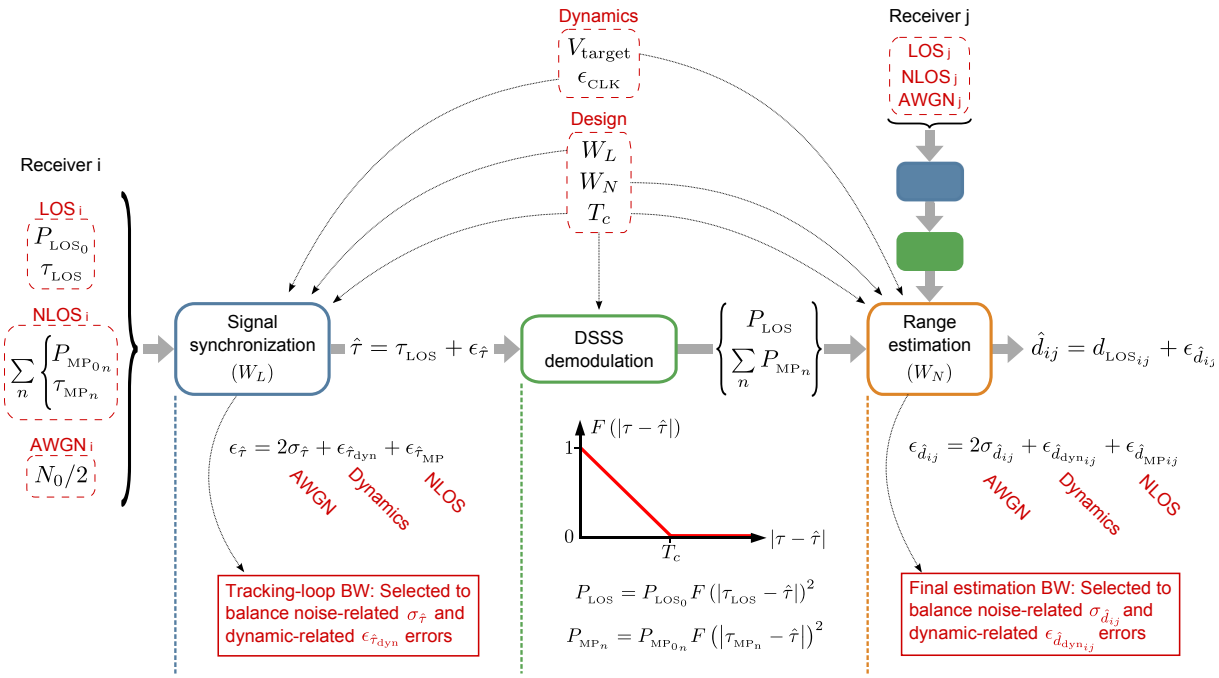

Figure 6.1: Complete error model of the ranging system

- Dynamics: depending on: (i) delay drifts due to the lack of synchronism between emitter and receiver caused by frequency errors ϵ_{CLK} in the signal generation, and (ii) real variations of the delay in the received signal caused by movement of the emitter boarded in a target moving at certain speed V_{target} in relation to the receivers.

- Design: containing the main design parameters of the system, being the selected chip period T_c, the equivalent bandwidth W_L of the delay tracking-loop (adapted to the dynamics defined by frequency errors) and the final estimation bandwidth W_N (adapted to the dynamics defined by the target movement since frequency errors are canceled in the differential estimation).

Several assumptions and considerations, summarized next, have been applied in the analyses that led to the development of this model.

- The relationships between parameters on the model have been obtained considering the signal structure defined in 3.3.2.1.

- Following the considerations related to the signal optimization in 3.3.2.1, chip and sine frequencies are set equal to half the IR channel bandwidth, i.e., the channel bandwidth is $2/T_c$. This signal design provides high received signal power with little distortion while allowing good delay and phase estimations.

- Received powers P_{LOS_0} and $P_{\text{MP}_{0n}}$ are already attenuated (≈ -0.5 dB) by the bandlimited IR channel in relation to the full-bandwidth signal. Distortion in the received signal has not been considered in the theoretical developments, nevertheless, results from previous chapters show that it can be reasonably neglected.

- Noise is considered flat in the channel bandwidth, following a Gaussian distribution and bandlimited in $2/T_c$ by the antialiasing filter before digitization. Those are adequate assumptions considering that the dominant contribution is wideband thermal noise, added to the received signal in the low level conditioning electronics of the generated photocurrent.

6.1.1 Signal synchronization

The inputs to the model of the synchronization stage are the input signal parameters relative to LOS, NLOS and AWGN, the emitter and receiver clocks error ϵ_{CLK}, the chip period T_c and the tracking loop equivalent bandwidth W_L. This stage outputs the estimated delay $\hat{\tau}$, formed by the true value of the LOS delay τ_{LOS} and the total delay estimation error $\epsilon_{\hat{\tau}}$. The estimation error is formed by the addition of the three main error contributions of this stage: noise, dynamics and multipath.

$$\epsilon_{\hat{\tau}} = 2\sigma_{\hat{\tau}} + \epsilon_{\hat{\tau}_{\text{dyn}}} + \epsilon_{\hat{\tau}_{\text{MP}}} \tag{6.1}$$

The noise related error is caused by the AWGN present in the input signal. The total error is calculated considering two times the standard deviation $\sigma_{\hat{\tau}}$ of the tracking jitter. This error depends on the received signal SNR in relation to the LOS component, defined as

$$\text{SNR} = \frac{P_{\text{LOS}_0}}{N_0/2} \tag{6.2}$$

the loop equivalent bandwidth W_L, and the chip period T_c. As calculated and validated in 4.3.1, it can be adequately approximate to

$$\sigma_{\hat{\tau}} = \frac{T_c}{8}\sqrt{\frac{W_L}{\text{SNR}}} \tag{6.3}$$

The dynamic error $\epsilon_{\hat{\tau}_{\text{dyn}}}$ is introduced by the delay drifts caused by the emitter-receiver lack of synchronism. It depends on the tolerance of the emitter and receiver master clocks ϵ_{CLK} and the loop dynamics defined by its equivalent bandwidth W_L. Assuming a worst case in which the deviations from the nominal frequency in both emitter and receiver clocks are of opposite sign and equal to ϵ_{CLK}, the dynamic error can be approximate to

$$\epsilon_{\hat{\tau}_{\text{dyn}}} = \frac{2\epsilon_{\text{CLK}}10^{-6}}{4W_L} \tag{6.4}$$

Finally, the multipath error $\epsilon_{\hat{\tau}_{\text{MP}}}$ is caused by the presence of NLOS components in the received signal. Its analysis in section 4.3.3 of chapter 4 has been addressed by studying the zero-crossing point of the discrimination function in relation to its multipath-free version. The analysis of this crossing point did not yield a close form expression, so it is numerically computed from equation (4.73) in every case, depending on the power and delay relationships between LOS and NLOS components.

6.1.2 DSSS demodulation

The inputs to the model of the demodulation stage are the LOS and NLOS components powers and delays, the chip period T_c and the delay estimated by the previous stage $\hat{\tau}$. This stage outputs the demodulated signals to be processed by the phasemeter. In the model, these outputs are represented by the powers, P_{LOS} and P_{MP_n}, of the received components that have been despread to the sinusoidal modulation narrowband around $1/T_c$ after the demodulation. As analyzed in 5.2, these despread powers depend on the original power of the corresponding component and its alignment with the estimated delay $\hat{\tau}$.

$$\begin{aligned} P_{\text{LOS}} &= P_{\text{LOS}_0} F\left(|\tau_{\text{LOS}} - \hat{\tau}|\right)^2 \\ P_{\text{MP}_\text{n}} &= P_{\text{MP}_{0\text{n}}} F\left(\left|\tau_{\text{MP}_\text{n}} - \hat{\tau}\right|\right)^2 \end{aligned} \tag{6.5}$$

where $F\left(|\tau - \hat{\tau}|\right)^2$ is the function that models the normalized despread power depending on the demodulation alignment, being

$$F\left(|\tau - \hat{\tau}|\right)^2 = \begin{cases} \left|R(f) * G(f, \tau - \hat{\tau})\right|^2_{f=\frac{1}{T_c}} & \text{if} \quad |\tau - \hat{\tau}| \leq T_c \\ 0 & \text{if} \quad |\tau - \hat{\tau}| > T_c \end{cases} \tag{6.6}$$

where the expression of $\left|R(f) * G(f, \tau - \hat{\tau})\right|^2$ is that of equation (5.15).

6.1.3 Range estimation

This part of the model comprises the phasemeter and the final differentiation between two receivers. Its inputs from every receiver are the despread LOS and NLOS powers yielded by the previous stage, the original LOS and NLOS delays, the original noise density $N_0/2$ (whose properties are not modified by the demodulation as demonstrated in 5.2.1), the target speed V_{target}, the chip period T_c and the final estimation bandwidth W_N. The output of this stage is the final differential distance estimation $\hat{d}_{ij}$, formed by the true value of the distance difference $d_{\text{LOS}_{ij}}$ between both LOS paths plus the total differential distance estimation error $\epsilon_{\hat{d}_{ij}}$. This total error is, similarly to the total delay estimation error, formed by the addition of the three main error contributions of this stage: noise, dynamics and multipath.

$$\epsilon_{\hat{d}_{ij}} = 2\sigma_{\hat{d}_{ij}} + \epsilon_{\hat{d}_{\text{dyn}_{ij}}} + \epsilon_{\hat{d}_{\text{MP}ij}} \tag{6.7}$$

The noise-relate error, modeled as two times the estimated distance standard deviation $\sigma_{\hat{d}_{ij}}$, depends on the SNR of the demodulated signal of every receiver, the chip time T_c and the final estimation bandwidth W_N, and can be approximate to

$$\sigma_{\hat{d}_{ij}} = \frac{cT_c}{2\pi} \sqrt{W_N \left(\frac{1}{\text{SNR}_i} + \frac{1}{\text{SNR}_j} \right)} \tag{6.8}$$

where the SNR is calculated for every receiver considering the initial noise density $N_0/2$ and the total demodulated power in the phasemeter narrowband, being

$$\mathrm{SNR}_i = \frac{P_{T_i}}{N_0/2} \tag{6.9}$$

for receiver i, where P_{T_i} is the total multipath-affected power of the demodulated signal in that receiver, being

$$\begin{aligned} P_{T_i} = &\frac{1}{2}\left\{\sqrt{2P_{\mathrm{LOS}_i}}\cos\left(\phi_{\mathrm{LOS}_i}\right) + \sum_{n=1}^{L}\left[\sqrt{2P_{\mathrm{MP}_{i_n}}}\cos\left(\phi_{\mathrm{MP}_{i_n}}\right)\right]\right\}^2 \\ &+ \frac{1}{2}\left\{\sqrt{2P_{\mathrm{LOS}_i}}\sin\left(\phi_{\mathrm{LOS}_i}\right) + \sum_{n=1}^{L}\left[\sqrt{2P_{\mathrm{MP}_{i_n}}}\sin\left(\phi_{\mathrm{MP}_{i_n}}\right)\right]\right\}^2 \end{aligned} \tag{6.10}$$

where

$$\begin{aligned} \phi_{\mathrm{LOS}_i} &= \frac{d_{\mathrm{LOS}_i} 2\pi}{cT_c} \\ \phi_{\mathrm{MP}_{i_n}} &= \frac{d_{\mathrm{MP}_{i_n}} 2\pi}{cT_c} \end{aligned} \tag{6.11}$$

Note that the noise-related error in the estimated distance does not only depend on noise in the input signal, but also on the dynamic and multipath errors from the synchronization stage. The total accuracy in the estimated delay defines the amount of LOS and multipath recovered power, hence the SNR available for the phase estimation.

The dynamic error in this stage does not depend on synchronism errors between emitter and receiver since those are equal for every receiver, hence canceled in the differential estimation. The delay variation to be tracked is that introduced by the displacement of the target where the emitter is boarded. The dynamic error depends on the target speed V_{target} (defined, as a worst case, in the direction of the receivers) and the final estimation bandwidth W_N.

$$\epsilon_{\hat{d}_{\mathrm{dyn}_{ij}}} = \frac{V_{\mathrm{target}}}{2W_N} \tag{6.12}$$

Finally, the multipath error $\epsilon_{\hat{d}_{\mathrm{MP}ij}}$ is the addition of the multipath errors in the individual phase estimations for every receiver, being

$$\epsilon_{\hat{d}_{\mathrm{MP}ij}} = \frac{cT_c}{2\pi}\left(\phi_{T_i} - \phi_{\mathrm{LOS}_i} - \phi_{T_j} + \phi_{\mathrm{LOS}_j}\right) \tag{6.13}$$

where ϕ_{T_i} and ϕ_{T_j} are the multipath-affected estimated phases, being

$$\phi_{T_i} = \mathrm{atan}\left\{\frac{\sqrt{2P_{\mathrm{LOS}_i}}\sin\left(\phi_{\mathrm{LOS}_i}\right) + \sum_{n=1}^{L}\left[\sqrt{2P_{\mathrm{MP}_{i_n}}}\sin\left(\phi_{\mathrm{MP}_{i_n}}\right)\right]}{\sqrt{2P_{\mathrm{LOS}_i}}\cos\left(\phi_{\mathrm{LOS}_i}\right) + \sum_{n=1}^{L}\left[\sqrt{2P_{\mathrm{MP}_{i_n}}}\cos\left(\phi_{\mathrm{MP}_{i_n}}\right)\right]}\right\} \tag{6.14}$$

for receiver i.

Note that multipath error in the final estimation depends on the despread LOS and NLOS power in the output of the demodulation stage. These powers are themselves dependent on the

total accuracy of the previous delay estimation, this is, final multipath error is not only defined by the existing multipath situation, but also by the noise and dynamic errors in the previous stage.

The complete model will be used to compare the results from the measurements with the expected results from the theoretical analysis computed under the same conditions of SNR, dynamics and multipath.

6.2 System operation

This section provides a brief sequential example of the system operation, where the relevant internal signals involved in each stage are shown.

When the system is initialized, every receiver starts the delay acquisition process in which possible delay candidates are tested by correlation with the incoming signal. This process is performed in parallel for a number of signals, determined by the number of expected targets to be localized, each having an assigned PRN sequence for multiplexing. Figure 6.2 shows an epoch (for a 15 chips long sequence) of the received signals and the local replica used for correlation in both the acquisition and tracking stages. Figure 6.3 shows the PSD[1] computed for the received signal using the FFT[2]. The line components corresponding to the 15 chips long epochs, i.e., separated approximately by 1.667 MHz, can be clearly seen. This measured PSD can be compared with the modeled PSD of the emitted and bandlimited received signal in figures 3.19 to 3.19 of section 3.3.2.2. Figure 6.4 shows the correlation between both signals.

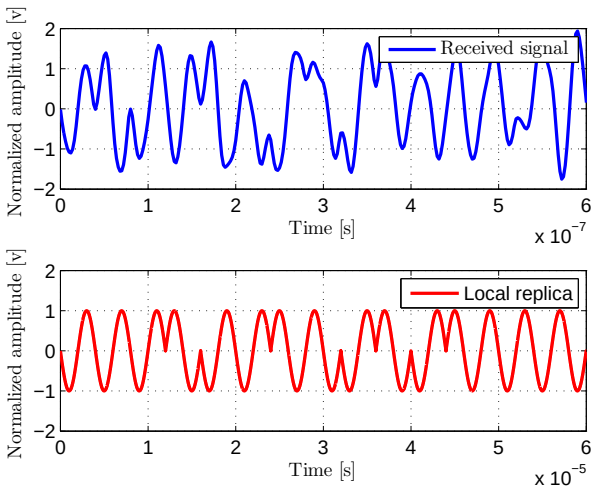

Figure 6.2: Received signal and local replica for correlation (not synchronized). 1 epoch of a 15 chips sequence at 25 MHz

Once the delay acquisition is completed, the DLL-based tracking stage is initialized in a locked state with the selected delay and starts keeping track of variations in the incoming signal. The tracking stage does not only provide fast and continuous tracking of the delay variations

[1] Power Spectral Density
[2] Fast Fourier Transform

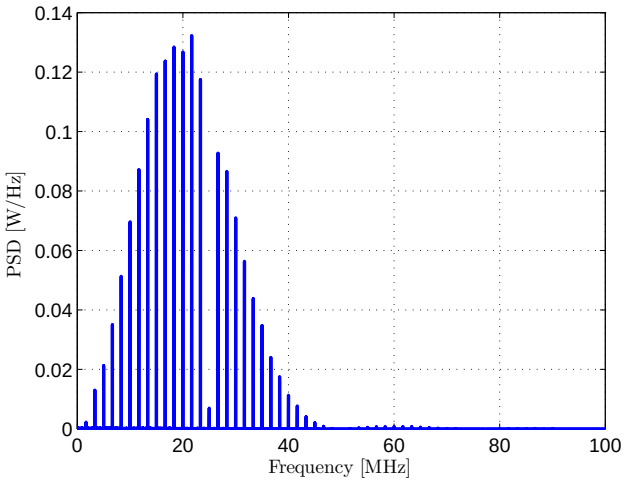

Figure 6.3: PSD of the received signal

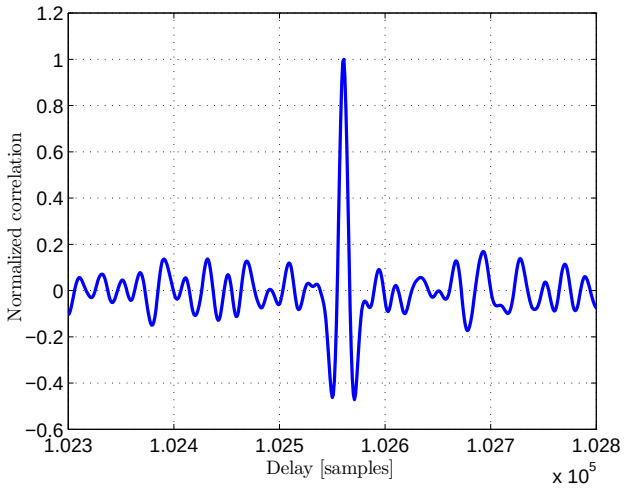

Figure 6.4: Normalized correlation between received signal and local replica

but also a finer resolution in the estimation. Figure 6.5 shows the estimated delays for two receivers in a measurement window of 2 ms. The depicted delays correspond to both the initial acquisition $\hat{\tau}_0$ and the tracked delay $\hat{\tau}$. During the first 200 μs the acquisition is being performed, after which the DLL is locked and starts updating the estimated delay with the changes in the incoming signal. The resolution of this estimation depends on the local replicas used in the DLL correlators. In this example, the replicas are stored with a sampling-rate of 1 GS/s, what provides time steps of 1 ns. Note that the absolute estimated delay contains an unknown offset due to the lack of an absolute reference between emitter and receivers.

Figure 6.6 shows the internal signals of the ELDLL in the same measurement window of figure 6.5. The blue, green and red signals are the prompt, early and late correlation values respectively; the yellow signal is the output of the loop filter, this is, the error signal or discriminator built by low-pass filtering the subtraction of the early and late correlation values; and the black lines show the instantaneous value of the threshold the error signal is compared with for updating the current delay estimation.

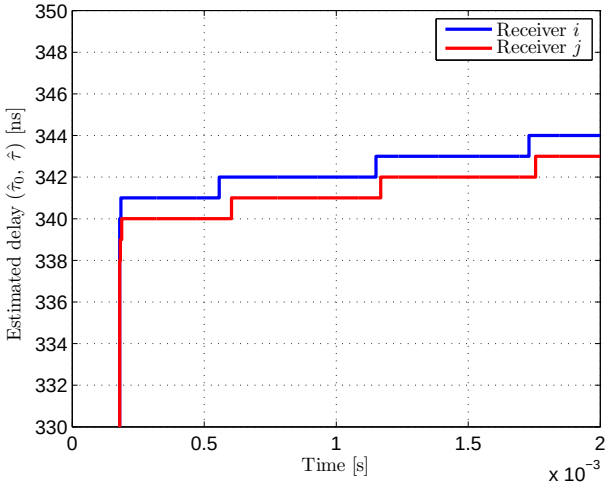

Figure 6.5: Estimated delays for receivers i and j. Delay acquisition ($\hat{\tau}_0$) up to 200 μs and delay tracking ($\hat{\tau}$)

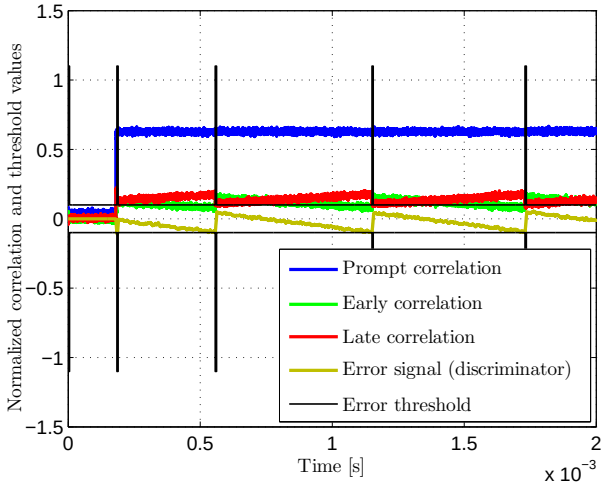

Figure 6.6: Internal signals of the ELDLL for receiver i

An analog implementation of the DLL, or a digital one where the local signals are generated with a numerically controlled oscillator (NCO), would need no threshold, since the error signal could directly drive a phase detector to correct the current delay and drive the error towards zero. However, in this digital implementation, local signals are stored in a memory as oversampled versions of the expected received signals. This memory outputs the local signals with certain phase at the receivers sampling rate, and this phase is corrected by a simple comparison with a threshold defined by the memory resolution. The oversampling factor in relation to the receiver sampling rate defines the resolution of the local generator, and consequently the resolution of the calculated correlations. This implementation has been chosen for simplicity. A standard NCO-based signal generation would provide better efficiency in terms of memory usage, but it would also present a limited delay resolution in the phase to amplitude conversion, which is usually performed by selecting every output sample from a look-up-table.

When the error signal goes out of the threshold-limited range around zero, the value of the

estimated delay is updated to take the next or previous possible phase, depending on the error growing positive or negative, so that the local prompt signal stays as synchronized as possible with the received signal. If the DLL is locked, an equal value for the early and late correlations means that the input and local replica are perfectly aligned, so the error signal is zero and the prompt correlation value is maximum. A drift in the correlation and error values can be observed in figure 6.6 for receiver i. In this example, the target is static, so this drift does not correspond to a real variation of the input signal delay, but to an apparent variation caused by the frequency errors between emitter and receivers. A similar variation appears in receiver j, as the received signal comes from the same emitter, and its local references are generates based on a master clock shared by both receivers. This apparent delay variation is, therefore, common to both receivers and will be canceled in the differential measurement in the phasemeter.

Figure 6.7 shows a detail of figure 6.6 when a delay update is performed. When the error signal goes under the negative threshold, the estimated delay is updated and the local signals generator start outputting a new phase, closer to the actual received signal phase. It can be observed how, after the delay updating, the early and late correlations values are closer to each other, and the prompt correlation slightly increases its value. The DLL is designed so that the threshold is increased after every delay update during some μs to avoid a second update before the new correlation values are stable.

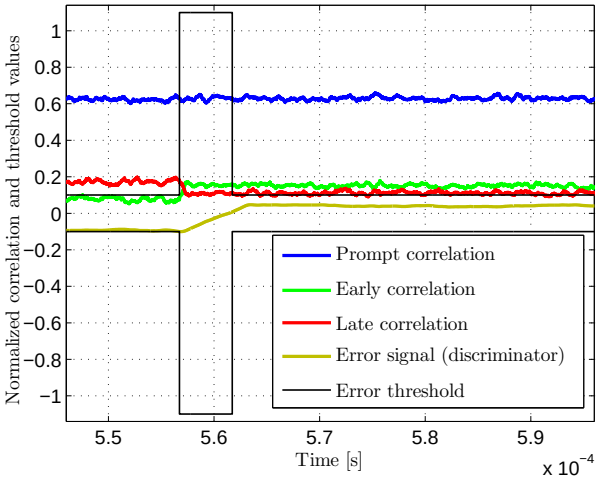

Figure 6.7: Internal signals of the ELDLL for receiver i. Detail of a delay update event

After the initial delay is acquired, simultaneously to the delay tracking, the received signal is demodulated by multiplying it with a local replica of the PRN used in the emitter for frequency spreading the sine signal power. The local PRN is generated, similarly to the local replicas used in in the correlators of the acquisition and tracking stages, with a phase defined by the estimated delay continuously outputted by the DLL. Figure 6.8 shows the signals involved in the demodulation process. The upper plot shows the received signal in a multipath-free situation and the time-aligned local PRN. The lower plot shows the demodulated signal, where the phase shifts introduced in the sine modulation by the PRN in the emitter are undone, despreading the sine signal power back to its narrowband. The demodulated signal is then processed by the phasemeter to extract its phase and calculate the differential distance together with the phase

information from another receiver.

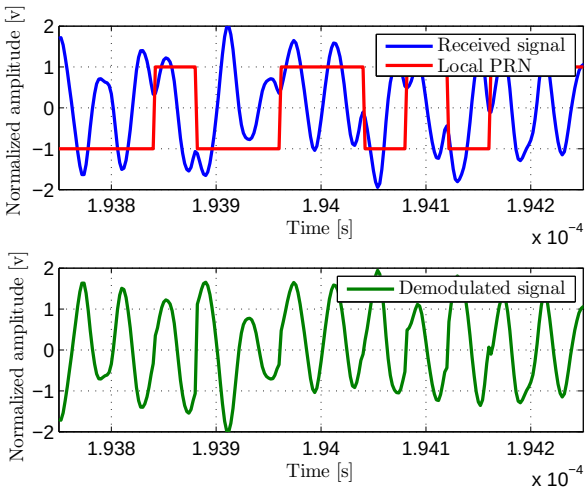

Figure 6.8: DSSS demodulation

Figure 6.9 shows the outputs $\hat{\phi}_i$ and $\hat{\phi}_j$ of the phasemeters of the two receivers. These signals contain the phase information and a continuous varying component that depends on the frequency errors between emitter and receiver, which causes a frequency difference between the received signals and the internal I/Q references. In this example, where 10ppm accurate clocks are considered, this varying component takes values of some hundreds of Hz. These frequency errors are similar for both receivers, hence canceled in the subtraction, as can be seen in the differential phase signal $\hat{\phi}_{ij}$. Note that the arctangent operator used to extract the single phases after the I/Q demodulation is bounded in $\pm\pi/2$, thus the phase jumps in the differential measurement have to be corrected by a simple unwrapping algorithm after the subtraction. This differential phase is finally converted into the estimated differential distance considering the wavelength of the sinusoidal modulation.

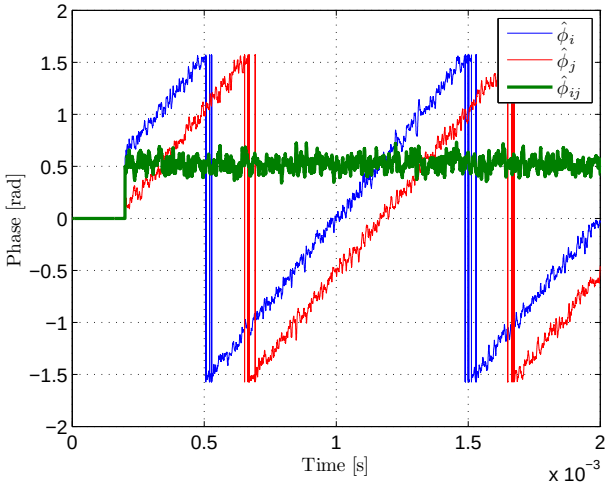

Figure 6.9: Single $\left(\hat{\phi}_i,\ \hat{\phi}_j\right)$ and differential $\left(\hat{\phi}_{ij}\right)$ phase estimations

6.3 Test set-up

The measurements used in the results, as well as most of the validation measurements of every individual stage shown in previous chapters, have been carried out with a digital implementation of the proposed architecture. The full ranging system has been implemented in Simulink using components from the Signal Processing Blockset, and is run using a discrete-time step. This guarantees that, even if the prototype cannot process the input signals in real time, it behaves exactly as it would if implemented in an ASIC or FPGA. The diagrams of the system implementation are included in appendix A.

An IR link with the required features is currently under development, meanwhile, an emulation of a 50 MHz optical link has been developed to generate the input signals that are used to evaluate the whole system performance. The signals are obtained using a wired connection between two AFGs (Tektronix AFG3252 and AFG3022B) and a simultaneous-sampling oscilloscope (Tektronix MSO4104). Two oversampled versions of the noise-free emitted signals are generated in Matlab and D/A converted by one AFG. The relative delay between both signals (corresponding to the signals simultaneously reaching two receivers) can be selected with ps resolution during the signal generation. The noise contributions for both signals are generated with the adequate power spectral densities in a different AFG, and added to the signals in the analog channel before digitization. Multipath components corresponding to every channel, if existing, are added to the original signals before D/A conversion. The complete signals, already affected by noise and multipath, are then simultaneously digitized by the oscilloscope. Finally, a digital filter after digitization emulates the effect of the bandwidth limitation caused by the optical channel and the AAF. A D/A conversion rate of 2GS/s and a sampling rate of 5GS/s are used in the AFG and oscilloscope respectively. Taking into account that the useful signal bandwidth is 50 MHz, these rates provide, in one hand, a good representation of the generated signal in the analog domain and, in the other hand, an oversampled (in relation to the required sampling rates in a practical implementation) version of the received signal, which allows a frequency response in the digital filter that emulates closely that of the analog channel and AAF. The final digital signals are downsampled to the required rate before being introduced in the Simulink signal processing architecture to obtain results emulating different sampling rates in the digitizer.

Figure 6.10 shows a diagram of the complete test set-up and figure 6.11 shows a picture of the signal generation part of the setup. The two AFGs and the oscilloscope are connected to a PC[3] with Matlab for generation of the original signals before D/A conversions in one of the AFGs and for collecting the digitized sequences form the oscilloscope for their subsequent processing in Simulink.

Figures 6.12 and 6.13 show oscilloscope snapshots of the generated signals in a test with 5 MHz chip rate. In both cases the blue channel represents an ideal signal where none of the effects of the emulation has been added. The yellow channel represents a received signal in multipath-free conditions for two different distances between emitter and receiver, hence different SNR. Apart from the noise addition, the effect of the channel bandwidth can also be clearly seen. The

[3]Personal Computer

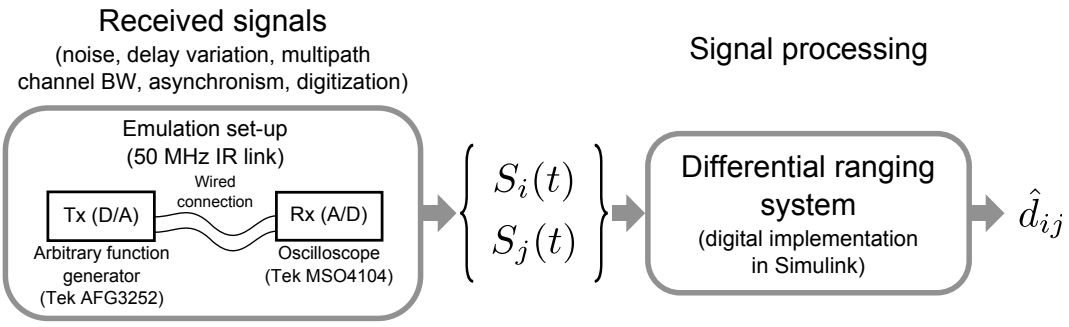

Figure 6.10: Diagram of the test set-up

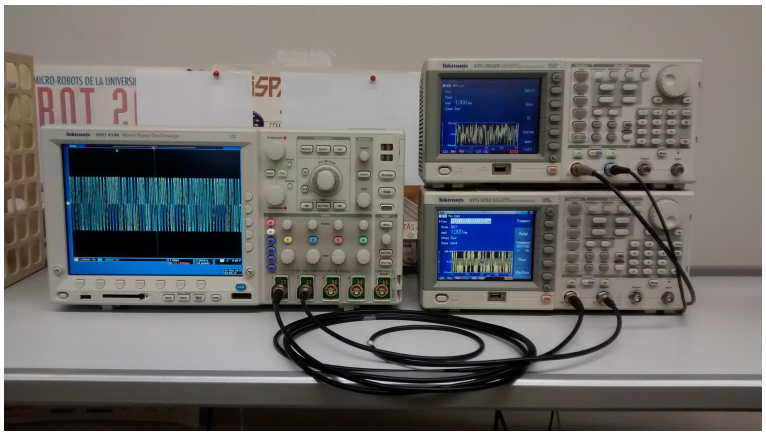

Figure 6.11: Picture of the signal generation instruments for the test set-up. Left: Oscilloscope Tektronix MSO4104 (digitization), up-right: AFG Tektronix AFG3022B (noise addition), down-right: AFG Tektronix AFG3252 (signal generation)

average level in the snapshots is arbitrary, all received signals generated by the emulation set-up represent the AC-coupled IMDD voltage after signal conditioning.

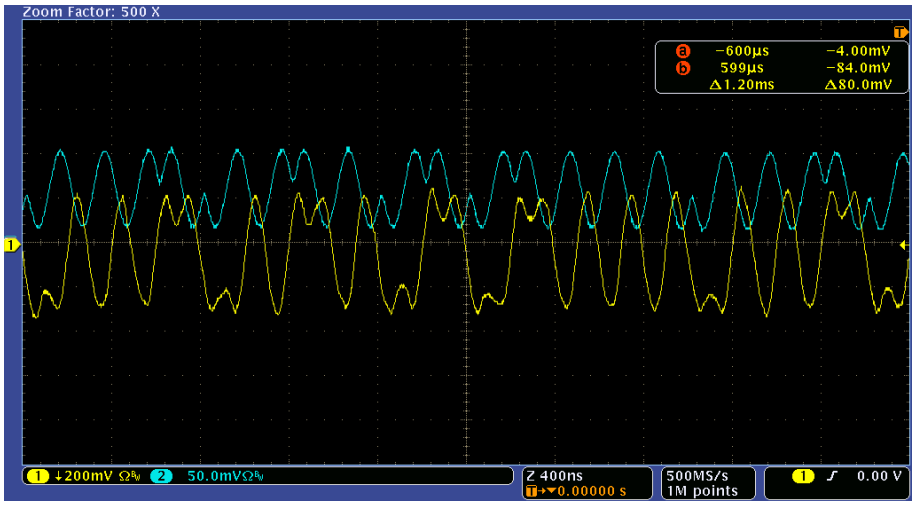

Figure 6.12: Oscilloscope snapshot of an ideal signal (blue) and received signal (yellow) emulating an emitter-receiver distance of 1 m

Figure 6.13: Oscilloscope snapshot of an ideal signal (blue) and received signal (yellow) emulating an emitter-receiver distance of 3 m

6.4 Global performance

The global performance of the whole system is evaluated in this section under the conditions defined for the scenario described next, using the emulation of the 50 MHz IR link to generate the input signals.

This section includes tests to evaluate the general system performance in terms of mean error and standard deviation under different static conditions. The impact of multipath effects on accuracy is also evaluated, however, the next section is specifically dedicated to multipath mitigation, where the multipath error yielded by the proposed system is compared with the expected error in standard PoA ranging under equivalent conditions.

6.4.1 Test scenario

The global performance tests are based on the scenario shown in figure 6.14. The SNR levels, delays and power of the LOS and multipath components are calculated for these scenario to generate the test signals in the IR link emulation. Two receivers are placed on the ceiling of the environment, 3.5 m apart and elevated 2.5 m from the floor. The emitter moves in an horizontal plane 0.35 m from the floor. The possible target positions are those shown in figure 6.15. The index given to the positions in this figure will be further used in this section for referencing them. This configuration has been chosen to represent a practical full range of target positions in relation to a pair of receivers providing a differential measurement. Figure 6.16 shows a possible receiver configuration to cover an area of approximately 12 m^2. Observing the figure, one can see how the selected test points are a good representation of the possible target positions regarding every differential distance measurement.

The SNR levels have been calculated with the parameters of the practical 50 MHz link defined in 3.1.3.1. Table 6.1 shows the differential distance and SNR levels in every receiver that correspond to each of the target positions. The SNR values as a function of the target position

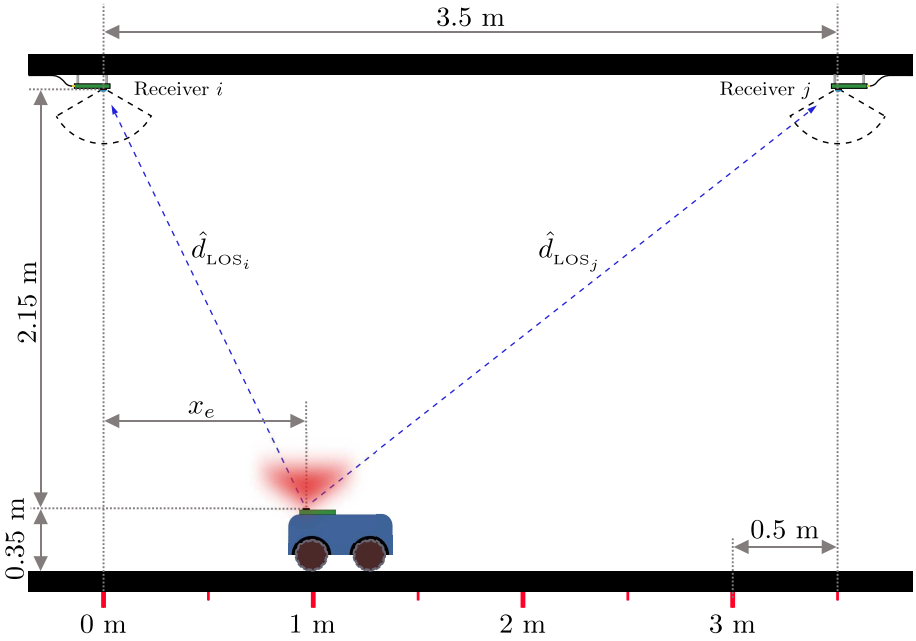

Figure 6.14: Diagram (side-view) of the test scenario

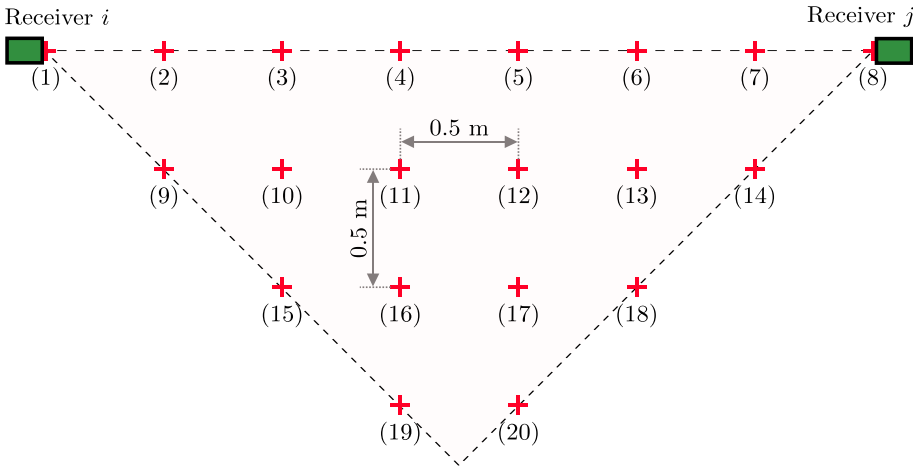

Figure 6.15: Diagram (top-view) of the test scenario. Test points

are represented in figure 6.17. The combined SNR between both receivers is defined as

$$\mathrm{SNR}_{ij} = \frac{\mathrm{SNR}_i \mathrm{SNR}_j}{\mathrm{SNR}_i + \mathrm{SNR}_j} \tag{6.15}$$

Note that, despite the individual SNR values are maximum when the target is exactly under the corresponding receiver, i.e., positions (1) and (8), the differential measurement is affected by the signal quality of both receivers. Due to this, the positions where precision is maximized are those close to the middle point between both receivers. These are the positions where the combined SNR from both receivers is higher. Thus, positions where the expected accuracy is higher are those where SNR levels from both receivers are balanced, i.e., the central positions of the grid, such as (4), (5), (11), (12), (16) or (17). This can be easily seen in figure 6.18, where the combined SNR between both receivers is represented with a color scale in a 2D plot of the test grid.

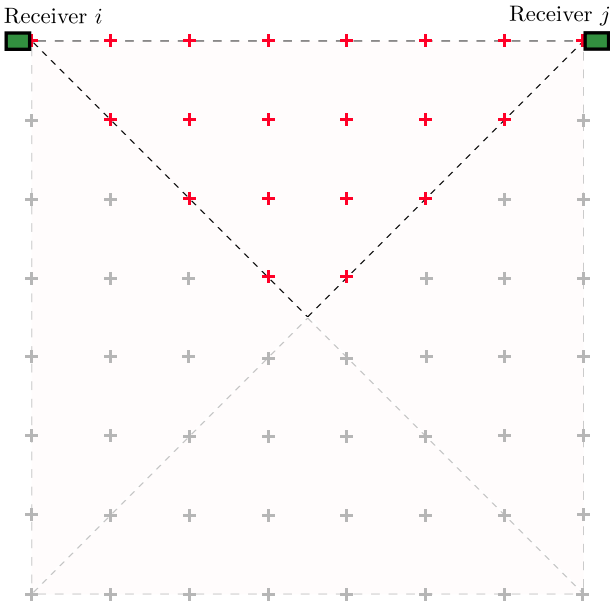

Figure 6.16: Example of cell construction with the selected test grid

Table 6.1: Differential distance true values and SNR levels in every position of the test scenario

Target position P	Differential distance $d_{\mathrm{LOS}_{ij}}$ [m]	Signal quality SNR_i [dBHz]	SNR_j [dBHz]
(1)	-1.958	84.1	61.6
(2)	-1.483	83.2	65.3
(3)	-0.926	80.7	69.2
(4)	-0.315	77.2	73.3
(5)	0.315	73.3	77.2
(6)	0.926	69.2	80.7
(7)	1.483	65.3	83.2
(8)	1.958	61.6	84.1
(9)	-1.461	82.3	65
(10)	-0.912	79.9	68.8
(11)	-0.31	76.6	72.8
(12)	0.31	72.8	76.6
(13)	0.912	68.8	79.9
(14)	1.461	65	82.3
(15)	-0.872	77.8	67.7
(16)	-0.296	74.8	71.3
(17)	0.296	71.3	74.8
(18)	0.872	67.7	77.8
(19)	-0.277	72.3	69.2
(20)	0.277	69.2	72.3

Regarding multipath, the specular reflection model defined in 3.2.1.1, with one single multipath component per receiver, is used. As demonstrated in 3.2.3, this model represents a worst case situation in the vast majority of positions for the ceiling-floor reflected multipath. Table 6.2 shows the parameters related to multipath, in which the NLOS-to-LOS distances and power ratios for every position are shown. Given data correspond to receiver i. Equivalent values for receiver j can be easily derived from these by taking into account the test grid symmetrical geometry, e.g., the data corresponding to position (2) for receiver i is equivalent to the data corresponding to position (7) for receiver j.

Note that using a specular reflection model for multipath introduces high differences in the severity of the multipath situation depending on the target position. As can be observed in the

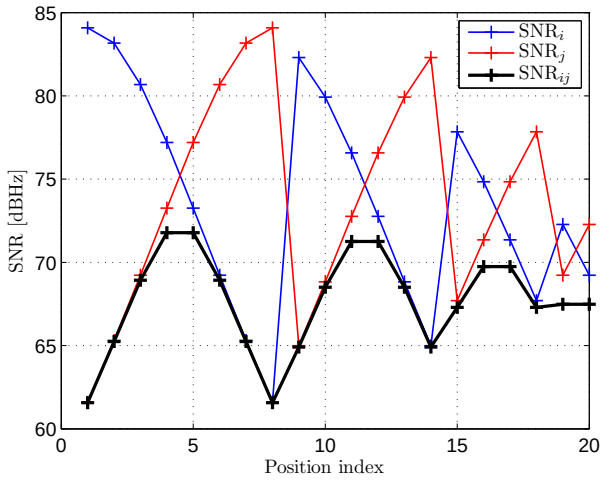

Figure 6.17: SNR level in every receiver and combined SNR as a function of target position

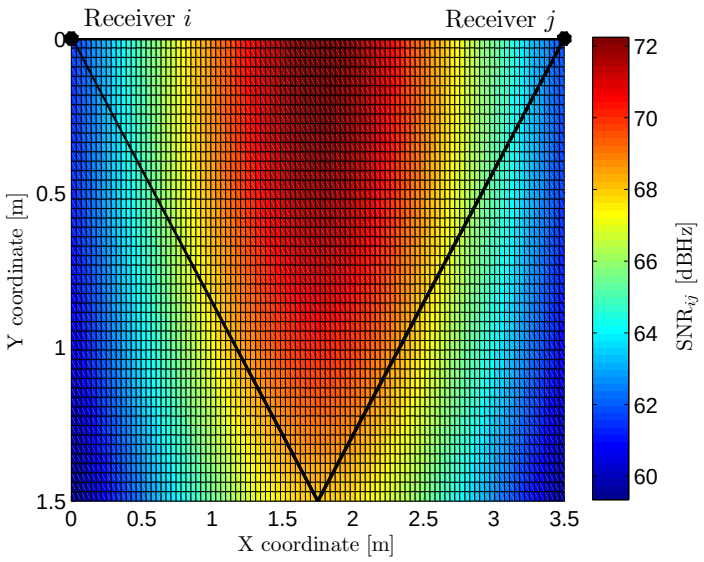

Figure 6.18: Combined SNR surface as a function of target position

table, relative multipath power in positions far away from a receiver are very high, reaching values above 20% of the LOS power, however, when the target is close to a receiver, the power of multipath components that reache it is smaller than 1% of the LOS power. Considering the effect on both receivers, worst multipath situations will again correspond to the positions close to one receiver, where the severe multipath effects in the other one will yield high errors in the differential mesurement.

Figure 6.19 shows graphical representations of these parameters for both receivers, where those corresponding to receiver i are highlighted with wider lines. 6.19.a shows the LOS, NLOS and NLOS-to-LOS distances for every position, while 6.19.b shows the NLOS-to-LOS power ratios.

Observing the figures, one can see that positions (1) and (8), as well as (2) and (7) to a lesser extent, will be particularly affected by multipath. Relative multipath power in those positions is very high for one of the receivers. In addition, NLOS-to-LOS distances are shorter

Table 6.2: Differential distance true values and multipath parameters (receiver i) in every position of the test scenario

Target position P	Differential distance $d_{\mathrm{LOS}_{ij}}$ [m]	NLOS-to-LOS distance $\frac{d_{\mathrm{MP}_i} - d_{\mathrm{LOS}_i}}{cT_c}$ [chips]	NLOS-to-LOS power $\frac{P_{\mathrm{MP}_i}}{P_{\mathrm{LOS}_i}} \cdot 100$ [%]
(1)	-1.958	0.42	0.3
(2)	-1.483	0.41	0.4
(3)	-0.926	0.4	0.6
(4)	-0.315	0.39	1.2
(5)	0.315	0.37	2.6
(6)	0.926	0.36	5.7
(7)	1.483	0.34	11.6
(8)	1.958	0.32	22.1
(9)	-1.461	0.41	0.4
(10)	-0.912	0.4	0.7
(11)	-0.31	0.39	1.4
(12)	0.31	0.37	2.9
(13)	0.912	0.35	6.1
(14)	1.461	0.34	12.3
(15)	-0.872	0.39	1.1
(16)	-0.296	0.38	1.9
(17)	0.296	0.37	3.8
(18)	0.872	0.35	7.5
(19)	-0.277	0.37	3.2
(20)	0.277	0.36	5.7

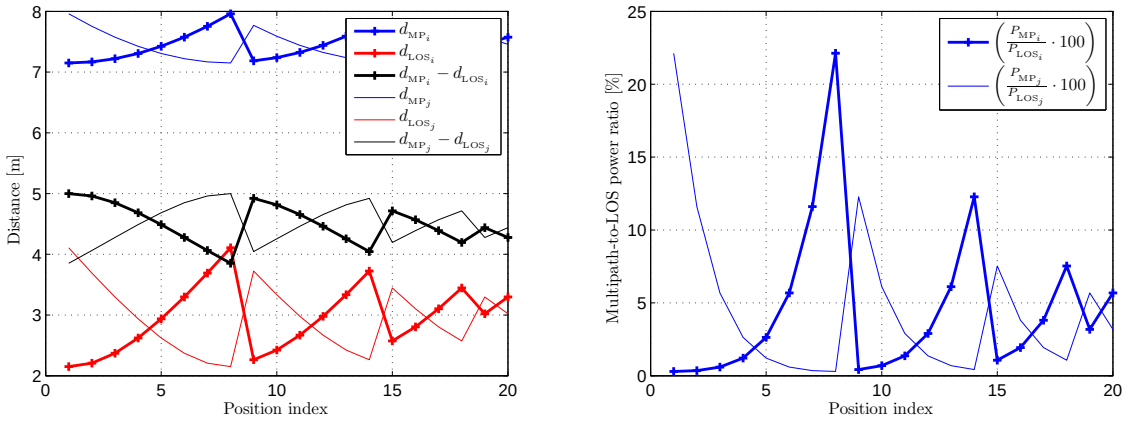

(a) NLOS, LOS and NLOS-to-LOS distances

(b) NLOS-to-LOS power ratios

Figure 6.19: Multipath parameters as a function of target position

in those positions for the affected receiver, e.g., 0.32 chips longer than the LOS path for the worst case positions (1) and (8). This, apart from creating a severe multipath situation, limits the mitigation capability of the system, that rely on the separation with the LOS component for multipath attenuation.

6.4.2 Results

Three different tests have been carried out to evaluate the global system performance:

- Noise-free and multipath-free: static measurements on every test position, where only the variation of the delay true value for the LOS path is considered.

- Multipath-free: static measurements on every test position, where the input signal in every receiver, apart from the corresponding LOS delay, contains the adequate noise level to achieve the corresponding SNR shown in table 6.1 and figures 6.17 and 6.18.
- Noise and multipath: static measurements on every test position including the corresponding noise levels and a dominant multipath component whose power and delay in every receiver correspond to those shown in table 6.2 and figure 6.19.

All these tests are static from the target point of view and dynamic from the frequency error point of view since asynchronism is inherently provided by the emulation set-up. In the low level, this implies that the delay acquisition and tracking stages, together with the single channel section of the phasemeters before the subtraction, are operating in dynamic conditions tracking the delay drifts due to asynchronism; only the final differential phase measurement, once the common frequency error is canceled in the differentiation, is static. The inclusion of tests with moving targets is proposed for future contributions. However, it is reasonable to expect results that agree with the theoretical model as the partial dynamic tests were successful. In addition, the most demanding dynamics (delay variations approximately 3 orders of magnitude faster) are those derived from asynchronism, which have been properly tested with good results in the complete architecture.

All test has been carried out using a system configuration, regarding its design parameters, derived from previous chapters to optimize the used of the available optical link and to balance dynamic and static errors:

- Chip rate $1/T_c$ is set at 25 MHz, as assumed in previous chapters, for maximizing accuracy in a 50 MHz optical link.
- Tracking loop bandwidth W_L is set to 3.5 kHz, which was calculated in 4.3.4 as an adequate value to balance dynamic and static errors, where the dynamics are dominated by the delay drifts caused by emitter-receiver clocks asynchronism.
- Final estimation bandwidth W_N is set to 500 Hz. The optimum value for balancing static and dynamic errors was calculated in 5.3.4, being approximately 60 Hz for tracking targets moving at 1 m/s. A higher value has been set for processing the measurements for practical reasons, related to the maximum time window that the test set-up can process. Using a higher bandwidth allows using smaller time windows in the digitized signals, hence having smaller computation time and memory usage, without loosing statistical confidence in the parameters measured on the results. The results obtained with this value for W_N are adequate to validate and estimate the system performance. It should be noted, however, that the selected value of 500 Hz makes the system dynamics too fast for the target speed and SNR conditions of the test scenario, benefiting the dynamic performance against the static one. This will make noise contributions to introduce an error approximately 3 times higher than the one that could be achieved with the optimum bandwidth calculated in 5.3.4. Equivalently, dynamic errors yielded with this bandwidth will be approximately 9 times smaller. This will be taken into account in the comments about the system performance limits extracted from these results.

- The sampling rate used for the input signals is 500 MS/s and the local signals are generated with a resolution of 1 GS/s. These rates are well above the minimum required for an adequate representation of the analog signals, taking into account that the AAF limits the signal and noise bandwidth to 50 MHz. Some other considerations related to sampling-rate are commented next.

All the following results will be affected by the resolution limits associated to the sampling rate in the signal demodulation, addressed in 5.2.2. The simulations included in the chapter show that, for the conditions used in these tests, i.e., 500 MS/s at 25 MHz chip rate with local signals generated with 1 GS/s, distance steps of approximately 6 cm can be expected. This error source will appear in the results. However, it should be noted that, as seen in the operation example, this error becomes a zero mean contribution for linearly varying delays, which is how the system would normally operate due to the emitter-receiver asynchronism. This error could not be properly averaged in the tests due to hardware limitations of the signal processing stage, which, in its current inefficient Simulink implementation, does not allow processing signals longer than some milliseconds. In addition, this error can be reduced by simply using a higher sampling frequency (with the corresponding increase in hardware cost), therefore, to provide a useful characterization of the real system trade-offs and limitations caused by noise, the variance of the measurements has been calculated after canceling the effect of the specific sampling resolution used in the tests. Histograms of the measurements for every position are provided for the multipath free tests, so that the error due to the discretized demodulation can be distinguished from the Gaussian deviations in the measurements caused by noise.

6.4.2.1 Noise-free and multipath-free test

This test aims at evaluating the behavior of the system in close-to-ideal conditions. Input signals are generated considering only the distance true value associated to every position, without any noise or multipath addition. Consequently, the only error sources are: the small noise floor added by the signal generator and digitizer (including both analog and quantization noise), the clock drifts between the signal generator and the digitizer, and the effects introduced by the discretization of the input signals.

The results of this test are not compared with the theoretical model, since the only error source that is taken into account in the error model is the emitter-receiver clock asynchronism. This error is canceled in the differential measurement, so it only has an effect on the delay estimation error, which itself causes an SNR reduction in the demodulation. Given that this test is noise-free in practical terms (residual noises yield SNR levels well-above 100 dBHz that will not be reached by the required optical link in real scenarios), standard deviations of the results (in the sub-mm level) are not shown.

An oscilloscope snapshot with an example of the input signals generated for this test is shown in figure 6.20.

Figure 6.21.a shows the measured differential distances in every test position, while figure 6.21.b shows the distance true values $\left(d_{ij_{\mathrm{TV}}}\right)$ and the average estimated values $\left(\hat{d}_{ij}\right)$. In both

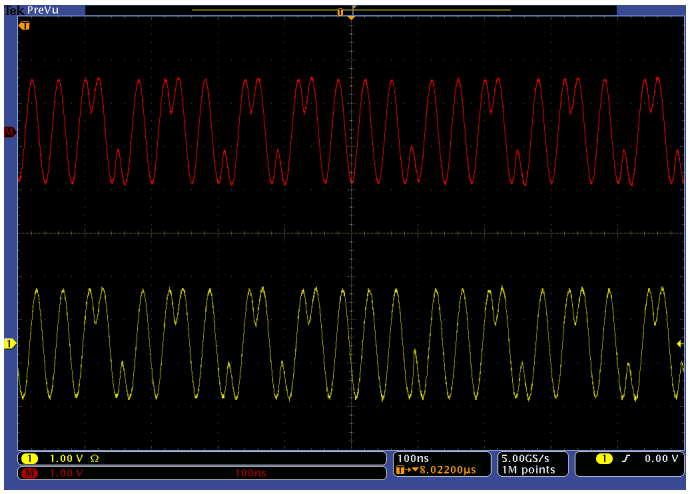

Figure 6.20: Oscilloscope snapshot of the input signals in noise-free and multipath-free conditions

figures the X-axes correspond to the index number assigned to every position following the definition given in figure 6.15. Figure 6.21.a shows the instantaneous distance estimations using a final bandwidth of 500 Hz, where 900 measurements per position are plotted. In figure 6.21.b the distance true values for every position are drawn with blue circles while the average estimated values are drawn in red dots, the latter being calculated with a bandwidth of approximately 2.5 Hz.

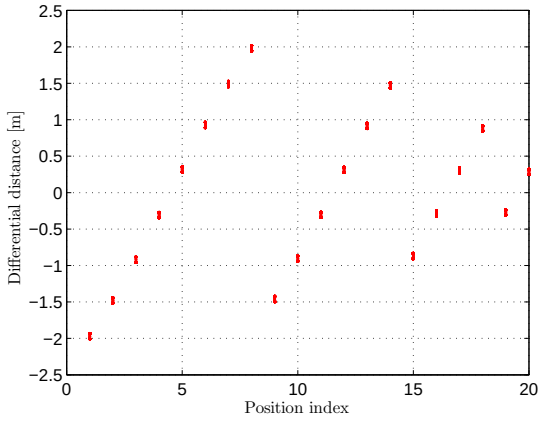

(a) Estimated distances $\hat{d}_{ij}$

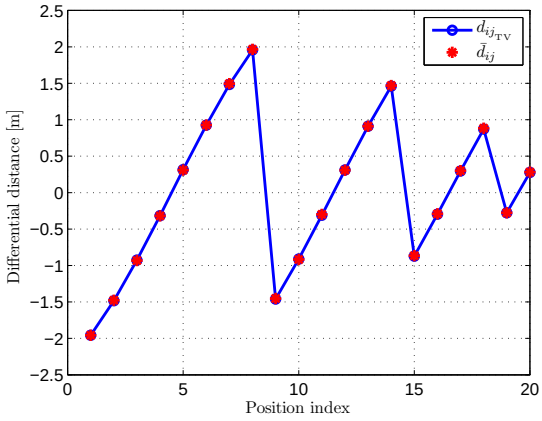

(b) Distance true values $d_{ij_{\mathrm{TV}}}$ and mean estimated values $\bar{d}_{ij}$

Figure 6.21: Distance true and estimated values for every position. Static, noise-free and multipath-free measurements

Figures 6.22 and 6.23 show histograms of the measurements in every position. The true and average values are also depicted in blue and dashed red lines respectively. It can be seen how two Gaussian distributions (having low dispersion due to the low noise levels in this test) appear separated by approximately 7 cm in every position. This is the effect of the sampling rate in demodulation. Observing the histograms, one can see that the measurement tend to distribute between two possible distance values depending on the distance true vale, i.e., more measurements are centered in the possible discrete distance which is closer to the actual true

value. This makes this contribution to behave as a pulse wide modulation, yielding an average error that tends to zero for a large enough measurement interval, as explained in section 5.2.2.

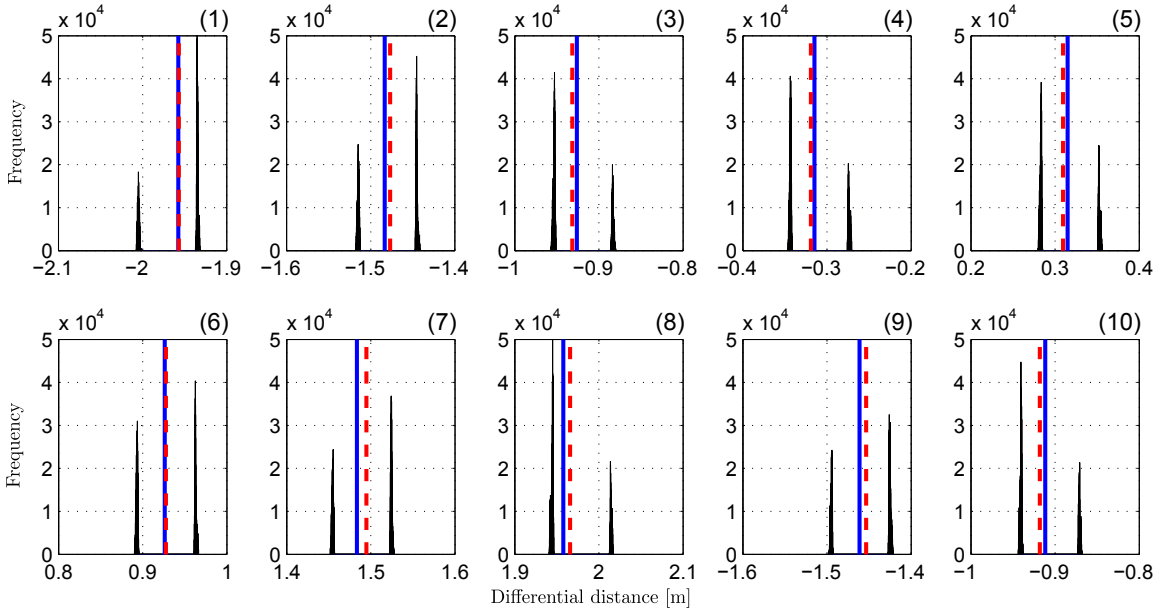

Figure 6.22: Histogram of estimated values $\hat{d}_{ij}$, distance true values $d_{ij_{\mathrm{TV}}}$ (blue) and mean estimated values $\bar{d}_{ij}$ (red) for positions (1) to (10). Static, noise-free and multipath-free measurements

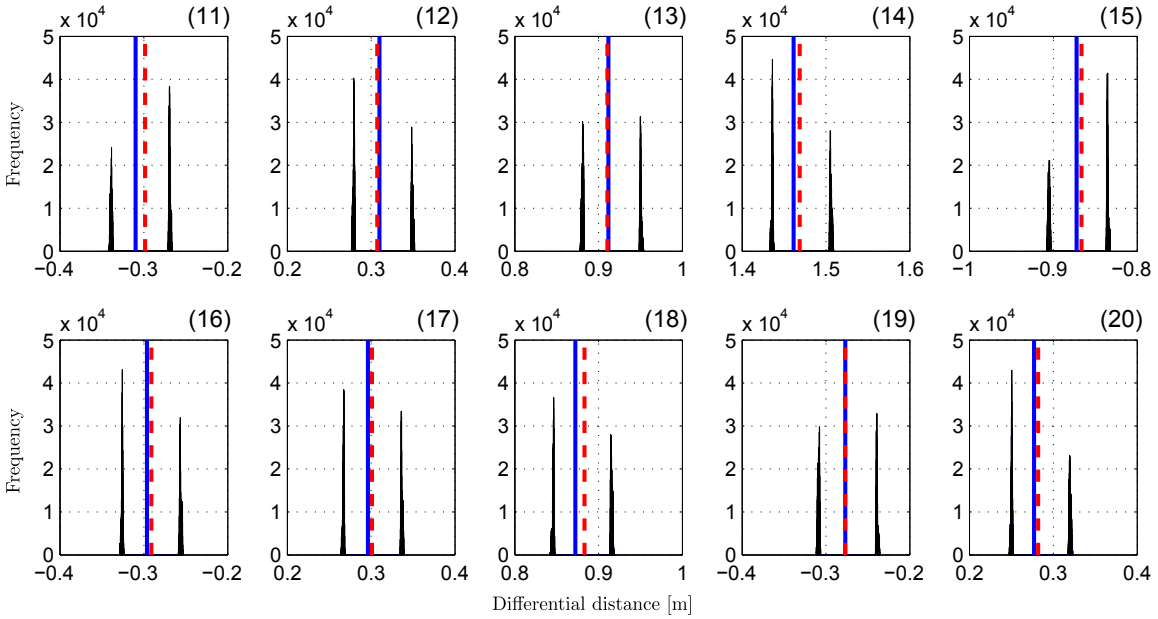

Figure 6.23: Histogram of estimated values $\hat{d}_{ij}$, distance true values $d_{ij_{\mathrm{TV}}}$ (blue) and mean estimated values $\bar{d}_{ij}$ (red) for positions (11) to (20). Static, noise-free and multipath-free measurements

Figure 6.24 shows the mean error $\left(\bar{d}_{ij} - d_{ij_{\mathrm{TV}}}\right)$ in every position. It can be seen that the mean error in these close-to-ideal conditions is smaller than 1 cm for all the positions. As

previously commented, this error is not considered as an accuracy limit for the study since it is mainly caused by discretization and could be reduced using both higher sampling rates and longer integration times.

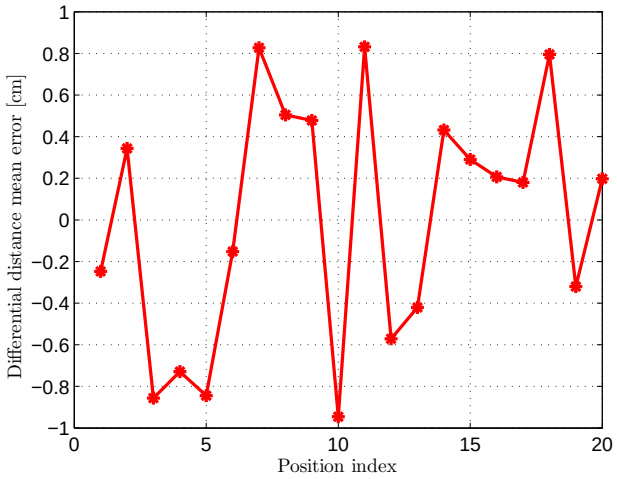

Figure 6.24: Mean error $\bar{d}_{ij} - d_{ij_{\mathrm{TV}}}$ for every position. Static, noise-free and multipath-free measurements

The results obtained with this test demonstrate the basic system operation in close-to-ideal conditions. The system is able to synchronize with the received signals for demodulation while keeping track of the varying delay caused by the emitter-receivers lack of synchronism, and to properly estimate differential distances in static and low-noise conditions. The dominant accuracy limit in this test is that caused by the discretized demodulation, which, for the signal and sampling rates used in the tests (25 MHz and 500 MS/s respectively), yields maximum errors of 1 cm.

6.4.2.2 Multipath-free test

This test evaluates the system performance including realistic noise levels depending on the received optical power for every target position. The received signals are generated with the adequate differential delays and SNR level for every position, following the data in table 6.1 and figures 6.17 and 6.18. Similarly to the previous test, the delay drift caused by frequency errors between emitter and receivers and the effect of the received signals discretization are also included.

Oscilloscope snapshots with examples of the noise-affected input signals generated for this test is shown in figures 6.25 and 6.26.

Figure 6.27.a shows the measured differential distances in every test position, while figure 6.27.b shows the distance true values $\left(d_{ij_{\mathrm{TV}}}\right)$ and the average estimated values $\left(\hat{d}_{ij}\right)$.

Similarly to the previous test, figures 6.28 and 6.29 show histograms of the measurements in every position. In this case, it can be seen how measurement dispersion around the two possible values in every position is higher due to the higher noise levels. In the lower SNR positions, such as (1), (2), (7), (8), (9) or (14), the two Gaussian distributions of the measurements are

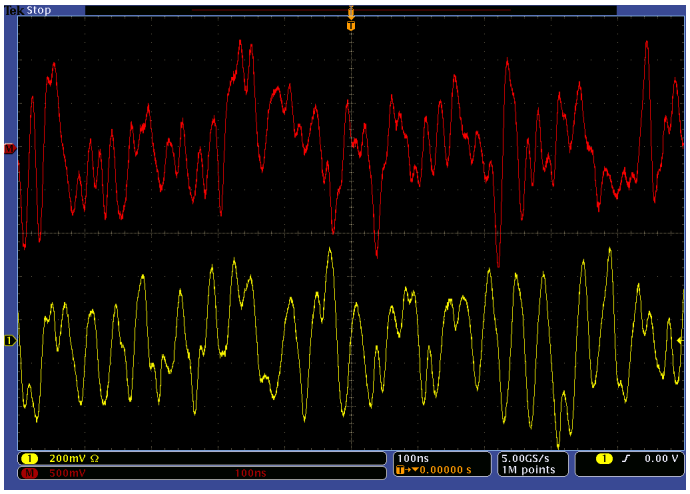

Figure 6.25: Oscilloscope snapshot of the input signals in multipath-free conditions. Red signal: SNR=65 dBHz. Yellow signal: SNR=80 dBHz

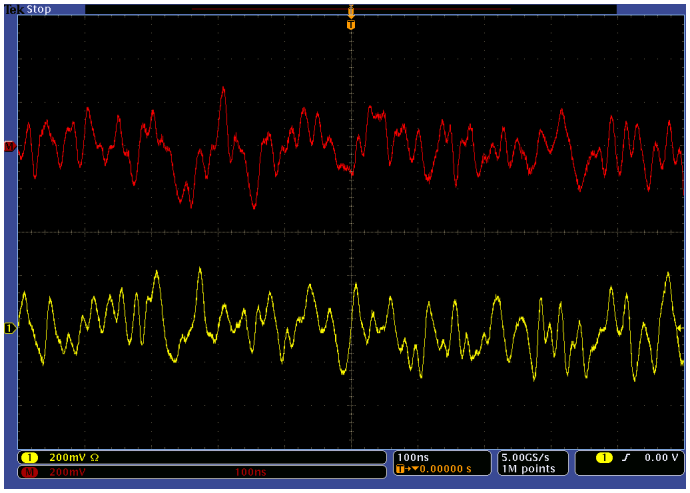

Figure 6.26: Oscilloscope snapshot of the input signals in multipath-free conditions. SNR of both signals is 70 dBHz

overlapped and cannot be distinguished. The cause and implications of these steps, that depend on the sampling rate, where already discussed in the beginning of this subsection (6.4.2).

Figure 6.30 shows the mean error $\left(\bar{d}_{ij} - d_{ij_{\mathrm{TV}}}\right)$ for every position. It can be seen that mean errors are higher than those yielded by the noise-free test, being close to 3 cm in three positions while staying under 2 cm for the rest. Individual test has been repeated in some positions using the same conditions with double (1 GS/s) and half (250 MS/s) of the sampling rate used in the test. The results show that this error is also proportional to the sampling rate, meaning that it is probably related with the discretized demodulation process and, equally to the distance resolution errors, it can be easily reduced (assuming an increase in the system cost) by applying higher sampling rates. In any case, the formal investigation of this effect is suggested for future works.

Figure 6.31 shows the standard deviation of the measurements in every position $\left(\sigma_{\hat{d}_{ij}}\right)$. The figure compares the measured results with the theoretical expected values calculated using the

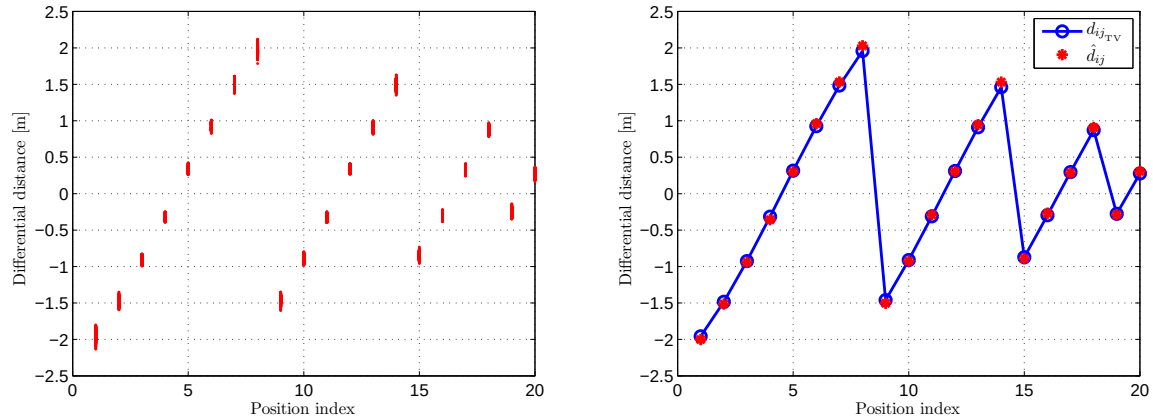

(a) Estimated distances $\hat{d}_{ij}$

(b) Distance true values $d_{ij_{\mathrm{TV}}}$ and mean estimated values $\bar{d}_{ij}$

Figure 6.27: Distance true and estimated values for every position. Static multipath-free measurements

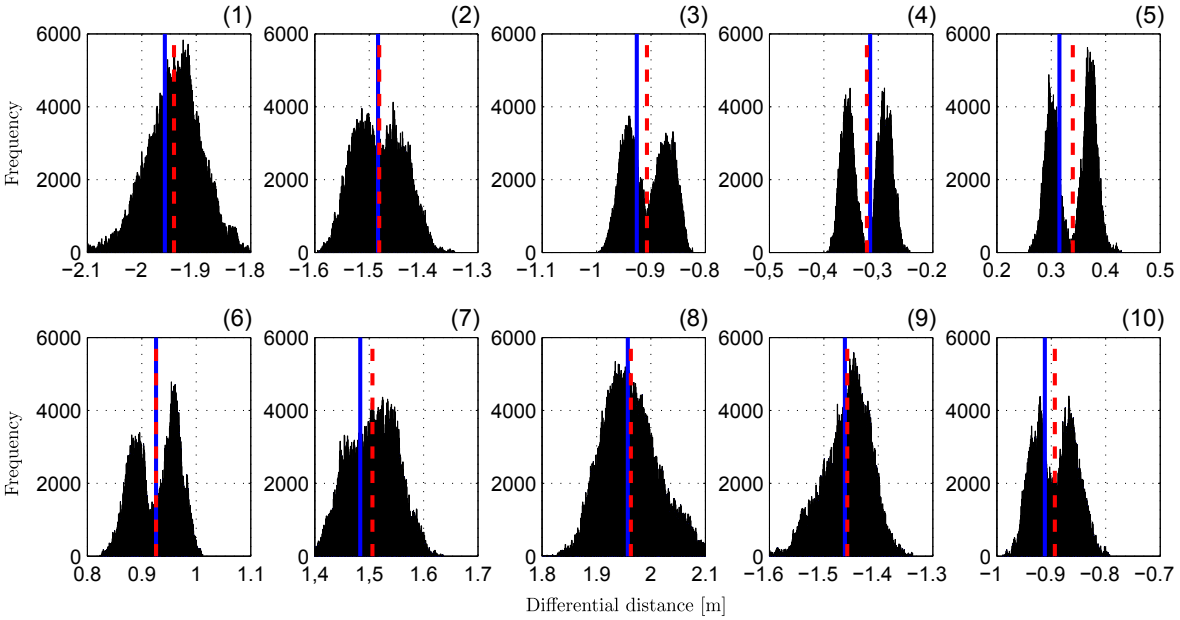

Figure 6.28: Histogram of estimated values $\hat{d}_{ij}$, distance true values $d_{ij_{\mathrm{TV}}}$ (blue) and mean estimated values $\bar{d}_{ij}$ (red) for positions (1) to (10). Static multipath-free measurements

model of the system derived in previous chapters and summarize in 6.1. Theoretical expected standard deviations are depicted with blue circles while measured values are plotted using red dots. The deviation has been calculated removing the effect of the distance steps caused by the discretized demodulation, i.e., it is the weighted (by number of samples) average of the standard deviations of both Gaussian distributions shown in figures 6.28 and 6.29 for every position. This correction has been made to provide a good representation of the system precision limits due to noise independently of sampling rate.

This test aims at validating the error model regarding noise and evaluating the system

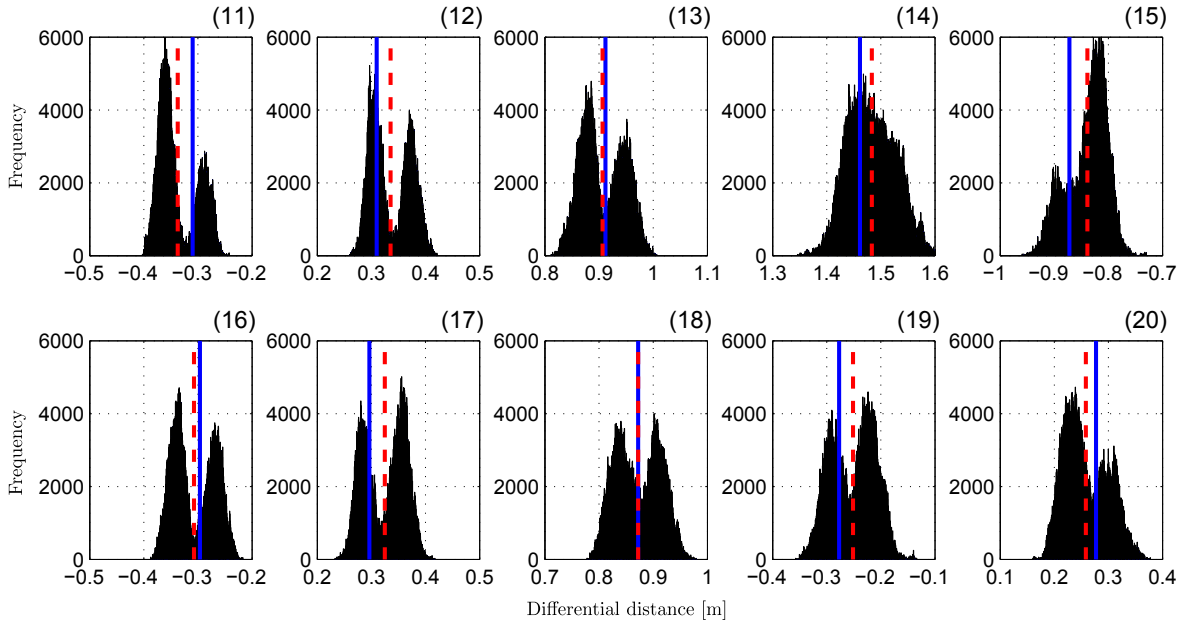

Figure 6.29: Histogram of estimated values $\hat{d}_{ij}$, distance true values $d_{ij_{\mathrm{TV}}}$ (blue) and mean estimated values $\bar{d}_{ij}$ (red) for positions (11) to (20). Static multipath-free measurements

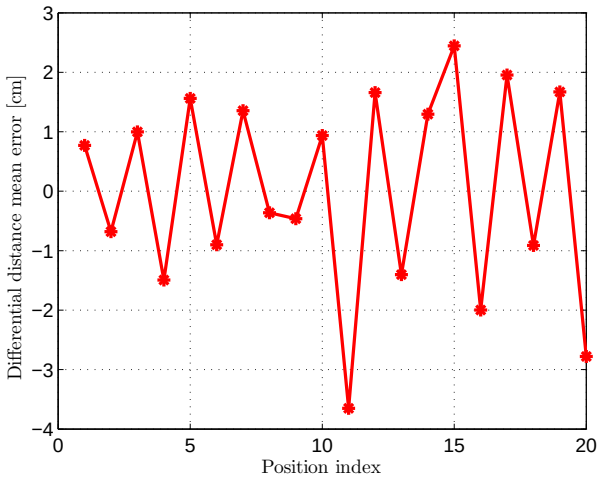

Figure 6.30: Mean error $\bar{d}_{ij} - d_{ij_{\mathrm{TV}}}$ for every position. Static multipath-free measurements

performance under realistic SNR levels. As can be seen in the figure, the measured deviations are slightly higher than the theoretical one, however, this difference is smaller than 0.5 cm in most cases and the observed trends in the deviation depending on the test position are very similar between the measurements and the model. The achieved results can be reasonably considered as a good validation of the error model for the global system performance affected by noise. Noise is the dominant precision-limiting factor in the proposed architecture. These results also show that the system performance in the defined scenario, which is a good representation of a standard (low-ceiling) indoor environment, can yield precision errors below 7 cm in two standard deviations, while most test positions do not surpass 5 cm.

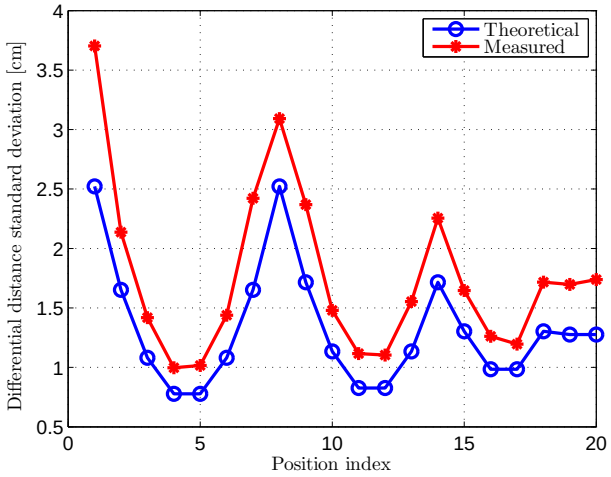

Figure 6.31: Standard deviation $\sigma_{\hat{d}_{ij}}$ of estimated distances for every position. Static multipath-free measurements

6.4.2.3 Noise and multipath test

This test evaluates the system performance in the most realistic and demanding conditions. All the principal error sources in static conditions are considered: every received signal contains the SNR and multipath corresponding to each position. As in previous multipath tests, one dominant multipath component is considered, taking the power and delays calculated in the previous section and shown in table 6.2 and figure 6.19, assuming specular reflection and a reflectivity of 0.6 in ceiling and floor materials. The clock drift between emitter and receivers is also included in the test.

An oscilloscope snapshot with an example of the noise and multipath-affected input signals generated for this test is shown in figure 6.32.

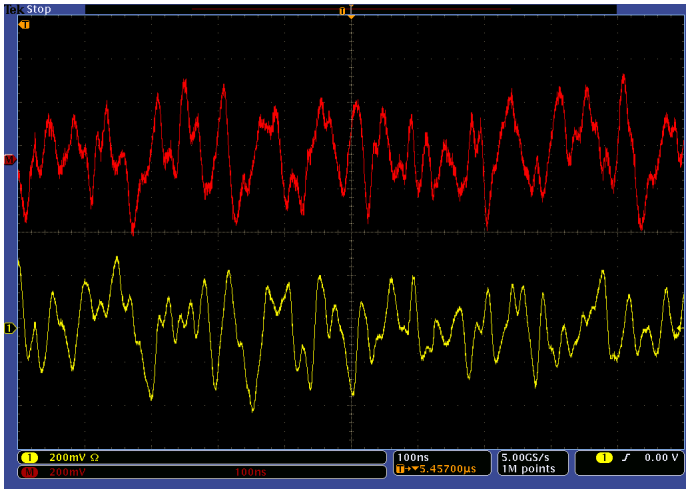

Figure 6.32: Oscilloscope snapshot of the input signals affected by noise and multipath. Red signal: SNR=80 dBHz, NLOS-to-LOS delay: 0.32 chips, NLOS-to-LOS power: 22%. Yellow signal: SNR=80 dBHz, NLOS-to-LOS delay: 0.42 chips, NLOS-to-LOS power: 0.3%

Figure 6.33.a shows the measured differential distances in every test position, and figure

6.33.b shows the distance true values $\left(d_{ij_{\mathrm{TV}}}\right)$ and the average estimated values $\left(\hat{d}_{ij}\right)$. Final SNR levels are rather comparable to those of the multipath-free test, hence yielding similar histograms than those in figures 6.28 and 6.29 except for the mean values, so they are not provided for this test. The only relevant differences are the mean distances to the true value for each position, which, in this multipath-affected case, are much higher.

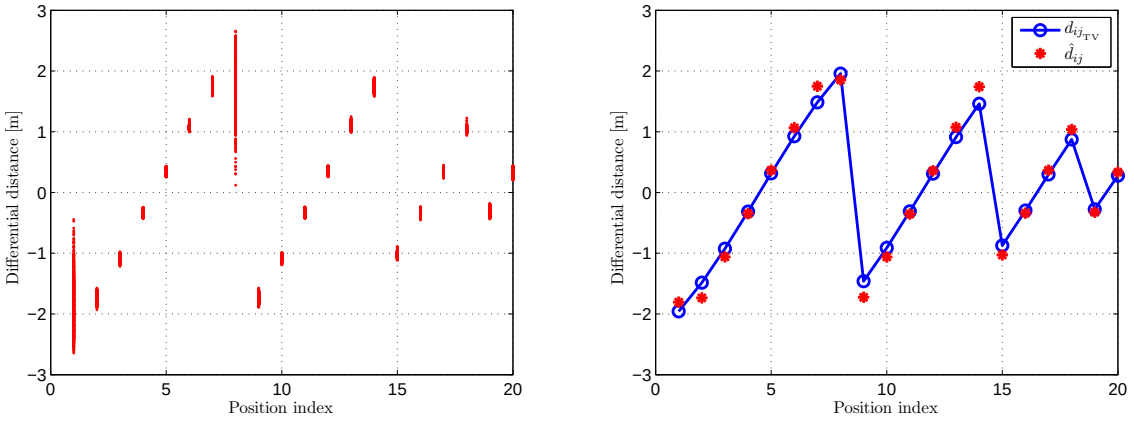

(a) Estimated distances $\hat{d}_{ij}$

(b) Distance true values $d_{ij_{\mathrm{TV}}}$ and mean estimated values $\bar{d}_{ij}$

Figure 6.33: Distance true and estimated values for every position. Static measurements

This can be appreciated in figure 6.34, where the mean errors $\left(\bar{d}_{ij} - d_{ij_{\mathrm{TV}}}\right)$ for every position are plotted. It can be seen that the mean error takes very high values due to multipath, reaching errors higher than 25 cm in the worst-case positions. As expected from the multipath parameters in the test scenario given in table 6.2 and figure 6.19, multipath errors become more critical when the distance difference is high, i.e., when the target is much closer to one of the receivers. In this situation, NLOS-to-LOS power ratio is very high due to the bad angle of arrival of the LOS component. In addition, NLOS-to-LOS delays are minimum in those positions, what reduces multipath rejection in the system. The results show this tendency, generally agreeing with the theoretical expectation, where the mean errors reach higher values for positions closer to one of the receivers. This situation, according to the multipath parameters, should be maximum in positions (1) and (8), however, in the results, mean errors in those positions are smaller and do not follow the expected tendency. Observing the measurements distribution in figure 6.33.a or the standard deviation results in figure 6.35, it is clear that the system is not able to operate properly in the conditions of positions (1) and (8). Those positions have a very low SNR level inherently. When multipath is considered, the highly detrimental situation imposed by the specular assumption further reduces those SNR levels, and makes the system work under its SNR thresholds, where no valid estimations can be made. These thresholds, which affect both the delay synchronization and phase estimation stages, were explained in the corresponding sections 4.2.1 and 5.3.1. The evaluation of the internal signals of the system for test positions (1) and (8) shows that both the initial acquisition and tracking stages provide valid estimations. It is after the signal demodulation under strong multipath effects when the SNR of the signal in the farthermost receiver takes values under the minimum required level. This threshold was

obtained by simulation in 5.3.1 for an estimation bandwidth of 500 kHz, as used in the tests. As can be seen in figure 5.12, the minimum required SNR in this case is approximately 60 dBHz. Observing figure 6.17, one can see that the input SNR for the farthermost receiver in positions (1) and (8) is approximately 61.6 dBHz, which would easily go under the threshold after a small reduction in the demodulation stage caused by multipath.

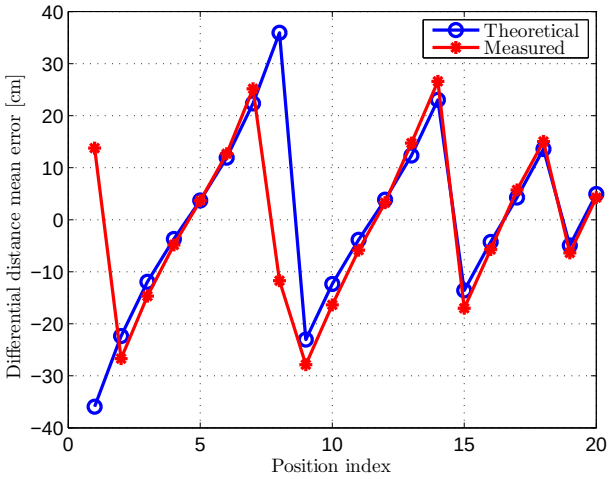

Figure 6.34: Mean error $\bar{d_{ij}} - d_{ij_{\mathrm{TV}}}$ for every position. Static measurements

Figure 6.35 shows the standard deviation of the measurements in every position $\left(\sigma_{\hat{d}_{ij}}\right)$. The measurements, plotted in red dots, are compared with the theoretically expected standard deviations, plotted in blue circles, which has been calculated from the model summarized in the beginning of this chapter. In this case, the model, apart from considering the propagation of noise related errors though the synchronization and differential ranging stages, also takes into account the effect of multipath in the delay estimation and the subsequent recovered power for the LOS and multipath components in the demodulation. The measurements closely agree with the model expected values, with average differences smaller than 0.5 cm but for positions (1) and (8). In these positions, as explained before, the system operates under its minimum required SNR and is not able to provide a valid estimation.

These results clearly show the critical impact of multipath on the measurement, still being, despite the mitigation provided by the proposed system (which will be further analyzed in the next section), the main accuracy limit of this approach. It should be noted, however, that the multipath defined for the tests, i.e., assuming specular reflection in both ceiling and floor so that only one powerful multipath component reaches every receiver, is a worst-case situation compared to the diffuse reflection with a high number of multipath components that would generally appear in a real situation. Realistic multipath errors can be expected to be smaller than the ones yielded by this test, what would also avoid the SNR of the signals in positions (1) and (8) to go under its minimum level. This, however, will be analyzed in more detail in the next section on multipath mitigation.

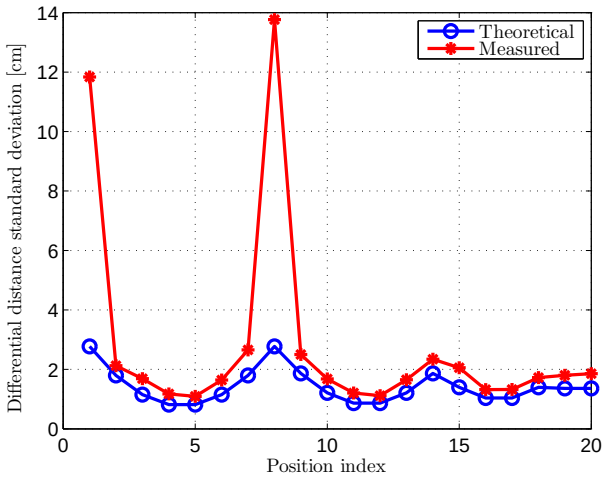

Figure 6.35: Standard deviation $\sigma_{\hat{d}_{ij}}$ of estimated distances for every position. Static measurements

6.5 Multipath performance

This section is specifically devoted to the multipath behavior of the proposed system. Several test have been performed in static and noise-free conditions to validate the system model regarding multipath and evaluate the performance of the system depending on the features of a multipath scenario. The multipath mitigation capability of the system is analyzed by comparing measured multipath errors with the expected error if standard PoA-based ranging with sinusoidal signals is applied under the same conditions.

After defining the test scenario in section 6.5.1, the system model is first specifically validated regarding multipath error in subsection 6.5.2.1, the multipath error yielded by the system is then compared to standard PoA ranging for different geometrical conditions on the scenario regarding room height and distance between emitter and receiver in section 6.5.2.2. Finally, the specular and diffuse multipath models explained in 3.2.1 are compared in section 6.5.2.3 by evaluating the measured errors using signals generated using both.

6.5.1 Test scenario

As explained in 3.2, this work focuses in the NLOS contributions caused by the double reflection in ceiling and floor surfaces of the environment, since this is the general and most problematic multipath situation that affects this technology. All the tests are based on the scenario shown in figure 6.36, which was used to develop the specular and diffuse multipath propagation models described in 3.2.1.

The multipath error is evaluated as a function of the two main parameters of this scenario, being ceiling height h and emitter-receiver horizontal distance x_{er}. The dependence with ceiling height is measured for values from 2.5 m to 8 m in steps of 0.5 m when the horizontal separation between emitter and receiver is either 0 or 3.5 m. The dependence with horizontal separation is evaluated for values between 0 and 3.5 m in 0.5 m steps when ceiling height is 2.5 m and 5 m.

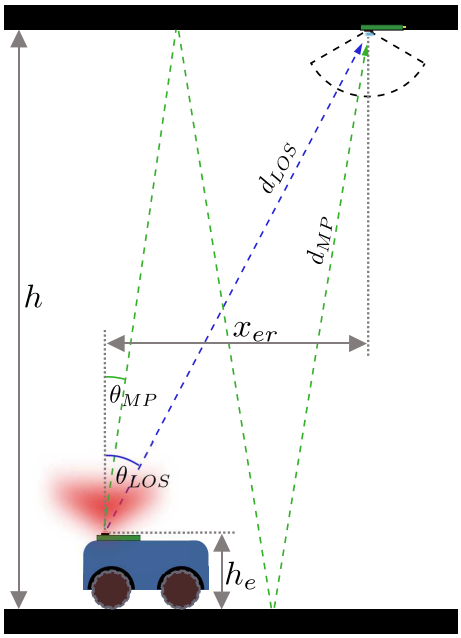

Figure 6.36: Ceiling-floor reflection diagram with the geometric parameters used in the model

The values for the distance and power ratio of LOS and NLOS components corresponding to every test and used to generate the input signals are provided in the following figures. The figures show only the values derived from the specular multipath model, formed by a single NLOS component. The values for the diffuse model are not provided since the input signal in this case is actually formed by the sum of some hundreds of NLOS components, each having its specific delay and power.

Figures 6.37 and 6.38 show graphical representations of the multipath parameters as a function of ceiling height. Figures 6.37.a and 6.38.a show the LOS, NLOS and NLOS-to-LOS distances for every ceiling height and two different horizontal separations, while figures 6.37.b and 6.38.b show the NLOS-to-LOS power ratio.

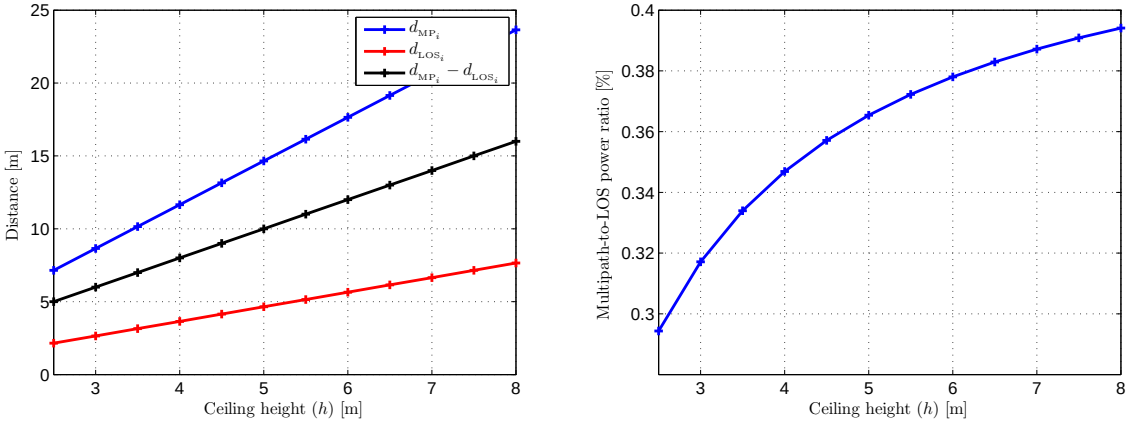

(a) NLOS, LOS and NLOS-to-LOS distances

(b) NLOS-to-LOS power ratios

Figure 6.37: Multipath parameters as a function of ceiling height h when emitter-receiver horizontal distance x_{er} is 0 m

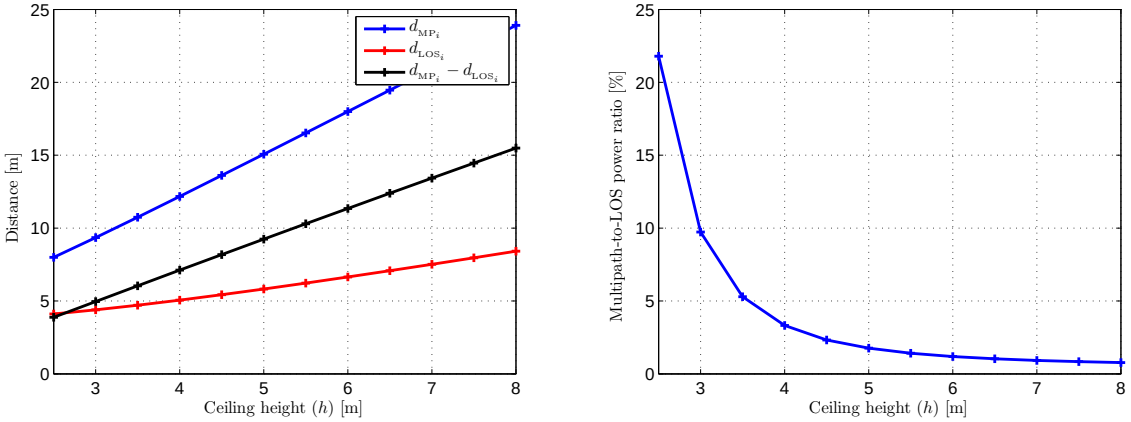

(a) NLOS, LOS and NLOS-to-LOS distances (b) NLOS-to-LOS power ratios

Figure 6.38: Multipath parameters as a function of ceiling height h when emitter-receiver horizontal distance x_{er} is 3.5 m

Figures 6.39 and 6.40 show graphical representations of the multipath parameters as a function of horizontal separation. Figures 6.39.a and 6.40.a show the LOS, NLOS and NLOS-to-LOS distances for every emitter-receiver horizontal distance and two different ceiling heights, and figures 6.39.b and 6.40.b show the NLOS-to-LOS power ratio for the same situations.

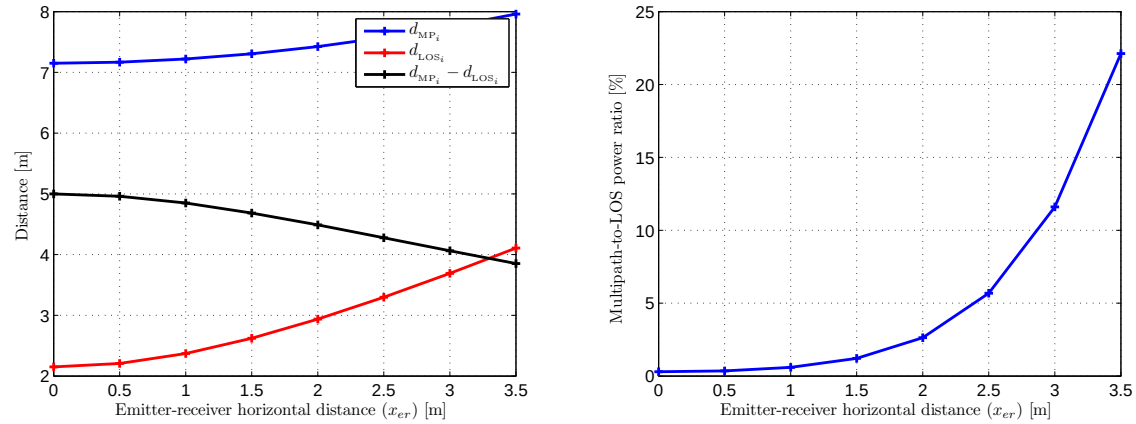

(a) NLOS, LOS and NLOS-to-LOS distances (b) NLOS-to-LOS power ratios

Figure 6.39: Multipath parameters as a function of emitter-receiver horizontal distance x_{er} when ceiling height h is 2.5 m

Equally to previous tests, the multipath-affected input signals introduced to the Simulink implementation of the measuring architecture are generated using the IR-link emulation set-up explained in section 6.3. In all cases, to simplify the interpretation of the results to understand the effect of multipath in every receiver, non-differential range measurements are performed. The system is inherently differential, so these are achieved by measuring the differential ranges between the multipath-affected signal and the signal received in the same position in multipath-free conditions. This way, the measured ranges are directly the multipath error in the conditions defined for the receiver.

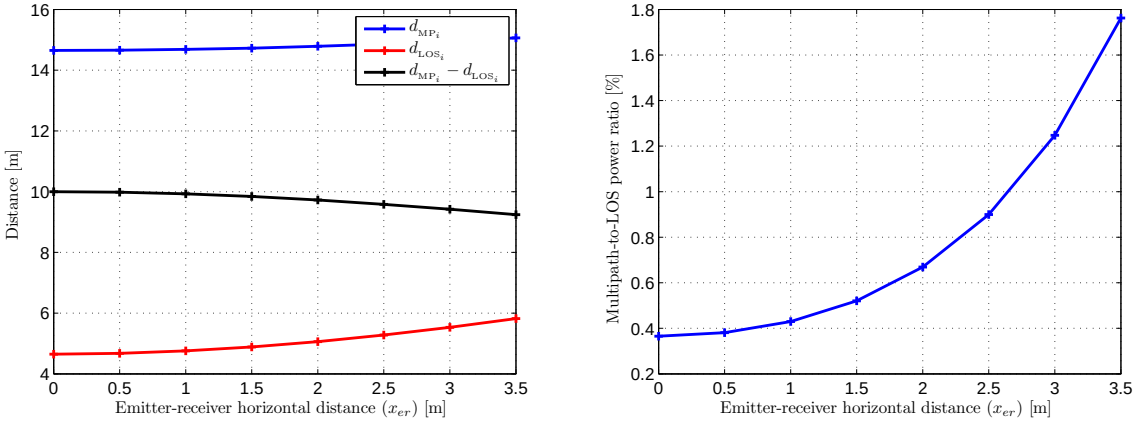

(a) NLOS, LOS and NLOS-to-LOS distances

(b) NLOS-to-LOS power ratios

Figure 6.40: Multipath parameters as a function of emitter-receiver horizontal distance x_{er} when ceiling height h is 5 m

An oscilloscope snapshot with an example of the input signals generated for these tests is shown in figure 6.41.

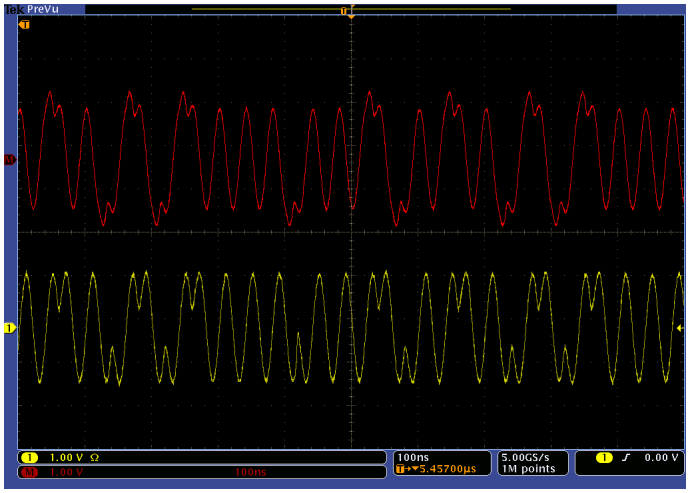

Figure 6.41: Oscilloscope snapshot of the input signals in noise-free conditions. Red signal: NLOS-to-LOS delay: 0.32 chips, NLOS-to-LOS power: 22%. Yellow signal: multipath-free

6.5.2 Results

6.5.2.1 Validation of the error model regarding multipath

These tests aim to validate the error model developed for the proposed system using the derivations of its theoretical performance obtained in chapters 4 and 5, and summarized in section 6.1 of this chapter. The mean error in the estimated distances in static and noise-free conditions has been measured when the input signals are contaminated with NLOS components, and compared with the expected error yielded by the model under the same conditions. The validation is performed with multipath-affected signals generated using only the specular model for simplicity.

The error model allow a high number of multipath components, limited by the computational requirements of the multipath error calculations in the tracking stage. This error, as commented in the specific section, is calculated by simulation in every case; and these simulations could not be performed with the very high number of components yielded by the diffuse multipath model.

Figure 6.42 shows the measured error $\bar{d} - d_{\mathrm{TV}}$ compared with the theoretical expected error as a function of ceiling height, sweeping values from 2.5 m to 8 m. The test is performed for two different horizontal distances between emitter and receiver. Figure 6.42.a shows the results when the target is directly under the receiver and figure 6.42.b shows the results when the horizontal separation between both is 3.5 m, representing the maximum separation between them as defined in the test scenario for the global performance tests depicted in figure 6.14.

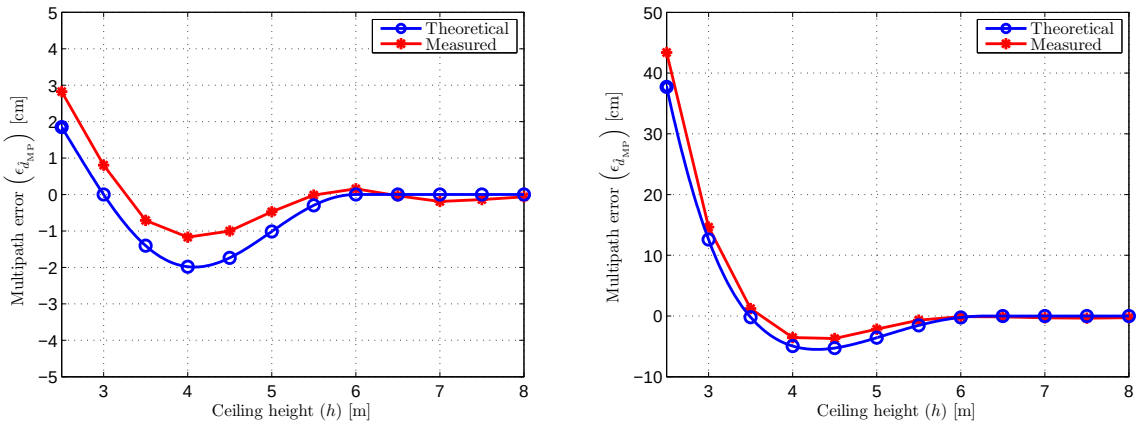

(a) $x_{er} = 0$ m (b) $x_{er} = 3.5$ m

Figure 6.42: Multipath error $\bar{d} - d_{\mathrm{TV}}$ as a function of ceiling height h for two different emitter-receiver horizontal distances $x_{er} = (0,\ 3.5)$ m. Measured error compared with theoretical system model (signals generated with specular multipath model)

Figure 6.43 shows the complementary tests to the previous one, also comparing measured errors with the theoretical expected ones yielded by the model. In this case, the horizontal distance between emitter and receiver is swept from 0 (vertical alignment) to 3.5 m for two different ceiling heights: 2.5 m, shown in figure 6.43.a and 5 m, shown in figure 6.43.b.

Observing the results, a clearly critical situation can be simultaneously seen in both tests in figures 6.42.b and 6.43.a. These results show that multipath error when the specular model is considered takes significantly high values when the ceiling height becomes smaller and the separation between emitter and receiver is increased, as can be seen, in the extreme cases, for $h = 2.5$ m and $x_{er} = 3.5$ m. This geometric dependencies of the multipath error are analyzed in more depth and compared to the diffuse multipath assumption in the next subsection.

Regarding the model validation, the results show an acceptable agreement with the theoretical error model. Differences smaller than 1 cm are generally obtained in most cases, but for the situations when the error takes very high values of several dm. The differences in these cases are slightly higher than 10 % of the measured errors. In all cases the tendencies observed in the errors depending on geometry are well represented by the error model. An accurate estimation of errors in the cm/sub-cm level cannot be obtained with the current model, however, it can

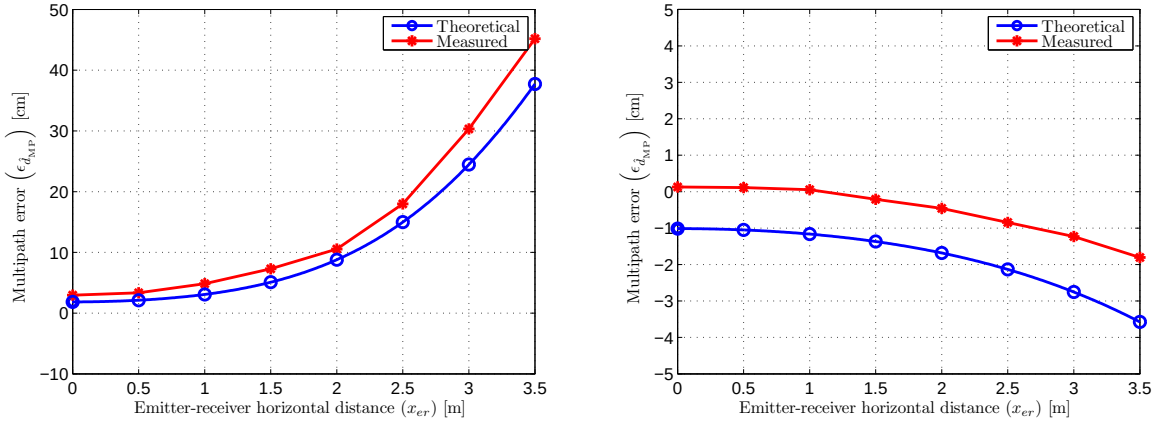

(a) $h = 2.5$ m (b) $h = 5$ m

Figure 6.43: Multipath error $\bar{d} - d_{\mathrm{TV}}$ as a function of emitter-receiver horizontal distance x_{er} for two different ceiling heights $h = (2.5,\ 5)$ m. Measured error compared with theoretical system model (signals generated with specular multipath model)

be used as an adequate tool for the evaluation of the expected system performance affected by multipath. Given the degree of similarity between the model results and the measurements, it is reasonable to think that the accuracy in a theoretical estimation of multipath errors in certain real environment would be more limitted by the accuracy of the multipath propagation model than by the system error model.

6.5.2.2 Multipath mitigation

The following tests are focused on studying the capacity of the proposed system to reduce multipath errors. The multipath mitigation capabilities of the system are evaluated by comparison with standard PoA ranging, where phase-shifts are measured on simple sinusoidal intensity modulated signals, as implemented in the previous version of the optical LPS developed in [Martín-Gorostiza et al., 2011].

The model applied to calculate the expected multipath error in PoA ranging under the same conditions used to perform the measurements is a simple interference model between sinusoidal components of the same frequency. This model was developed in 3.2.2 and validated in 5.3.2 with specific measurements using the phasemeter implementation, and it proved to be a good approximation of multipath effects in PoA. The geometry-dependent power and delay relationships between LOS and NLOS paths yielded by the specular and diffuse multipath models are applied both for the signal generation to perform the measurements and for computing the multipath errors in the PoA model.

The PoA multipath error model is equivalent to the multipath error model of the phasemeter of the proposed system, summarized in (6.13) and (6.14). In these tests, as previously commented, both receivers are virtually placed in the same position, one of them processing multipath-free signals, so that the estimated differential distance directly represents a single-range multipath error.

An indicator of the multipath mitigation capacity of the system is calculated for each set of results, defined as the error reduction rate of the measurements compared to PoA expressed as a %, being

$$\left| \frac{\epsilon_{\hat{d}_{\mathrm{MP}}} - \epsilon_{\hat{d}_{\mathrm{PoA}}}}{\epsilon_{\hat{d}_{\mathrm{PoA}}}} \right| \cdot 100 \tag{6.16}$$

where $\epsilon_{\hat{d}_{\mathrm{MP}}}$ is the single-range measured multipath error and $\epsilon_{\hat{d}_{\mathrm{PoA}}}$ is the PoA multipath error computed with the model. Note that, due to the cyclic behavior of multipath error in the PoA model, the computed error is 0 in some particular positions and the mitigation rate cannot be calculated.

The comparison between the model results and the measured errors are a good indicator of the improvement in multipath behavior of the proposal compared to the previous alternative, which is itself a good representative of a standard ranging solution to fulfill the application requirements.

As commented in 3.2.1, the diffuse model provides a good approximation given the magnitude of the errors that it causes compared to the real multipath effects measured in the test of the previous system [Pallarés-Puerto, 2010]. Consequently, the following test, when performed using the diffuse model, can be also considered as an approximate estimation of the expected errors in the defined scenarios.

Equally to the model validation in the previous subsection, these tests have been performed sweeping both ceiling height and horizontal distance between emitter and receiver, using signals generated with the specular and diffuse multipath models in both cases.

Multipath mitigation with specular reflection model

Figure 6.44 show the measured absolute mean error compared to the expected error in PoA as a function of ceiling height when specular multipath is assumed. Figure 6.44.a and 6.44.b show the resulting errors for an emitter-receiver separation of 0 m and 3.5 m respectively, while figures 6.44.c and 6.44.d show the associated multipath error reduction rates for both distances.

Figure 6.45 show the equivalent results as a function of the horizontal separation between emitter and receiver, i.e., absolute mean error and error reduction rates using the specular reflection model. Figure 6.45.a and 6.45.b show the resulting errors for a ceiling height of 2.5 m and 5 m respectively, while figures 6.45.c and 6.45.d show the multipath error reduction rates for each ceiling height.

The previous results, depicted in figures 6.44 and 6.45, were obtained with multipath contributions to the input signal calculated using the specular reflection model defined in section 3.2.1.1. It should be noted that this model defines, in general, a more critical multipath scenario than the more realistic diffuse model, as will be seen in the comparison between the results with both reflection models in subsection 6.5.2.3, and was demonstrated in 3.2.3 for PoA ranging.

Observing the measured errors, one can see that the expected PoA error in the most critical multipath situations for low ceiling height and high emitter-receiver separation, already seen in the validations measurements, is of similar value than the measurements. This is, the proposed system hardly provides any multipath attenuation in these conditions. This is mainly caused

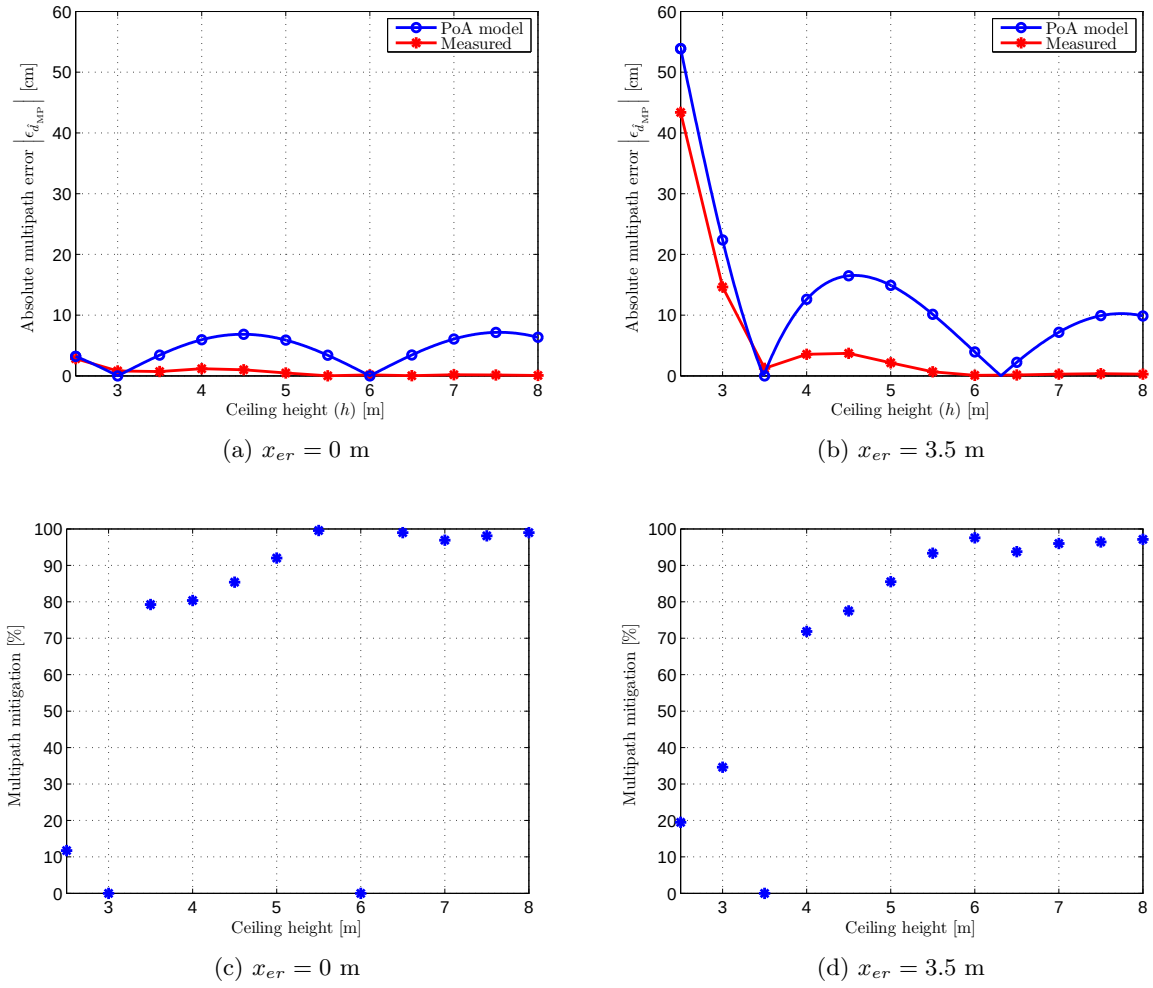

(a) $x_{er} = 0$ m (b) $x_{er} = 3.5$ m

(c) $x_{er} = 0$ m (d) $x_{er} = 3.5$ m

Figure 6.44: Absolute multipath error $\left|\bar{d} - d_{\mathrm{TV}}\right|$ and mitigation rate % as a function of ceiling height h for two different emitter-receiver horizontal distances $x_{er} = (0,\ 3.5)$ m. Measured error compared with estimated error in PoA ranging (signals generated with specular multipath model)

by the high NLOS-to-LOS power in this situation due to the unfavorable LOS reception angle, causing the delay estimated by the synchronization stage to yield a high multipath error. This, together with the small separation between components, reduces the despread power for the LOS component in the demodulation process while hardly attenuating that of the NLOS component. Therefore, the final signal in the phasemeter is still severely affected by it, yielding errors close to 50 cm where multipath has been hardly reduced by 10 %.

When ceiling height is increased in the results in figure 6.44, the delay between LOS and NLOS components becomes higher, but, mainly, multipath power is much smaller. The synchronization stage can provide delay estimations closer to the true LOS delay in these conditions, so that the demodulation process can effectively recover the LOS power while maintaining the NLOS power spread. The system becomes very effective in reducing the error in all the positions but the ones with very low ceiling, reaching mitigation rates higher than 70 % independently of the vertical alignment between emitter and receiver for any environment where the ceiling is

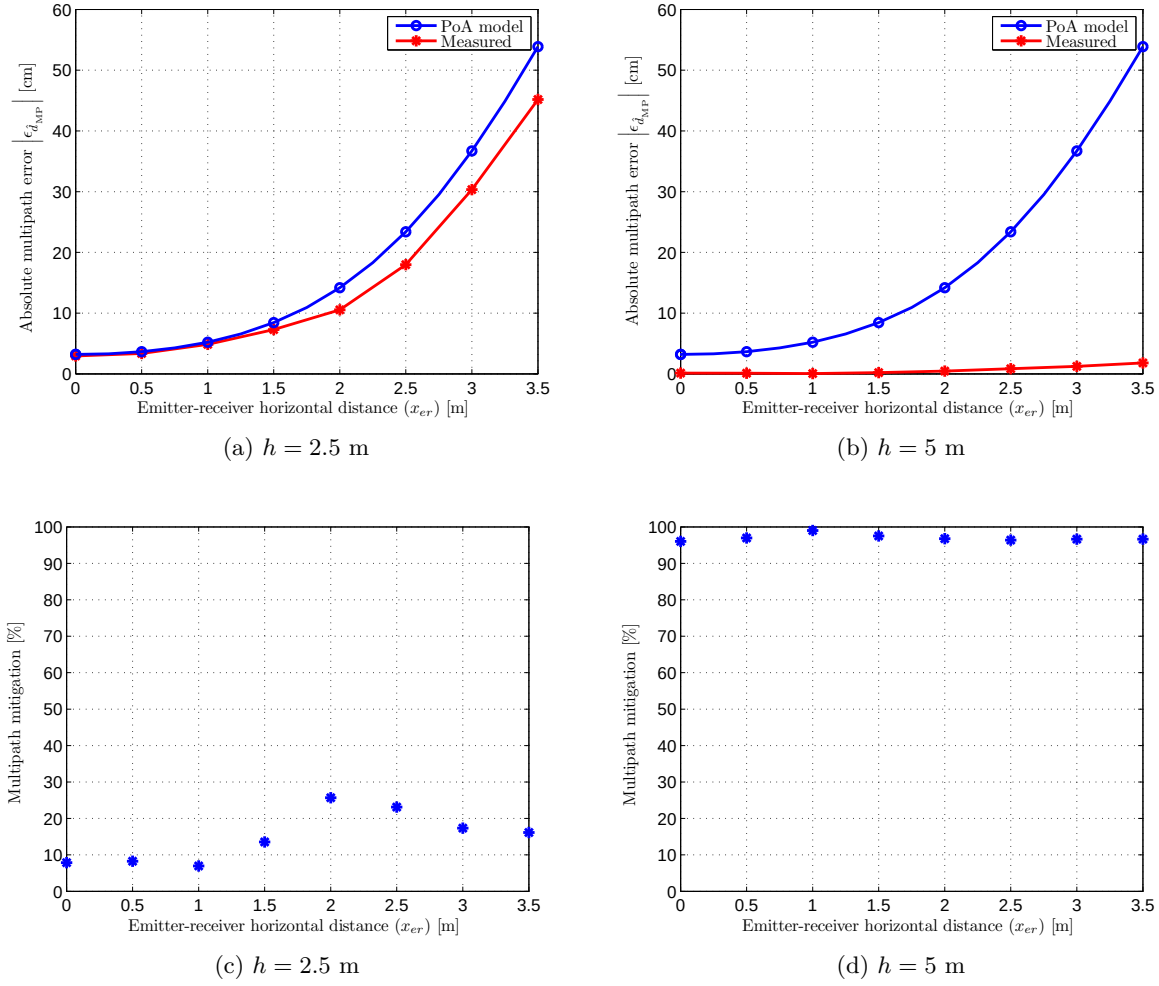

(a) $h = 2.5$ m

(b) $h = 5$ m

(c) $h = 2.5$ m

(d) $h = 5$ m

Figure 6.45: Absolute multipath error $\left|\bar{d} - d_{\text{TV}}\right|$ and mitigation rate % as a function of emitter-receiver horizontal distance x_{er} for two different ceiling heights $h = (2.5,\ 5)$ m. Measured error compared with estimated error in PoA ranging (signals generated with specular multipath model)

higher than 3.5 m.

Observing the results in figure 6.45.a and 6.45.c, the low capacity of the system for reducing multipath for very low ceiling heights can be observed, independently of the emitter-receiver alignment. On the other hand, observing figures 6.45.b and 6.45.d, very good mitigation levels can be seen for the larger environment of 5 m height, where mitigation levels are higher than 95 % independently of the emitter-receiver vertical alignment.

Two general conclusions can be drawn form this test where specular reflection is assumed:

- Multipath error affecting certain receiver has a critical influence in the measurements, both in standard PoA ranging and the proposed system, when the scenario has very low ceiling and the horizontal separation between the emitter and the specific receiver is high.
- The effectiveness of the proposed system to reduce multipath error is strongly related with ceiling height, and rather independent from the emitter-receiver separation if specular

multipath is considered. The system hardly reduces multipath errors in environments with ceilings below 3 m, however, mitigation rates are rapidly increased for higher room heights. Multipath is reduced more than 90 % when the ceiling is higher than 5 m. This is fundamentally related to the NLOS-to-LOS delay, since all the test cases where mitigation is poor correspond to delay differences below 6 m, i.e., half of the chip length.

Multipath mitigation with diffuse reflection model

The following figures show the results for tests equivalents to the previous ones, i.e., multipath errors as a function ceiling height and emitter-receiver horizontal distance, but applying the diffuse reflection model to generate the input signals and to compute the PoA errors.

Figure 6.46.a and 6.46.b show the measured and computed absolute mean errors as a function of ceiling height when the emitter-receiver vertical alignment is 0 m and 3.5 m respectively, while figures 6.46.c and 6.46.d show the multipath error reduction rates calculated for both.

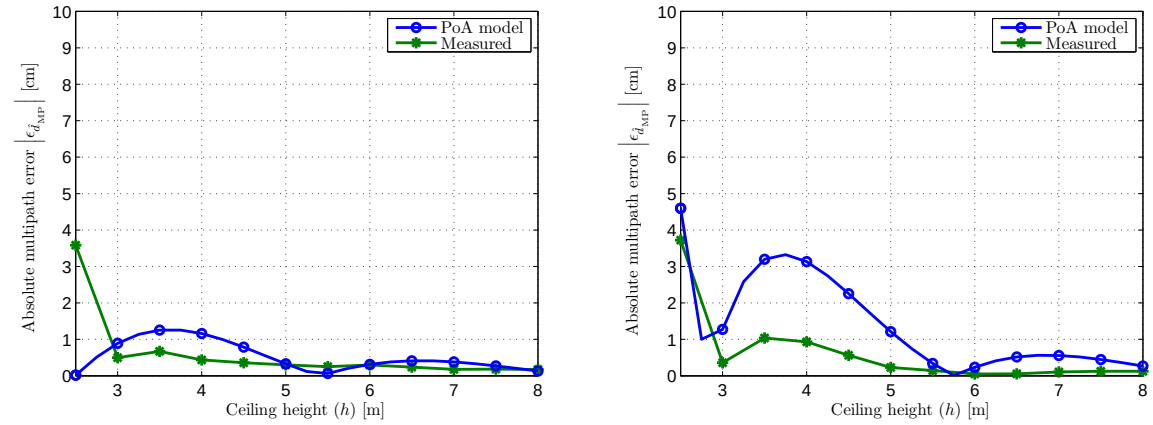

(a) $x_{er} = 0$ m (b) $x_{er} = 3.5$ m

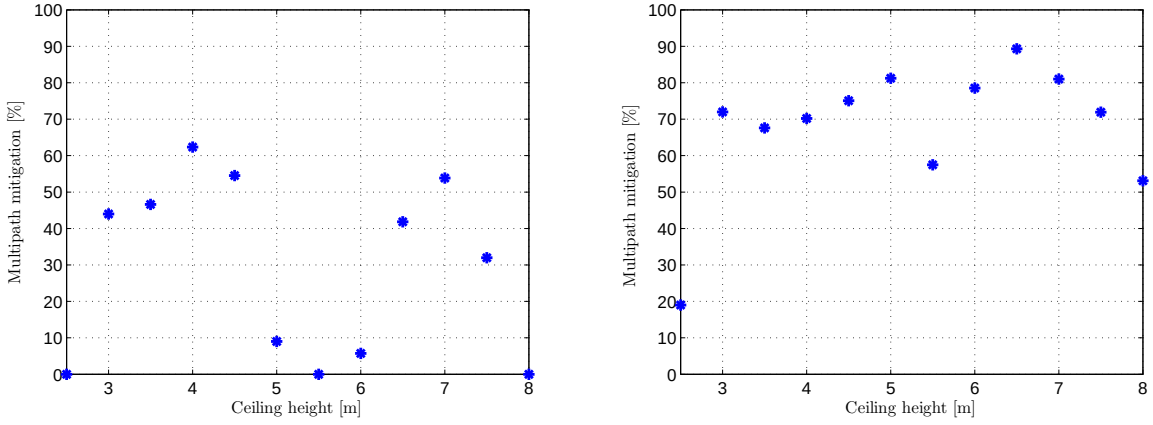

(c) $x_{er} = 0$ m (d) $x_{er} = 3.5$ m

Figure 6.46: Absolute multipath error $\left|\bar{d} - d_{\mathrm{TV}}\right|$ and mitigation rate % as a function of ceiling height h for two different emitter-receiver horizontal distances $x_{er} = (0,\ 3.5)$ m. Measured error compared with estimated error in PoA ranging (signals generated with diffuse multipath model)

Figure 6.47.a and 6.47.b depict the measured and computed absolute mean errors as a

function of emitter-receiver horizontal distance for ceiling heights of 2.5 m and 5 m respectively, and figures 6.47.c and 6.47.d show their associated multipath error reduction rates.

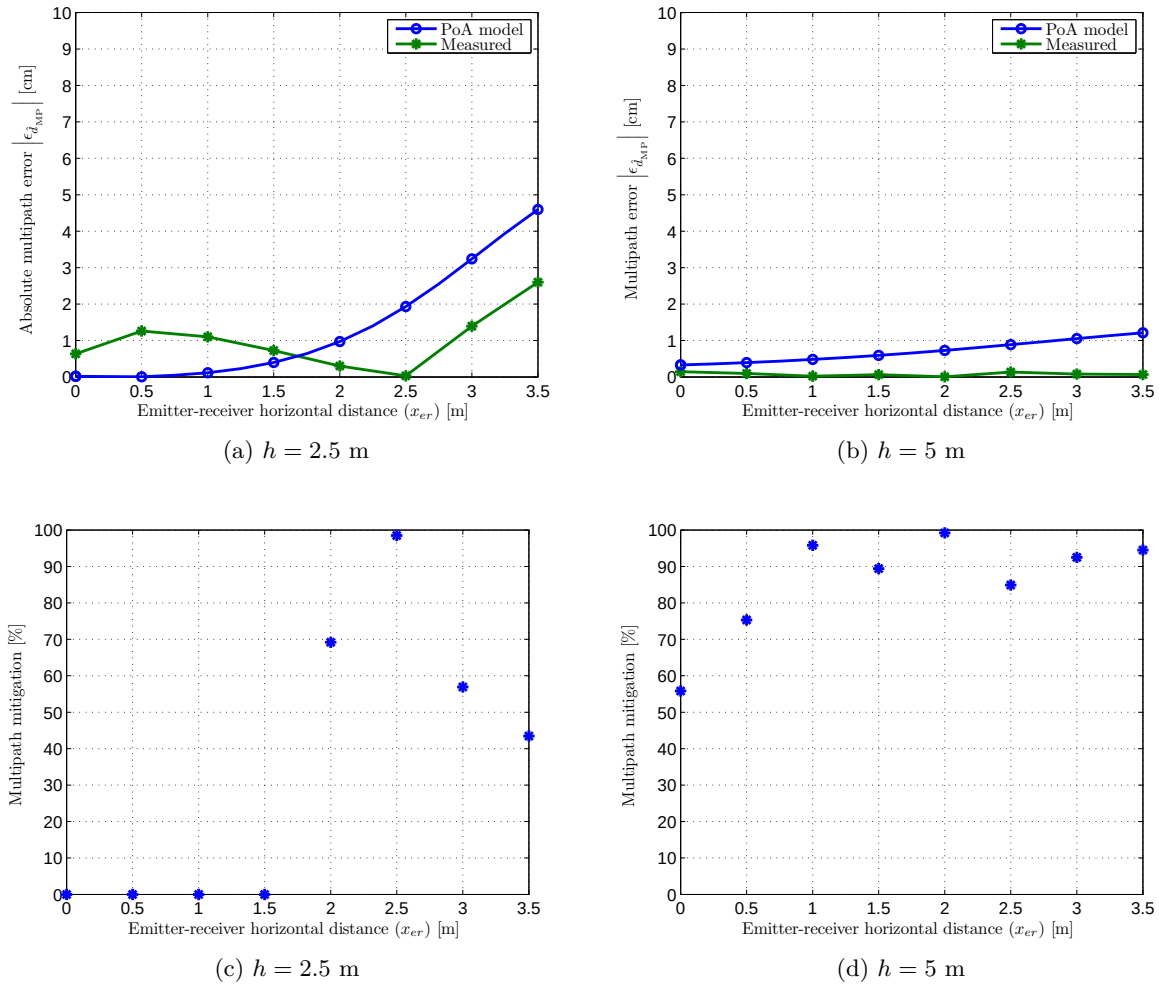

(a) $h = 2.5$ m

(b) $h = 5$ m

(c) $h = 2.5$ m

(d) $h = 5$ m

Figure 6.47: Absolute multipath error $\left|\bar{d} - d_{\text{TV}}\right|$ and mitigation rate % as a function of emitter-receiver horizontal distance x_{er} for two different ceiling heights $h = (2.5,\ 5)$ m. Measured error compared with estimated error in PoA ranging (signals generated with diffuse multipath model)

In the set of results in figures 6.46 and 6.47, a behavior similar to the tests with the specular assumption can be seen, nevertheless, significantly different magnitudes are observed. The highest errors are again observed in the combination of low ceiling and high emitter-receiver separation, although in this case, when the more realistic assumption of diffuse reflection for NLOS component is made, the maximum measured and estimated errors are smaller than 5 cm, in contrast to the very high errors close to 50 cm for the specular model.

Observing figures 6.46.a and 6.46.c, significant conclusions on the mitigation capabilities of the system when the emitter and the receiver are vertically aligned cannot be made. The measured errors, independently of ceiling height, are very low, smaller than 0.5 cm in most cases. However, the errors yielded by the PoA model are also very low, showing a very friendly multipath situation, where multipath effects are probably mixed with other small error contributions of the system (note that mean errors in the cm level where already observed in the multipath-free

tests in section 6.4). Slightly better observations can be made from figures 6.46.b and 6.46.d, when the emitter and receiver are vertically misaligned by 3.5 m. In this case, an increase in the mitigation rate for higher ceilings can be seen. The measured and model errors are, however, still very low and could be mixed with other small accuracy-reducing contributions.

A similar situation occurs with the tests varying emitter-receiver vertical alignment in figures 6.47.a, 6.47.b, 6.47.c and 6.47.d. The yielded errors, both by the PoA model and the measurements, are in the range of 1-2 cm in most positions. No reliable conclusions about the mitigation capabilities of the system can be made for the results with the low ceiling in 2.5 m. The results with a ceiling height of 5 m, although having very small errors too, do show a clear behavior comparing the PoA model results and the measurements, where, despite the small values, a distinguishable reduction of the error provided by the system can be seen in all the positions.

The main conclusions than can be drawn for the tests when the diffuse reflection model is applied are:

- The multipath error, both in the PoA model and the measurements with the proposed system, is generally much lower in contrast with the specular model. A specific comparison between the measurements with both models is done in the next section.
- The mitigation capabilities of the system are not easy to be concluded from these tests, since the measured errors are very low and of comparable magnitude to other error sources already observed in the multipath-free tests. Nevertheless, considering the similar tendencies with the tests using the specular model, it is reasonable to draw the same conclusion from these results, i.e., the system effectiveness in mitigating multipath is mainly dependent on ceiling height, reaching much better multipath attenuation values for high ceiling environment rather independently from the emitter-receiver alignment.

6.5.2.3 Comparison between specular and diffuse multipath models

The measured errors shown in the previous subsection varying the scenario geometry are shown next without including the PoA model expected errors. The results measured under the same conditions with both the specular and the diffuse multipath models are depicted together, aiming to easily compare the effect of using each model.

Figure 6.48 shows the measured mean errors as a function of ceiling height for two different emitter-receiver horizontal distances when the multipath contributions in signal introduced in the measuring architecture have been calculated using either the specular or the diffuse reflection assumptions.

Figure 6.49 shows equivalent results, i.e., measured mean errors depending on the multipath model applied for generating the input signal, as a function of the vertical alignment between emitter and receiver for two different room heights.

Observing the figures, a significant difference between them associated to some particular geometric conditions stands out, agreeing with the comparison made in 3.2.3 using the PoA multipath error model. The measured errors when both models are used, although not having

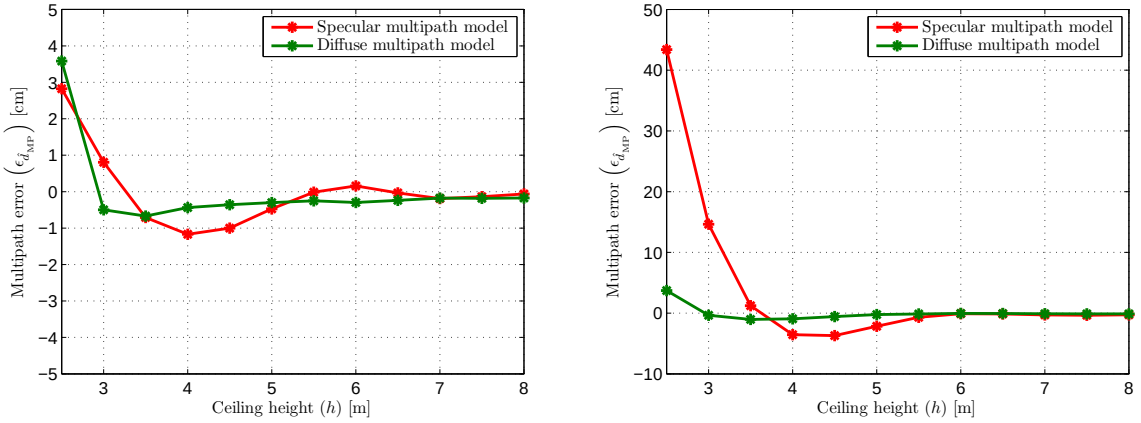

(a) $x_{er} = 0$ m (b) $x_{er} = 3.5$ m

Figure 6.48: Multipath error $\bar{d} - d_{\mathrm{TV}}$ as a function of ceiling height h for two different emitter-receiver horizontal distances $x_{er} = (0,\ 3.5)$ m, when multipath is generated using either specular or diffuse multipath model

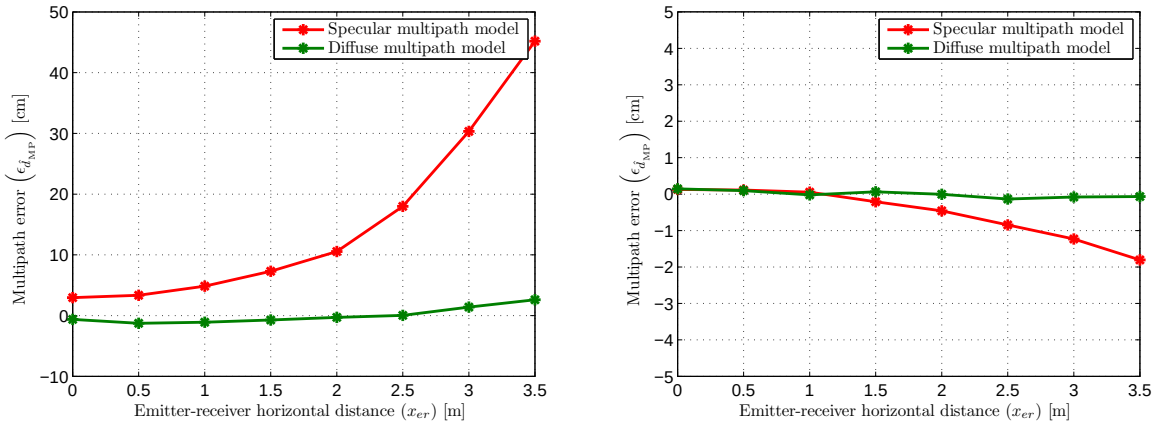

(a) $h = 2.5$ m (b) $h = 5$ m

Figure 6.49: Multipath error $\bar{d} - d_{\mathrm{TV}}$ as a function of emitter-receiver horizontal distance x_{er} for two different ceiling heights $h = (2.5,\ 5)$ m, when multipath is generated using either specular or diffuse multipath model

similar behavior when the geometric parameters are changed, are of similar magnitude in most test cases, staying below 4 cm but for the low ceiling configuration. In this specific case, the specular model tests yield much higher multipath errors that reach some tens of cm, becoming a clear worst case situation for this scenario. The diffuse reflection model is initially a more realistic approximation to NLOS propagation in real environments, taking into account the generally diffuse properties of most standard surface materials used in construction. This, however, has not been properly proved, so both models were used for the test to provide more information on the system multipath behavior and widen the obtained results to obtain better conclusions on the multipath behavior of the proposal. A proper validation of both models with optical tests to conclude whether they are a good representation of indoor multipath depending on room geometry is not the goal of this work and will be proposed for future contributions.

6.6 Summary and discussion

In this chapter, the global and specific multipath performance of the proposal have been tested and validated.

The theoretical derivations from chapters 4 and 5 about the effect of the main error sources on every stage have been integrated into a global error model, in order to be compared with the measured results for validation. This model takes into account the parameters of the input signals for the LOS component, NLOS components and input noise, system dynamics that depend on target displacement and frequency errors, and design parameters related to the architecture and the signal structure. The model links all the stages to derive how the different error components and signal parameters propagate through the system, and their impact on the accuracy and precision of the differential range measurement. To illustrate the joint operation of the whole system a sample case of the complete procedure has also been provided, showing the most relevant signals, both internal and external, involved in the measurement process.

A prototype of the ranging architecture has been implemented in Simulink. An optical link that fulfills the power and frequency requirements of the system is currently under development, so the validation of the proposed method has been performed using an emulation system for generating the received signals to be processed by the digital system. The emulation system is based on a two-channel wired connection between high performance AFG and oscilloscope, which introduce the effect of digitization and the lack of synchronism between the signals generated in the emitter and the local references in the receiver. Apart from these, the emulation set-up produces signals with configurable parameters regarding the LOS component, an arbitrary number of NLOS components, AWGN and link bandwidth.

A practical indoor scenario has been defined and reproduced using the signals generated by the emulator. The scenario is formed by a pair of receivers separated 3.5 m, and placed 2.5 m high. The emitter is 0.35 m above the floor. 20 possible positions have been defined for the emitter, in a configuration that would be adequate for forming an easily scalable 12.25 m^2 square positioning cell using 5 receivers. The power and noise levels in the received signals are obtained by radiometric calculations taking into account the scenario geometry and the characteristics of the IR link and signal conditioning proposed in section 3.1.3.1 of chapter 3, for a chip rate of 25 MHz. The maximum distance between the emitter and one receiver is 4.1 m and the SNR levels range from 61.6 to 84.1 dBHz. In the multipath-affected tests, the power and delay of the NLOS components have been calculated using both multipath propagation models defined in section 3.2.1 of chapter 3. The design parameters of the tracking stage and phasemeter are selected considering the optimizations in the corresponding chapters. The early-late spacing in the ELDLL is 0.25 chips and the tracking loop bandwidth is set to 3.5 kHz. The final measurement bandwidth is set to 500 Hz for practical reasons related to limitations of the test set-up. However, it is noteworthy that the optimization for a speed target of 1 m/s yielded a value of 60 Hz, what would produce noise-related errors approximately 3 times smaller.

In the first place, the global performance of the system has been evaluated in the defined scenario and compared to the global error model. An initial test in close-to-ideal conditions (SNR>100 dBHz and multipath-free) shows a residual mean error below 1 cm for all the test

positions, caused by the discretized demodulation. When relevant noise levels are present in the input, this mean error associated to the discretized signals is increased to values below 3 cm for all the positions. Experimental tests have demonstrated that this effect is directly related to sampling rate and can be mitigated using faster digitization, although its formal investigation is suggested for future works. The test including noise shows a good agreement with the expected errors yielded by the model. The average difference between the measured results and the model is smaller than 0.5 cm. The precision error in the defined scenario is better than 5 cm in two standard deviations in 18 of the 20 test points. The test including noise and multipath has been performed using the specular multipath model, which represents a worst-case situation regarding power of the multipath interference. The mean error in this test, clearly dominated by multipath, is close to 30 cm in the worst positions where the system can provide estimations. This test also shows that when SNR is very low in the most unfavorable positions, a critical multipath situation can further reduce the available SNR and make the system go below the SNR threshold required for the estimations. Nevertheless, this situation is not expected in practical system operation with weaker non-specular multipath components.

After the global performance evaluation, tests specifically evaluating multipath behavior have been conducted. These tests study the effect of multipath on the mean error of the measurements, varying the ceiling height and the horizontal distance between emitter and receivers. The evaluated height varies from 2.5 m to 8 m, and the horizontal separation between emitter and receiver varies from 0 (vertically aligned) to 3.5 m. In the first place the measurements have been compared with the error model for its validation regarding multipath. The differences between the error predicted by the model and the measured one is smaller than 1 cm in most cases, except for those with very high multipath error. The differences in those cases are slightly larger than 10%. These results also show the most critical geometric configurations regarding multipath, associated to low ceiling height and large emitter-receiver separation.

The measured errors, now using both the specular and the diffuse multipath propagation models, are then compared with the model of multipath error in PoA ranging developed in 3.2.2 and validated in 5.3.2. The goal of these tests is to evaluate the mitigation capabilities of the proposal compared to a standard PoA approach that uses sinusoidal modulation as in previous research in IR ranging applied to indoor localization. The results show that the mitigation effectiveness of the proposed system is strongly related with ceiling height and barely affected by the horizontal distance. When the ceiling is lower than 3 m, the mitigation rate compared to PoA remains between 10 and 20 %. The measured mean error in the worst case (low ceiling and large emitter-receiver separation) reaches 45 cm for the specular model and 4 cm for the diffuse model. On the other hand, mitigation rates higher than 70 % are achieved for ceilings higher than 4 m, and around 95 % from 5.5 m. The measured mean error due to multipath in those cases is smaller than 1 cm in all the tests. The observed dependence with ceiling height is mainly related with the delay difference between the LOS path and the fastest NLOS paths. The effectiveness in the despreading process to reject multipath is strongly related with the demodulation delay in relation to the chip duration. With low ceilings, the short delay difference between LOS and multipath components cause a high despread of NLOS.

The multipath tests demonstrate that reducing the chip duration, i.e., using higher chip rates,

is a fundamental step for improving the multipath performance of the proposal. The allowable chip rate is basically defined by the optical link bandwidth. The advances in manufacturing technology of optoelectronic devices allow a positive expectation in the performance of new LEDs available in the short future, reaching faster response times while maintaining power. On the other hand, APDs, which provide higher received power and bandwidth, are being considered as future alternatives for the IR link. Therefore, in the next years it is reasonable to expect a significant increase in the multipath mitigation effectiveness of this method, i.e., rejectable multipath distances are reduced in a factor approximately proportional to the increase in the optical bandwidth of available devices.

Chapter 7

Conclusions and future works

The novel contributions and conclusions of this thesis are provided in this chapter, followed by the publications derived from it. Finally, some relevant future investigations from here on are suggested.

7.1 Conclusions

The specific conclusions regarding the global analysis of the problem and the design and performance of every stage where specifically provided in the final section of the corresponding chapters 3, 4 and 5. Here, a brief discussion and summary of the novelty and contributions of this work are provided, followed by more detailed conclusions.

A differential ranging method for indoor localization using non coherent IR signals has been proposed and validated. This work contributes towards enabling IR-DToA indoor localization by reducing the effect of the dominant error source: multipath interferences.

Indoor positioning based on this technology provides a valid alternative to other indoor technologies, mainly cameras, US and UWB systems, that offer adequate performance for precision-demanding applications such as robotics or autonomous vehicles. Some of the strengths of this optical approach are its high independence from the illumination conditions and immunity to the acoustic background, being also able to operate in environments with strong RF radiation and heavily occupied RF channels. Other positive aspects of this approach are: high immunity to interferences from other signals provided by the spread spectrum coding, easy multiplexing for several mobile units by CDMA and simplicity of the hardware boarded on the mobile unit since all the processing and computations are performed in the fixed infrastructure in the environment. In addition, the expected power and bandwidth improvements in available opto-electronic devices have a direct impact on performance (including multipath mitigation), what allows having a very positive expectation about the reachable accuracy in the short term using the same proposed architecture operating at higher chip rates. On the other hand, the current main drawbacks of this alternative are the requirement of good quality synchronization between receivers, the inability to operate in NLOS conditions and the high requirements in terms of computational load and digitization.

Contributions

The novelty of this work lies in the following contributions:

- This work contributes to reducing the gap towards the practical applicability of IR-DToA measurements for accurate indoor localization by defining a technique that provides precise range measurements while mitigating the critical effect of multipath interferences. Furthermore, the expected short-term increase in the frequency response of available optoelectronic devices for direct optical detection will proportionally increase precision and multipath mitigation rates of the proposal, so as to positively expect reaching sub-cm accuracies within the following years.
- The proposed ranging method is based on an original mixed ToA/PoA-approach. The architecture and the signal structure use and benefit from both PRN ranging and phase-based CW ranging techniques.
- The multipath rejection properties of spread spectrum modulation have been applied to non-coherent optical ranging. This concept was priorly used in interferometry with approximately know delays. The method has been adapted to a situation where the delay is not known but estimated in real time.
- The delay estimation is performed using a tracking technique typical from RF spread spectrum communications and satellite ranging. A baseband ELDLL has been designed and adapted to the particular constrains of the optical application and the specifically designed ranging signal. In addition, narrow correlation spacing is applied in the construction of the loop discriminator for further multipath rejection.
- This work provides a performance analysis and solution for non-directional ranging, which has been seldom addressed using optical signals and presents a strong trade-off between SNR and coverage that rarely affects other optical ranging applications.

General conclusions

The general conclusions derived from this thesis are summarized next:

- The proposal meets the fundamental requirements defined in the research objectives. Evaluated in the conditions set by an IR link achievable with up-to-date devices and a practical geometry (chip rate: 25 MHz, SNR>60 dBHz, horizontal distance between receivers: 3.7 m, vertical distance between emitter and receivers: 2.15 m to 6 m), the proposed method provides:
  - Adequate precision under realistic noise levels and tracking of moving targets. The final estimation bandwidth is calculated to balance noise-related errors and tracking errors due to movement of the target.
  - Multipath reduction down to acceptable levels. The mitigation efficiency strongly depends on room geometry in the current link conditions. In any case, high mitigation efficiency will be achieved with higher link bandwidth in the short term.

  - Support for operation with asynchronous emitter-receiver processing defined by realistic clock errors. The loop bandwidth of the tracking stage is calculated to balance tracking jitter and tracking errors due to asynchronism.
  - Easy multiplexing for simultaneous measurements of several targets using CDMA. This is a potential capability of the system which has not been implemented, and its optimization is proposed for future contributions.

- Apart from the definition and evaluation of the proposal, a global error model of the system taking into account input noise, dynamic effects and multipath has been derived and validated. This model can be used to study of the expected performance of the proposal in different situations for designing the localization system. It can also be used to make predictions of the expected improvement when new optoelectronic devices allow the construction of a better (higher power and bandwidth) optical link.

- Given that a minimum signal quality level (certain SNR value) is reached, the investigations during this work conclude that the optical bandwidth is the fundamental parameter that defines the system performance, being directly related to both precision regarding noise and multipath mitigation. Taking into account the required measurement bandwidth in the delay and phase estimations (in the kHz and tens of Hz range respectively given the assumed clock error and target speed) this minimum signal quality level is approximately 60 dBHz, which can be currently reached with up-to-date devices operating at 25 MHz chip rate for a wide range of vertical distances between emitter and receivers up to 6 m if their horizontal separation is smaller than 4 m.

- The Early-Late processing with the defined symbols in the delay tracking stage using narrow correlator spacing has proven very effective. Both precision and multipath rejection in the delay estimates are high and sometimes comparable to the final estimation results after the phasemeter. Further investigations on the possibility of a simplified version of the system based only on delay tracking are proposed for future works.

- Apart from the tracking loop bandwidth and final measurement bandwidth used to balance static and dynamic performance, the spacing between the early and late correlators in the synchronization stage is a key design parameter for the system performance. Its selection is related to the loop noise transfer and loop sensitivity. Therefore, it conditions tracking jitter, robustness in terms of probability to loss lock and multipath rejection in the delay estimation. The analysis demonstrates that values between 0.1 and 0.6 chips provide stable low tracking jitter, while smaller multipath errors are achieved using smaller early-late spacing.

- Considering the differential nature of the measured ranges, the quality of synchronism between receivers has a direct impact on the estimation error. This is currently one of the most demanding requirements of the proposal and finding methods to relax this effect is an important step to improve the scalability and cost features of the proposal.

Conclusions regarding system performance

The proposed system has been evaluated emulating an IR-link which allows 25 MHz chip-rate operating in an indoor scenario 2.5 m high where receivers are separated 3.5 m. The expected SNR range in these conditions is [60 - 85] dBHz. The allowed target speed used to define the measurement bandwidth is 1 m/s. The expected frequency error between emitter and receiver is 1ppm. In these conditions:

- The achieved precision in two standard deviations is better than 5 cm in 90% of test positions, and the maximum precision error in two standard deviations is 7.5 cm.
- Using the tracking and measurement bandwidth that yield the given precision, the system is able to track delay variations caused by frequency differences between emitter and receiver in the order of μs/s. Available TCXO are already better than 1ppm, meaning that stronger filtering could be used in the signal synchronization for further reduction of noise-related errors.
- Differential distance variations caused by a target moving at 1 m/s can be tracked with an error smaller than 5 cm.
- A sustained increase in transmitted optical power and bandwidth with non-coherent sources and photodetectors can be expected over the next years considering the technological tendencies. The noise-related performance of the system is directly proportional to both parameters. An IR link with 200 MHz bandwidth, which allows 100 MHz chip rates, would relax the trade-off between precision and dynamic tracking, reducing noise-related errors by a factor of 4 while maintaining the same update rate.

Conclusions regarding multipath performance

Multipath has been evaluated as a function of the scenario geometry (horizontal distance between emitter and receiver and ceiling height, linked to the vertical distance between emitter and receiver) in noise-free conditions using the delays and powers provided by two multipath propagation models: specular and diffuse. The results are compared with a validated multipath error model in single-frequency PoA ranging. The test is also performed using 25 MHz chip rate. The following conclusions regarding multipath can be derived from this work:

- The main multipath effect suffered by this localization approach is the double ceiling-floor reflection, as wall reflections can be generally avoided by limiting the FoV of the receivers. This is, therefore, the multipath situation used to evaluate the multipath performance of the proposal.
- Scenarios with low ceiling (smaller than 3 m) cause critical multipath effects that reach 45 cm in the worst case. In these situations, the proposal only provides 10% to 20% mitigation rates compared to standard PoA.
- When the ceiling height is increased above 4 meters, multipath error stays below 1 cm in all the tests. Mitigation rates in these situations are above 70 % (more than 90% for vertical distances higher than 5.5 m).

- The tests have demonstrated that the effectiveness of the system to reject multipath is strongly related with the vertical distance between emitter and receiver, what suggest a strong dependence with the minimum delay difference between LOS and NLOS components. According to these results, the proposed method provides effective multipath mitigation for NLOS-to-LOS path differences higher than 2/3 of the chip length, i.e., 8 m using a chip rate of 25 MHz.

- Using faster chip rates would have a direct impact on the multipath mitigation performance. Similarly to the precision results, the expected advances in available optoelectronic devices with higher working frequencies will yield better multipath rejection in a factor approximately proportional to the increase in optical bandwidth. If the proposed system is implemented with an IR link with 200 MHz bandwidth that allows a chip rate of 100 MHz, high multipath rejection can be expected for path differences higher than 2 m. This performance would imply effective reduction of the vast majority of indoor multipath effects in the given IR-PoA localization approach.

7.2 Publications derived from the thesis

Peer-reviewed journals

- Salido-Monzú, D., Meca-Meca, F. J., Martín-Gorostiza, E., and Lázaro-Galilea, J. L. (2015). SNR degradation in undersampled phase measurement systems. Submitted to *Measurement*.

- Salido-Monzú, D., Martín-Gorostiza, E., Lázaro-Galilea, J. L., Martos-Naya, E., and Wieser, A. (2014). Delay tracking of spread-spectrum signals for indoor optical ranging. *Sensors*, 14(12):23176-23204.

Conferences

- Salido-Monzú, D., Martín-Gorostiza, E., Lázaro-Galilea, J. L., Domingo-Pérez, F., and Wieser, A. (2013). Multipath mitigation for a phase-based infrared ranging system applied to indoor positioning. In *Proc. of the 2013 International Conference on Indoor Positioning and Indoor Navigation*.

- Salido-Monzú, D., Martín-Gorostiza, E., García-Castaño, J., Martínez-Rey, M., and Rodríguez-Navarro, D. (2012). Sub-Nyquist sampling on a narrowband low-SNR phase-shift measurement. In *Proc. of the 2012 Seminario Anual de Automática, Electrónica Industrial e Instrumentación*.

- Salido-Monzú, D., Lázaro-Galilea, J. L., Meca-Meca, F. J., Pallarés-Puerto, L., and J. García Castaño (2011). Caracterización de sistemas de adquisición de datos simultáneos. In *Proc. of the 2011 Seminario Anual de Automática, Electrónica Industrial e Instrumentación*.

- Salido-Monzú, D., Lázaro-Galilea, J. L., Martín-Gorostiza, E., and Meca-Meca, F. J. (2011). Sistema de posicionamiento local basado en medida de desfases sobre infrarrojo. In *Libro de las III Jornadas de Jovenes Investigadores de la Universidad de Alcalá*.

7.3 Future works

This thesis has meant the first step in the study of the proposed ranging method. It has been focused on the general definition of the method and the investigation of its design basics, feasibility and potential benefits. Several continuation lines open from this point. These are fundamentally related to enabling the practical implementation of the method by further study and optimization of the design and implementation of an optical link and a system prototype that allow real-time operation for extensive field-testing.

The main potential future works and contributions are:

- Design and implementation of an IR link that meets the system requirements. This link should balance and maximize the trade-off between transmitted power, channel bandwidth and coverage per sensor. This task is already under development with a design formed by APD-based receivers for increased bandwidth and optical gain, and a LED-based multi-point emitter for increased bandwidth and emitted power. The excess of noise in the APDs and the jitter effects in the multi-point emitter are currently under investigation.

- Evaluation of the proposal in real indoor scenarios, where dynamic and extensive multipath tests can be performed, once the adequate optical link is available.

- Implementation of the proposed architecture in a digital platform that allows real-time operation. A first approach to this task has been made by efficiently implementing a complete two channel measuring unit for 25 MHz chip rate sampled at 125 MS/s in a Spartan 6 FPGA. The prototype has been validated with simulated signals while the signal acquisition stage is still to be implemented.

- Development of a complete set of measuring units that allow the construction of a test cell for localization, so that the positioning performance of the method can be evaluated with field tests.

- Study of alternatives that allow relaxing the high quality synchronism currently required between receivers.

- Comparative investigation of the performance of the delay tracking stage against the performance of the complete system, to evaluate the conditions in which the former alone could provide accurate enough ranging.

- Deeper study and further optimization of the design by:

  - Analysis of the probability of loss of lock and mean time to lose lock in the tracking stage affected by noise depending on its design parameters.

  - Optimization of the signal structure. This includes the investigation of optical PRN sequences taking into account their effect on accuracy and their multiplexing performance. In addition, pulse shaping techniques can be applied to the defined symbols to improve the use of the available bandwidth by correcting distortion effects.

- Specific analysis of the multiplexing operation of the proposal by, after selecting the most adequate PRN sequences, analyzing the effect of multiuser interferences on performance.
- Deeper study of distortion effects by expanding the theoretical performance derivations to take them into account, using a more complete indicator of the signal quality such as SINAD[1] instead of SNR.
- Deeper study of the demodulation process, linked to the previous point by also considering distortion effect and overlapping of negative frequency components, aiming to achieve a more accurate model of this demodulation process and evaluating possible error contributions associated to the demodulation delay.
- Further analysis of the effect of signal discretization on the achieved performance. This could either be addressed by an specific study of the effect of sampling rate in the demodulation process, which was detected as the stage where sampling effects are more significant, or by translating the relevant parts of the performance study to the discrete-time domain.
- Study of the benefits and considerations of including feedback of the final estimation to improve the accuracy in the delay used for the DSSS demodulation, hence increasing the recovery of LOS power for the phasemeter.

[1] Signal-to-Noise and Distortion Ratio

Bibliography

[Abramovici et al., 1992] Abramovici, A., Althouse, W. E., Drever, R. W., Gürsel, Y., Kawamura, S., Raab, F. J., Shoemaker, D., Sievers, L., Spero, R. E., Thorne, K. S., Vogt, R. E., Weiss, R., Whitcomb, S. E., and Zucker, M. E. (1992). LIGO: The laser interferometer gravitational-wave observatory. *Science*, 256(5055):325–33.

[Agrež, 2008] Agrež, D. (2008). Interpolation in the frequency domain to improve phase measurement. *Measurement*, 41(2):151–159.

[Alsindi et al., 2009] Alsindi, N., Alavi, B., and Pahlavan, K. (2009). Measurement and modeling of ultrawideband ToA-based ranging in indoor multipath environments. *IEEE Transactions on Vehicular Technology*, 58(3):1046–1058.

[Alsindi and Pahlavan, 2004] Alsindi, N. and Pahlavan, K. (2004). Performance of TOA estimation algorithms in different indoor multipath conditions. In *Proc. of the 2004 IEEE Wireless Communications and Networking Conference*, pages 495–500.

[Atia et al., 2013] Atia, M. M., Noureldin, A., and Korenberg, M. J. (2013). Dynamic online-calibrated radio maps for indoor positioning in wireless local area networks. *IEEE Transactions on Mobile Computing*, 12(9):1774–1787.

[Baetz et al., 2005] Baetz, W., Braasch, J., and Holzapfel, W. (2005). Noise-modulated optomechatronic distance-measuring system. *IEEE Transactions on Industrial Electronics*, 52(4):944–952.

[Bargh and de Groote, 2008] Bargh, M. and de Groote, R. (2008). Indoor localization based on response rate of bluetooth inquiries. In *Proc. of the 2008 ACM international workshop on Mobile entity localization and tracking in GPS-less environments*, pages 49–54.

[Barnes et al., 2002] Barnes, J., Rizos, C., Wang, J., Small, D., Voigt, G., and Gambale, N. (2002). High precision indoor and outdoor positioning using LocataNet. *Positioning*, 1(5):73–82.

[Bayoud, 2006] Bayoud, F. (2006). Leica's pinpoint EDM technology with modified signal processing and novel optomechanical features. In *Proc. of the 2006 Conference of the International Federation of Surveyors*, pages 1–16.

[Blankenbach and Norrdine, 2010] Blankenbach, J. and Norrdine, A. (2010). Position estimation using artificial generated magnetic fields. In *Proc. of the 2010 International Conference on Indoor Positioning and Indoor Navigation*, pages 1–5.

[Bottomley et al., 2000] Bottomley, G. E., Ottosson, T., and Wang, Y.-P. E. (2000). A generalized RAKE receiver for interference suppression. *IEEE Journal on Selected Areas in Communications*, 18(8):1536–1545.

[Braasch, 2001] Braasch, M. (2001). Performance comparison of multipath mitigating receiver architectures. In *Proc. of the 2001 IEEE Aerospace Conference*, pages 1309–1315.

[Braasch and DiBenedetto, 2001] Braasch, M. and DiBenedetto, M. (2001). Spread-spectrum ranging multipath model validation. *IEEE Transactions on Aerospace and Electronic Systems*, 37(1):298–304.

[Branzel et al., 2013] Branzel, A., Holz, C., Hoffmann, D., Schmidt, D., Knaust, M., Luhne, P., Meusel, R., Richter, S., and Baudisch, P. (2013). GravitySpace: Tracking users and their poses in a smart room using a pressure-sensing floor. In *Proc. of the 2013 SIGCHI Conference on Human Factors in Computing Systems*, pages 725–734.

[Casas et al., 2006] Casas, R., Marco, A., Guerrero, J. J., and Falcó, J. (2006). Robust estimator for non-line-of-sight error mitigation in indoor localization. *EURASIP Journal on Advances in Signal Processing*, 2006:1–9.

[Chan et al., 2009] Chan, E. C. L., Baciu, G., and Mak, S. C. (2009). Using Wi-Fi signal strength to localize in wireless sensor networks. In *Proc of the 2009 International Conference on Communications and Mobile Computing*, pages 538–542.

[Chang et al., 2010] Chang, N., Rashidzadeh, R., and Ahmadi, M. (2010). Robust indoor positioning using differential wi-fi access points. *IEEE Transactions on Consumer Electronics*, 56(3):1860–1867.

[Chen and Dovis, 2011] Chen, X. and Dovis, F. (2011). Enhanced CADLL structure for multipath mitigation in urban scenarios. In *Proc. of the 2011 ION International Technical Meeting*, pages 678–686.

[Chen et al., 2011] Chen, X., Dovis, F., Pini, M., and Mulassano, P. (2011). Turbo architecture for multipath mitigation in global navigation satellite system receivers. *IET Radar, Sonar & Navigation*, 5(5):517.

[Cheng et al., 2014] Cheng, J., Yang, L., Li, Y., and Zhang, W. (2014). Seamless outdoor/indoor navigation with WIFI/GPS aided low cost Inertial Navigation System. *Physical Communication*, 13:31–43.

[Cobb, 1997] Cobb, S. (1997). *GPS pseudolites*. Doctoral thesis, Standford University.

[Dardari et al., 2009] Dardari, D., Conti, A., Ferner, U., Giorgetti, A., and Win, M. Z. (2009). Ranging with ultrawide bandwidth signals in multipath environments. *Proceedings of the IEEE*, 97(2):404–425.

[De Angelis et al., 2013] De Angelis, A., Dwivedi, S., and Handel, P. (2013). Characterization of a flexible UWB sensor for indoor localization. *IEEE Transactions on Instrumentation and Measurement*, 62(5):905–913.

[de Vine et al., 2009] de Vine, G., Rabeling, D. S., Slagmolen, B. J. J., Lam, T. T.-Y., Chua, S., Wuchenich, D. M., McClelland, D. E., and Shaddock, D. A. (2009). Picometer level displacement metrology with digitally enhanced heterodyne interferometry. *Optics Express*, 17(2):828–837.

[Dragunas and Borre, 2010] Dragunas, K. and Borre, K. (2010). Indoor multipath mitigation. In *Proc. of the 2010 International Conference on Ubiquitous Positioning, Indoor Navigation and Location-Based Services*, pages 1–7.

[Dupuy and Lescure, 2002] Dupuy, D. and Lescure, M. (2002). Improvement of the FMCW laser range-finder by an APD working as an optoelectronic mixer. *IEEE Transactions on Instrumentation and Measurement*, 51(5):1010–1014.

[Dupuy et al., 2001] Dupuy, D., Lescure, M., and Cousineau, M. (2001). A FMCW laser range-finder based on a delay line technique. In *Proc. of the 2001 IEEE Instrumentation and Measurement Technology Conference*, pages 1084–1088.

[Esteban et al., 2009] Esteban, J. J., Bykov, I., García Marín, A. F., Heinzel, G., and Danzmann, K. (2009). Optical ranging and data transfer development for LISA. *Journal of Physics: Conference Series*, 154(1):012025.

[Esteban Delgado et al., 2009] Esteban Delgado, J. J., García Marín, A. F., Bykov, I., Heinzel, G., and Danzmann, K. (2009). Free-space laser ranging and data communication. In *Proc. of the 2009 Workshop on Positioning, Navigation and Communication*, pages 275–281.

[Evans et al., 2002] Evans, M., Mavalvala, N., Fritschel, P., Bork, R., Bhawal, B., Gustafson, R., Kells, W., Landry, M., Sigg, D., Weiss, R., Whitcomb, S., and Yamamoto, H. (2002). Lock acquisition of a gravitational-wave interferometer. *Optics Letters*, 27(8):598.

[Fenton and Jones, 2005] Fenton, P. and Jones, J. (2005). The theory and performance of NovAtel Inc.'s Vision Correlator. In *Proc. of the 2005 ION GNSS Conference*, pages 1–9.

[Fernández et al., 2007] Fernández, I., Mazo, M., Lázaro, J. L., Pizarro, D., Santiso, E., Martín, P., and Losada, C. (2007). Guidance of a mobile robot using an array of static cameras located in the environment. *Autonomous Robots*, 23(4):305–324.

[García-Núñez, 2013] García-Núñez, E. (2013). *Efficient complementary sequences-based architectures and their application to ranging measurements.* Doctoral thesis, University of Alcalá.

[Gelmini et al., 1994] Gelmini, E., Minoni, U., and Docchio, F. (1994). Tunable, double-wavelength heterodyne detection interferometer for absolute-distance measurements. *Optics Letters*, 19(3):213.

[Gerberding et al., 2013] Gerberding, O., Sheard, B., Bykov, I., Kullmann, J., Delgado, J. J. E., Danzmann, K., and Heinzel, G. (2013). Phasemeter core for intersatellite laser heterodyne interferometry: modelling, simulations and experiments. *Classical and Quantum Gravity*, 30(23):235029.

[González et al., 2009] González, J., Blanco, J., Galindo, C., Ortiz-de Galisteo, A., Fernández-Madrigal, J., Moreno, F., and Martínez, J. (2009). Mobile robot localization based on Ultra-Wide-Band ranging: A particle filter approach. *Robotics and Autonomous Systems*, 57(5):496–507.

[Gustafsson et al., 2005] Gustafsson, F., Gunnarsson, F., Gustaffsson, F., and Gunnarsson, F. (2005). Mobile positioning using wireless networks. *IEEE Signal Processing Magazine*, 22(4):41–53.

[Harle, 2013] Harle, R. (2013). A Survey of Indoor Inertial Positioning Systems for Pedestrians. *IEEE Communications Surveys & Tutorials*, 15(3):1281–1293.

[Hashimoto, 2005] Hashimoto, H. (2005). Intelligent interactive spaces - integration of IT and robotics. In *Proc. of the 2005 IEEE Workshop on Advanced Robotics and its Social Impacts*, pages 85–90. IEEE.

[Haverinen and Kemppainen, 2009] Haverinen, J. and Kemppainen, A. (2009). Global indoor self-localization based on the ambient magnetic field. *Robotics and Autonomous Systems*, 57(10):1028–1035.

[He et al., 2013] He, Z., Ma, Y., and Tafazolli, R. (2013). Improved high resolution TOA estimation for OFDM-WLAN based indoor ranging. *IEEE Wireless Communications Letters*, 2(2):163–166.

[Hide et al., 2010] Hide, C., Botterill, T., and Andreotti, M. (2010). Low cost vision-aided IMU for pedestrian navigation. In *Proc. of the 2010 International Conference on Ubiquitous Positioning, Indoor Navigation and Location-Based Services*, pages 1–7.

[Hinderling, 2006] Hinderling (2006). Method and devide for deriving geodetic distance data.

[Hol et al., 2009] Hol, J. D., Dijkstra, F., Luinge, H., Schon, T. B., and Schön, T. (2009). Tightly coupled UWB/IMU pose estimation. In *Proc. of the 2009 IEEE International Conference on Ultra-Wideband*, pages 688–692.

[Holm, 2009] Holm, S. (2009). Hybrid ultrasound-RFID indoor positioning: Combining the best of both worlds. In *Proc. of the 2009 IEEE International Conference on RFID*, pages 155–162.

[Holm and Nilsen, 2010] Holm, S. and Nilsen, C.-I. C. (2010). Robust ultrasonic indoor positioning using transmitter arrays. In *Proc. of the 2010 International Conference on Indoor Positioning and Indoor Navigation*, pages 1–5.

[House et al., 2011] House, S., Connell, S., Milligan, I., Austin, D., Hayes, T. L., and Chiang, P. (2011). Indoor localization using pedestrian dead reckoning updated with RFID-based

fiducials. In *Proc. of the 2011 International Conference of the IEEE Engineering in Medicine and Biology Society*, pages 7598–601.

[Ido et al., 2009] Ido, J., Shimizu, Y., Matsumoto, Y., and Ogasawara, T. (2009). Indoor navigation for a humanoid robot using a view sequence. *The International Journal of Robotics Research*, 28(2):315–325.

[Isleif et al., 2014] Isleif, K.-S., Gerberding, O., Köhlenbeck, S., Sutton, A., Sheard, B., Goß ler, S., Shaddock, D., Heinzel, G., and Danzmann, K. (2014). Highspeed multiplexed heterodyne interferometry. *Optics Express*, 22(20):24689–24696.

[Jiménez-Ruiz et al., 2012] Jiménez-Ruiz, A. R., Seco-Granja, F., Prieto-Honorato, J. C., and Guevara-Rosas, J. I. (2012). Accurate pedestrian indoor navigation by tightly coupling foot-mounted IMU and RFID measurements. *IEEE Transactions on Instrumentation and Measurement*, 61(1):178–189.

[Jung et al., 2011] Jung, S.-Y., Hann, S., and Park, C.-S. (2011). TDOA-based optical wireless indoor localization using LED ceiling lamps. *IEEE Transactions on Consumer Electronics*, 57(4):1592–1597.

[Kilpela et al., 2001] Kilpela, A., Pennala, R., and Kostamovaara, J. (2001). Precise pulsed time-of-flight laser range finder for industrial distance measurements. *Review of Scientific Instruments*, 72(4):2197–2202.

[Kim and Kim, 2013] Kim, S. J. and Kim, B. K. (2013). Dynamic ultrasonic hybrid localization system for indoor mobile robots. *IEEE Transactions on Industrial Electronics*, 60(10):4562–4573.

[Kjæ rgaard et al., 2010] Kjæ rgaard, M., Blunck, H., Godsk, T., Toftkjæ r, T., Christensen, D., and Grø nbæk, K. (2010). Indoor positioning using GPS revisited. *Pervasive Computing*, 45(1):38–56.

[Kocur et al., 2009] Kocur, D., Rovnáková, J., and Svecová, M. (2009). Through wall tracking of moving targets by M-sequence UWB radar. *Towards Intelligent Engineering and Information Technology*, pages 349–364.

[Kohoutek et al., 2010] Kohoutek, T. K., Mautz, R., and Donaubauer, A. (2010). Real-time indoor positioning using range imaging sensors. In *Proc. of SPIE Photonics Europe*, pages 77240K1–77240K8.

[Kuhn et al., 2010] Kuhn, M., Merkl, B., Fathy, A., and Mahfouz, M. (2010). Real-time non-coherent UWB positioning radar with millimeter range accuracy: Theory and experiment. *IEEE Transactions on Microwave Theory and Techniques*, 58(1):9–20.

[Kurz et al., 2008] Kurz, O., Rohmer, G., and Science, S. (2008). A new multipath detection and mitigation approach for pseudolite systems. In *Proc. of the 2002 International Technical Meeting of the Satellite Division of The Institute of Navigation*, pages 2024–2031.

[Kwak and Lee, 2004] Kwak, J. J. S. and Lee, J. H. J. (2004). Infrared transmission for intervehicle ranging and vehicle-to-roadside communication systems using spread-spectrum technique. *IEEE Transactions on Intelligent Transportation Systems*, 5(1):12–19.

[Larranaga et al., 2010] Larranaga, J., Muguira, L., Lopez-Garde, J. M., and Vazquez, J. I. (2010). An environment adaptive ZigBee-based indoor positioning algorithm. In *Proc. of the 2010 International Conference on Indoor Positioning and Indoor Navigation*, pages 1–8.

[Lay et al., 2007] Lay, O. P., Dubovitsky, S., Shaddock, D. A., and Ware, B. (2007). Coherent range-gated laser displacement metrology with compact optical head. *Optics letters*, 32(20):2933–2935.

[Lázaro-Galilea et al., 2015] Lázaro-Galilea, J. L., de la Llana-Calvo, A., and Salido-Monzú, D. (2015). Modeling of optical signal propagation considering multipath components. Numerical approximation. Technical report, GEINTRA Reseach Group, University of Alcalá.

[Leppäkoski et al., 2010] Leppäkoski, H., Tikkinen, S., and Takala, J. (2010). Optimizing radio map for WLAN fingerprinting. In *Proc. of the 2010 International Conference on Ubiquitous Positioning, Indoor Navigation and Location-Based Services*, volume 227890, pages 1–8.

[Li and Pahlavan, 2004] Li, X. and Pahlavan, K. (2004). Super-resolution TOA estimation with diversity for indoor geolocation. *IEEE Transactions on Wireless Communications*, 3(1):224–234.

[Liang et al., 2012] Liang, Y. R., Duan, H. Z., Yeh, H. C., and Luo, J. (2012). Fundamental limits on the digital phase measurement method based on cross-correlation analysis. *Review of Scientific Instruments*, 83(9):95110.

[Liu et al., 2007] Liu, H., Darabi, H., Banerjee, P., and Liu, J. (2007). Survey of wireless indoor positioning techniques and systems. *IEEE Transactions on Systems, Man and Cybernetics, Part C (Applications and Reviews)*, 37(6):1067–1080.

[Liu et al., 2013] Liu, R. P., Hedley, M., and Yang, X. (2013). WLAN Location Service with TXOP. *IEEE Transactions on Computers*, 62(3):589–598.

[Lohan et al., 2006] Lohan, E. S., Lakhzouri, A., and Renfors, M. (2006). Feedforward delay estimators in adverse multipath propagation for Galileo and modernized GPS signals. *EURASIP Journal on Applied Signal Processing*, 2006:1–19.

[Losada et al., 2010] Losada, C., Mazo, M., Palazuelos, S., Pizarro, D., and Marrón, M. (2010). Multi-camera sensor system for 3D segmentation and localization of multiple mobile robots. *Sensors*, 10(4):3261–79.

[Luo and Law, 2012] Luo, Y. and Law, C. L. (2012). Indoor positioning using UWB-IR signals in the presence of dense multipath with path overlapping. *IEEE Transactions on Wireless Communications*, 11(10):3734–3743.

[Lymberopoulos and Priyantha, 2013] Lymberopoulos, D. and Priyantha, B. (2013). Indoor localization using FM signals. *IEEE Transactions on Mobile Computing*, 12(8):1502–1517.

[Martín-Gorostiza, 2011] Martín-Gorostiza, E. (2011). *Sistema de posicionamiento local para localización absoluta de robots móviles en espacios inteligentes mediante infrarrojos*. Doctoral thesis, University of Alcalá.

[Martín-Gorostiza et al., 2011] Martín-Gorostiza, E., Lázaro-Galilea, J. L., Meca-Meca, F. J., Salido-Monzú, D., Espinosa-Zapata, F., and Pallarés-Puerto, L. (2011). Infrared sensor system for mobile-robot positioning in intelligent spaces. *Sensors*, 11(5):5416–5438.

[Martín-Gorostiza et al., 2010] Martín-Gorostiza, E., Meca-Meca, F. J., Lázaro-Galilea, J. L., Martos-Naya, E., Naranjo-Vega, F., and Esteban-Martínez, O. (2010). Coverage-mapping method based on a hardware model for mobile-robot positioning in intelligent spaces. *IEEE Transactions on Instrumentation and Measurement*, 59(2):266–282.

[Martín-Gorostiza et al., 2009] Martín-Gorostiza, E., Meca-Meca, F. J., Lázaro-Galilea, J. L., Salido-Monzú, D., Pallarés-Puerto, L., and Moral-Alcaraz, A. (2009). Error corrections in phase-shift measurement for robot infrared localization in intelligent spaces. In *Proc. of the 2009 IEEE International Workshop on Robotic and Sensors Environments*, pages 92–97.

[Massa et al., 2002] Massa, J., Buller, G., Walker, A., Smith, G., Cova, S., Umasuthan, M., and Wallace, A. (2002). Optical Design and Evaluation of a Three-Dimensional Imaging and Ranging System Based on Time-Correlated Single-Photon Counting. *Applied Optics*, 41(6):1063.

[Massa et al., 1998] Massa, J. S., Buller, G. S., Walker, A. C., Cova, S., Umasuthan, M., and Wallace, A. M. (1998). Time-of-Flight Optical Ranging System Based on Time-Correlated Single-Photon Counting. *Applied Optics*, 37(31):7298.

[Mautz, 2012] Mautz, R. (2012). *Indoor positioning technologies*. Habilitation thesis, ETH Zürich.

[Mautz and Tilch, 2011] Mautz, R. and Tilch, S. (2011). Optical indoor positioning systems. In *Proc. of the 2011 International Conference on Indoor Positioning and Indoor Navigation*, pages 21–23.

[Mazuelas et al., 2009] Mazuelas, S., Bahillo, A., Lorenzo, R. M., Fernandez, P., Lago, F. A., Garcia, E., Blas, J., and Abril, E. J. (2009). Robust Indoor Positioning Provided by Real-Time RSSI Values in Unmodified WLAN Networks. *IEEE Journal of Selected Topics in Signal Processing*, 3(5):821–831.

[McGraw and Braasch, 1999] McGraw, G. and Braasch, M. (1999). GNSS multipath mitigation using gated and high resolution correlator concepts. In *Proc. of the 1999 National Technical Meeting of The Institute of Navigation*, pages 333–342.

[Medina et al., 2013] Medina, C., Segura, J. C., and De la Torre, A. (2013). Ultrasound indoor positioning system based on a low-power wireless sensor network providing sub-centimeter accuracy. *Sensors*, 13(3):3501–26.

[Mostofi et al., 2014] Mostofi, N., Elhabiby, M., and El-Sheimy, N. (2014). Indoor localization and mapping using camera and inertial measurement unit (IMU). In *Proc. of the 2014 IEEE/ION Position, Location and Navigation Symposium*, pages 1329–1335.

[Nakamura et al., 2000] Nakamura, K., Hara, T., Yoshida, M., Miyahara, T., and Ito, H. (2000). Optical frequency domain ranging by a frequency-shifted feedback laser. *IEEE Journal of Quantum Electronics*, 36(3):305–316.

[Nasipuri and El Najjar, 2006] Nasipuri, A. and El Najjar, R. (2006). Experimental evaluation of an angle based indoor localization system. In *Proc. of the 2006 International Symposium on Modeling and Optimization in Mobile, Ad Hoc and Wireless Networks*, pages 1–9.

[Nunes, 2007] Nunes, F. (2007). Gating functions for multipath mitigation in GNSS BOC signals. *IEEE Transactions on Aerospace and Electronic Systems*, 3(3):951–964.

[Pallarés-Puerto, 2010] Pallarés-Puerto, L. (2010). *Estudio de la problemática de la detección de infrarrojos en interiores para el desarrollo de una celda de posicionamiento en robótica móvil.* Master thesis, University of Alcalá.

[Peng et al., 2011] Peng, J., Zhu, M., and Zhang, K. (2011). New algorithms based on sigma point Kalman filter technique for multi-sensor integrated RFID indoor/outdoor positioning. In *Proc. of the 2011 International Conference on Indoor Positioning and Indoor Navigation*, pages 1–4.

[Pesatori et al., 2012] Pesatori, A., Norgia, M., Svelto, C., Zucco, M., Stupka, M., and De Marchi, A. (2012). High-Resolution Mode-Locked Laser Rangefinder With Harmonic Downconversion. *IEEE Transactions on Instrumentation and Measurement*, 61(5):1536–1542.

[Peterson et al., 1995] Peterson, R., Ziemer, R., and Borth, D. (1995). *Introduction to spread-spectrum communications*, volume 995. Prentice Hall New Jersey.

[Pietrzyk and von der Grun, 2010] Pietrzyk, M. M. and von der Grun, T. (2010). Experimental validation of a TOA UWB ranging platform with the energy detection receiver. In *Proc. of the 2010 International Conference on Indoor Positioning and Indoor Navigation*, pages 1–8.

[Pizarro et al., 2009] Pizarro, D., Mazo, M., Santiso, E., Marron, M., and Fernandez, I. (2009). Localization and geometric reconstruction of mobile robots using a camera ring. *IEEE Transactions on Instrumentation and Measurement*, 58(8):2396–2409.

[Prieto et al., 2009] Prieto, J., Jimenez, A., Guevara, J., Ealo, J., Seco, F., Roa, J., and Ramos, F. (2009). Performance evaluation of 3D-LOCUS advanced acoustic LPS. *IEEE Transactions on Instrumentation and Measurement*, 58(8):2385–2395.

[Priyantha, 2005] Priyantha, N. (2005). *The cricket indoor location system.* Doctoral thesis, Massachusetts Institute of Technology.

[Ramos et al., 2004] Ramos, P. M., da Silvai, M. F., and Serra, A. C. (2004). Low frequency impedance measurement using sine-fitting. *Measurement*, 35(1):89–96.

[Riehle et al., 2011] Riehle, T. H., Anderson, S. M., Lichter, P. A., Condon, J. P., Sheikh, S. I., and Hedin, D. S. (2011). Indoor waypoint navigation via magnetic anomalies. In *Proc. of the 2011 International Conference of the IEEE Engineering in Medicine and Biology Society*, pages 5315–8.

[Rizos et al., 2010] Rizos, C., Roberts, G., Barnes, J., and Gambale, N. (2010). Experimental results of Locata: A high accuracy indoor positioning system. In *Proc. of the 2010 International Conference on Indoor Positioning and Indoor Navigation*, pages 1–7.

[Saad and Nakad, 2011] Saad, S. and Nakad, Z. (2011). A Standalone RFID Indoor Positioning System Using Passive Tags. *IEEE Transactions on Industrial Electronics*, 58(5):1961–1970.

[Salido-Monzú, 2011] Salido-Monzú, D. (2011). *Caracterización de un sistema de posicionamiento local basado en medida digital de fase*. Master thesis, University of Alcalá.

[Salido-Monzú et al., 2011] Salido-Monzú, D., Lázaro-Galilea, J. L., Martín-Gorostiza, E., and Meca-Meca, F. J. (2011). Sistema de posicionamiento local basado en medida de desfases sobre infrarrojo. In *Libro de las III Jornadas de Jovenes Investigadores de la Universidad de Alcalá*, pages 1–8.

[Salido-Monzú et al., 2012] Salido-Monzú, D., Martín-Gorostiza, E., García-Castaño, J., Martínez-Rey, M., and Rodríguez-Navarro, D. (2012). Sub-Nyquist Sampling on a Narrowband Low-SNR Phase-Shift Measurement. In *Proc. of the 2012 Seminario Anual de Automática, Electrónica Industrial e Instrumentación*, pages 1–6.

[Salido-Monzú et al., 2013] Salido-Monzú, D., Martín-Gorostiza, E., Lázaro-Galilea, J. L., Domingo-Pérez, F., and Wieser, A. (2013). Multipath mitigation for a phase-based infrared ranging system applied to indoor positioning. In *Proc. of the 2013 International Conference on Indoor Positioning and Indoor Navigation*, pages 1–10.

[Salido-Monzú et al., 2014] Salido-Monzú, D., Martín-Gorostiza, E., Lázaro-Galilea, J. L., Martos-Naya, E., and Wieser, A. (2014). Delay tracking of spread-spectrum signals for indoor optical ranging. *Sensors*, 14(12):23176–23204.

[Salido-Monzú et al., 2015] Salido-Monzú, D., Meca-Meca, F. J., Martín-Gorostiza, E., and Lázaro-Galilea, J. L. (2015). SNR degradation in undersampled phase measurement systems. *Measurement*, (submitted).

[Sanchez-Fernandez et al., 2007] Sanchez-Fernandez, M., Aguilera-Forero, M., Garcia-Armada, A., Sánchez-Fernández, M., Aguilera-Forero, M., and García-Armada, A. (2007). Performance analysis and parameter optimization of DLL and MEDLL in fading multipath environments for next generation navigation receivers. *IEEE Transactions on Consumer Electronics*, 53(4):1302–1308.

[Segers et al., 2014] Segers, L., Tiete, J., Braeken, A., and Touhafi, A. (2014). Ultrasonic multiple-access ranging system using spread spectrum and MEMS technology for indoor localization. *Sensors*, 14(2):3172–3187.

[Segura et al., 2010] Segura, M., Hashemi, H., Sisterna, C., and Mut, V. (2010). Experimental demonstration of self-localized Ultra Wideband indoor mobile robot navigation system. In *Proc. of the 2010 International Conference on Indoor Positioning and Indoor Navigation*, pages 1–9. IEEE.

[Shaddock, 2007] Shaddock, D. A. (2007). Digitally enhanced heterodyne interferometry. *Optics letters*, 32(22):3355–3357.

[Skog et al., 2010] Skog, I., Nilsson, J. O., and Händel, P. (2010). Evaluation of zero-velocity detectors for foot-mounted inertial navigation systems. In *Proc. of the 2010 International Conference on Indoor Positioning and Indoor Navigation*, pages 1–6.

[Ureña et al., 2007] Ureña, J., Hernández, A., Jiménez, A., Villadangos, J. M., Mazo, M., García, J. C., García, J. J., Álvarez, F. J., De Marziani, C., Pérez, M. C., Jiménez, J. A., Jiménez, A. R., and Seco, F. (2007). Advanced sensorial system for an acoustic LPS. *Microprocessors and Microsystems*, 31(6):393–401.

[Valtonen et al., 2009] Valtonen, M., Mäentausta, J., and Vanhala, J. (2009). Tiletrack: Capacitive human tracking using floor tiles. In *Proc. of the 2009 IEEE International Conference on Pervasive Computing and Communications*, pages 1–10.

[Van de Velde and Steendam, 2012] Van de Velde, S. and Steendam, H. (2012). CUPID algorithm for cooperative indoor multipath-aided localization. In *Proc. of the 2012 International Conference on Indoor Positioning and Indoor Navigation*, pages 1–6.

[Van Dierendonck et al., 1992] Van Dierendonck, A., Fenton, P., and Ford, T. (1992). Theory and performance of narrow correlator spacing in a GPS receiver. *Navigation*, 39(3):265–283.

[van Nee, 1992] van Nee, R. (1992). The Multipath Estimating Delay Lock Loop. In *Proc. of the 1992 IEEE International Symposium on Spread Spectrum Techniques and Applications*, pages 39–42.

[Varshavsky et al., 2007] Varshavsky, A., de Lara, E., Hightower, J., LaMarca, A., and Otsason, V. (2007). GSM indoor localization. *Pervasive and Mobile Computing*, 3(6):698–720.

[Veitsel et al., 1998] Veitsel, V., Zhdanov, A., and Zhodzishsky, M. (1998). The mitigation of multipath errors by strobe correlators in GPS/GLONASS receivers. *GPS Solutions*, 2(2):38–45.

[Walker, 2008] Walker, W. D. (2008). Sub-microdegree phase measurement technique using lock-in amplifiers. In *Proc. of the 2008 IEEE International Frequency Control Symposium*, pages 825–828.

[Wan and Zhan, 2011] Wan, X. and Zhan, X. (2011). The research of indoor navigation system using pseudolites. *Procedia Engineering*, 15:1446–1450.

[Wang et al., 2001] Wang, C.-C., Trivedi, S., Jin, F., Khurgin, J., Temple, D., Hommerich, U., Gad, E., and Corder, A. (2001). Interferometer-less coherent optical range finder. In *Proc. of the 2001 International Conference on Lasers and Electro-Optics*, pages 45–46.

[Wang et al., 2009] Wang, H., Narayanan, R. M., and Zhou, Z. O. (2009). Through-wall imaging of moving targets using UWB random noise radar. *IEEE Antennas and Wireless Propagation Letters*, 8:802–805.

[Want et al., 1992] Want, R., Hopper, A., Falcão, V., and Gibbons, J. (1992). The active badge location system. *ACM Transactions on Information Systems*, 10(1):91–102.

[Ward et al., 1997] Ward, A., Jones, A., and Hopper, A. (1997). A new location technique for the active office. *IEEE Personal Communications*, 4(5):42–47.

[Weilenmann, 2010] Weilenmann, J. (2010). Multi-targeting method for measuring distance according to the phase measuring principle.

[Weill, 2002] Weill, L. R. (2002). Multipath Mitigation using Modernized GPS Signals: How Good Can it Get? In *Proc. of the 2002 International Technical Meeting of the Satellite Division of The Institute of Navigation*, pages 493–505.

[Weinstein and Weiss, 1984] Weinstein, E. and Weiss, A. (1984). Fundamental limitations in passive time-delay estimation–Part II: Wide-band systems. *IEEE Transactions on Acoustics, Speech, and Signal Processing*, 32(5):1064–1078.

[Weiss and Weinstein, 1983] Weiss, A. and Weinstein, E. (1983). Fundamental limitations in passive time delay estimation–Part I: Narrow-band systems. *IEEE Transactions on Acoustics, Speech, and Signal Processing*, 31(2):472–486.

[Williams and Wickramasinghe, 1986] Williams, C. C. and Wickramasinghe, H. K. (1986). Optical ranging by wavelength multiplexed interferometry. *Journal of Applied Physics*, 60(6):1900.

[Wu and Dempster, 2011] Wu, J. and Dempster, A. (2011). The "BOC-Gated-PRN", a multipath mitigation technique for BOC (n, n) waveforms. *IEEE Transactions on Aerospace and Electronic Systems*, 47(2):1136–1153.

[Wu et al., 2007] Wu, S., Ma, Y., Zhang, Q., and Zhang, N. (2007). NLOS error mitigation for UWB ranging in dense multipath environments. In *Proc. of the 2007 IEEE Wireless Communications and Networking Conference*, pages 1567–1572.

[Xiaoli and Katuo, 1998] Xiaoli, D. and Katuo, S. (1998). High-accuracy absolute distance measurement by means of wavelength scanning heterodyne interferometry. *Measurement Science and Technology*, 9(7):1031–1035.

[Yang and Shao, 2015] Yang, C. and Shao, H.-r. (2015). WiFi-based indoor positioning. *IEEE Communications Magazine*, 53(3):150–157.

[Zhang et al., 2009] Zhang, G., Woon, O. H., Wang, W., Krishnan, S., Chin, F., and Chung, K. C. (2009). Time-frequency domain delay estimation algorithm for multipath and interference mitigation in UWB positioning systems. In *Proc. of the 2009 IEEE International Conference on Ultra-Wideband*, pages 698–701.

[Zhang et al., 2010] Zhang, J., Li, B., Dempster, A., and Rizos, C. (2010). Evaluation of high sensitivity GPS receivers. In *Proc. of the 2010 International Symposium on GPS/GNSS*, pages 1–6.

[Zhang and Kavehrad, 2012] Zhang, W. and Kavehrad, M. (2012). A 2-D indoor localization system based on visible light LED. In *Proc. of the 2012 IEEE Photonics Society Summer Topical Meeting Series*, pages 80–81.

[Zhang et al., 2014] Zhang, Y., Tan, J., Zeng, Z., Liang, W., and Xia, Y. (2014). Monocular camera and IMU integration for indoor position estimation. In *Proc. of the 2014 International Conference of the IEEE Engineering in Medicine and Biology Society*, pages 1198–1201.

[Zhou et al., 2011] Zhou, Y., Law, C. L., Guan, Y. L., and Chin, F. (2011). Indoor elliptical localization based on asynchronous UWB range measurement. *IEEE Transactions on Instrumentation and Measurement*, 60(1):248–257.

Appendix A

Simulink implementation of the system

The Simulink diagrams that implement the digital prototype of the proposed system are provided in this appendix. The following figures correspond to:

- A.1: Top-level diagram of the system used for the simulation tests. This system includes the complete processing architecture for one channel (acquisition, tracking, demodulation and phasemeter), the effect of the emitter and receiver transfer functions, and the IR link with one multipath component. The second channel is the sine signal used to modulate the emitted signal, which is fed directly into the phasemeter for reference.
- A.2: Top-level diagram of the system used for the emulation tests. This system includes the complete differential processing architecture for two channels (2x acquisition, 2x tracking, 2x demodulation and phasemeter). The input signals are directly fed into the acquisition stage since the effect of the emitter, channel and receiver transfer functions is already added in the emulated signal generation set-up.
- A.3 - [A_emitter]: Diagram of the discrete transfer function that simulates the emitter frequency response.
- A.4 - [B_link]: Diagram of the discrete system that simulates the link response including time-dependent delay and power of the LOS and one NLOS components.
- A.5 - [C_receiver]: Diagram of the discrete transfer function that simulates the receiver frequency response.
- A.6 - [F_code_demod]: Diagram of the mixer that implements the DSSS demodulation stage.
- A.7 - [D_coarse_acq]: Diagram of the delay acquisition stage.
- A.8 - [E_tracking]: Diagram of the delay tracking stage based on an ELDLL architecture.
- A.9 - [G_IQ_demod]: Diagram of the differential phasemeter based on two I/Q demodulators.

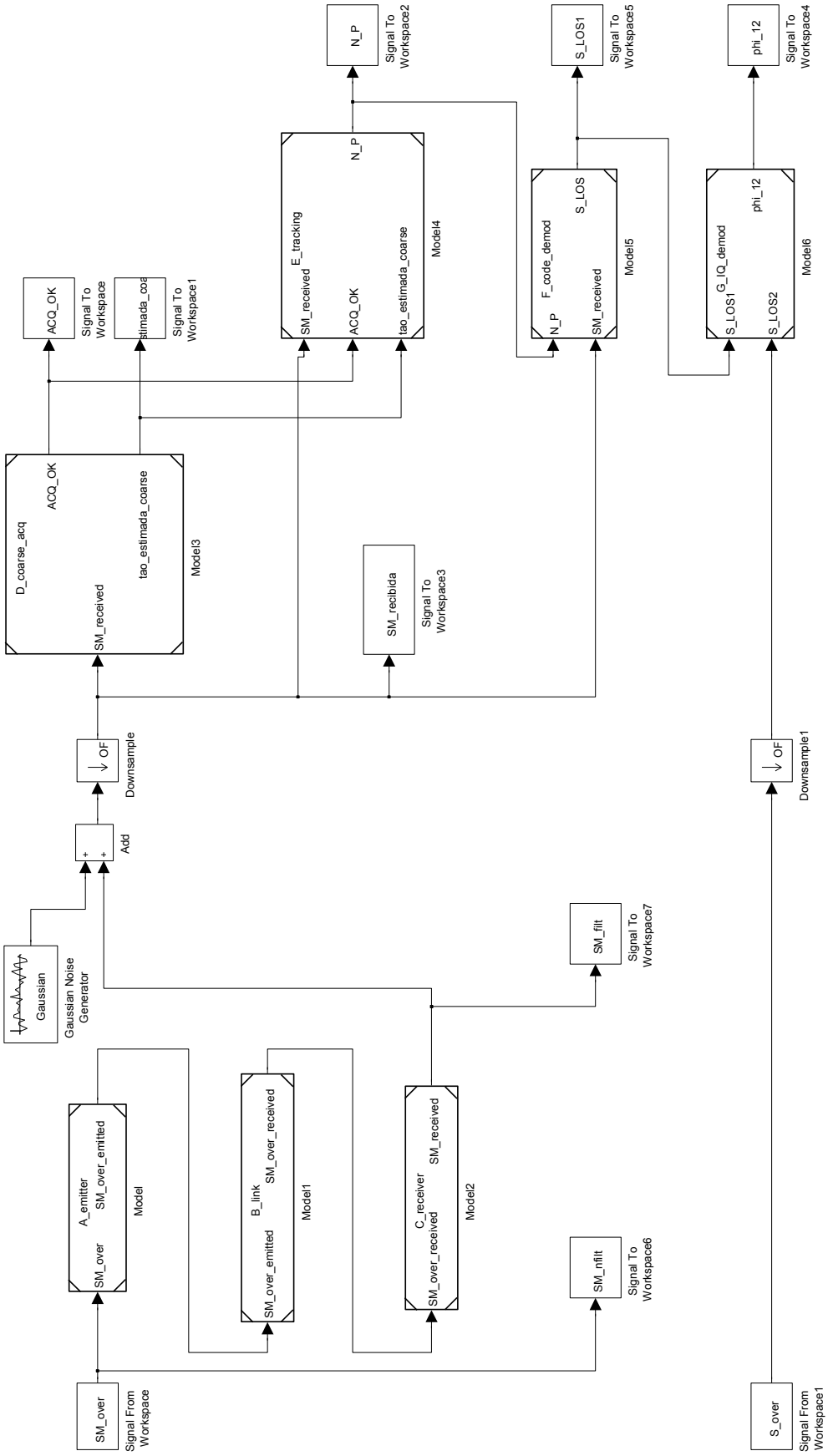

Figure A.1: Diagram of the top-level system for the simulation measurements

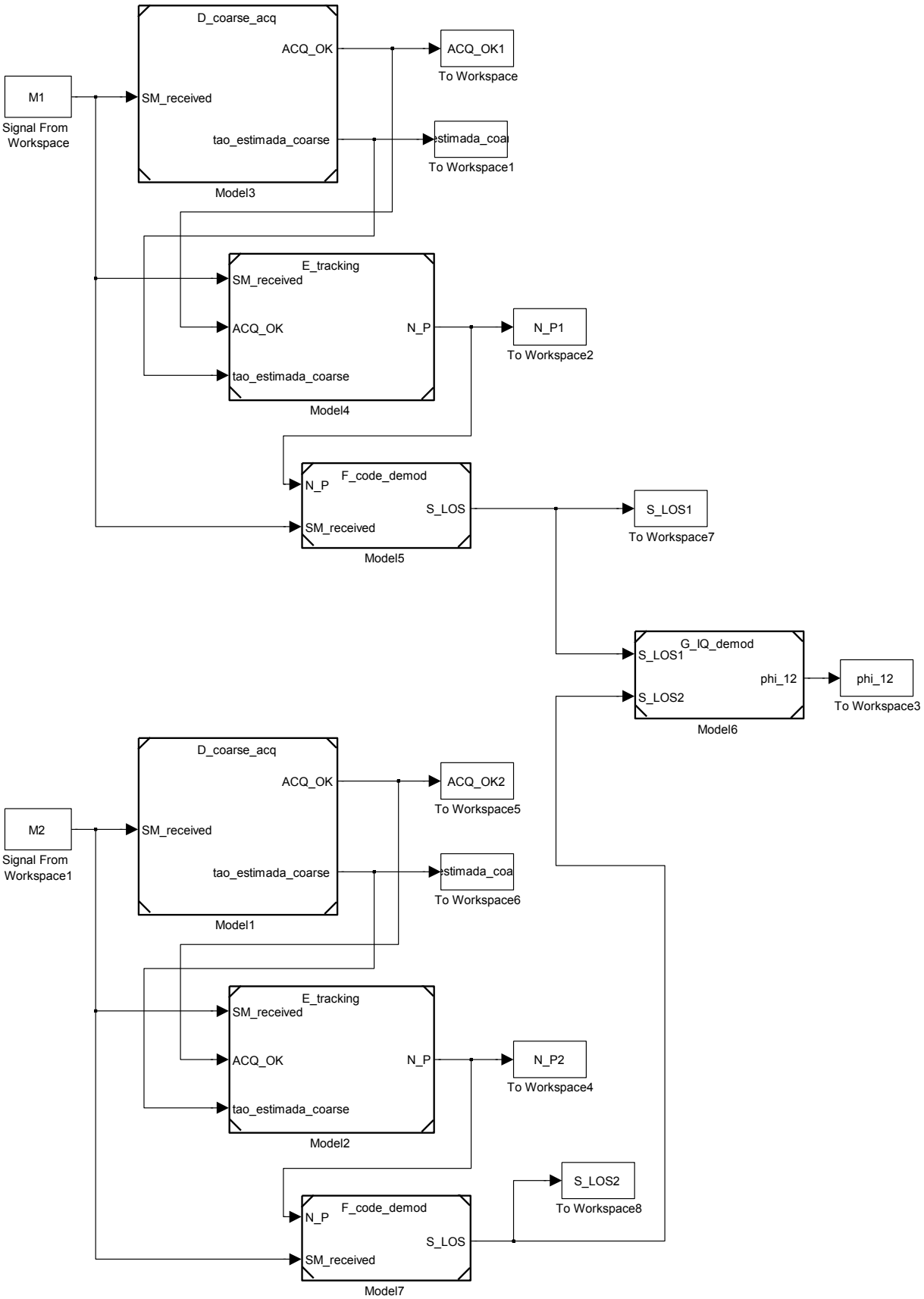

Figure A.2: Diagram of the top-level system for the emulation measurements

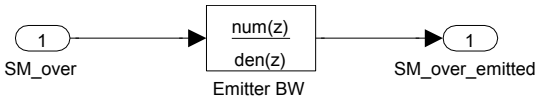

Figure A.3: Diagram of the emitter transfer function

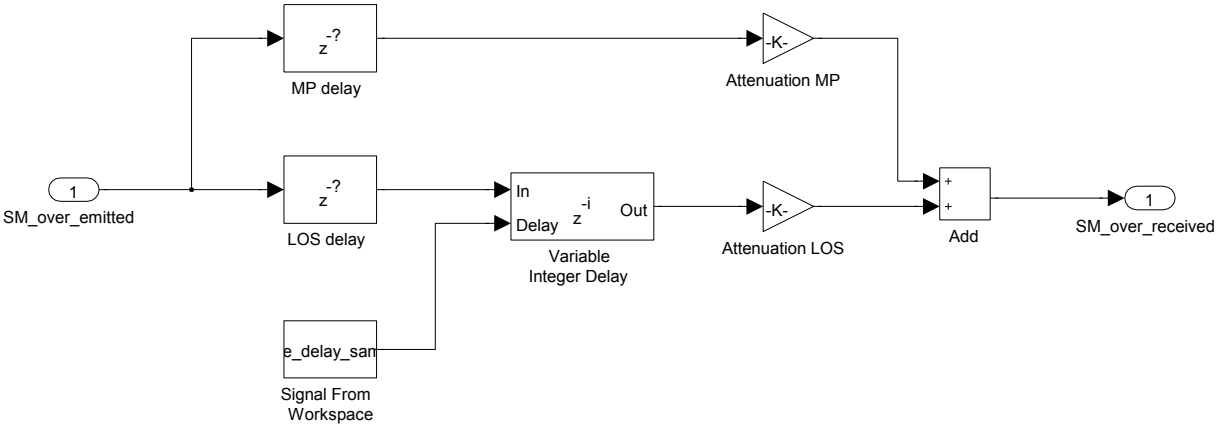

Figure A.4: Diagram of the link transfer function

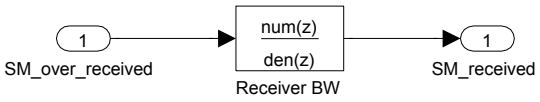

Figure A.5: Diagram of the receiver transfer function

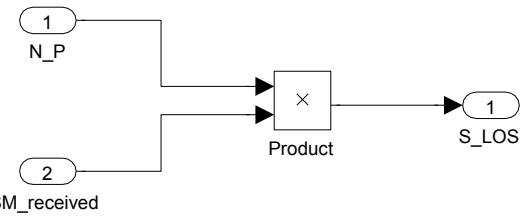

Figure A.6: Diagram of the DSSS demodulation stage

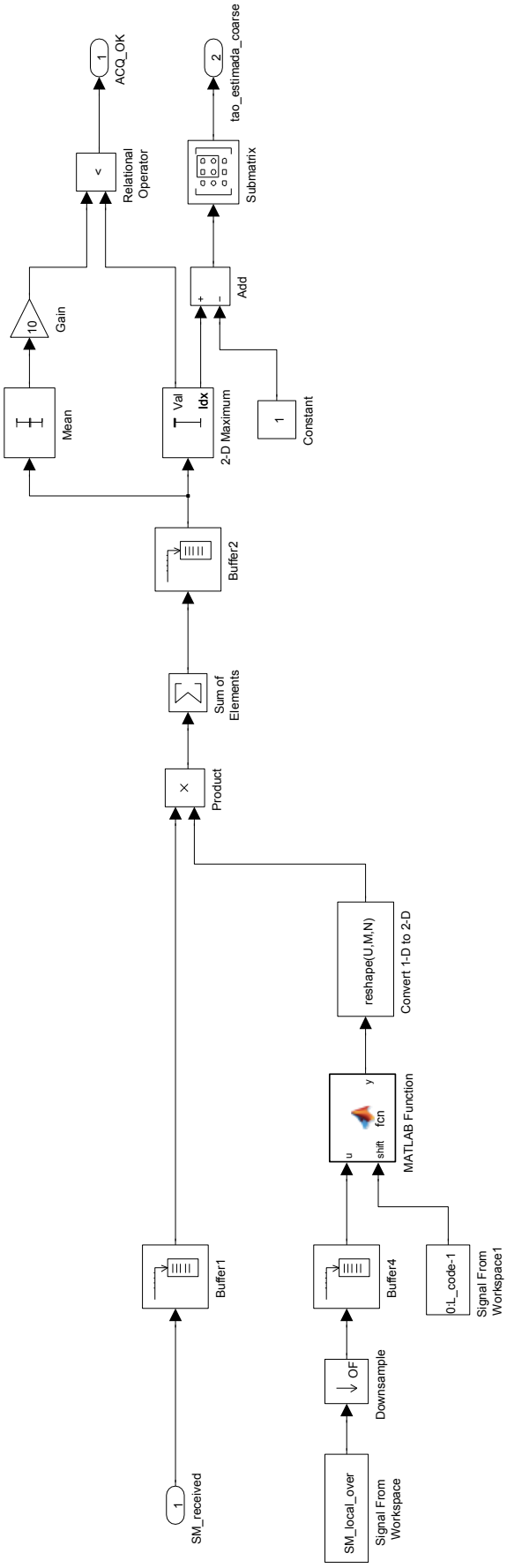

Figure A.7: Diagram of the delay acquisition stage

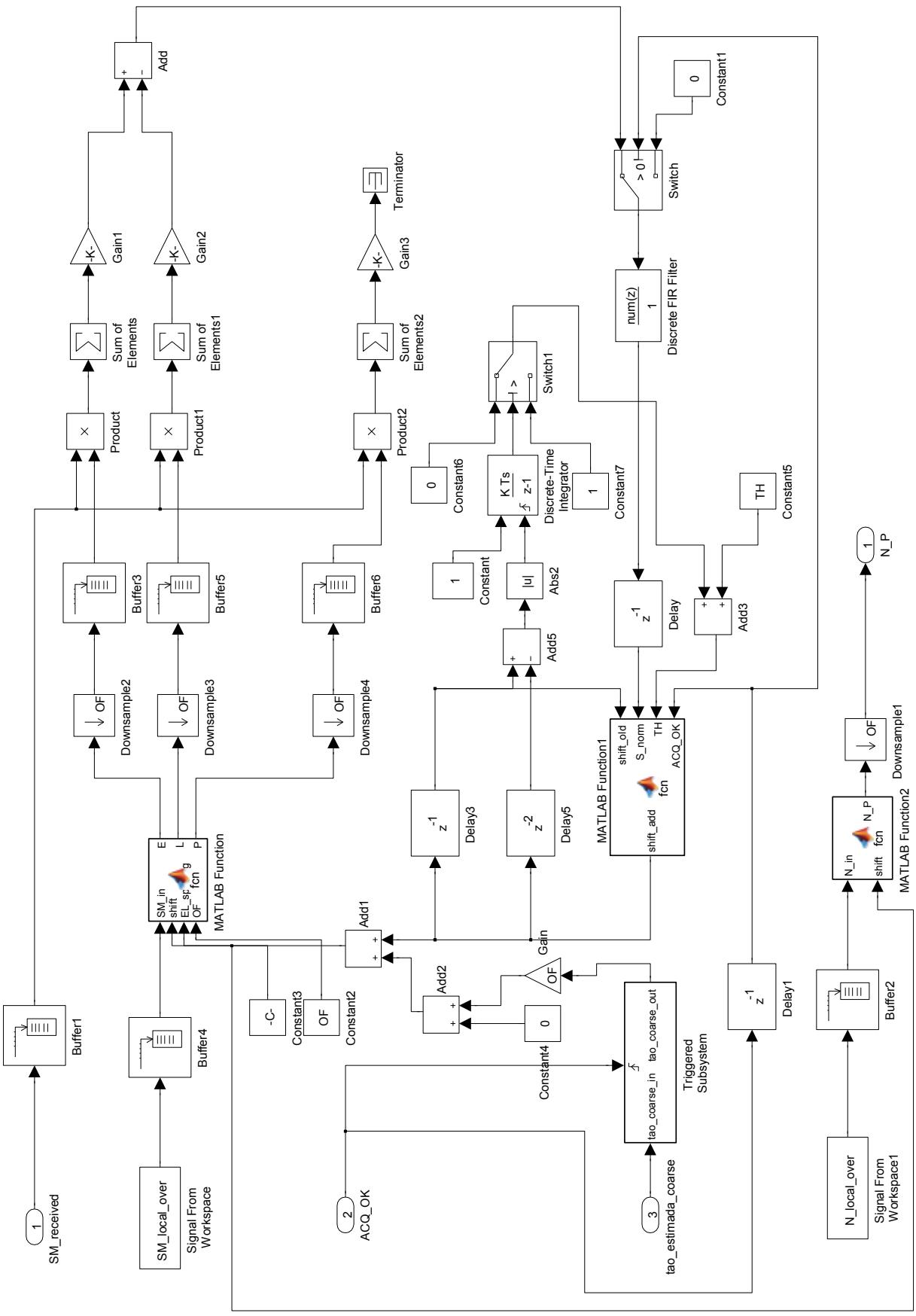

Figure A.8: Diagram of the delay tracking stage (ELDLL)

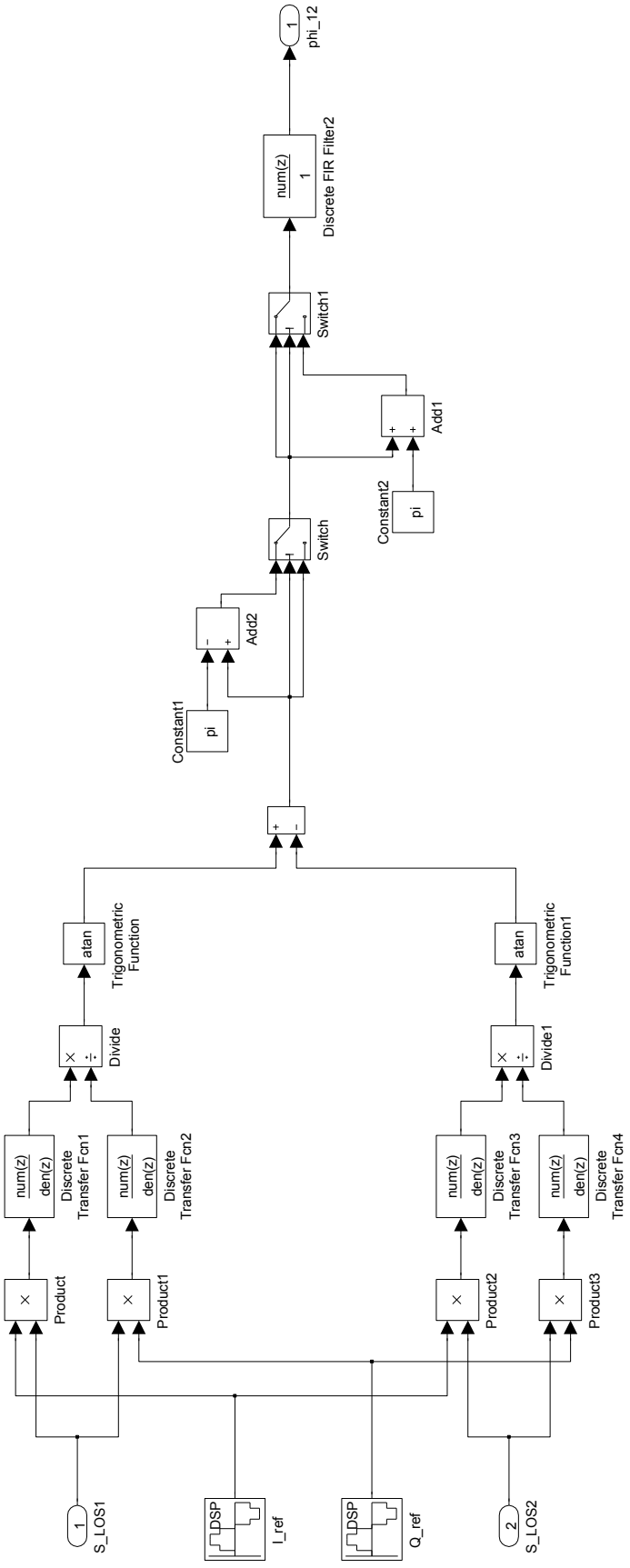

Figure A.9: Diagram of the differential phasemeter (I/Q demodulation)